MULTI-SCALE SIMULATIONS OF SINGLE-WALLED CARBON NANOTUBE ATOMIC FORCE MICROSCOPY AND DENSITY FUNCTIONAL THEORY CHARACTERIZATION OF FUNCTIONALIZED AND NON-FUNCTIONALIZED SILICON SURFACES

Thesis by

Santiago de Jesus Solares Rivera

In Partial Fulfillment of the Requirements

for the Degree of

Doctor of Philosophy

California Institute of Technology

Pasadena, California

2006

(Defended 11 May 2006)

To my wife, Melissa

ACKNOWLEGEMENTS

I thank God for life, family, and friends, and for all the gifts He constantly gives us. I cannot even begin to count all the good things I have received.

I thank my wonderful wife, Melissa, for being a loving and supporting companion.

I thank my parents, Santiago and Catalina, for providing me with a loving home and for all their hard work in raising our family. I thank my siblings, Arturo and Doris, for adding color to my life.

I thank the rest of our family and friends in various countries, who in so many ways have contributed and continue to contribute to all the things in which I participate.

I thank my advisor, professor William Goddard, for the many opportunities he has provided me with, for everything he has taught me, and above all for his friendship and trust.

I thank my co-advisors and instructors, Doctors Mario Blanco (a very generous and supportive friend who has spent so much of his busy time teaching me many of the methods upon which my research rests) and Siddharth Dasgupta, Professors Pat Collier, Jim Heath, and Nate Lewis, as well as the Chemical Engineering Faculty, especially Professors Zhen-Gang Wang and Konstantinos Giapis, for their teaching, guidance, and friendship. Very special thanks also to Kathy Bubash.

I thank all the members of the Materials and Process Simulation Center (very special thanks to Shirley Wu, Jenny Du, Darryl Willick, and Welison Floriano) and all of my

teachers and mentors at previous institutions for sharing their lives and experiences with me.

Last but not least, I thank all the Caltech staff who works hard to provide us with the wonderful environment we have. I have enjoyed the friendship of *so many* persons here that the pages of this document would not be sufficient to write all the good things I have to say about them.

ABSTRACT

This dissertation focuses on two theoretical research topics: *Multiscale Simulations of Single-Walled Carbon Nanotube Atomic Force Microscopy* (AFM, chapters 1 through 3) and *Density Functional Theory Characterization of Functionalized and non-functionalized Silicon Surfaces* (chapters 4 through 8). The first topic presents the development of an AFM simulation methodology, based on first principles, which incorporates the atomistic details of probe, sample, and impurities in the construction of the images. It also includes studies of the influence of common artifacts (such as elastic deformations and imaging multistability) and probe structure (tilt angle and number of walls in the carbon nanotube probe) on image quality. The second topic concerns the structure and energetics of reconstructed and unreconstructed silicon (111) surfaces (either functionalized with groups such as methoxy and methyl or without functionalization) and non-functionalized copper-silicon surfaces and crystals. These studies lead to novel findings such as the formation of a full stacking fault on the methylated Si(111) surface in the presence of large etch pits and the quantification of the surface energy path of the Si(111) 1x1 → DAS 7x7 reconstruction. Most of this work was done in collaboration with experimental groups and is in agreement with the most current experimental results.

TABLE OF CONTENTS

Chapter 1: Influence of Elastic Deformation on Single-Walled Carbon Nanotube AFM Probe Resolution*

ABSTRACT. We have previously reported that 4-6 nm diameter single wall carbon nanotube (SWNT) probes used for tapping-mode atomic force microscopy (AFM) can exhibit lateral resolution that is significantly better than probe diameter when imaging prone nanotubes on a flat SiO_2 surface. To further investigate this phenomenon, accurate models for use in atomistic molecular dynamics simulations were constructed based on transmission electron microscopy (TEM) and atomic force microscopy (AFM) data. Probe-sample interaction potentials were generated utilizing force fields derived from *ab initio* quantum mechanics calculations and material bulk and surface properties, and the resulting force curves were integrated numerically with the AFM cantilever equation of motion. The simulations demonstrate that under the AFM imaging conditions employed elastic deformations of both the probe and sample nanotubes result in a decrease of the apparent width of the sample. This behavior provides an explanation for the unexpected resolution increase and illustrates some of the subtleties involved when imaging with SWNT probes in place of conventional silicon probes. However, the generality of this

---

* Reproduced with permission from Shapiro, I.R.; Solares S.D.; Esplandiu, M.J.; Wade, L.A.; Goddard W.A. III; and Collier C.P.; *J. Phys. Chem. B* **2004,** *108,* 13613.

phenomenon for other AFM imaging applications employing SWNT probes remains to be explored.

1. Introduction

To date, numerous papers have described the preparation of both multi-wall and single-wall carbon nanotube AFM probes.[1-5] SWNT probes offer topographic imaging resolution superior to that of conventional silicon AFM tips due to their unique chemical and mechanical properties, high aspect ratios, and molecular-scale dimensions.[6-10] In a recent publication we described an efficient SWNT probe fabrication methodology and correlated the structures (acquired by TEM) of 14 probes with the quality of AFM images they produced when imaging a prone SWNT sample.[11] By comparing the observed AFM resolution with the diameter of the probe nanotube measured from the TEM image, we found that the lateral resolution is on average 1.2 times the nanotube probe diameter. This value approaches the expected ideal ratio of unity in the absence of thermal vibrations and bending effects of the probe.[12]

Surprisingly, we have found that in approximately one third of the cases, the apparent lateral resolution of the probe nanotube was actually *better* than expected based on its diameter. In one case (shown in Figure 6 of reference 11) , which forms the basis for the computational work presented here, we found that the lateral resolution from a 5.5 nm diameter SWNT probe was 1.2 nm, just 22% of the probe diameter. Here and in previous investigations we define the lateral resolution of a SWNT probe as the difference between the measured height of a sample, which can be determined to high precision with AFM, and the measured diameter (full width at the noise-floor), as outlined in

Figure 1. In an ideal case, the limiting resolution equals the diameter of the probe. This simplified model, in which the probe and sample are considered to be incompressible objects, has commonly been used to describe AFM resolution.[2,4,5] However, simple geometrical arguments alone cannot explain the sub-diameter resolution we reported. The potential for SWNT AFM probes to be used as common research tools requires a more thorough understanding of how the physical, chemical, and mechanical properties of SWNT probes affect image resolution.

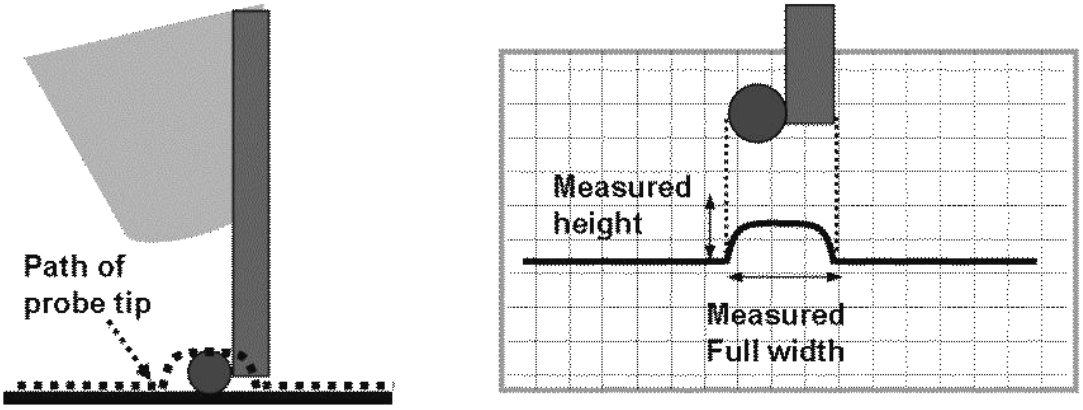

Figure 1: Schematic illustration of the relationship between probe diameter and lateral resolution. The left panel shows a model for a SWNT probe imaging a prone nanotube on a flat surface. The right panel shows the resulting cross sectional profile, from which the width and height of the imaged nanotube are measured. In this simple geometric model, the full width is equal to the sum of the diameters of the probe and sample nanotubes.

To this end, we present here a quantitative atomistic molecular dynamics investigation of SWNT AFM probe behavior in the context of tapping-mode topographic imaging.

The dimensions of the probes and samples are on the order of 1-50 nm, placing them within the range of atomistic simulations. To elucidate the actual tip-sample interactions that give rise to the observed phenomena, we have used TEM - AFM correlation data[11] to construct realistic molecular models of an open-ended SWNT probe interacting with a prone SWNT sample on a flat hydroxyl-terminated silicon surface. These models were used to generate accurate potential curves at different positions of the probe relative to the sample. Integration of the resulting forces into the equation of motion for an oscillating cantilever yielded simulated topographic cross-section profiles that corroborate the experimental results. These simulations indicate that under the AFM conditions employed, both probe bending and localized deformations of the probe and sample SWNTs strongly influence the topographic profile measured with AFM. The reversible elastic nature of these deformations is demonstrated both experimentally and in simulations.

2. Methods

Fabrication, characterization, and imaging with SWNT AFM probes has been described previously.[11] The effective lateral resolution of each probe was obtained by imaging, under ambient conditions in air, a carbon nanotube lying prone on a flat native-oxide silicon surface. To acquire accurate sample height and width measurements using amplitude-modulated AFM it was necessary to first carefully calibrate the response of the system over a wide range of operational parameters, most importantly the oscillation amplitude of the SWNT probe. For example, to understand the effects that vertical compression of a sample nanotube by the AFM probe had on the lateral resolution,

repeated measurements of the sample nanotube height as a function of probe oscillation amplitude were performed for both conventional silicon and SWNT AFM tips. In all cases, the driving amplitudes employed were kept below the limit corresponding to a 10% reduction in the apparent height of the sample nanotube due to compression. In addition, we measured force calibration curves, which consist of scans of the damped oscillation amplitude as a function of the average tip-sample separation for a given cantilever driving force. The force calibration curves revealed the presence of coexisting attractive and repulsive tip-sample interaction regimes.[13,14] Bistable switching of the cantilever oscillation between the two regimes manifests itself as sudden changes in the observed sample height and width.[15] In general, we avoided these amplitude instabilities and the concomitant experimental artifacts by operating the AFM cantilever with a driving force sufficient to give a free-air oscillation amplitude greater than 20 nm. Consequently, all AFM data presented here can be considered in the repulsive regime or "intermittent contact" mode.

The simulation of the AFM tip motion was carried out by integrating the equation of motion for a damped harmonic oscillator at each AFM scan point on the sample using the experimental parameter values contained in Table 1:

$$m\frac{d^2 z(Z_c,t)}{dt^2} = -kz(Z_c,t) - m\frac{\omega_o}{Q}\frac{dz(Z_c,t)}{dt} + F_{ts}(z_{ts}) + F_o\cos(\omega t), \qquad (1)$$

where $z(Z_c,t)$ is the instantaneous tip position with respect to its average position (Z_c), k is the harmonic force constant for the displacement of the tip with respect to its equilibrium rest position, m is the effective mass, $\omega_0 = \sqrt{k/m}$ is the free resonant frequency, Q is the quality factor, z_{ts} is the instantaneous tip position *with respect to the sample*, $F_{ts}(z_{ts})$

$_{IS}$ the calculated tip-sample interaction force, and $F_O\cos(\omega t)$ is the oscillating driving force applied to the cantilever.

Table 1: Tapping-mode AFM parameters used for numerical simulations.

Cantilever spring constant	k = 4.8 N/m
Cantilever quality factor	Q = 150
Cantilever resonant frequency	$\omega/2\pi$= 47.48 kHz
Free air oscillation amplitude	A_o = 39 nm
Amplitude set-point	A_{sp} = 15.4 nm
Excitation force	F_o = 1.25 nN

The use of this equation to describe tip motion approximates the SWNT tip-cantilever ensemble as a point-mass harmonic oscillator. Nevertheless, this model has been used extensively for numerical treatment of tapping-mode AFM with conventional probes.[13,16,17,20] Although the actual dynamics of the oscillating cantilever in the presence of the probe-sample interactions are nonlinear, the validity of the harmonic approximation for modeling conventional tapping mode AFM imaging in air has been demonstrated with both theory and experiment for the range of parameters used here. We tested the validity of this approximation for the case where an individual SWNT is attached to the end of the silicon AFM tip by plotting the cantilever trajectory as a function of time from Equation (1) and found that over 99% of the excitation energy resides in the fundamental frequency.

Prior to integrating Equation (1) we obtained the required tip-sample interaction forces using atomistic models, as explained in detail below. All molecular dynamics (MD) simulations were carried out using Cerius2 molecular simulations software (Accelrys, San Diego, CA). The MD force field parameters were optimized by fitting the material bulk and surface properties such as elasticity moduli, vibrational frequencies, and surface geometry both to experimental data and to rigorous quantum mechanics calculations on clusters representative of the silicon and graphene systems under study. Equation (1) was integrated using the Verlet algorithm to fourth-order accuracy for the tip position and second-order accuracy for the tip velocity.[18]

Realistic atomistic models were constructed for the SWNT probe used for tapping mode AFM imaging. Every effort was made to match the model structures and simulation conditions as closely as possible to corresponding experimental values, including the nanotube probe diameter, length, angle relative to the substrate normal, and the fine structure at the probe end. All silicon surfaces were (100) and were terminated with hydroxyl groups. The probe was a (40,40)[19] armchair SWNT (5.4 nm diameter, 45 nm length, with 5 nm of fixed atoms at one end of the probe to simulate its attachment site at the AFM tip) constructed from approximately 25,000 carbon atoms. The sample was a (16,16) armchair SWNT (2.2 nm diameter, 10 nm length) constructed from approximately 2600 carbon atoms. The sample SWNT was kept fixed at both ends during the calculations to simulate a very long nanotube, which is unlikely to displace laterally during AFM tapping. Similar models were generated for a conventional silicon tip interacting with the sample nanotube. Several of these models are shown in Figure 2.

The tip-sample interaction potentials were constructed by vertically approaching the sample with the probe nanotube at 0.05 nm intervals, at each point optimizing the system

geometry by minimization of the potential energy (additional calculations performed at 300 K showed that the potentials did not significantly change with inclusion of thermal vibrations at room temperature. See supporting information). The gradient of this energy-position function with respect to the vertical tip position is the tip-sample interaction force.

In order to reduce the computational cost of the molecular simulations, each model of a nanotube on the surface included only a small section of the silicon surface, sufficient to obtain an accurate description of the SWNT probe interactions with the sample. This does not give an accurate description of the interaction of the tip with the silicon surface for the cases in which the SWNT tip deforms and slips against one side of the sample nanotube and makes contact with the underlying substrate. To correct this, another model was constructed *without* a sample nanotube on the substrate to obtain the interaction forces between the tip and the bare silicon surface. The deformation of the tip was considered in all cases when calculating the relative position of the surface and the end of the tip for each scan point.

This procedure provides a discrete set of points, and so regression analysis with simple functional forms (e.g., polynomials or functions of the form $1/r^n$) was performed in order to obtain continuous force-position curves, which can be programmed easily into the AFM dynamics integration code. The forces for a given vertical position of the tip may have different values, depending on whether the tip has slipped relative to the sample SWNT. This was accounted for during the construction of the force-position curves and incorporated into the integration of the cantilever equation of motion.

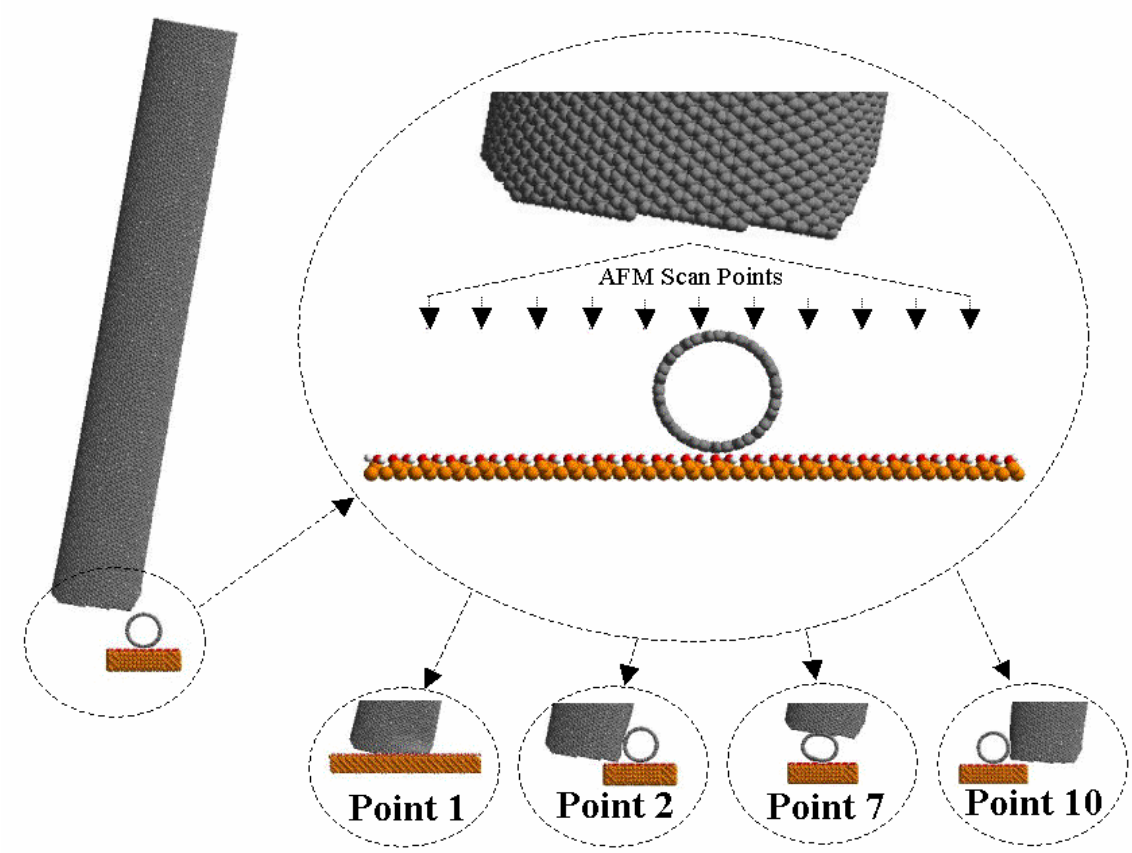

Figure 2: Illustration of the models used to construct the tip-sample interaction profile. The models were constructed based on experimental TEM and AFM data. The final tip position during the AFM scan is shown for four of these points. The corresponding force curves are shown in Figure 3.

3. Results and Discussion

A series of eleven curves showing probe-sample force versus height were generated at evenly-spaced points along the line perpendicular to the axis of the sample nanotube. The separation between adjacent points was 1 nm. Figure 2 shows the location of the eleven scan points relative to the sample nanotube, and four of the corresponding tip-

sample force curves are shown in Figure 3 (all 11 energy-position curves, from which these force curves were obtained by differentiation, are provided in the supporting information). The abscissa on all graphs in Figure 3 corresponds to the distance between the lowest atom on the SWNT tip and the highest atom of the Si(100)-OH surface. Negative values on this axis correspond to elastic deformations in nanotube and surface geometry, including local deformation of the probe as well as slight deformation of the Si-OH surface.

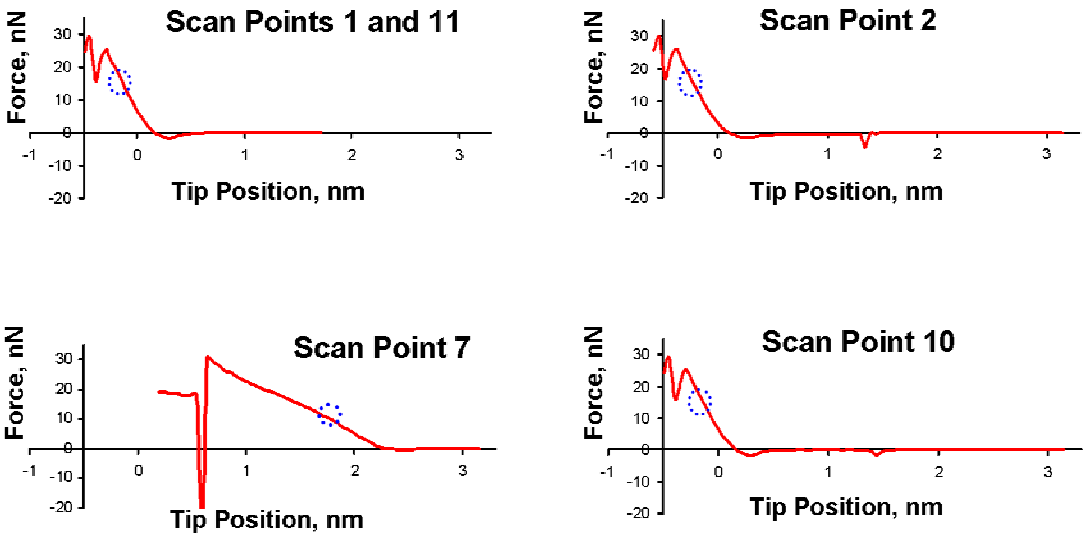

Figure 3: Tip-sample force curves calculated for four of the eleven scan points shown in Figure 2. The abscissa on all graphs corresponds to the distance between the lowest atom on the SWNT tip and the highest atom of the Si(100)-OH surface. The small blue circle in each plot indicates the lowest position that the probe tip reached during the subsequent AFM imaging simulation.

Each of the eleven probe-sample force curves generated along the scan line was then inserted into Equation (1) and integrated for the average tip positions relative to the substrate (Z_c) ranging from 50 to zero nm using actual imaging parameter values[11]. For each scan point and tip position, Equation (1) was integrated numerically for 0.02 seconds with a 0.1 ns integration step (to fourth order accuracy with respect to the time step-size) to determine the oscillation amplitude of the cantilever as a function of its vertical position (the initial tip position was set equal to its equilibrium position, i.e., $z(Z_c,0) = 0$, and the initial velocity was set to zero in all cases). This numerical procedure is analogous to acquiring a "force calibration curve" for each scan point in Figure 2.

The result of these calculations was a curve showing the cantilever equilibrium oscillation amplitude as a function of the average vertical position of the tip for each point along the scan direction. Two of these curves are shown as insets in Figure 5. The simulated cross-section trace in Figure 5 was then constructed by plotting the locus of tip position values, which maintained the oscillation amplitude at the set-point value of 15.4 nm. Note that the average tip-sample separation for each scan point is given relative to the bare silicon oxide substrate.

The construction of tip-sample interaction force curves through molecular simulations of large finite systems underestimates the long-range attractive forces present in the system. This is because the calculation of non-bonded interaction energies between pairs of atoms is generally limited to a cutoff radius on the order of 1 nm or less to reduce the cost of the computation (the number of non-bonded interactions, which scales with the square of the number of atoms in the simulation, can account for over 90% of the computation costs of a typical system). Underestimating the long-range attractive forces, and hence the region of positive force gradient, can alter the predicted regions of

amplitude bistability.[13] However, at the free oscillation amplitude employed here, $A_0 = 39$ nm, the average force will be determined almost exclusively by the repulsive part of the tip-sample interaction potential,[16] and thus the underestimation of the attractive contribution will have negligible influence on the simulated topographic profile.

Under ambient conditions, a thin film of water is adsorbed on hydrophilic surfaces such as SiO_2. The formation of a meniscus, or liquid bridge between the surface and the probe, will result in an additional attractive capillary force that depends on probe-sample distance.[21] We did not include the effects of adsorbed water in our model. We do not expect that inclusion of these effects will significantly change the nanoscopic interactions between the probe and sample nanotubes predicted by the simulations. Future work will address this issue.

Simple models of AFM resolution assume that the probe is a rigid, incompressible cylinder with a flat or hemispherical end. In practice this is not the case. High magnification TEM images show that the ends of the probe nanotubes are generally open due to ablation from an electrical etching procedure used to shorten the nanotube probes to useful lengths.[2,4] Purely geometric arguments suggest that an open-ended tube with protruding asperities could, for extremely low-relief samples, provide resolution comparable to the asperity diameter rather than the full diameter of the probe, in direct analogy to results published using silicon probes.[22] However, probe asperities are unlikely to be important when imaging a sample nanotube that has a diameter (height above the surface) comparable to that of the probe.

The Young's modulus of SWNTs is approximately 1.25 TPa along the tube axis.[23] Because of this very high stiffness only a small amount of longitudinal compression of the tube occurs during AFM imaging. However, Snow and coworkers have shown that

SWNT probes are susceptible to bending due to their high aspect ratio if not oriented vertically relative to a surface.[12] This bending can be minimized by shortening the nanotube probe so that it protrudes less than 100 nm beyond the supporting silicon tip.

While SWNTs have exceptional longitudinal stiffness, radially they are far more compliant,[24] a characteristic which permits localized deformation of the nanotube walls in addition to large-scale bending along the tube axis. The susceptibility of nanotubes to radial deformation is predicated upon two competing effects: the energy cost associated with strain of the nanotube as it is deformed from its equilibrium cylindrical geometry and the stabilization that a compressed nanotube gains due to increased interlayer van der Waals attractions. These two competing effects scale in opposite directions with increased nanotube diameter, such that larger SWNTs are easier to deform radially than smaller diameter tubes.[25] We have previously observed that SWNTs attached to silicon AFM tips via the pick-up method tend to be 4-6 nm, which is larger than the tubes observed lying prone upon the pick-up substrate (1-3 nm).[11] We postulated that the increase in net binding energy with larger diameter nanotubes stems from the interplay between van der Waals forces and the geometric stiffness of a nanotube. The resulting radial "softness" of these larger nanotubes not only increases the energy with which they bind to a silicon probe during pick-up, but also has significant implications when they are subsequently used for AFM imaging.

Our molecular dynamics simulations show lateral slipping of the probe nanotube relative to the sample nanotube due to both bending along the length of the probe and localized radial deformation of the probe and sample at the point of contact (illustrated in Figure 4 and the supporting information). This behavior is a function of the structures and relative orientations of the probe and sample nanotubes, the applied tip-sample force,

and the position (in the x-y plane) of the probe nanotube relative to the sample nanotube. The smaller the x-y distance between the center of the probe tube and the axis of the sample tube, the larger the force required to deform the nanotubes and cause them to slip past one another. That is, when the probe presses on the edge of the sample nanotube, a smaller amount of force is required to cause it to slip laterally than when it presses on the crown of the sample nanotube. The simulations show this deformation behavior to be completely reversible and elastic (images illustrating reversibility are provided in the supporting information). Experimentally, the elasticity is demonstrated by the fact that we have not observed the topographic cross sections to change significantly during imaging at a given amplitude set-point, and the TEM images taken of each probe subsequent to AFM imaging show no alterations of the nanotube structure, such as kinks or buckles.

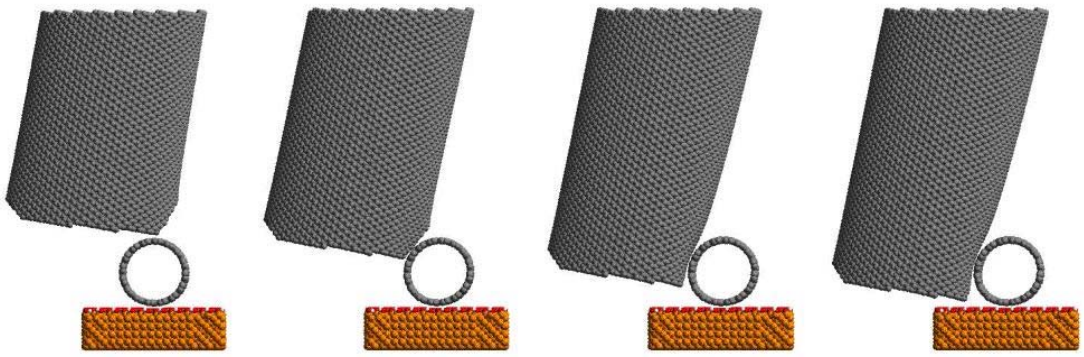

Figure 4: Illustration of the slipping phenomenon of the SWNT probe past the SWNT sample for scan point 3. Both bending along the length of the probe and local deformation contribute to slipping. The picture shows that the simulated probe is more susceptible to deformation, although the sample nanotube does deform slightly. This is

due to the larger diameter of the probe (5.4 vs. 2.2 nm), which decreases its radial rigidity.

This lateral slipping and deformation of the probe nanotube explains the observation of sub-probe-diameter effective resolution. In amplitude-feedback tapping mode AFM, modulation of the cantilever oscillation amplitude depends on the average strength of the tip-sample forces.[26] The AFM controller adjusts the extension of the z-piezoelectric element in order to hold the amplitude of the cantilever oscillation at the fixed value designated by the amplitude set-point (an independent variable set by the user). The resulting z-piezo voltage corrections are converted to units of length and output as the topographic height data. If the probe and sample deform negligibly under the associated tapping forces, the sample height can be measured accurately to within the precision of the piezoelectric element, typically < 1Å. However, if either material is significantly deformable, the resultant z-piezo data represents a more complex convolution of probe and sample structure.

The simulations conducted here indicate that when the probe SWNT is tapping on an edge of the sample SWNT, the subsequent repulsive forces deform *both* nanotubes sufficiently to allow them to slip past one another without significantly influencing the cantilever oscillation amplitude. In fact, when the very edges of the probe and sample tubes come into contact, the net tip-sample force is actually attractive rather than repulsive due to the large area of favorable contact between the graphitic surfaces. This is illustrated in the force curves for scan points 2 and 10 by the fact that the net force is negative between the two local minima, corresponding to the region in which the probe and the sample are slipping past one another. Once lateral slipping takes place, the resulting tip-sample interaction is dominated by the repulsive forces between the probe

SWNT and the Si/SiO_2 surface. Thus, for that particular x-y position, the AFM controller does not "see" the sample nanotube. Only when the probe SWNT is positioned closer to the crown of the prone sample SWNT are the interaction forces between the probe and sample nanotubes high enough to cause sufficient damping of the cantilever oscillation amplitude. At scan point 7, which corresponds to the probe tapping on the crown of the sample nanotube, no slipping can take place under the imaging conditions given in Table 1 because the maximum tip-sample repulsive force does not exceed the necessary threshold: ~30 nN. Here, the cantilever amplitude is damped by the sample nanotube, and the AFM records the interaction. The net result is that the topographic data indicates an apparent nanotube width which is smaller than the sum of the probe and sample SWNT diameters.

A quantitative representation of this phenomenon is illustrated in Figure 5. The lower half of the Figure shows the effective cross section of a sample nanotube calculated from the MD and AFM dynamics simulations, obtained when using a SWNT probe under the repulsive tapping conditions given in Table 1. This scan shows two important features that are also observed experimentally. First, the apparent probe resolution for this simulation is 2.0 nm, 37% of the probe diameter. Additionally, the simulated cross section is asymmetric, which is a direct consequence of the specific SWNT probe geometry, particularly the tilt-angle, that favors probe-sample slipping more on one side of the sample than on the other.

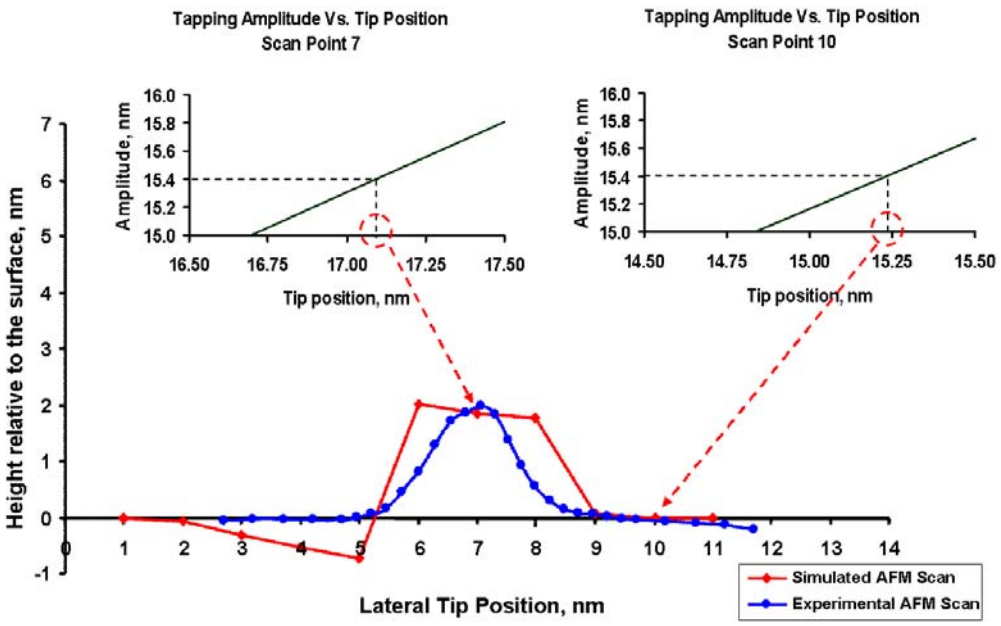

Figure 5: Schematic depiction of the construction of an AFM scan from molecular and AFM dynamics simulations. The two inset amplitude-distance curves illustrate how the measured height is obtained for each scan point at an amplitude set-point of 15.4 nm. The resulting AFM cross sectional height is given relative to the average tip separation from the bare SiO_2 surface. The horizontal axis corresponds to the scan points shown in Figure 2. For comparison, the cross section from experimental data has been overlaid on the same scale with its center point arbitrarily positioned to match up with the center of the simulated cross section.

In contrast, MD simulations have shown that a conventional silicon probe does not slip under the same imaging conditions. This is because the rigidity of the silicon probe requires higher forces to induce deformation, while the larger radius of curvature of the probe tip actually generates smaller lateral forces compared to a SWNT probe. The different behavior is also due to the chemical properties of crystalline silicon, which strongly influence the surface-surface interactions with the SWNT sample, as well as the

attractive van der Waals forces between the larger silicon tip and the silicon surface. These two parameters in particular, probe compressibility and adhesion forces, are transformed in a highly nonlinear way by the response of the oscillating tip.[27] Thus, SWNT probes perform in a fundamentally different manner than silicon probes, not merely when imaging prone carbon nanotubes, but for a variety of samples.

We have also simulated a smaller diameter SWNT probe since previous reports have described nanotube probes in the 1-3 nm diameter range.[1,2,4,7] Smaller diameter nanotube probes should be far less susceptible to localized radial deformation due to their increased geometric stiffness against compression (as seen with the sample nanotube, Figure 4). However, the bending mode along the length of a thinner probe should actually be softer since the flexural rigidity scales as r^4.[28] The probe was a (16,16) armchair SWNT (2.2 nm diameter, 20 nm length) which had approximately the same aspect ratio as the larger 5.4 nm probe used in this study. As before, the probe nanotube was oriented at 15˚ relative to the surface normal, and the sample nanotube was 2.2 nm in diameter and 10 nm in length. Images from the simulation are incorporated in the supporting information and show that slipping also occurs for the thinner probe when tapping on the edge of the sample nanotube. For this probe, the slipping is almost entirely due to bending and not to local deformation. The corresponding tip-sample force curve indicates that the force opposing the slipping motion of the probe was negligible.

Dekker and coworkers have reported previously that as a function of driving amplitude in tapping mode imaging, a conventional silicon AFM probe can vertically compress a 1.4 nm single-wall nanotube lying on a flat surface, resulting in a decreased apparent *height*.[29] This experimental observation is consistent with previously reported experimental measurements and molecular dynamics simulations, which described radial

deformation of 1-3 nm single-wall carbon nanotubes by both van der Waals forces and external static loads.[30-32] Here we show that in tapping-mode AFM, the associated forces deform the probe nanotube in addition to the sample, strongly influencing the subsequently measured effective *lateral* resolution.

Our molecular dynamics simulations confirm that some vertical compression of a prone sample nanotube occurs under standard tapping-mode AFM conditions for both conventional silicon AFM probes and SWNT probes. However, the simulations predict that this effect is, at most, 10% of the sample tube diameter for 1-3 nm SWNTs and occurs primarily when the probe nanotube is tapping on the crown of the sample nanotube (see for example, point 7 in Figure 2). This corresponds well with our experimental calibration of sample tube compression under the tapping mode operating parameters employed. The increase in lateral resolution, on the other hand, is due to the highly localized deformation and bending of the probe nanotube along the edges of the sample nanotube and is therefore not affected significantly by vertical compression.

4. Conclusions

By correlating experimental data with atomistic molecular dynamics simulations, we have characterized how the unique properties of SWNT AFM probes can strongly influence topographic imaging fidelity. Probe bending and mutual local deformation of both the probe and sample nanotubes under typical tapping-mode AFM forces can result in a reduction of the measured width of the sample tube and, consequently, an ostensive improvement of the lateral resolution to the extent that the resolution can appear to be better than expected from the measured diameter of the nanotube probe. We are

interested in determining whether a similar increase of apparent resolution is observed when imaging less compliant samples, such as metallic or semiconducting nanoparticles.

Given the interest in nanoscale physical and biological phenomena, SWNT probes are likely to evolve into a more common research tool. A complete understanding of probe behavior in the context of atomic force microscopy is therefore critical. It is important to note that the lateral resolution reported here is an apparent value, arising from the simplified definition set forth in the introduction, and was studied for the specific case of 4-6 nm diameter SWNT probes imaging 2-3 nm diameter SWNTs adsorbed on a flat surface. In practice, the resolving power of an AFM probe is dependent upon the experimental context. It is of particular importance to determine whether the observed deformation phenomenon results in a net gain or loss of structural information when SWNT probes are used to image soft nanoscale samples such as biological macromolecules. The improvement in the apparent resolution due to radial deformation of the probe nanotube in this study was a consequence of the relatively high driving forces applied to the AFM cantilever. Tapping mode AFM imaging performed in this repulsive regime with conventional probes has been shown to damage biomolecules.[14] In addition, resolution less than the probe diameter could complicate interpreting AFM images quantitatively.

The combination of probe structure determination, characterization of imaging resolution, and simulated dynamic behavior described here has highlighted practical differences between carbon nanotube probes and conventional silicon probes. This work also underscores the usefulness of atomistic simulations in describing the dynamic nanoscale interactions involved in scanning probe microscopy.

Acknowledgement: The authors thank Professor Stephen Quake, Dr. Jordan Gerton and Ms. Yuki Matsuda for essential discussions. Ian Shapiro, Maria Esplandiu and Patrick Collier were supported by Caltech startup funds, and by Arrowhead Research. Santiago Solares and William Goddard were supported by NSF-NIRT grant CTS-0103002. Wade was supported by the Caltech President's Fund and NASA contract NAS7-1407.

SUPPORTING INFORMATION

1. Tables of force field parameters:

TABLE S-1: Force Field Energy Expression

Total Energy	$E = E_{\text{bond stretch}} + E_{\text{angle bend}} + E_{\text{torsion}} + E_{\text{stretch-bend-stretch}} + E_{\text{stretch-stretch}} + E_{\text{van der Waals}}$ *
Bond Stretch Energy Type Harmonic	$E = \frac{1}{2} K_b (R - R_o)^2$
Bond Stretch Energy Type Morse	$E = D_o (e^{-\alpha(R-R_o)} - 1)^2$ where $\alpha = \sqrt{\frac{K_b}{2D_o}}$

Angle Bend Energy Theta Harmonic	$E = \frac{1}{2} K_\theta (\theta - \theta_o)^2$
Angle Bend Energy Cosine Harmonic	$E = \frac{1}{2Sin^2\theta_o} K_\theta (Cos\theta - Cos\theta_o)^2$
Torsion Energy Dihedral	$E = \frac{1}{2} K_t [1 - d_t Cos(n_t \phi)]$
Stretch-Bend-Stretch Energy R-Cosine	$E = (Cos\theta - Cos\theta_o)[C_{ij}(Rij - Rij_o) + C_{jk}(Rjk - Rjk_o)]$
Stretch-Stretch Energy R-R	$E = K_{ss}(Rij - Rij_o)(Rjk - Rjk_o)$
Van der Waals Energy Morse	$E = D_o(\chi^2 - 2\chi)$ where $\chi = e^{\frac{-\gamma}{2}(\frac{R}{R_o} - 1)}$
Van der Waals Energy Lennard-Jones 6-12	$E = D_o((\frac{R_o}{R})^{12} - 2(\frac{R_o}{R})^6)$

***** The present study did not consider charged samples or probes; hence the energy expression does not include electrostatic energy terms.

TABLE S-2: Force Field Atom Types

H_	Non-acid hydrogen
H___A	Acid hydrogen
C_3	SP^3 carbon
C_2G	SP^2 graphite carbon
O_3	SP^3 oxygen
Si0	Bulk silicon
SiS	Surface silicon
SiOH	Surface silicon connected to OH group
SiH	Surface silicon connected to H_

TABLE S-3: Harmonic Bond Stretch Parameters

Atom 1	**Atom 2**	**K_b**	**R_o**
SiOH	O_3	700.0000	1.5870
O_3	H___A	500.0000	1.0000
C_3	H_	662.6080	1.1094
C_3	C_3	699.5920	1.5140
C_2G	H_	700.0000	1.0200
C_2G	C_3	739.8881	1.4860
H_	H_	700.0000	0.7500

TABLE S-4: Morse Bond Stretch Parameters

Atom 1	**Atom 2**	K_b	R_o	D_o
SiOH	H_	382.3870	1.4830	92.6000
SiH	H_	382.3870	1.4830	92.6000
Si0	Si0	193.0936	2.3810	73.7000
SiOH	Si0	193.0936	2.3810	73.7000
SiH	Si0	240.0660	2.3810	73.7000
SiOH	SiOH	193.0936	2.3810	73.7000
SiH	SiH	193.0936	2.3810	73.7000
C_2G	C_2G	720.0000	1.4114	133.0000
SiS	Si0	193.0936	2.3810	73.7000
SiS	SiS	193.0936	2.3810	73.7000

TABLE S-5: Angle Bend Parameters

Atom 1	Atom 2	Atom 3	Type	K_θ	θ_o
C_2G	C_2G	C_2G	Cosine harmonic	196.1300	120.0000
C_2G	C_2G	C_3	Cosine harmonic	196.1300	120.0000
C_3	C_2G	C_3	Cosine harmonic	188.4421	120.0000
C_2G	C_3	C_2G	Cosine harmonic	220.2246	109.4710
C_3	C_3	C_3	Cosine harmonic	214.2065	109.4710
C_3	C_2G	H_	Cosine harmonic	98.7841	120.0000
Si0	SiH	H_	Cosine harmonic	42.2500	115.1400
Si0	Si0	Si0	Cosine harmonic	31.2682	105.0467
C_3	C_3	H_	Cosine harmonic	117.2321	109.4710
C_2G	C_3	H_	Cosine harmonic	121.6821	109.4710
C_2G	C_3	C_3	Cosine harmonic	220.2246	109.4710
C_2G	C_2G	H_	Cosine harmonic	103.1658	120.0000
Any	O_3	Any	Theta harmonic	100.0000	104.5100
H_	SiOH	H_	Cosine harmonic	58.2560	110.9530
Si0	SiOH	O_3	Cosine harmonic	102.7429	109.4710
SiOH	SiOH	Si0	Cosine harmonic	31.2682	105.0467
SiOH	Si0	Si0	Cosine harmonic	31.2682	105.0467
SiOH	Si0	SiOH	Cosine harmonic	31.2682	105.0467
SiH	SiH	Si0	Cosine harmonic	31.2682	105.0467
Si0	SiH	Si0	Cosine harmonic	31.2682	105.0467
SiH	Si0	SiH	Cosine harmonic	31.2682	105.0467
SiS	Si0	Si0	Cosine harmonic	31.2682	105.0467
SiS	Si0	SiS	Cosine harmonic	31.2682	105.0467

Si0	SiOH	Si0	Cosine harmonic	31.2682	105.0467
SiOH	SiOH	O_3	Cosine harmonic	102.7429	109.4710
SiH	SiH	H_	Cosine harmonic	42.2500	115.1400
Si0	SiS	Si0	Cosine harmonic	31.2682	105.0467
SiS	SiS	Si0	Cosine harmonic	31.2682	105.0467
O_3	SiOH	H_	Cosine harmonic	57.6239	109.4710

TABLE S-6: Torsion Parameters

Atom 1	**Atom 2**	**Atom 3**	**Atom 4**	**K_t**	**n_t**	**d_t**
C_2G	C_2G	C_2G	C_2G	85.1200	2.0000	1.0000
Any	C_2G	C_2G	Any	100.0000	2.0000	1.0000
Any	C_2G	C_3	Any	2.0000	3.0000	-1.0000
Any	C_3	C_3	Any	2.0000	3.0000	-1.0000
Any	SiOH	O_3	Any	2.0000	3.0000	-1.0000

TABLE S-7: Stretch-Bend-Stretch Parameters

Atom 1	**Atom 2**	**Atom 3**	**Rij**	**Rjk**	**θ_o**	**C_{ij}**	**C_{jk}**
Si0	Si0	Si0	2.3810	2.3810	109.4712	-14.8184	-14.8184

TABLE S-8: Stretch-Stretch Parameters

Atom 1	**Atom 2**	**Atom 3**	**K_{ss}**	**Rij_o**	**Rjk_o**
Si0	Si0	Si0	3.6001	2.3810	2.3810

TABLE S-9: van der Waals Parameters

Atom 1	Atom 2	Type	D_o	R_o	γ
H_	H_	Morse	0.018145	3.56979	10.70940
H___A	H___A	LJ 6-12	0.000099	3.19499	N/A
C_3	C_3	LJ 6-12	0.146699	3.98300	N/A
C_2G	C_2G	Morse	0.098999	3.993999	10.96300
O_3	O_3	LJ 6-12	0.095700	3.404599	N/A
Si0	Si0	LJ 6-12	0.310000	4.269999	N/A
SiS	SiS	LJ 6-12	0.310000	4.269999	N/A
SiOH	SiOH	LJ 6-12	0.310000	4.269999	N/A
SiH	SiH	LJ 6-12	0.310000	4.269999	N/A
C_2G	H_	Morse	0.034710	3.744610	12.25614
SiOH	C_2G	LJ 6-12	0.175186	4.132000	N/A
Si0	C_2G	LJ 6-12	0.175186	4.132000	N/A
SiH	C_2G	LJ 6-12	0.175186	4.132000	N/A
SiS	C_2G	LJ 6-12	0.175186	4.132000	N/A
O_3	C_2G	LJ 6-12	0.097336	3.699299	N/A

The original parameters used to create these force fields were developed in the Materials and Process Simulation Center (California Institute of Technology). [33,34,35] Additional parameters were added to study mixed systems (containing silicon, graphitic systems, oxygen, and hydrogen) by applying arithmetic and/or geometric combination rules to existing parameters, by quantum mechanics calculations conducted by Weiqiao Deng, Richard Muller, and William A. Goddard III or by using generic terms from the Dreiding Force Field.[36]

2. Energy-position and force-position curves from MD simulations:

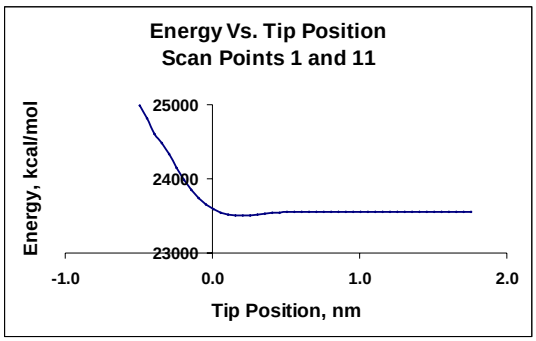

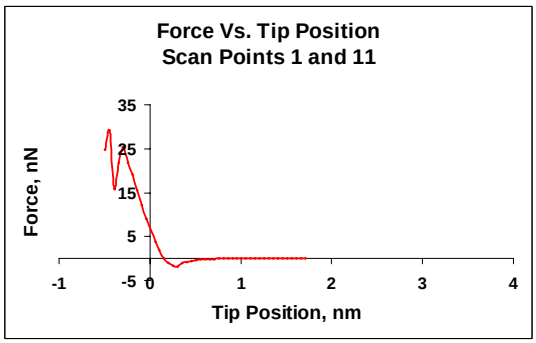

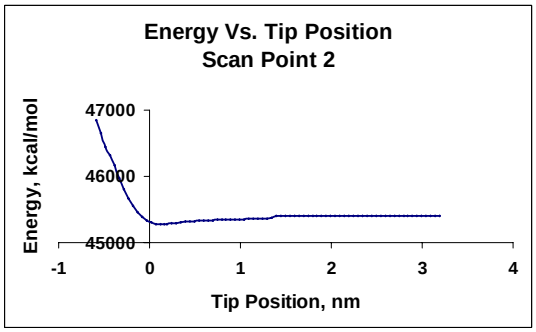

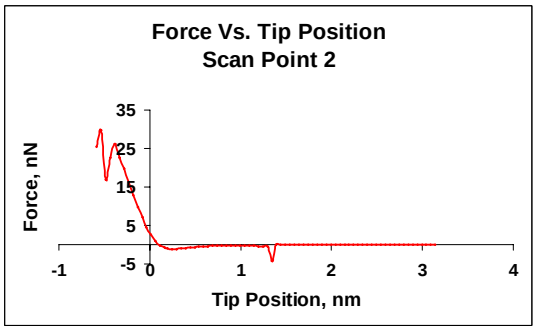

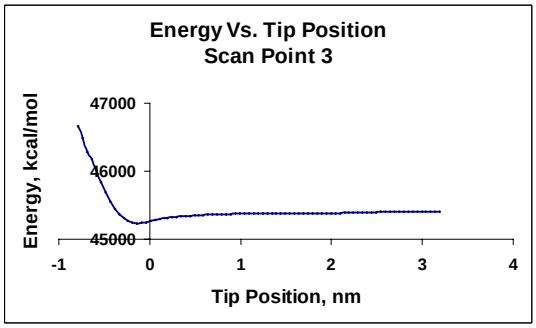

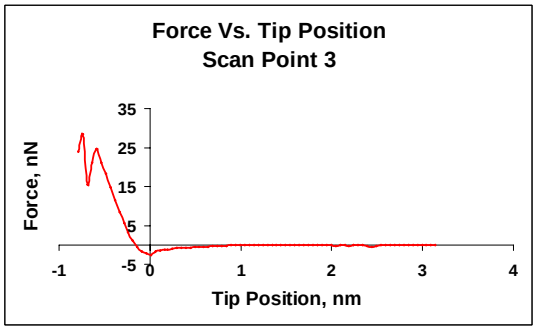

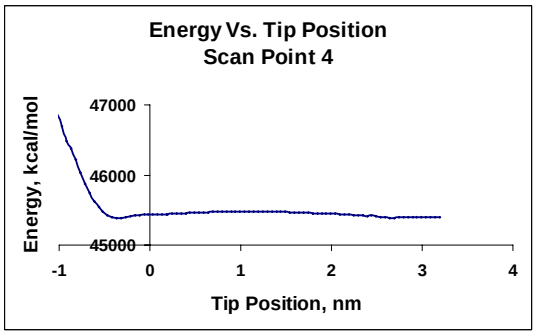

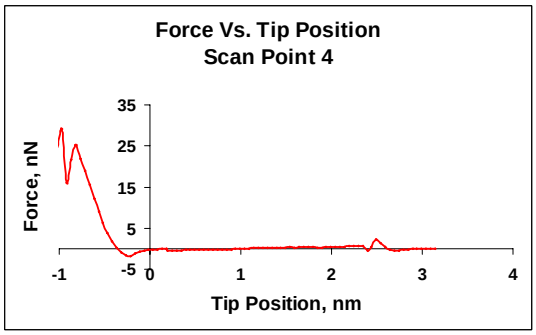

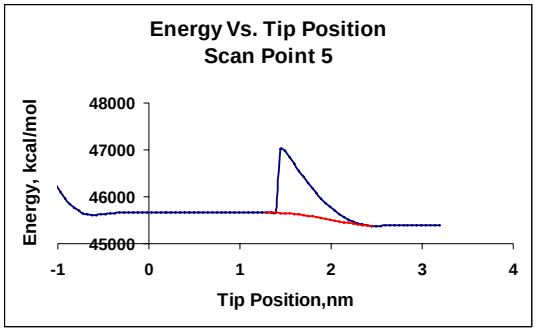
Energy Vs. Tip Position
Scan Point 5
Energy, kcal/mol
48000
47000
46000
45000
-1
0
1
2
3
4
Tip Position,nm

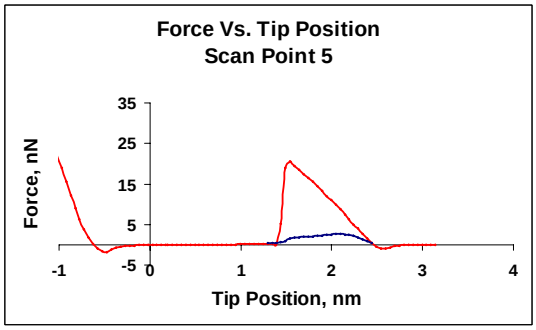
Force Vs. Tip Position
Scan Point 5
Force, nN
35
25
15
5
-5
-1
0
1
2
3
4
Tip Position, nm

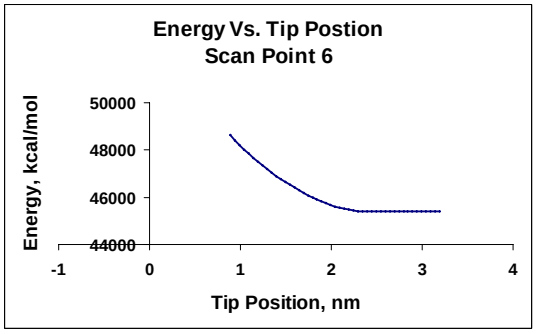
Energy Vs. Tip Postion
Scan Point 6
Energy, kcal/mol
50000
48000
46000
44000
-1
0
1
2
3
4
Tip Position, nm

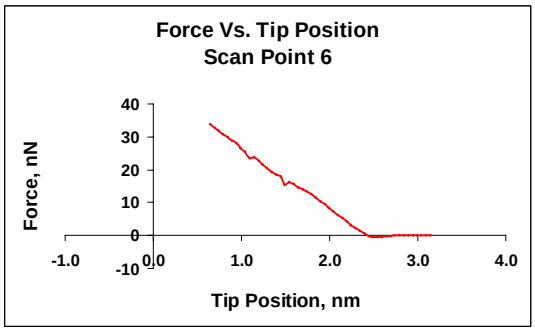
Force Vs. Tip Position
Scan Point 6
Force, nN
40
30
20
10
0
-10
-1.0
0.0
1.0
2.0
3.0
4.0
Tip Position, nm

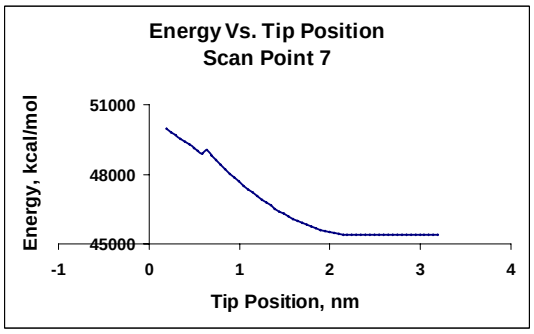
Energy Vs. Tip Position
Scan Point 7
Energy, kcal/mol
51000
48000
45000
-1
0
1
2
3
4
Tip Position, nm

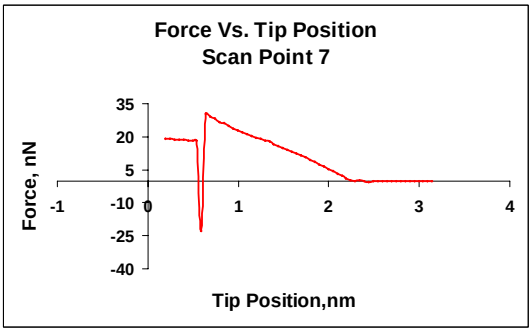
Force Vs. Tip Position
Scan Point 7
Force, nN
35
20
5
-10
-25
-40
-1
0
1
2
3
4
Tip Position,nm

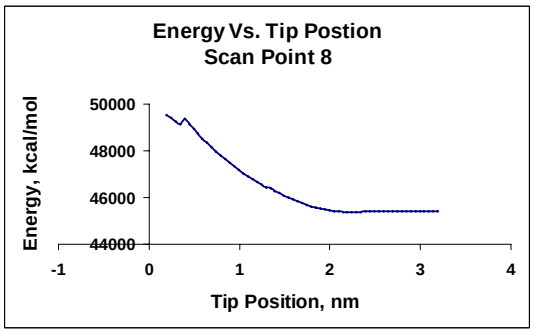
Energy Vs. Tip Postion
Scan Point 8
Energy, kcal/mol
50000
48000
46000
44000
-1
0
1
2
3
4
Tip Position, nm

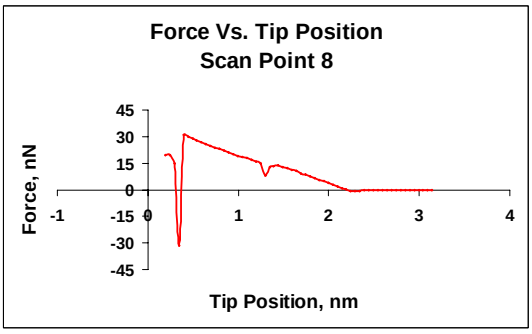
Force Vs. Tip Position
Scan Point 8
Force, nN
45
30
15
0
-15
-30
-45
-1
0
1
2
3
4
Tip Position, nm

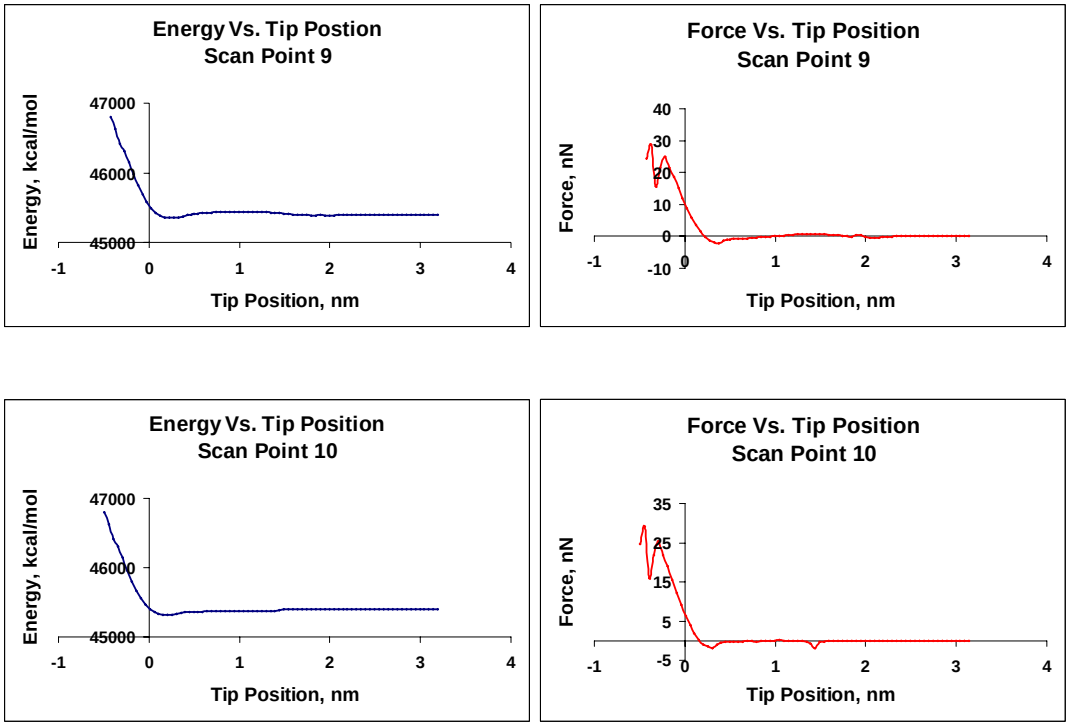

Figure S-1: Energy-distance and force-distance profiles generated for various probe positions, corresponding to the scan points in Figure 2 of the manuscript.

3. Effect of thermal vibrations

The tip-sample potentials and the corresponding force curves were constructed at zero kelvin to minimize the cost of the simulations. However, thermal vibration calculations at 300 K show that the potentials would not be significantly different at room temperature. The additional thermal energy would have the effect of lowering the energy barriers that the system needs to overcome in order for the probe to slip off the sample. This is only relevant for scan points 6, 7, and 8 for which the probe did not slip at the tip-sample forces present during tapping mode imaging. Only at much higher forces (~30

nN) did the probe "snap" off the sample nanotube at these points. The force and energy curves presented here show that the energy requirement to cause these points to snap is the same as that required to longitudinally compress the probe by one full nm, which is much greater than the available thermal energy. Our calculations show that the maximum horizontal displacement of any atom on the tip of the probe at 300 K is below 0.095 nm (less than 1.8% of the probe width), which would not significantly change the relative position of probe and sample. The amplitude of the vertical vibrations is less than 0.055 nm.

4. Characterization of SWNT deformation modes

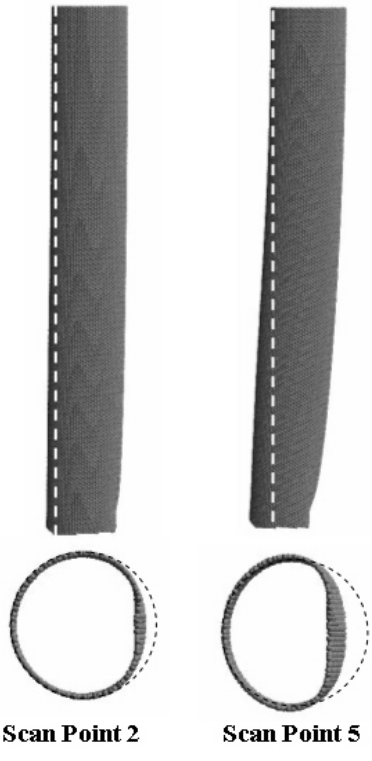

Figure S-2: Degree of probe bending shown for two extreme cases: scan point 2, the point on the scan where the 5.4 nm diameter probe nanotube first comes into contact with the sample nanotube, and scan point 5, the last point for which slipping occurred during the imaging simulation. The local deformation of the tip is also shown in the bottom pictures (the probe images have been rotated from their original tilted position to illustrate the amount of bending that they undergo). The images show that both bending and local deformation contributes significantly to the reduction in the probe's effective resolution for this SWNT diameter.

5. Slipping of smaller SWNT probes: 2.2 nm diameter, 20 nm in length

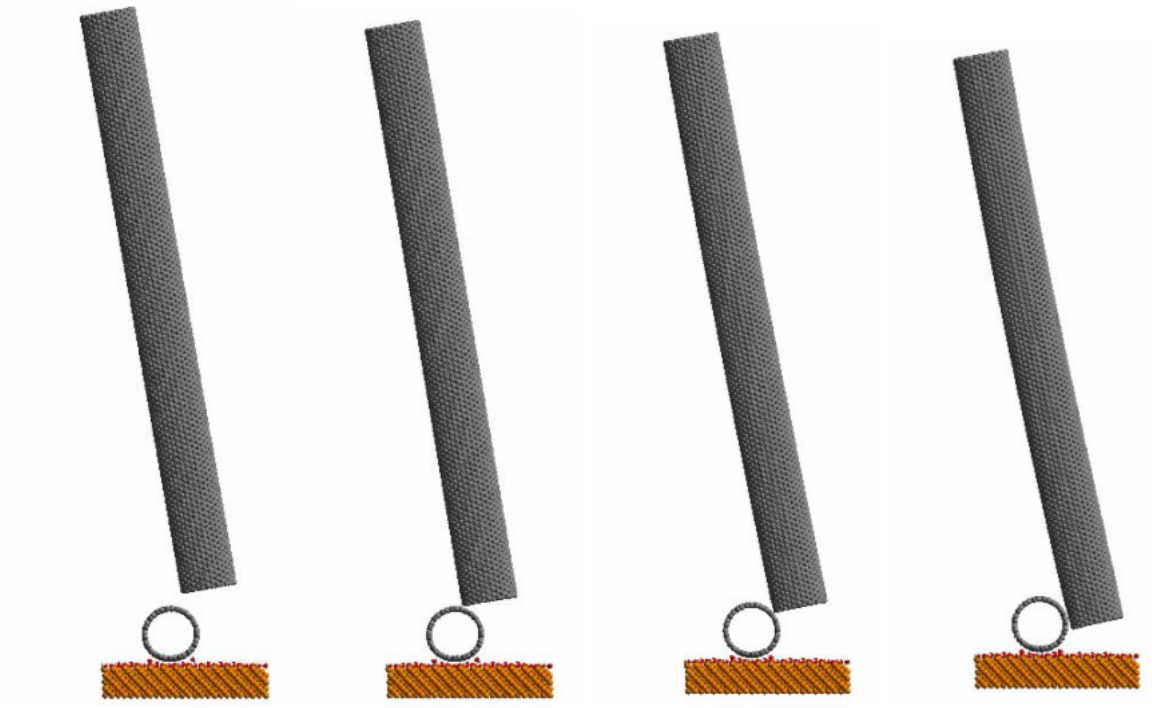

Figure S-3: The images from the simulation with the 2.2 nm diameter probe show that slipping also occurs for smaller probes, although it is primarily due to bending and not to local deformation due to the higher radial stiffness for the thinner SWNT probes. In order to slip, the probe needed to displace laterally a distance of approximately 0.5 nm (22% of the sample diameter).

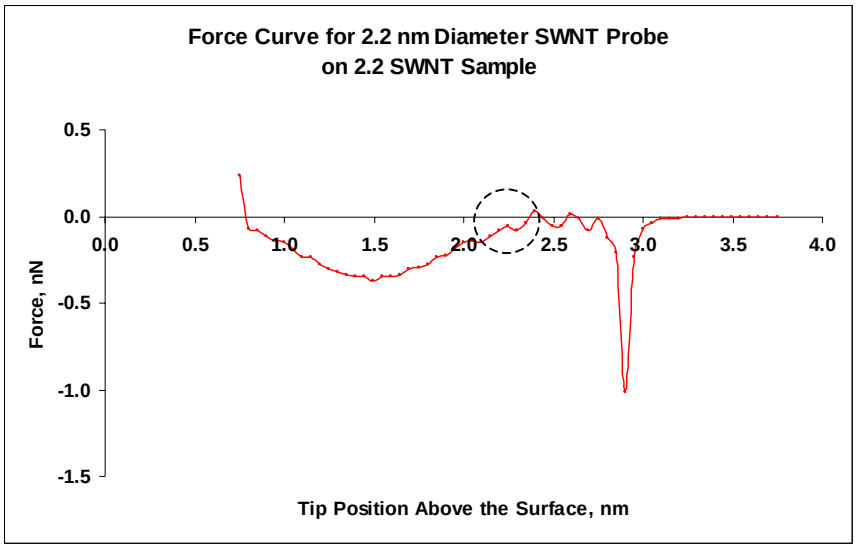

Figure S-4: Force curve for the 2.2 nm SNWT probe. The dashed circle shows the region where slipping occurs. As the graph shows, there is no significant force opposing the snapping motion of the probe. The negative peak in the force is due to snap-to-contact as the probe first approaches the sample.

6. Illustration of reversibility in SWNT probe-sample interaction

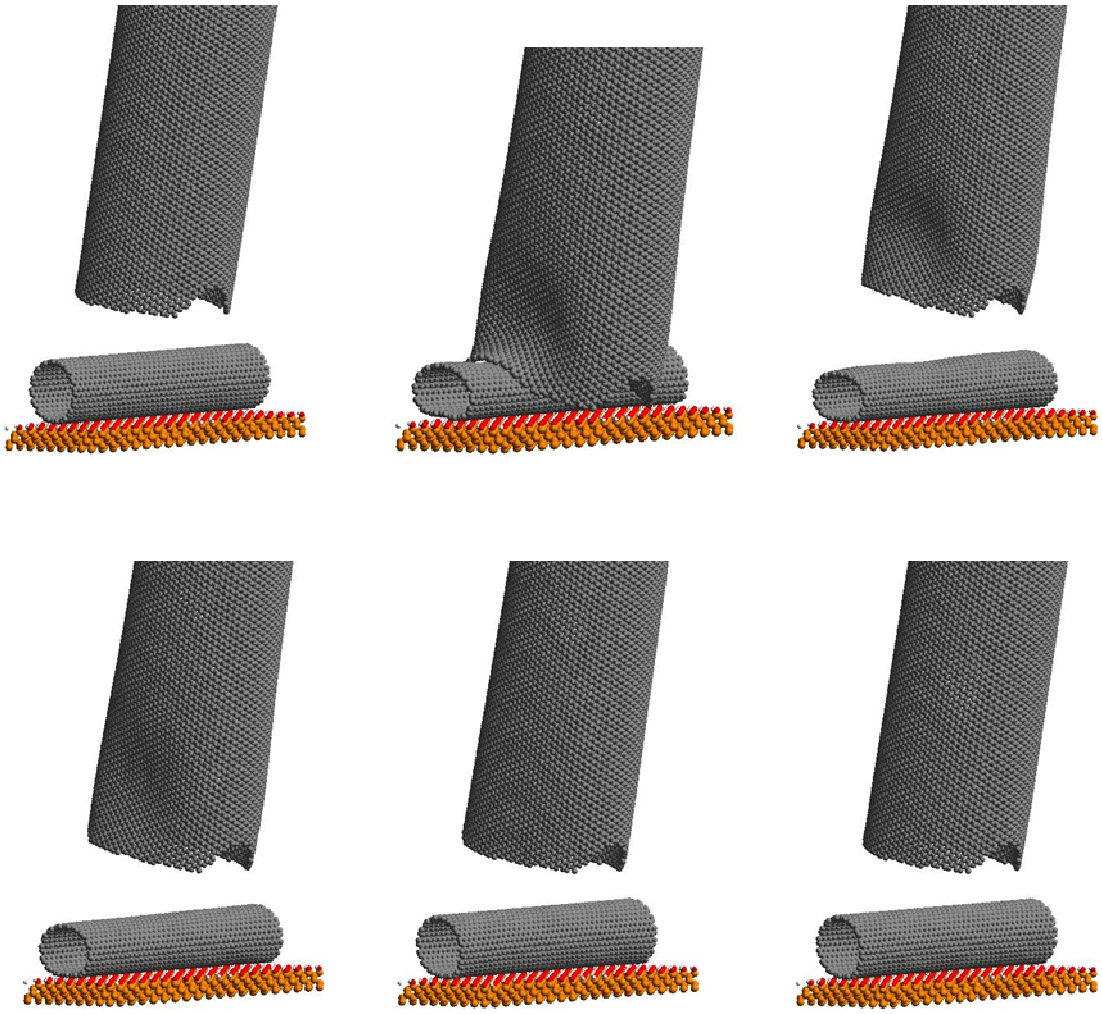

Figure S-5: Sequential images illustrating the reversible elastic nature of the deformation phenomenon. The top image on the left corresponds to the SWNT tip and sample before contact for scan point 6. The second image corresponds to the tip compressing the SWNT with a force of 33 nN (approximately twice the maximum tip-sample force observed during imaging). Images 3-6 correspond to intermediate geometry relaxation steps of the probe and sample after the probe has retracted. Note that the time

required for geometry relaxation is on the order of 20 *ps,* one order of magnitude smaller than the integration time step used for AFM dynamics simulations (0.1 *ns*). This guarantees that the probe and sample are able to relax before the tip impacts the sample a second time.

REFERENCES:

1. Cheung, C-L; Hafner, J. H.; Odom, T. W.; Kyoungha, K.; Lieber, C. M. *Appl. Phys. Lett.* **2000**, *76*, 3136.

2. Wong, S. S.; Wooley, A. T.; Joselevich, E.; Cheung, C. L.; Lieber, C. M. *J. Am. Chem. Soc.* **1998**, *120*, 8557.

3. Campbell, P. M.; Snow, E. S.; Novak, J. P.; *Appl. Phys. Lett*. **2002**, *81*, 4586.

4. Hafner, J.H.; Cheung, C.L.; Oosterkamp, T.H.; Lieber, C.M.; *J. Phys. Chem. B* **2001**, *105*, 743.

5. Choi, N.; Uchihashi, T.; Nishijima, H.; Ishida, T.; Mizutani, W.; Akita, S.; Nakayama, Y.; Ishikawa, M.; Tokumoto, H.; *Jpn. J. Appl. Phys*. **2000**, *39*, 3707.

6. Dai, H.; Hafner, J.H.; Rinzler, A.G.; Colbert, D.T.; Smalley, R.E. *Nature* **1996**, *384,* 147.

7. Wong, S. S.; Woolley, A. T.; Odom, T. W.; Huang, J-L.; Kim, P.; Vezenov, D. V.; Lieber, C. M. *Appl. Phys. Lett.* **1998**, *73*, 3465.

8. Hafner, J. H.; Cheung, C. L.;. Wooley, A. T.; Lieber, C. M.; *Progr. Biophys. Mol. Biol*. **2001**, *77*, 73.

9. Stevens, R. M. D.; Frederick, N. A.; Smith, B. L.; Morse, D. E.; Stucky G. D.; Hansma P. K. *Nanotechnology* **2000**, *11*, 1.

10. Nguyen, C. V.; Stevens, R. M. D.; Barber, J.; Han, J.; Meyyapan, M. *Appl. Phys. Lett.* **2002**, *81*, 901.

11. Wade, L. A.; Shapiro, I. R.; Ma, Z.; Quake, S. R.; Collier, C. P. *Nano Lett*. **2004**, *4*, 725.

12. Snow, E. S.; Campbell, P. M.; Novak, J. P. *Appl. Phys. Lett.* **2002**, *80*, 2002.

13. García, R.; San Paulo, A. *Phys. Rev. B.* **1999**, *60*, 4961.

14. San Paulo, A.; García, R. *Biophys. J*. **2000**, *78*, 1599.

15. García, R.; San Paulo, A. *Phys. Rev. B.* **2000**, *61*, R13381.

16. San Paulo, A.; García, R. *Phys. Rev. B.* **2002**, *66* 041406(R).

17. San Paulo, A.; García, R. *Phys. Rev. B.* **2001**, *64*, 193411,

18. Frenkel, D.; Smit, B. *Understanding Molecular Simulation*; Academic Press: San Diego, CA, 2002, pp. 69-71.

19. For an explanation of (n,m) designation, see Jeroen, W. G.; Wildoer, L. C.; Venema, A. G.; Rinzler, R.; Smally, E.; Dekker, C. *Nature* **1998**, *391*, 59.

20. Rodriguez, T.R.; García, R. *Appl. Phys. Lett*. **2002**, *80*, 1646.

21. García, R.; Calleja, M.; Rohrer, H. *J. Appl. Phys.* **1999**, *86*, 1898.

22. Engel, A.; Müller, D. *Nat. Struct. Biol.* **2000**, *7*, 715.

23. Krishnan, A.; Dujardin, E.; Ebbesen T.W.; Yianilos, P.N.; Treacy, M. M. J. *Phys. Rev. B*

1998, *58*, 14013.

24. Shen, W.; Jiang, B.; Han, B. S.; Xie, S-S. *Phys. Rev. Lett*. **2000**, *84*, 3634.

25. Gao, G.; Çağin, T.; Goddard, W.A. *Nanotechnology* **1998**, *9*, 184.

26. García, R.; Perez, R. *Surf. Sci. Rep*. **2002**, *47*, 197.

27. Lee, S. I.; Howell, S.W.; Raman, A.; Reifenberger, R. *Phys. Rev. B.* **2002**, *66*, 115409.

28. Wilson, N.R.; Macpherson, J.V. *Nano Lett.* **2003**, *3*, 1365.

29. Postma, H. W. C.; Sellmeijer, A.; Dekker, C. *Adv. Mat.* **2000**, *12*, 1299.

30. Hertel, T.; Walkup, R. E.; Avouris, P. *Phys. Rev. B* **1998**, *58*, 13870.

31. Li, C.; Chow, T-W.; *Phys. Rev. B* **2004**, *69*, 073401.

32. Ruoff, R.S.; Tersoff, J.; Lorents, D. C.; Subramoney, S.; Chan, B. *Nature* **1993**, *364*, 514.

33. Musgrave, C.B., **1995.** PhD Dissertation Thesis: *"Molecular Mechanics and ab Initio Simulations of Silicon (111) Surface Reconstructions, Semiconductors and*

Semiconductor Superlattices, H Abstraction Tool for Nanotechnology, Polysilanes, and Growth of CVD Diamond" California Institute of Technology.

34. Guo, Y.J. **1992.** PhD Dissertation Thesis: *"Molecular Simulations of Buckyball Fullerenes. Quantum Chemistry Studies on High Tc Superconductors"* California Institute of Technology.

35. Guo, Y.J.; Karasawan N.; Goddard W.A. III. *Nature*, **1991,** *351*, 6326.

36. Mayo, S.; Olafson, B.; Goddard, W. A. III. *J. Phys. Chem*. **1990**, 94, 8897.

Chapter 2: Mechanisms of Single-Walled Carbon Nanotube Probe-Sample Multistability in Tapping Mode AFM Imaging*

ABSTRACT. When using single-walled carbon nanotube (SWNT) probes to create AFM images of SWNT samples in tapping mode, elastic deformations of the probe and sample result in a decrease in the apparent width of the sample. Here we show that there are two major mechanisms for this effect, smooth gliding and snapping, and compare their dynamics to the case when a conventional silicon tip is used to image a bare silicon surface. Using atomistic and continuum simulations, we analyze in detail the shape of the tip-sample interaction potential for three model cases and show that in the absence of adhesion and friction forces, more than two discrete, physically meaningful solutions of the oscillation amplitude are possible when snapping occurs (in contrast to the existence of one attractive and one repulsive solution for conventional silicon AFM tips). We present experimental results indicating that a continuum of amplitude solutions is possible when using SWNT tips and explain this phenomenon with dynamic simulations that explicitly include tip-sample adhesion and friction forces. We also provide simulation results of SWNT tips imaging Si(111)-CH_3 surface step edges and Au

---

* Reproduced with permission from Solares, S.D.; Esplandiu, M.J.; Goddard, W.A. III; and Collier, C.P.; *J. Phys. Chem. B* **2005,** *109,* 11493.

nanocrystals, which indicate that SWNT probe multistability may be a general phenomenon not limited to SWNT samples.

1. Introduction

Carbon nanotubes have been used successfully as AFM tips to image a variety of samples, including surfaces, biomolecules, and other types of nanoscale samples in both contact and non-contact mode. [1-7,9,10] These scanning probes have shown significant potential for numerous applications due to their robustness, flexibility, small dimensions, and chemical stability, which can lead to reduced sample damage and finer resolution imaging than can be obtained with conventional silicon tips. [2,3,8-10] SWNTs are of particular interest due to their macromolecular-scale dimensions.

Theoretical and experimental studies of AFM tapping-mode imaging have shown that this process is subject to bistability, i.e., it is possible to obtain two solutions of the AFM cantilever oscillation amplitude for a given set of imaging parameters. It has also been shown that there are cases where more than two solutions are mathematically possible but for which only two of them are physically meaningful. [11] Since the AFM imaging process in tapping mode depends on the oscillation amplitude of the cantilever, good images require that the regions where bistability occurs be avoided. Often there is no systematic procedure to do this, and AFM operators have to rely on their intuition and previous experience.

It is known that the two solutions of the oscillation amplitude of the cantilever occur depending on whether the *average* gradient of the tip-sample interaction force is positive

or negative. [11,12] In general, a typical tip-sample interaction potential contains a long-range attractive region and a short-range repulsive region, as do the well-known Morse and Lennard-Jones potentials, for example. The *gradient* of the tip-sample interaction force (negative of the *second* derivative of the potential with respect to the tip position) is positive in most of the attractive region and is negative in most of the repulsive region. If the region of positive force gradient dominates the tip-sample interaction for a given set of imaging parameters (attractive regime) the resulting phase shift of the AFM tip oscillation relative to the excitation force will be greater than 90º, and if the region of negative force gradient dominates (repulsive regime) the phase shift will be below 90º. [11,12] Note that throughout this paper we use the terms "phase" and "phase shift" interchangeably.

This study uses a previously reported simulation methodology (Chapter 1) based on molecular dynamics (MD) and classical AFM dynamics (AFMD)[13] to show that the tip-sample interaction between SWNT AFM tips and samples does not always correspond to a simple potential like the one described above and that the interaction between the tip and the sample can give rise to potentials of different shapes, which may give more than two *physically meaningful* solutions for the oscillation amplitude during tapping-mode AFM imaging. We also show that if tip-sample adhesion and friction forces are significant, it is possible to obtain a continuum of amplitude solutions, all of which are physically meaningful. In such cases it is more appropriate to speak of imaging multistability rather than bistability (we note that this type of *effective* multistability due to the combination of sample and substrate interaction potentials with non-conservative

forces is different than the one described in references 11 and 12, where a *single* interaction potential gives rise to two different oscillation states).

Specifically, we analyze the tip-sample interaction potential of a SWNT AFM tip imaging a prone SWNT on a flat substrate. We have previously reported that for these systems it is possible to obtain a measured sample width that is smaller than the true sample width due to the elastic deformation of the tip and sample, which slide past one another. Here we show that this sliding phenomenon can occur in two different modes, one where the tip and sample glide smoothly past one another, and a second mode in which the tip initially compresses the sample and then snaps off, involving a sudden lateral "jump" to the side of the sample. In the absence of tip-sample adhesion and friction forces, the first mode gives rise to two amplitude solutions (as is typical with conventional silicon tips), and the second mode gives rise to four solutions due to the existence of *two* regions where the gradient of the tip-sample interaction force is positive and *two* regions where it is negative. In the presence of tip-sample adhesion and friction forces, these sliding phenomena can give rise to a continuum of amplitude solutions which exhibit smooth, continuous transitions between the attractive and repulsive regimes, in contrast to the discontinuities observed when using conventional silicon tips.

Finally, we describe theoretical simulations of Si(111)-CH_3 surface step edges and Au nanocrystals, which show that SWNT probe multistability is a general phenomenon that can occur for a wide variety of samples, whenever snapping of the nanotube probe takes place.

2. Methods

2.1 Experimental

The fabrication, characterization and imaging process employed using SWNT tips has been previously described. [6] A Digital Instruments[§] (Santa Barbara, CA) Multimode atomic force microscope with a Nanoscope IV controller was used for this work. As-grown SWNTs were mounted onto silicon AFM tips (FESP, NanoWorld) using the pick-up technique developed by Lieber and coworkers.[14] The experimental results presented here correspond to a SWNT AFM tip with diameter and length of approximately 5.5 and 40 nm, respectively, tilted 15 degrees with respect to the vertical direction (a transmission electron microscopy image of this probe[6,13] is provided in the supporting information), mounted on a silicon tip with dimensions given in Table 1. These experimental results correspond to tapping-mode measurements for which the AFM tip was oscillating directly above the SWNT sample (a detailed procedure is provided in the supporting information). The relevant imaging and geometry parameters are listed in Table 1 and are the same as those used in the theoretical simulations. The cantilever driving frequency was the same as the resonance frequency in all cases.

[§] http://www.elecdir.com/site/store/10602/index.html

2.2 Theoretical

The MD/AFMD simulation methodology has also been previously described (Chapter 1). [13] It consists of modeling the AFM cantilever tip as a point mass using the damped harmonic oscillator equation of motion with the introduction of tip-sample interaction forces obtained through atomistic simulations of tip and sample. Our tip-sample interaction potentials include both short- and long-range van der Waals interactions between each atom in the tip (both the SWNT and the supporting silicon tip) and the sample and substrate. The long-range interactions are introduced as a correction to the molecular simulation result via the Hamaker equation for an atom (for each atom in the SWNT tip) or a sphere (for the Si tip) interacting with the surface of a semi-infinite solid (MD calculations usually neglect long-range attractive interactions since they use cutoffs on the order of 1 nm in the calculation of van der Waals interactions).

The equation of motion for a damped harmonic oscillator is the following:

$$m\frac{d^2 z(Z_c,t)}{dt^2} = -kz(Z_c,t) - m\frac{\omega_o}{Q}\frac{dz(Z_c,t)}{dt} + F_{ts}(z_{ts}) + F_o\cos(\omega t), \qquad (1)$$

where $z(Z_c,t)$ is the instantaneous tip position with respect to its equilibrium rest position (Z_c), k is the harmonic force constant for the displacement of the tip with respect to its equilibrium rest position, m is the AFM cantilever's effective mass, $\omega_0 = \sqrt{k/m}$ is the free resonant frequency, Q is the quality factor, z_{ts} is the instantaneous tip position *with respect to the sample*, $F_{ts}(z_{ts})$ is the calculated tip-sample interaction force, and

$F_0\cos(\omega t)$ is the oscillating driving force applied to the cantilever (we used $\omega = \omega_o$ as in our experiments). The oscillation amplitude is obtained directly from the tip trajectory. The phase is obtained from its Fourier transform. Our previous publication describes in detail the software and MD parameters used in the calculations. [13] The references for the MD parameters for Au nanocrystals and Si(111)-CH_3 surfaces are provided in supporting information.

In this study we analyze three model cases in detail:

1) 17-nm-radius conventional silicon tip tapping on a bare silicon surface.
2) 40,40 SWNT tip tapping on the edge of a 16,16 SWNT sample, such that smooth gliding occurs when the probe descends on the sample as shown at the top of Figure 1.
3) 40,40 SWNT tip tapping on a 16,16 SWNT sample, such that the probe first compresses the sample and then snaps past it as shown at the bottom of Figure 1. Our analysis includes more than one variation of this case, depending on the magnitude of the force required for snapping to occur.

For each of these tip-sample potentials, Equation 1 was solved numerically for eight different values of the excitation force amplitude (F_o) corresponding to free oscillation amplitudes (A_o) ranging from 5 to 40 nm in increments of 5 nm, and for cantilever rest positions (Z_c) ranging from 5 to 40 nm above the surface in increments of 0.5 nm. This provided the oscillation amplitude as a function of A_o *and* Z_c for a given initial velocity (V_o) and position of the tip. This procedure was repeated for three different values of V_o:

0.0025 nm/s, 0 nm/s, and -0.0025 nm/s. In all cases, the initial tip position was set equal to its equilibrium position, i.e., $z(Z_C,0)=0$. These sets of data for each potential were used to construct the "phase space" representations of the oscillation amplitude solutions as a function of the variables A_o, Z_c, and V_o.

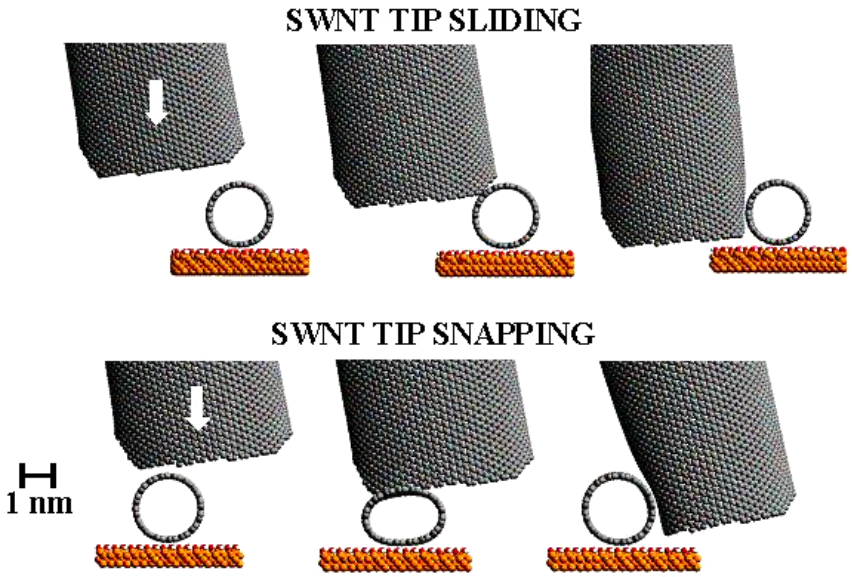

Figure 1. 40,40 SWNT tip imaging a sample 16,16 SWNT in *smooth gliding* mode (top) and *snapping* mode *(bottom)*. In the first case the deformation of the sample is negligible and the tip and sample are able to slide past one another primarily due to tip bending and local deformation. In the second case the sample nanotube is initially compressed against the substrate, undergoing elastic deformation until the tip snaps off the sample.

We then constructed amplitude and phase curves (vs. Z_c) for tip-sample interaction potentials that exhibited snapping, both with and without the inclusion of adhesive and frictional forces. Adhesive forces were added at the point where the tip first contacts the sample and at the point where the tip first contacts the substrate surface (after sliding past the sample), acting only during the upward motion of the tip as it was traveling away

from the sample. The magnitude of this adhesive force was selected to be within the range given in the work of other authors.[15-17]

Table 1: Geometry and AFM simulation parameters

Geometry parameters:	
Silicon tip radius, imaging end	17 nm
Silicon tip, base of pyramid	6800 nm
Silicon tip length	17500 nm
SWNT tip diameter	5.5 nm (simulated as a 40,40 SWNT)
SWNT tip length	40 nm
SWNT tip tilt angle	15 degrees
Sample SWNT diameter	2.1 nm (simulated as a 16,16 SWNT)
Imaging parameters:	
AFM cantilever force constant	4.8 N/m
AFM cantilever resonant frequency	47.48 kHz
AFM cantilever quality factor	150
Integration time step	0.1 ns
Integration time	0.02 s
Calculated cantilever effective mass	5.3933×10^{-11} kg

The added tip-sample frictional dissipation force was proportional to the negative of the tip velocity and acted only when tip and sample were in direct physical contact. This friction force was introduced through the use of two different values of the quality factor in the integration of Equation 1: the free oscillation quality factor, Q_f, when tip and sample were *not* in contact, and a (significantly lower) contact quality factor, Q_c, when

they were in contact and sliding past one another. The effective quality factor, *Q*, was thus varied between these two values in the integration of Equation 1. There is no information available on the magnitude of these tip-sample friction forces during imaging, so we varied the contact quality factor between 0.005 and 0.05 times the free oscillation quality factor until we were able to reproduce the features observed in the experimental results (this is equivalent to assuming that for a given tip velocity, the tip-sample friction forces are between 20 and 200 times greater than the air damping forces experienced by the free oscillating cantilever). Our introduction of a tip-sample dissipation force proportional to the velocity is an approximation similar to that used in describing Newton's law of viscosity for the case of two parallel plates sliding with respect to one another while a Newtonian fluid is being sheared between them. [20] The true nature of the tip-sample interaction forces between SWNT AFM tips and samples depends on atomistic phenomena that are different than those present in a continuum description of a Newtonian fluid and is expected to exhibit complex, non-monotonic behavior,[21-24] but the results presented in the next section show that this model is able to reproduce the experimental results qualitatively.

Finally, in order to generalize our observations to other common geometries, we constructed the tip-sample interaction force curves for a 30,30 SWNT tip imaging a Si(111)-CH_3 surface step edge and a 4.7 nm Au nanoparticle on a Si(100)-OH surface, respectively, which we then used to construct the corresponding amplitude and phase curves (vs. Z_c) for A_o = 20 nm and for A_o = 10 nm, respectively, in the absence of tip-sample adhesion and friction forces.

3. Results

Figure 2 shows the tip-sample interaction force as a function of the tip position above the surface for the three model cases under study, in the absence of tip-sample adhesion and friction forces. Figure 2 (a) is the tip-sample interaction force curve for a conventional 17-nm-radius silicon tip imaging a bare silicon surface. It shows a well-defined long-range attractive region and a short-range repulsive region. Figure 2 (b), which corresponds to the SWNT *smooth gliding* mode, shows that the tip-sample interaction force exhibits a local (attractive) minimum just below 2.5 nm as the probe first approaches the sample. It remains slightly negative (attractive) as tip and sample slide past one another until a second minimum at approximately 0 nm is reached, after which it becomes repulsive and continues to increase monotonically with further downward displacement of the probe. Negative values of the tip position correspond to elastic deformations in the SWNT tip and the sample nanotube upon contact. Note that the tip-sample force remains slightly attractive as the probe and sample glide past one another even though they are both undergoing elastic deformation. MD simulations indicate that this is due to the favorable van der Waals interactions between their graphitic surfaces.

Figure 2 (c) corresponds to the SWNT *snapping* mode. As the graph shows, the force initially exhibits a local (attractive) minimum when the probe first approaches the sample and then starts increasing as the sample is compressed (black line). If the probe retracts before reaching a vertical separation of approximately 1.5 nm from the substrate surface (at a force of approximately 15 nN), it will return to its initial position along the same

path it followed to compress the sample. However, if the probe compresses the sample with a force that exceeds 15 nN, it will snap off as shown at the bottom of Figure 1, and the force will immediately decrease to a value close to zero. The probe will continue its downward trajectory until it reaches the substrate surface, where it will initially experience a small attractive force and then an increasingly repulsive force. When the probe retracts it will follow a different trajectory than when it initially approached the sample (red line) because snapping only occurs when the probe is moving downward.

Note that the magnitude of the attractive force at the force curve minimum is several times greater for a conventional tip (Figure 2 (a)) than a SWNT tip (Figures 2 (b) and (c), and Figure 2-S of the supporting information). This is due to the greater number of atoms in the solid silicon tip, which experience strong van der Waals attractions with the substrate surface at short range. Even for the same tip radius, SWNTs have significantly fewer atoms in close proximity to the surface due to their hollow geometries, resulting in much smaller attractive forces.

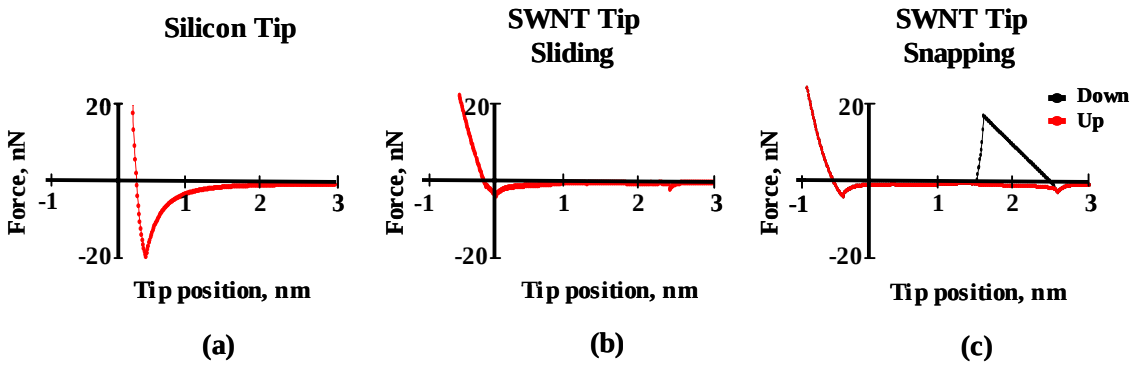

Figure 2. Tip-sample interaction force vs. tip position above the surface for a 17-nm-diameter silicon tip imaging a bare silicon surface (a) and for the SWNT tip imaging a prone SWNT in sliding (b) and snapping (c) modes. The tip sample interaction force

curve for the SWNT tip imaging a bare silicon surface is similar to curve (b) and is shown in Figure 2-S of the supporting information.

Numerical integration of Equation 1 shows that in the absence of tip-sample adhesion and friction forces, four solutions of the oscillation amplitude are possible for the snapping mode. Two of them –one in the attractive regime and one in the repulsive regime– correspond to the cases when the probe does *not* snap off the sample during the oscillation. If the probe snaps during the oscillation, then two more distinct solutions become available, one of them in the attractive regime and another one in the repulsive regime. Figure 3 shows the A_o-Z_c "phase space" representation of these four solutions for $V_o = 0$ in the absence of tip-sample adhesion and friction forces. The "phase space" representations for the conventional silicon tip and for the SWNT tip in smooth sliding mode, on the other hand, only show two solutions which correspond to the well-known attractive and repulsive regimes described previously by other authors (supporting information).[11-12] The phase space diagram in Figure 3 shows four distinct amplitude solutions. The white region corresponds to an *attractive* solution where the probe does not snap during the oscillation, the black regions correspond to a *repulsive* solution where the probe does not snap during the oscillation, the gray regions correspond to a *repulsive* solution where the probe snaps for every oscillation, and the small red region on the top right hand side of the diagram correspond to an *attractive* solution where the probe snaps for every oscillation. The red region is the smallest of all and corresponds to the cases where the probe has just enough energy to snap off the sample during each oscillation but is unable to reach the substrate surface. This diagram was constructed using the force curve of Figure 2 (c).

The AFM tapping mode phase and amplitude curves for the conventional silicon tip and for the SWNT smooth gliding mode as functions of tip-substrate separation distance (Z_c) clearly show the existence of only one attractive and one repulsive solution (supporting information).[11,12] The snapping mode amplitude and phase curves, on the other hand, show more diverse behavior. In order to visualize all the features of this process, we identified the points in the simulated amplitude and phase curves where the probe had snapped off the sample nanotube (Figure 4) with a different color (blue for the cantilever equilibrium positions for which the probe does *not* snap during the oscillation and red for the points for which it *does* snap during the oscillation). These curves correspond to a free oscillation amplitude (A_0) of 40 nm and an initial tip velocity (V_0) of zero. We note that the amplitude curve does not directly reveal transitions involving the long-range attractive (white areas in Figure 3), long-range repulsive (black areas in Figure 3) and short-range attractive solutions (red areas in Figure 3) to Equation 1. The only distinct jumps in the amplitude curve are those between the two repulsive solutions, one of which corresponds to the probe snapping every oscillation period of the tip (gray areas in Figure 3), and the other one to oscillations where snapping does not occur (black areas in Figure 3). The phase curve, however, *does* show all four solutions clearly, as well as the points where the system jumps between them. Most of the jumps correspond to jumps between the repulsive solutions (the phase is below 90º before and after the jump). This is consistent with the phase space diagram of Figure 3, which shows large borders between adjacent regions corresponding to repulsive solutions.

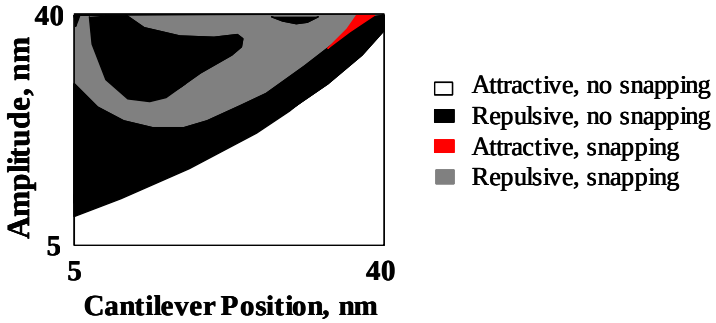

Figure 3. A_o-Z_c phase space representation of the oscillation amplitude solutions for SWNT tip-sample interactions corresponding to Figure 2 (c) for $V_0 = 0$, in the absence of tip-sample adhesion and friction forces. The corresponding phase space representations for $V_0 = -0.0025$ nm/s and $V_0 = 0.0025$ nm/s are qualitatively similar.

In the supporting information we provide phase and amplitude curves for the case when a 25 nN tip-sample adhesion force is added to force curve (c) of Figure 2. In this case, both attractive solutions and one repulsive solution are clearly discernible from the amplitude and the phase curves. The long-range repulsive solution does not occur due to the large adhesion (attractive) force, which dominates the interactions when the probe does not snap. These results suggest that adhesion forces can magnify the difference between the different solutions.

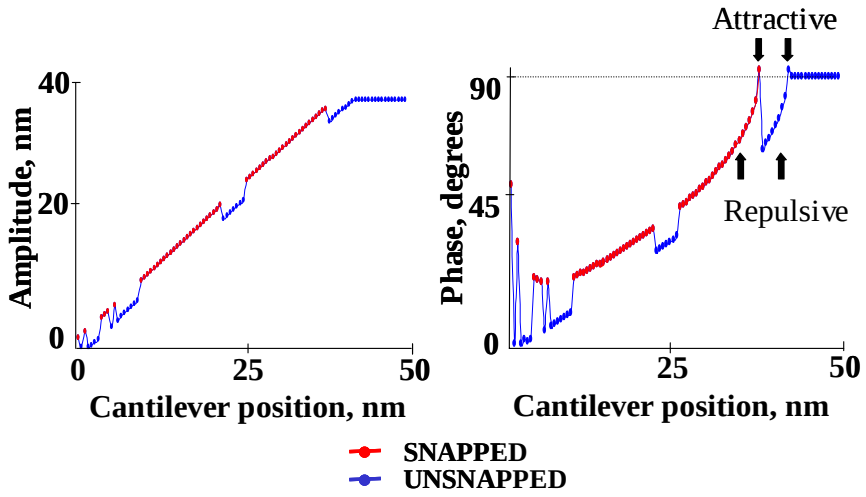

Figure 4. Amplitude and phase vs. cantilever position for the SWNT tip-sample interaction in *snapping* mode in the absence of tip-sample adhesion and friction forces. The free oscillation amplitude A_0 was 40 nm, and the initial tip velocity was set to zero in the simulation. The points where the tip snaps during every oscillation are shown in red, and those for which it does not snap are shown in blue. These curves were constructed using force curve (c) of Figure 2.

Figures 5 (a), 5 (b), and 5 (c) contain experimental results for a SWNT tip imaging a SWNT sample on a silicon oxide substrate for low, intermediate, and high values of A_o, respectively. In all three cases the SWNT tip was tapping directly on the crown of the sample SWNT. The phase curve of Figure 5 (a) exhibits a predominantly attractive regime, in *disagreement* with the theoretical simulation of Figure 4, which does not consider tip-sample adhesion and friction forces. Figures 5 (b) and 5 (c) show smooth variations of the phase and amplitude as the cantilever approaches the sample, including phase transitions between attractive and repulsive regimes *without* a discontinuity.

Figure 5 (c) shows that it is also possible to have smooth variations between the attractive and repulsive regimes *and* discontinuities on the same curve. The discontinuity of this curve, where the phase jumps from a value below 90º to a lower value, is similar to the jumps observed in Figure 4, indicating a transition between a regime where the probe snaps during each oscillation (henceforth referred to as a *snapped oscillation*) to a regime where the probe does not snap during the oscillation (henceforth referred to as an *unsnapped oscillation*) as the cantilever equilibrium position, Z_c, is lowered. The relative magnitude of the phase between the snapped and unsnapped oscillations is consistent with Figure 4, which shows that the phase is higher for snapped oscillations than for unsnapped oscillations. This is also consistent with the magnitude of the oscillation amplitude before and after the jump, which indicates that the oscillation amplitude is greater when snapping occurs. The amplitude curve shows two transitions, one from an unsnapped oscillation to a snapped oscillation and one from a snapped oscillation back to an unsnapped oscillation. Although the first transition is not as evident in the phase curve, this curve has an inflection point which indicates a change in the nature of the tip-sample interaction.

We also observed curves with similar behavior to that of a conventional silicon tip, although the range of Z_c corresponding to the attractive region was generally much larger. In general, the experimental measurements show significantly greater attractive regions than those calculated based on van der Waals interactions alone, suggesting the presence of other attractive interactions such as capillary or electrostatic forces.

Figure 6 shows three theoretical simulations using different snapping potentials where we have explicitly included tip-sample adhesion and frictional forces, as described above

in the theoretical methods section. All three simulated phase curves in Figure 6 are in close qualitative agreement with their experimental counterparts in Figure 5, although the transitions in the experimental amplitude curves in Figure 5 are more pronounced than in the corresponding simulations (see discussion below Figure 6). The curves in Figure 6 (a), which were constructed using the force curve of Figure 2 (c), indicate that the tip did not snap during the oscillation until the separation distance to the surface was nearly zero (indicated by the sharp minimum in the phase curve when Z_c approaches zero) and that the predominantly attractive region is a consequence of the large tip-sample adhesion and frictional components that were included in the tip-sample interaction.

Curves 5 (b) and 6 (b) correspond to cases where the force barrier is too high or the excitation force is too low for snapping to occur, and both attractive regions are a consequence of the adhesion force at the point of tip-sample contact, magnified by the friction force. As Z_c decreases in curve 6 (b), the phase initially increases due to the adhesion force. It gradually shows a decrease, becoming smaller than 90º as the probe begins to experience a repulsive force, and then increases when the adhesion force once again becomes dominant at even lower values of Z_c. The amplitude curve shows a smooth gradual increase and decrease indicating the transitions from attractive to repulsive and from repulsive back to attractive regimes.

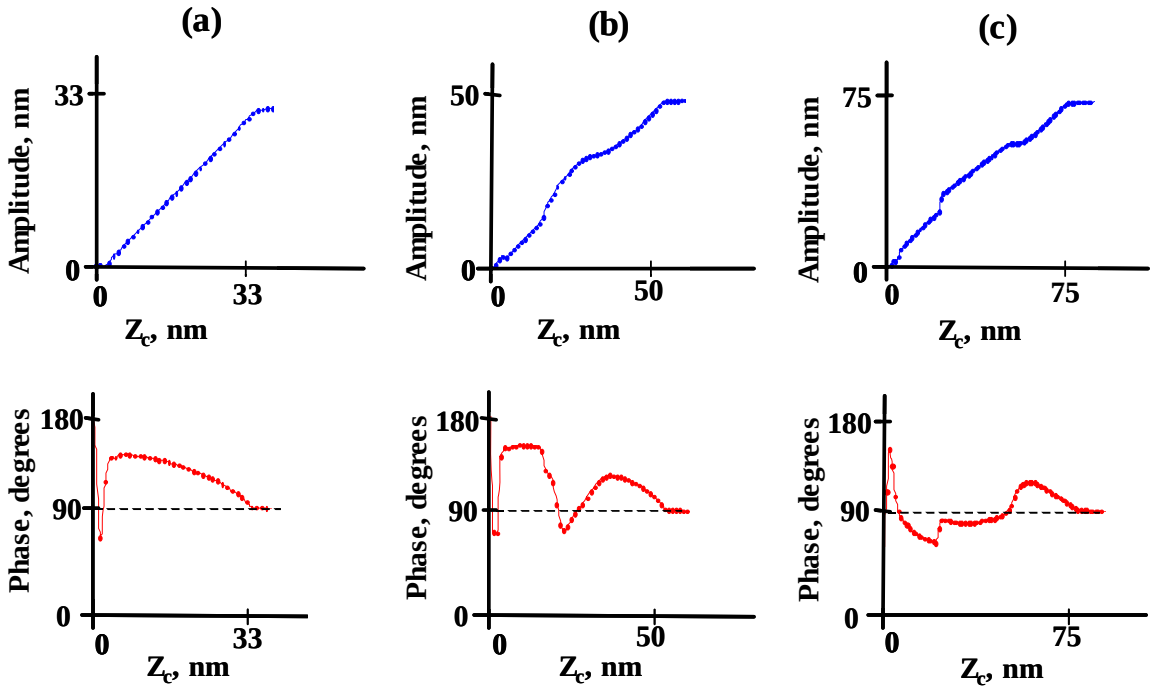

Figure 5. Experimental amplitude and phase vs. Z_c for a SWNT tip tapping directly on top of a sample SWNT on a silicon oxide substrate for different values of the free oscillation amplitude (A_0): (a) A_0=33 nm, (b) A_0=50 nm, (c) A_0=75 nm.

The simulations show that as the tip-sample friction forces increase (i.e. as Q_c is lowered), the transitions between attractive and repulsive regimes become smoother because the larger friction forces allow the probe to more gradually approach and move away from the sample during every oscillation, which causes the *average* tip-sample interaction force to vary smoothly from positive to negative and *vice-versa*.

The phase curve of Figure 6 (c) is similar to that of Figure 5 (c) except that it shows both snapping transitions clearly. This simulation was performed using different values of the friction and adhesion forces for snapped and unsnapped oscillations. The maximum of the adhesion force was set to 20 nN for unsnapped oscillations and to 5 nN

for snapped oscillations (this is reasonable since MD simulations show that the tip-sample contact area is significantly smaller after the tip snaps). The contact quality factor for snapped oscillations was set to 90% of the value for unsnapped oscillations.

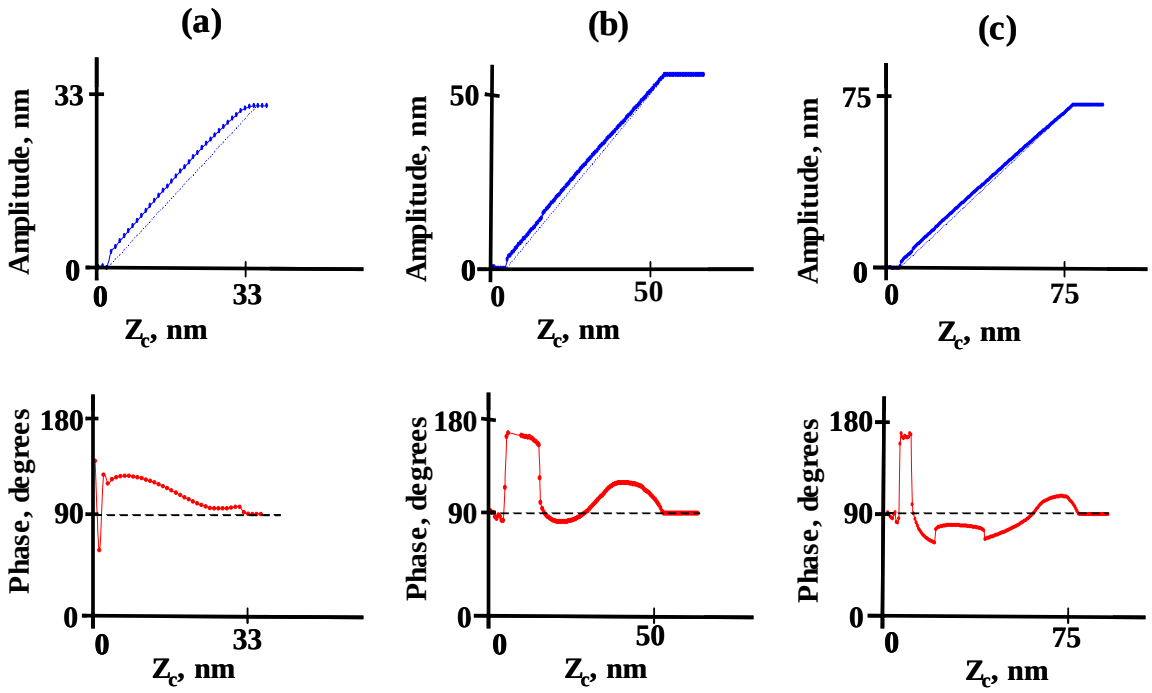

Figure 6. Simulated amplitude and phase vs. Z_c for snapping potentials with the inclusion of adhesion and friction forces for different values of the free oscillation amplitude (A_0): (a) A_0=33 nm, (b) A_0=50 nm, and (c) A_0=75 nm. We have included straight dotted lines for easier visualization of the curvature of the amplitude curves. The adhesion and friction force parameters are provided in the supporting information.

The probe was unable to reach the surface in any of the simulations corresponding to Figure 6, and thus the tip-*substrate surface* adhesion force did not play a role. The simulated amplitude curves in Figure 6 do not show the sharp transitions observed experimentally in Figure 5, although they do show smooth changes in slope that indicate gradual transitions from one regime to another. Within our model, these transitions in the

amplitude curves are more pronounced for small values of the friction force (i.e., for large values of Q_c, such as in Figure 4), but gradually disappear as the friction force increases (i.e., as Q_c is lowered), which reduces the distance that the probe is able to travel freely after snapping off the sample. The simulations corresponding to Figure 6 were performed using relatively low values of Q_c (increased friction) in order to match the experimental *phase* curves as closely as possible, which we found to be more useful in our discussion of tapping-mode AFM multistability.

In the supporting information section we provide the tip-sample energy and force curves and the amplitude and phase curves for the SWNT tips imaging a Si(111)-CH_3 surface step edge and a Au nanoparticle. These curves exhibit similar features to those of Figure 2 (c) and Figure 4, respectively, indicating that snapping can occur with these samples, and hence multiple solutions to the oscillation amplitude are also possible for these types of samples.

4. Discussion:

4.1 Silicon Tips vs. SWNT Tips

It is commonly accepted that the oscillation amplitude of an AFM cantilever, which can be closely modeled using the damped harmonic oscillator approximation (Equation 1), has only two solutions that are physically meaningful. However, this knowledge is based on the assumption that the tip-sample interaction potential has the general shape of a Morse or Lennard-Jones curve, where the potential is monotonically attractive at long ranges and monotonically repulsive at short ranges. Two of the model cases analyzed in

this study, the SWNT smooth gliding mode and the conventional silicon tip, correspond approximately to potentials of this type and, when integrated into Equation 1, do yield two solutions for the amplitude in the absence of tip-sample adhesion and friction forces.

Although the results for these two cases are qualitatively similar, there are some differences that are worth discussing. First, we note that the damping of the oscillation amplitude of the SWNT tip, due to interactions with the sample, is less than that of a conventional silicon tip for given values of Z_c and F_o, indicating greater penetration into the sample and surface as well as greater local elastic deformation of the nanotube, as confirmed through molecular simulations. This is an important consideration regarding the use of SWNTs for topographical imaging because it indicates that while SWNT tips are able to image high aspect features such as trenches and crevices in finer detail than silicon tips, as one would expect from their dimensions, they may not always provide an accurate representation of the sample due to local deformation, especially in highly repulsive regimes where the tip-sample interaction forces can be significant.

Another important difference between SWNT tips and conventional tips is that changes in both the attractive and repulsive forces are steeper functions of tip position for silicon tips than for SWNT tips (as shown in Figure 2). Silicon tips experience greater van der Waals attractive forces when close to the surface due to the larger number of atoms in the tip. The range of cantilever rest positions resulting in a long-range attractive solution should be significantly smaller for a nanotube probe compared to a conventional silicon tip because the attractive forces are smaller and operate over a shorter range. This means that for clean SWNTs, for which dispersion forces are the main interactions, most of the imaging is expected to take place in the repulsive regime. [5] Our calculated tip-sample van

der Waals forces are in agreement with the tight-binding calculations of Tagami et al. on clean tips and surfaces, which show maximum values of 1-1.5 nN for a fullerene tip on a silicon surface. [25,26] On the other hand, our calculated forces are significantly lower than those obtained from treating the SWNT tip as a sphere using the Hamaker equation; however, we feel this treatment is not adequate for a SWNT tip because such a tip is *not* a solid continuum sphere[19] and also because such an approximation neglects the local structural changes as well as the bending and sliding phenomena that can take place when SWNT tips are used. Although the use of the Hamaker equation of a sphere may in some cases give qualitatively satisfying results, these should be interpreted with caution, because this agreement may be a mathematical artifact and not necessarily an accurate description of the dynamics of the system.

4.2 Snapping

Understanding the snapping phenomenon of SWNT tips is fundamental to the development of SWNT AFM techniques. We have previously shown that snapping and sliding effects have direct influence on the probe resolution and measured sample width.[13] The results presented here show that snapping can also give rise to multiple solutions of the oscillating amplitude, including a continuum of solutions when large adhesion and friction forces are present.

A quick glance at the amplitude curve in figure 4 might suggest that it describes an imaging process with the usual bistability. [11,12] However, a closer analysis of the snapping potential (figure 2 (c)) and the phase curve (figure 4) reveals that the long-range

portion of the potential gives rise to two imaging solutions when the excitation force is small (too small to overcome the snapping barrier) or the probe is sufficiently far away from the sample. Two more solutions appear when the probe is able to snap off the sample due to a second overall attractive regime and a second overall repulsive regime. The phase space diagram of figure 3 shows that the repulsive solutions dominate the attractive solutions in the region where the probe and the sample are in contact ($Z_c < A_o$) in the absence of tip-sample adhesion and friction forces. The relative dominance of the repulsive solutions is a consequence of the particular tip-sample interaction potentials analyzed here and can be different for different tips and samples, but the existence of multiple solutions should be common to all tip-sample interaction potentials that exhibit snapping. This is confirmed by our simulations of SWNT tips imaging Si(111)-CH_3 surface step edges and Au nanocrystals (supporting information).

4.3 Importance of Adhesion and Friction

The experimental results for imaging with SWNT tips in Figure 5 show that the process takes place primarily in an attractive regime, in *disagreement* with the theoretical simulations of clean surfaces and samples. This indicates that either there is a significantly stronger attraction or adhesion of the SWNT tips to the surface than that corresponding to the van der Waals interactions alone, or that there are other important effects that have not been included in the equation of motion which magnify the effect of the small van der Waals attractive forces.

Jang et al. and Stifter et al.[15-17] have shown that the adhesive force of the AFM tip to the surface mediated by a water meniscus can be significant and in some cases dominant over the van der Waals forces (on the order of tens of nN). Lee et al. measured the adhesive force of a 10 nm multiwall nanotube tip to the surface and also showed that it is on the order of tens of nN[18]. Although clean SWNT tips are hydrophobic, it is possible that the ends are open and oxidized to form hydrophilic functional groups (such as carboxylate groups), especially when the fabrication procedures include severe treatments such as shortening through electric discharges between the tip and surface. [6] In this case it is likely that capillary forces play an important role in the imaging process.

As described in the methods section, we modeled the adhesion forces using values up to 21.5 nN with various decaying functional dependences on the tip position (see supporting information). Additionally, we find that the dissipation term in the cantilever equation of motion is not sufficient to account for the tip-sample friction forces since it only includes the friction of air acting on the oscillating cantilever. These friction forces can be modeled with a dissipation term that is proportional to tip velocity in a manner similar to Newton's law of viscosity,[20] with adjustment of an effective quality factor to achieve the correct order of magnitude agreement with experimental data. There is no easy way to determine this magnitude, and very little is known about these friction forces, but we can imagine that if frictional forces significantly affect the cantilever oscillation, they should be able to dissipate similar amounts of energy as the air damping forces, and since they act over much smaller distances, their effective quality factor should be much smaller than the free air quality factor (the coefficient of the dissipation term is inversely proportional to the quality factor in Equation 1). We used contact quality factor values

between 0.005 and 0.05 times the free oscillation value, which allowed us to obtain results similar to those obtained experimentally (compare Figures 5 and 6).

In our previous report[13] we presented a simulation of the cross-sectional scan of a prone SWNT, which shows "negative" height readings in the regions where the probe snapped or slid past the sample, in disagreement with the experimental result. These negative readings in the simulated scan were due to the probe bending around the sample before reaching the surface, which increased the distance the probe had to descend in order to reach the surface. The results presented here show that friction forces can prevent the tip from reaching the surface, thus reconciling our simulations with our experimental observations.

The experimental results of Figure 5 and the theoretical simulations of Figure 6 show that dissipation effects can also give rise to a continuum of amplitude solutions in addition to (or instead of) the usual discontinuous jumps between attractive and repulsive regimes. We can visualize this continuum of amplitude solutions as a collection of amplitude curves of the same slope, each corresponding to a different amplitude solution (as in the case of bistability, but with a greater number of solutions), which allow the amplitude to vary with arbitrary slope between smaller and larger values. Our results show that as the tip-sample friction increases, the separation between the different regimes becomes smaller, indicating that the number of possible solutions increases and the separation between them decreases. In the limit of large friction, the number of solutions should be infinite.

Lee and coworkers[18] reported that their experimental measurements with a multi-wall carbon nanotube tip did not show evidence of two coexisting regimes as is the case with

regular tips, and although the dimensions of their tip and the geometry of their sample are significantly different than ours, it is possible that their results can also be explained through the introduction of dissipation and adhesion effects that are present when nanotube tips are used. We point out that in this study we have assumed that all sliding phenomena whose friction forces significantly affect the tip oscillation occur between the tip and the sample, but it is also possible that slipping occurs at the attachment between the SWNT tip and the supporting silicon tip, which are kept in place primarily through van der Waals forces (significantly weaker than those due to covalent bonds).

4.4 Practical implications of multistability

It is well known that imaging parameters which lead to bistability[11,12] must be avoided in order to obtain good AFM images, so it is logical to expect the SWNT multistability phenomena described here to also affect image quality significantly. We have shown that these effects are different from bistability in that they include a combination of more than one single interaction potential (between the tip, the sample, and the substrate) with dissipative forces (adhesion and friction) and that they can be explained in terms of individual components related to each type of interaction. Below we discuss the practical implications of each effect separately.

The interaction of the SWNT probe with the *substrate* is responsible for the existence of one attractive and one repulsive amplitude solution, which emerges as a result of the coexistence of an attractive and a repulsive regime in the same tip-sample interaction

potential. This has been extensively discussed by numerous authors,[11,12] and our work reveals no additional knowledge.

Snapping and sliding phenomena and the existence of additional attractive and repulsive amplitude solutions as depicted in Figure 4 result from the interactions between the probe and the *sample*. These effects are not desired because they can distort the dimensions of the image,[13] but can be minimized by selecting the appropriate probe geometry, as discussed extensively in reference 6. In general, snapping and sliding are most likely to occur for probes that are highly tilted (> 30º with respect to the vertical axis), too long (> 55 nm for SWNT probes 5.5 nm in diameter), or with too high an aspect ratio (> 10). Irregular probe geometries on the imaging end can also be a contributing factor to these artifacts. Probes of lower aspect ratio, which are less likely to bend, can be advantageous, but using them requires caution, since extremely short probes (< 20 nm long) can also cause shadowing due to the long range interaction forces between the sample and the supporting silicon tip. [6] *Local* tip deformation can be reduced by using SWNTs of smaller diameters, but this requires using shorter probes due to the softer bending modes of thinner SWNTs. Finally, snapping can be minimized by imaging at lower oscillation amplitudes and higher amplitude setpoints corresponding to less repulsive regimes, which prevent the tip-sample interaction force from reaching the snapping point (see Figure 2 (c)).

The third and last aspect of multistability concerns the gradual transitions between attractive and repulsive regimes, described in Figures 5 and 6. The high quality images[6] obtained with the probe used to obtain our experimental results suggest that this effect

does not significantly affect image quality as long as the *sharp* transitions between attractive and repulsive imaging regimes are avoided.

Thus, the practical considerations for avoiding the deterioration of image quality due to multistability are the same as those used for selecting high quality SWNT probes[6] and avoiding bistability[11,12] in addition to evading the highly repulsive regimes that favor the occurrence of snapping.

5. Conclusions

We have highlighted fundamental differences in the tip-sample interactions between conventional silicon tips and SWNT tips used in tapping-mode AFM imaging and explained the effects of explicit tip-sample adhesion and friction forces. We have also shown that these interactions can be modeled through the individual inclusion of each effect into the equation of motion of a damped harmonic oscillator, thus providing insightful analytical connections between theory and experiment.

There are many sources of uncertainty which could explain the quantitative differences between our experimental and theoretical results, such as the knowledge of the exact relative position of tip and sample in the experiment, the exact tip and sample geometry, the nonlinearity of the tip position with respect to the supporting silicon tip position when the probe deforms, the presence of moisture and impurities on the surface, the exact behavior of adhesion forces, the true nature of the tip-sample friction forces, etc., but nevertheless, the agreement between theory and experiment is remarkable with this simple model. More detailed theoretical and experimental research is required with more

sophisticated assumptions of the tip-sample interaction, which we plan to address in greater detail in a future publication.

Acknowledgement: Santiago Solares and William Goddard were supported by the Microelectronics Advanced Research Corporation (MARCO) and its Focus Center on Function Engineered NanoArchitectonics (FENA). Maria Esplandiu and Patrick Collier were supported by Arrowhead Research.

SUPPORTING INFORMATION

1. SWNT probe TEM image

Figure S-1 shows the TEM image of the SWNT probe used for the experimental measurements. As the picture shows, the probe has diameter and length of approximately 5.5 and 40 nm, respectively, and is tilted 15º with respect to the axis normal to the surface.

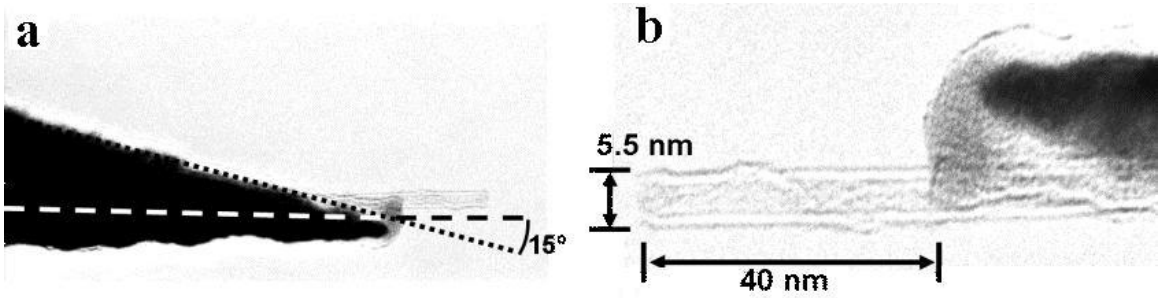

Figure S-1. TEM images of the SWNT probe used for the experimental measurements mounted on a conventional silicon tip. The picture on the left (a) shows that the SWNT probe is tilted 15º with respect to the axis normal to the substrate surface (dashed line). Picture (b) shows the SWNT probe dimensions. Reprinted from (*Nano Letters* **2004**, *4*, 725-731). Copyright (2004) American Chemical Society.

2. Experimental procedure to image directly above the sample SWNT

To ensure that the experimental amplitude and force curves (Figure 5 of the paper) were acquired with the SWNT tip tapping directly on the crown of the sample SWNT, we performed the following procedure. Prior to conducting any measurements, we waited several minutes to minimize any drift. Then, under very low drift conditions, we reduced the scan size to have the sample SWNT in the middle and almost occupying the entire field of view. We again zoomed into the middle of the window (i.e., to the sample SWNT axis), reduced the scan size to zero, and acquired the amplitude and phase curves. Finally, we zoomed out back to the scan size corresponding to the width of the SWNT in order to verify that the sample was still at the same position (i.e., at the center of the scan window as before the measurement). We only kept and evaluated the measurements

from cases in which the sample SWNT position did not change. In such cases, the acquired curves were reproducible.

3. Tip sample force curve of SWNT probe with silicon surface

Figure S-2 shows the tip-sample interaction force curve of the SWNT probe interacting with a bare silicon surface. This curve is similar to that of Figure 2 (b) of the paper, which corresponds to the same tip imaging a prone SWNT in sliding mode. The shifting of the force minimum is due to the presence of the sample, which requires that the probe bend around it before reaching the surface. The magnitude of the attractive force at the minimum is significantly smaller than for a conventional silicon tip (Figure 2 (a) of the paper).

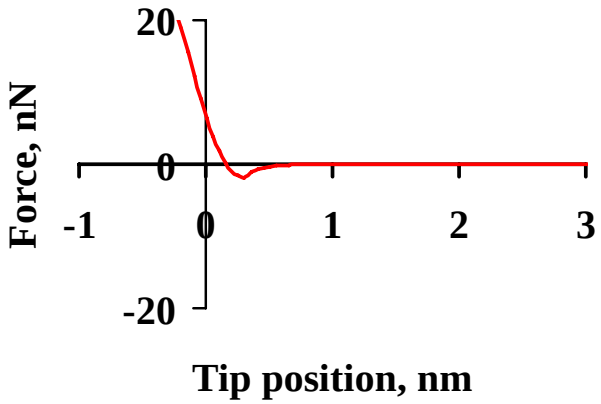

Figure S-2. Simulated tip-sample interaction force curve vs. tip position above the surface for the SWNT probe shown in Figure S-1 imaging a bare silicon surface.

4. Phase space representations

Figure S-3 shows the A_0-Z_c "phase space" representation of the oscillation amplitude solutions for the SWNT tip *smooth gliding* mode and for a silicon tip in the absence of tip-sample adhesion and friction forces. The initial tip velocity, V_0, was set to zero. In both cases there are two distinct solutions to the amplitude, one corresponding to the attractive regime (phase > 90º) and one corresponding to the repulsive regime (phase < 90º). Qualitatively similar results were obtained for V_0 = -0.0025 nm/s and for V_0 = 0.0025 nm/s. This is consistent with the previous work of other authors. [11]

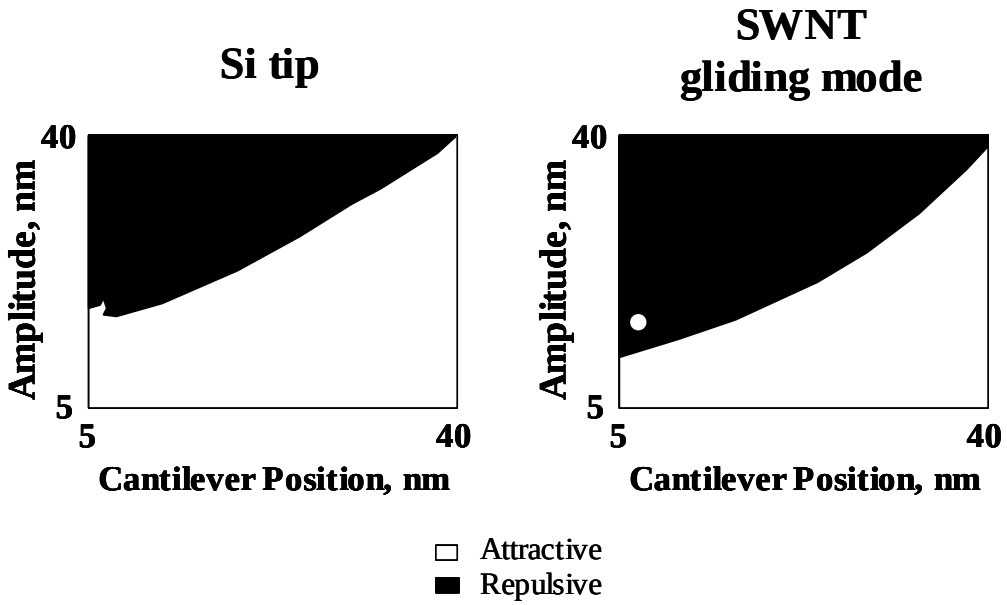

Figure S-3. A_0-Z_c phase space representation of the two amplitude solutions for the conventional silicon tip and for the SWNT tip in *smooth gliding* mode for V_0 = 0 in the absence of tip-sample adhesion and friction forces.

5. Phase and amplitude curves (vs. cantilever position)

Figure S-4 shows the upper portion of the amplitude- and phase-position curves (vs. Z_c) for the SWNT smooth gliding mode and for the conventional silicon tip on the same coordinate system for A_0 = 40 nm and for V_0 = 0 in the absence of tip-sample adhesion and friction forces. These curves show typical behavior, in agreement with the diagrams of Figure S-3, with two amplitude solutions and a discontinuity between them. [11,12] As the probe approaches the sample, the first solution occurs in the long-range attractive regime, and the second solution occurs in the short-range repulsive regime. The amplitude in the attractive regime is lower than the amplitude in the repulsive regime for given values of Z_c and F_0 (excitation force). The amplitude for the SWNT tip is larger than that of the conventional silicon tip for given values of Z_c and F_0, indicating greater probe penetration (as confirmed through MD simulations).

Figure S-5 shows a tip-sample interaction force curve, the amplitude curve and the phase curve for the snapping case of Figure 2 (c) of the paper with the inclusion of a 25 nN tip-sample adhesion force at the points of initial tip-*sample* and tip-*surface* contact. The two attractive solutions (a snapped and an unsnapped oscillation) and one repulsive solution (snapped oscillation) are clearly discernible from both the amplitude and the phase curves. The other repulsive solution (unsnapped oscillation) does not occur due to the large adhesion force (attractive), which dominates the repulsive interactions in the region where snapping does *not* occur. The tip-sample interaction force curve illustrates the different behavior of the force in the upward and downward trajectories of the tip due to snapping, which takes place only during the *downward* motion of the probe, and due to

the adhesion force, which acts only during the *upward* motion of the probe (the parameters and explicit functional forms used to model adhesion forces are given in tables S-1 and S-2).

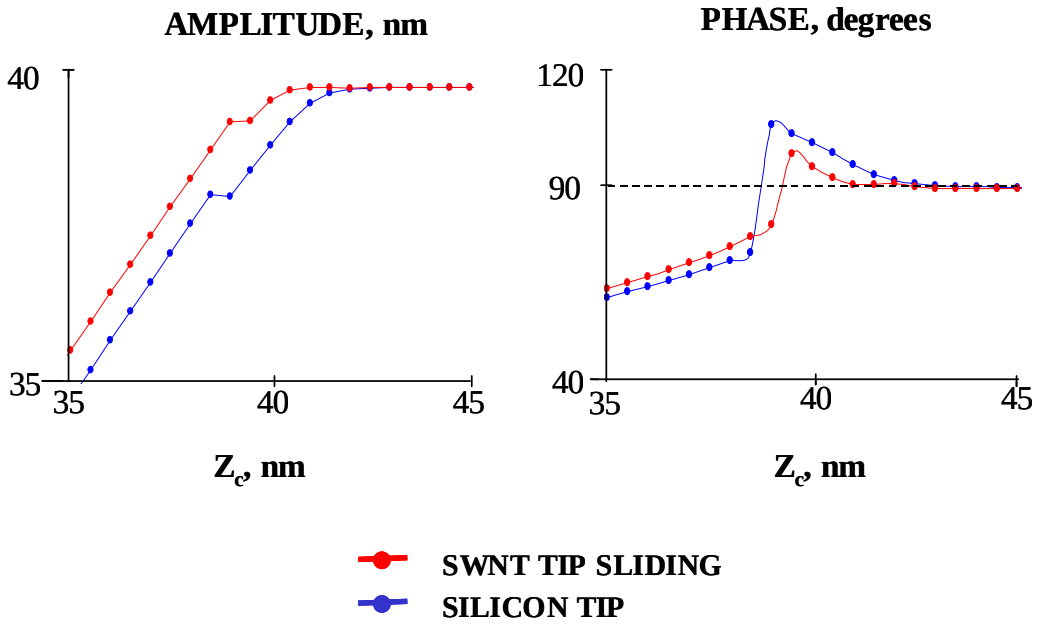

Figure S-4. Oscillation amplitude and phase vs. cantilever position for the Si tip (blue curves) and for the SWNT tip in *smooth gliding* mode (red curves) for A_0 = 40 nm and V_0 = 0 in the absence of tip-sample adhesion and friction forces.

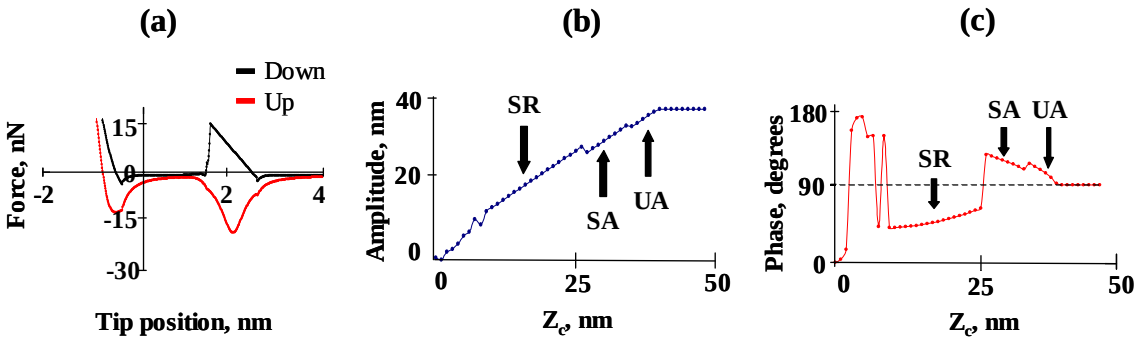

Figure S-5. Tip-sample force (a), amplitude (b), and phase (c) curves for the snapping case of Figure 2 (c) of the paper, with the inclusion of an adhesion force at the point

where tip-*sample* contact first occurs and at the point where tip-*substrate* contact first occurs. Three solutions of the amplitude are discernible in the amplitude and phase curves: the snapped and unsnapped attractive solutions (SA and UA) and the snapped repulsive solution (SR). Note that the abscissa corresponds to the instantaneous tip position (z_{ts}) in curve (a) and to the cantilever *rest* position (Z_c) in curves (b) and (c). A_0 = 40 nm for curves (b) and (c).

6. Adhesion and friction force parameters and functional forms

Table S-1 provides the magnitude of the adhesion forces and contact quality factors used to construct the results presented in Figure 6 of the paper. Different values were used depending on the magnitude of the free oscillation amplitude and on whether or not the probe was able to snap during the oscillation. Table S-2 contains the functional forms used to simulate the adhesion forces. z_{ts} represents the distance from the tip to the substrate surface. The value of z_{ts} for which tip-sample contact first occurs is 2.54 nm in all cases. In all cases the *magnitude* of the adhesion force has a maximum at a tip position slightly lower than the point of initial tip-sample contact and decreases in both directions, as illustrated in Figure S-5 (a). These functional forms, determined through trial and error, were the ones that allowed us to most closely reproduce the experimental results.

Table S-1: Magnitude of the contact quality factor and of the maximum adhesion force for the simulation results of Figure 6.*

	Figure 6 (a)	**Figure 6 (b)**	**Figure 6 (c)**
Contact quality factor, *unsnapped* oscillations	0.005	0.008	0.005
Contact quality factor, *snapped* oscillations	N/A	N/A	0.0045
Maximum adhesion force, *unsnapped* oscillations, nN	21.5	21.5	20
Maximum adhesion force, *snapped* oscillations, nN	N/A	N/A	5

*Note that snapping did not occur for the results shown in Figures 6 (a) and 6 (b), so no parameters are provided for *snapped* oscillations for those cases.

Table S-2: Functional forms used to simulate the adhesion forces (F_a) in the construction of the phase and amplitude curves shown in Figure 6 of the paper (z_{ts} is the tip-surface distance in nm).*

Simulation	**Functional form of the adhesion force**
Figure 6 (a)	$F_a = \frac{-21.5}{1+2.5(z_{ts}-1.86)^{2.75}}$, for $z_{ts} > 1.86$ $F_a = 1000 \mid z_{ts}-1.86 \mid^3 -21.5$, for $z_{ts} < 1.86$ and $z_{ts} > 1.58$
Figure 6 (b)	$F_a = \frac{-21.5}{1+2.5(z_{ts}-1.86)^{2.75}}$, for $z_{ts} > 1.86$ $F_a = 1000 \mid z_{ts}-1.86 \mid^3 -21.5$, for $z_{ts} < 1.86$ and $z_{ts} > 1.58$
Figure 6 (c), *unsnapped* oscillations	$F_a = \frac{-20}{1+2(z_{ts}-2)^2}$, for $z_{ts} > 2$ $F_a = \frac{-20}{1+275(z_{ts}-2)^4}$, for $z_{ts} < 2$ and $z_{ts} > 1.5$
Figure 6 (c), *snapped* oscillations	$F_a = \frac{-5}{1+75(z_{ts}-2)^2}$ for $z_{ts} > 2$ $F_a = \frac{-5}{1+275(z_{ts}-2)^4}$ for $z_{ts} < 2$ and $z_{ts} > 1.5$

*Recall that the adhesion force acts only during the upward motion of the probe *after it has contacted the sample.* Different functions were used for snapped and unsnapped oscillations in the construction of Figure 6 (c).

7. Simulation results for other sample geometries

7.1 Si(111)-CH_3 step edges

Figure S-6 contains the energy[13] and force curves for a 30,30 SWNT probe (4.1 nm diameter) approaching the step edge of a Si(111)-CH_3 surface (Figure S-7). The results indicate that snapping can occur for this type of geometry and dimensions. The labels on the curves of figure S-6 correspond to the MD snapshots of figure S-7 and show the behavior of the probe as it approaches the sample. The phase and amplitude curves are shown in figure S-8 (A_0 = 20 nm). Both the amplitude and the phase curves exhibit multistability, similar to the curves of Figure 4 of the paper.

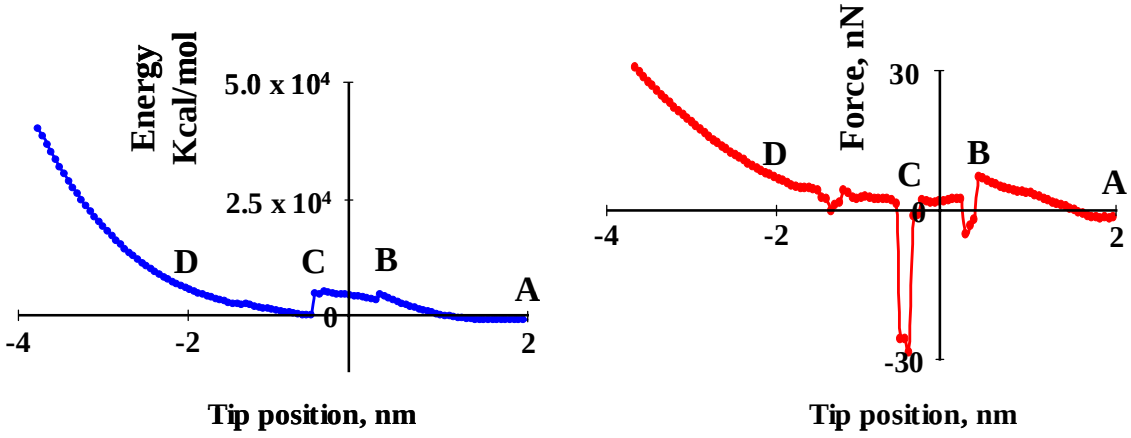

Figure S-6. Energy and force vs. tip position for a 30,30 SWNT tip approaching the step edge of a Si(111)-CH_3 surface. The labels A, B, C, and D correspond to the MD snapshots of Figure S-7.

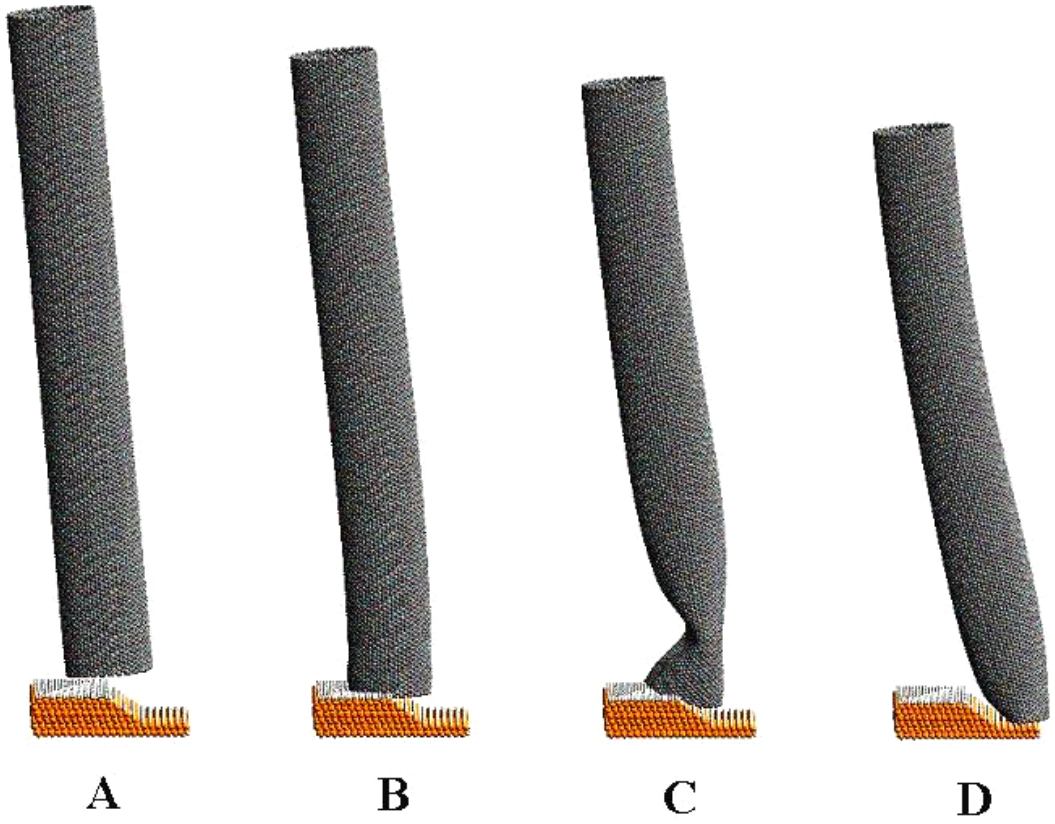

Figure S-7. MD snapshots of a 30,30 SWNT approaching the step edge of a Si(111)-CH_3 surface illustrating the snapping mechanism for this geometry. The labels correspond to those shown on the energy and force curves of Figure S-6.

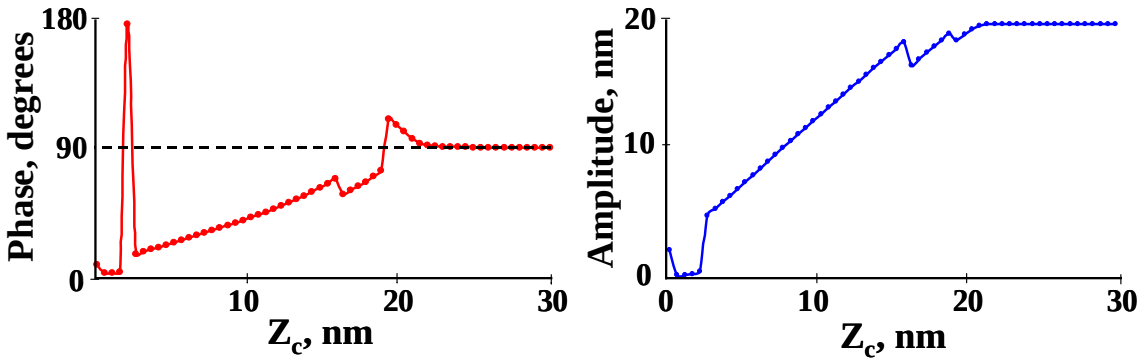

Figure S-8. Phase and amplitude curves constructed using the force curve of Figure S-6. Three amplitude solutions are clearly discernible in both curves (A_o = 20 nm).

7.2 Gold nanoparticles

Figures S-9, S-10, and S-11 show the results for the simulation of a 30,30 SWNT probe (4.1 nm diameter) imaging a 4.7 nm Au nanoparticle in the absence of adhesion and friction forces. These results confirm that snapping can also occur for this system. The amplitude curve shows well defined regions corresponding to the type of oscillation that took place (Figure S-11): region A is the free oscillating amplitude, regions B and E correspond to the range of cantilever positions for which the probe did not snap off the Au nanoparticle, region C corresponds to the range of cantilever positions for which the probe snapped off the Au nanoparticle every oscillation but did not reach the surface, and region D corresponds to the range of cantilever positions for which the probe snapped off the Au nanoparticle and reached the surface during every oscillation. The phase curve clearly shows the transitions between the different attractive and repulsive solutions.

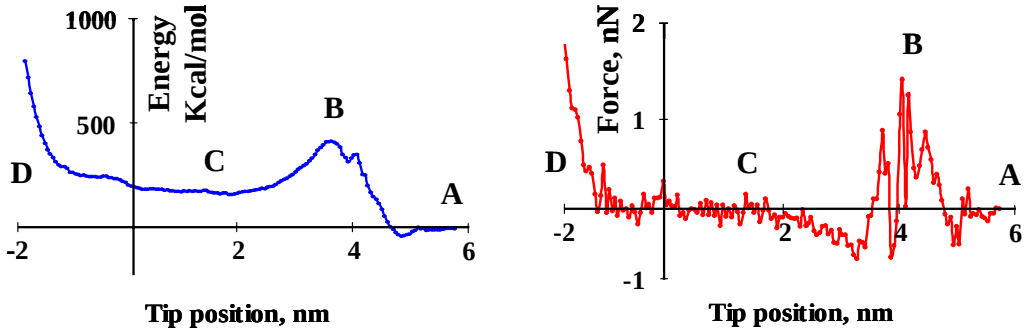

Figure S-9. Energy and force vs. tip position for a 30,30 SWNT tip imaging a 4.7 nm Au nanoparticle. The labels A, B, C, and D correspond to the MD snapshots of Figure S-10.

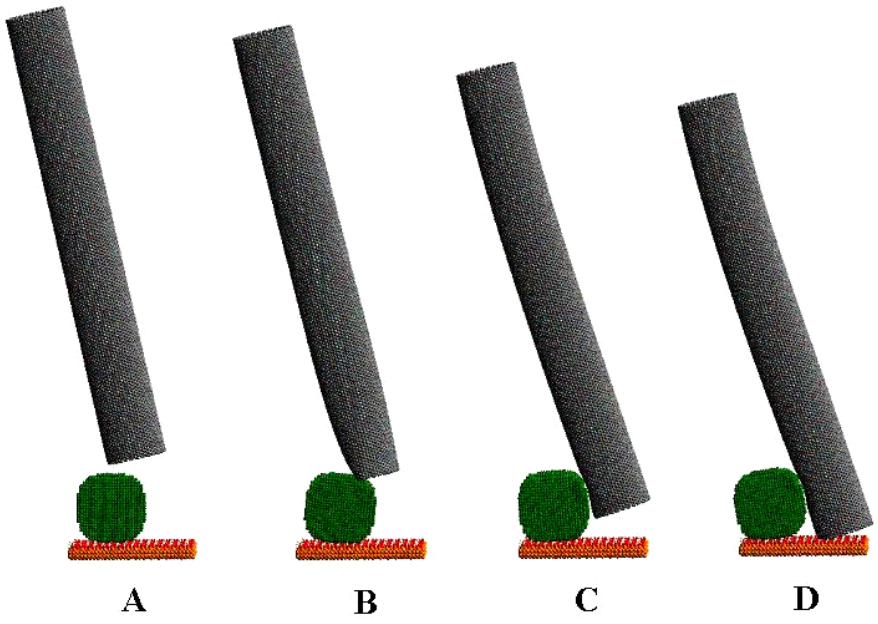

Figure S-10. MD snapshots of a 30,30 SWNT approaching a 4.7 nm Au nanoparticle, indicating that snapping can also occur for this system. The labels correspond to those shown on the energy and force curves of figure S-9.

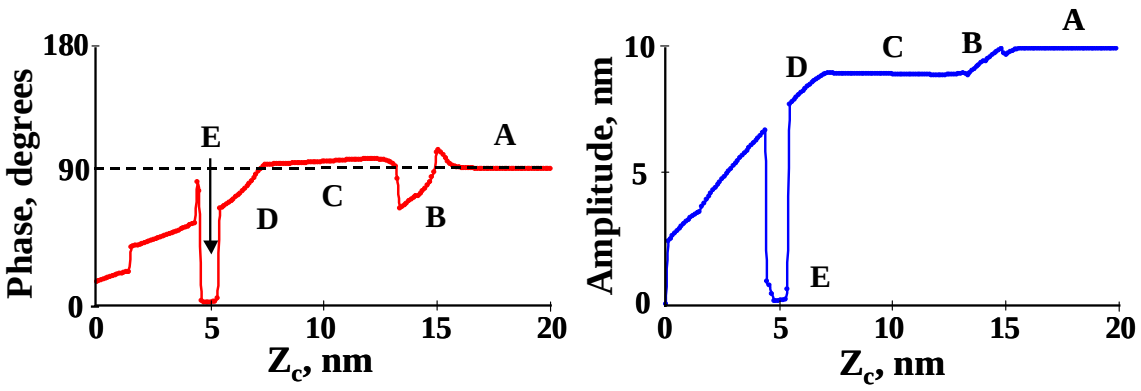

Figure S-11. Phase and amplitude curves constructed using the force curve of Figure S-9. Multiple regimes are clearly discernible in both curves: free oscillation (A), unsnapped oscillations (B and E), snapped oscillations without reaching the substrate surface (C), and snapped oscillations reaching the surface (D). A_0 = 10 nm.

8. Additional MD parameters

We have provided the MD parameters for SWNTs and Si systems in our previous publication. [13] The additional parameters, required for the simulation of the Si(111)-CH_3 surface step edge and for the Au nanoparticle, were taken from the Dreiding Force Field [27] (with the H-C-Si-Si torsion barrier adjusted to 2.945 kcal/mol based on ab initio QM calculations on the Si(111)-CH_3 surface) and from the work of Jang et al. [28] on Au surfaces (using a 6-12 Lennard-Jones function for the Au – C interaction, with R_o = 4.5 Angstroms, and D_o = 0.175 kcal/mol).

REFERENCES:

1. Bushnan, B.; Kasai, T.; Nguyen, C.V.; Meyyappan, M. *Microsys. Technol.* **2004**, *10*, 633.

2. Uchihashi, T.; Choi, N.; Tanigawa, M.; Ashino, M.; Sugawara, Y.; Nishijima, H.; Akita, S.; Nakayama, Y.; Tukumoto, H.; Yokoyama, K.; Morita S.; Ishikawa, M. *Jpn. J. Appl. Phys.* **2002**, *39*, 887.

3. Umemura, K.; Komatsu, H.; Uchihashi, T.; Choi, N.; Ikawa, S.; Nishinaka, T.; Shibata, T.; Nakayama, Y.; Katsura, S.; Mizuno, A.; Tokumoto, H.; Ishikawa M.; Kuroda, R. *Biochem. Biophys. Res. Comm.* **2001**, *281*, 390.

4. Bunch, J.S.; Rhodin, T.N.; McEuen, P.L. *Nanotechnology* **2004**, *15*, S76.

5. Chen, L.; Cheung, C.-L.; P. Ashby, P.; Lieber, C.M. *Nano Lett.* **2004**, *4*, 1725.

6. Wade, L.A.; Shapiro, I.R.; Ma, Z.; Quake, S.R.; Collier, C.P. *Nano Lett.* **2004**, 4, 725.

7. Hafner, J.H.; Cheung, C.L.; Woolley, A.T.; Lieber, C.M. *Prog. Biophys. Mol. Bio.* **2001**, 77, 73.

8. Guo, L.; Liang, J.; Dong, S.; Xu, Z.; Zhao, Q. *Appl. Surf. Sci.* **2004**, *228*, 53.

9. San Paulo, A.; Garcia, R. *Biophys. J.* **2000,** *78*, 1599.

10. Thomson, N.H. *J. Microscopy* **2005,** *217*, 193.

11. García, R.; Perez, R. *Surf. Sci. Reports* **2002**, *47*, 197.

12. García, R.; San Paulo, A. *Phys. Rev. B* **1999**, *60*, 4961.

13. Shapiro, I.R.; Solares, S.D.; Esplandiu, M.J.; Wade, L.A.; Goddard, W.A.; Collier, C.P. *J. Phys. Chem. B* **2004**, *108*, 13613.

14. Hafner, J.H.; Cheung, C.-L.; Oosterkamp, T.H.; Lieber, C.M. *J. Phys. Chem. B* **2001**, *105*, 743.

15. Jang, J.; Schatz, G.; Ratner, M. *J. Chem. Phys.* **2004**, *120*, 1157.

16. Jang, J.; Schatz, G.; Ratner, M. *Phys. Rev. Lett.* **2003**, *90*, 156104-1.

17. Stifter, T.; Marti, O.; Bhushan, B. *Phys. Rev. B.* **2000**, *62*, 13667.

18. Lee, S.I.; Howell, S.W.; Raman, A.; Reifenberger, R.; Nguyen, C.V.; Meyyappan, M. *Nanotechnology* **2004**, *15*, 416.

19. Snow, E.S.; Campbell, P.M.; Novak, J.P. *J. Vac. Sci. Technol. B* **2002**, *20*, 822.

20. McQuarrie, D.A.; ***STATISTICAL MECHANICS***, University Science Books, Sausalito, CA, 2000, 360-362.

21. Dickrell, P.L.; Sinnott, S.B.; Hahn, D.W.; Raravikar, N.R.; Schadler, L.S.; Ajayan, P.M.; Sawyer, W.G. *Tribol. Lett.* **2005,** *18,* 59.

22. Reimann, P.; Evstigneev, M. *New. J. Phys.* **2005,** *7*, 25.

23. Zhang, L.; Leng, Y.; Jiang, S. *Langmuir* **2003,** *19,* 9742.

24. Tsukruk, V.V.; Everson, M.P.; Lander, L.M.; Brittain, W.J. *Langmuir* **1996,** *12*, 3905.

25. Tagami, K.; Tsukada, M. *Surf. Sci.* **2001,** *493,* 56.

26. Tagami, K.; Sasaki, N.; Tsukada, M. *Appl. Surf. Sci.* **2001,** *172,* 301

27. Mayo, S. L.; Olafson, B. D.; Goddard, W. A. *J. Phys. Chem.* **1990**, *94*, 8897.

28. Jang, S.S.; Jang, Y.H.; Kim, Y-H.; Goddard, W.A.;, Flood, A.H.; Laursen, B.W.; Tseng, H-R.; Stoddart, J.F.; Jeppesen, J.O.; Choi, J.W.; Steuerman, D.W.; DeIonno, E.; Heath, J.R.; *J. Am. Chem. Soc.* **2005,** *127,* 1563.

Chapter 3: Influence of Carbon Nanotube Probe Tilt Angle on Effective Probe Stiffness and Image Quality in Tapping-Mode Atomic Force Microscopy*

ABSTRACT. Previous studies have shown that when using carbon nanotubes (CNT) as tapping-mode AFM probes, their tilt angle with respect to vertical (denoted ϕ) must be close to 0º to obtain high quality images and very poor images are obtained for $\phi > 30º$. Here we present a *quantitative* theoretical investigation of the effect of ϕ on tapping-mode AFM imaging for single- and multi-wall nanotube (SWNT and MWNT, respectively) probes of diameters 3.4 to 5.5 nm and aspect ratio 7.5, which have been found ideal for imaging via TEM. Using molecular and classical dynamics we investigate the effect of ϕ on CNT probe stiffness (quantified through the maximum gradient of the tip-sample interaction force) and show that it decreases linearly with increasing ϕ, becoming negligible at around $\phi \sim 40º$, thus confirming the conclusions of previous studies. We find that MWNT probe stiffness is proportional to the number of walls, but that the difference in stiffness between SWNTs and MWNTs also decreases linearly with increasing ϕ and becomes negligible at around $\phi \sim 40º$. The simulated

* Reproduced with permission from Solares, S.D.; Matsuda, Y.; and Goddard W.A. III; *J. Phys. Chem. B* **2005,** *109,* 16658. Copyright 2005, American Chemical Society.

cross-sectional scans of a sample SWNT using two different values of ϕ show that the image can be distorted and shifted laterally when ϕ is large, in some cases giving measured heights appreciably *greater* than the sample dimensions. We show analytically that the tip-sample forces that occur during imaging can be significantly lower when CNT probes are used instead of conventional probes, even in the absence of buckling, and that they can be further reduced by increasing ϕ. Based on this result we propose the design of free-standing kinked probes for the characterization of sensitive samples whereby the probe approaches the sample at a vertical orientation and possesses a tilted section that regulates the tip-sample interaction forces.

1. Introduction

Carbon nanotube (CNT) AFM probes have shown a significant potential for high resolution imaging due to their nanoscale dimensions, high-aspect ratio, stiffness, and chemical stability. [1-11] Various fabrication processes are available to manufacture CNTs and attach them to conventional AFM tips. [1,2,4-6,12-15] Although these methods are reliable and repeatable, challenges still exist in manufacturing probes that are capable of high quality imaging. It has been reported that the probe tilt angle with respect to the axis normal to the substrate, ϕ, is one of the most critical parameters affecting probe quality and that it must be below approximately 30° in order for high-quality imaging to be possible. [1,10,11,15,17,18] In general, probe quality decreases as ϕ increases, and the ideal probe has $\phi = 0°$. However, there has been little *quantitative* investigation of the effect of

ϕ *on image quality* for CNT probe diameters greater than 1 nm and on whether or not modulation this parameter can be advantageous.

We have previously described a methodology that combines molecular dynamics (MD) and classical dynamics (CD) to simulate tapping-mode AFM imaging (chapter 1). [19] With this method, one first calculates the forces and geometry changes experienced by the probe and the sample during imaging using MD. The tip-sample interaction forces are then integrated into the equation of motion of the oscillating cantilever to simulate the AFM operation and the construction of the image. This analysis treats the cantilever-tip ensemble as a point mass using the equation of motion of a damped harmonic oscillator, which has been used extensively to study these systems:[20]

$$m\frac{d^2z(Z_c,t)}{dt^2} = -kz(Z_c,t) - m\frac{\omega_o}{Q}\frac{dz(Z_c,t)}{dt} + F_{ts}(z_{ts}) + F_o\cos(\omega t), \qquad (1)$$

where $z(Z_c,t)$ is the instantaneous tip position with respect to the AFM cantilever rest position (Z_c), k is the harmonic force constant for the displacement of the tip with respect to Z_c, m is the cantilever's effective mass, $\omega_0 = \sqrt{k/m}$ is the free resonant frequency, Q is the quality factor, z_{ts} is the instantaneous tip *vertical* position *with respect to the sample*, $F_{ts}(z_{ts})$ is the *vertical component* of the tip-sample interaction force (calculated using MD), and $F_o\cos(\omega t)$ is the oscillating driving force applied to the cantilever. We used Q = 150, k = 4.8 N/m, and ω_o = 47.48 kHz for all calculations described here, corresponding to previously reported experimental and theoretical results. [19]

Using a 40,40 single wall carbon nanotube (SWNT) probe model constructed from the TEM image of an actual probe[19] (diameter 5.5 and aspect ratio 7.5, Figure 1), we first study the effect of ϕ on $F_{ts}(z_{ts})$ and its gradient upon contact with a Si(100)-OH surface. We show that the vertical probe stiffness, which we quantify as the maximum absolute value of the gradient of $F_{ts}(z_{ts})$ with respect to z_{ts} at the onset of lateral probe slippage, decreases linearly with increasing ϕ up to approximately $\phi = 40°$, beyond which it becomes negligible. We repeat the analysis for single-, double-, and triple-wall CNT probe models (multi-wall nanotubes, MWNT), all with an outer diameter of 3.4 nm and aspect ratio 7.5, and find that MWNT probe stiffness is proportional to the number of walls but that the difference in stiffness between SWNT and MWNT probes decreases linearly as ϕ increases and becomes negligible beyond approximately $\phi = 40°$. Using the 40,40 SWNT probe model with $\phi = 40º$, we simulate the tapping-mode AFM cross-sectional scan of a 16,16 SWNT (diameter 2.1 nm) lying prone on the surface and compare it to a previously reported high quality image obtained for $\phi = 15º$, which was shown to be in agreement with the experimental result. [19] This comparison illustrates the lateral image shifting and measured height distortion that takes place as ϕ increases, and shows that it is primarily the result of *simultaneous* contact between the probe and the sample *and* between the probe and the substrate, which reduces the probe's ability to bend. Finally, we describe tapping-mode AFM simulations based on Equation (1) for SWNT probes with different values of ϕ, which quantify its effect on the cantilever oscillation dynamics in terms of forces, oscillation amplitudes, and probe deformation, and compare the results to those obtained with a conventional 15-nm-radius Si tip. We

find that the tip-sample repulsive forces during imaging can be several times greater for Si tips than for CNT tips, even in the absence of buckling, and explain this difference in terms of the area under the tip-sample force curve, which corresponds to work used to stop the downward motion of the AFM cantilever as it approaches the surface every oscillation (this comparison focuses primarily on Si tips of conventional dimensions, i.e., with radii > 5 nm, which are the most common. However, in the supporting information we provide calculations, which suggest that if Si tips of dimensions comparable to those of SWNTs can be manufactured and maintained sharp during imaging, they can also lead to lower tip-sample interaction forces that are similar to those obtained with vertically aligned SWNTs).

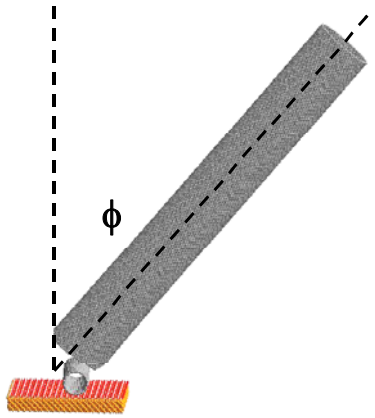

Figure 1. 32,000 atom model of a 40,40 SWNT probe, constructed from the TEM image of an actual probe,[19] interacting with a 16,16 SWNT sample on a Si(100)-OH surface. The probe diameter and length are 5.5 and 40 nm, respectively, and $\phi = 40°$. The sample is a 16,16 SWNT with diameter and length of 2.1 and 10 nm, respectively, whose ends were held fixed during imaging.

Our results confirm the general conclusions of previous experimental and theoretical studies, indicating that the optimum probe orientation is along the axis normal to the substrate surface, but they also suggest that probe stiffness can be modulated by controlling the tilt angle, thus enabling the tapping-mode AFM characterization of highly sensitive samples which are damaged by large tip-sample forces. We propose that the ideal probe to image such sensitive samples is a *free-standing* kinked probe (Figure 2) that approaches the sample at a nearly vertical orientation, thus ensuring high imaging resolution, and contains a tilted section that modulates the tip-sample interaction forces. We discuss current alternatives in manufacturing these probes and offer our design as a challenge to experimental research groups.

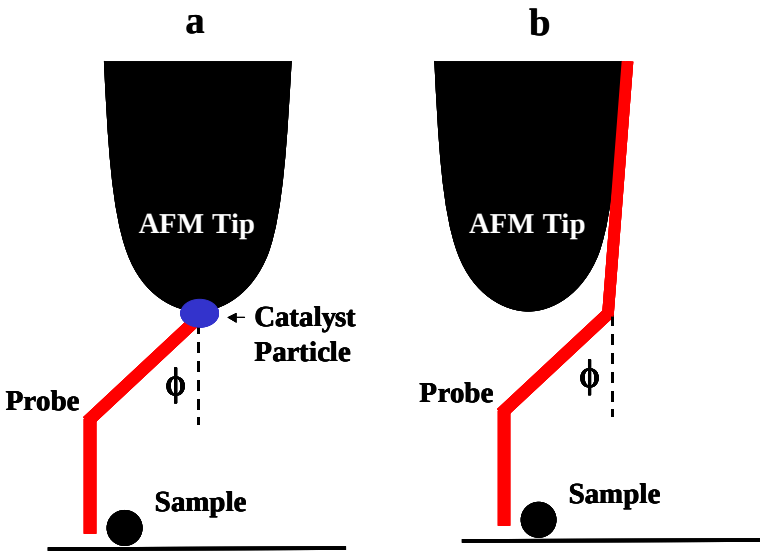

Figure 2. Illustration of *free-standing* kinked nanotube AFM probes containing a tilted section that acts as a spring, which modulates the tip-sample interaction force, and a vertical section, which ensures high imaging resolution. (a) Probe grown from a catalyst particle on the supporting tip. (b) Probe adsorbed onto the supporting tip.

2. Methods

A detailed description of the MD/CD AFM methods, force field functional forms and parameters, and simulation software is provided in reference 19. All tip-sample interaction force curves described here were constructed using *fully atomistic* models containing up to 32,000 atoms.

Note that throughout this paper "probe stiffness" refers to the *effective* stiffness of the probe in the *vertical* direction. Equation (1) is a *one-dimensional* equation describing the AFM cantilever motion only in the *vertical* direction.

2.1 SWNT and MWNT probe stiffness

To study the effect of ϕ on SWNT probe stiffness, we calculated the tip-sample interaction force as a function of the vertical tip position, $F_{ts}(z_{ts})$ in Equation (1), for the 40,40 SWNT probe in Figure 1 (diameter 5.5 nm and length 40 nm) approaching a Si(100)-OH surface using values of ϕ ranging from 0 to 60° at increments of 10°. We then calculated the gradient of these functions and determined the "terminal force gradient" which we define as the steepest value of the tip-sample force gradient observed when the probe is compressed against the surface (Figure 3 shows that the force curves for SWNT probes approach straight lines at the points of probe slippage, suggesting that the terminal force gradient can be used as a quantitative parameter in the description of CNT probe stiffness).

To quantify the dependence of probe stiffness on ϕ and the number of walls in MWNT probes, we constructed the tip-sample force curves for single-, double-, and triple-wall CNT probes of the same outer diameter and length (3.4 and 25 nm, respectively) imaging a Si(100)-OH surface for ϕ = 10, 25, and 40° and calculated their terminal force gradient. In all three cases, the outermost wall was modeled as a 25,25 SWNT (diameter 3.4 nm), and the inner walls were modeled as 20,20 (diameter 2.7 nm) and 15,15 (diameter 2.0 nm) SWNTs, as appropriate. The difference in diameters between adjacent probe walls was selected to fit the known interlayer distance in MWNTs (~0.35 nm).

To provide a comparison between CNT and conventional AFM tips, we also calculated $F_{ts}(z_{ts})$ for a 15-nm-radius Si tip imaging the same Si(100)-OH surface. We are primarily interested in providing a general comparison between SWNT tips and Si tips of radii greater than 5 nm, which are the most common. However we did perform a comparison between a 30,30 SWNT Tip and a Si tip of the same radius (~1.7 nm) and provide the results and general conclusions in the supporting information.

2.2 Image distortion for highly tilted probes

To study the distortion of a real image as ϕ increases, we calculated the AFM cross-sectional scan of a 16,16 SWNT lying prone on a Si(100)-OH surface using the probe model shown in Figure 1 with ϕ = 40° and plotted it on the same graph with a previously reported calculation performed on the same model but with ϕ = 15º, which gave a high quality image in agreement with the experimental result. [19] These cross-sectional scans were constructed using a free oscillation amplitude A_o = 39 nm and an amplitude setpoint

of 15.4 nm. Reference 19 provides the details of the theoretical procedure used to construct the images.

2.3 Cantilever oscillation dynamics

Here we constructed the oscillation amplitude curves (vs. cantilever rest position with respect to the surface, Z_c) for the 40,40 SWNT probe for ϕ = 0, 20, 30, and 40º; and for free oscillation amplitudes A_o = 20, 30, and 40 nm. This was done by inserting the force curves described in section 2.1 into Equation (1) and solving numerically for the tip position as a function of time, from which the oscillation amplitude is directly obtained. Since probe slippage occurred at low tip-sample forces for ϕ = 40º, we extrapolated the smooth portion of the corresponding force curve beyond the point of slippage using the terminal force gradient (as illustrated in Figure 3) to be able to compare the results to those obtained for lower values of ϕ, for which slippage did not occur during imaging. From the tip trajectory and the tip-sample force curves we also calculated the lowest vertical position of the AFM cantilever tip, Z_{min}, and the maximum tip-sample force, F_{max}, observed *during one full cantilever oscillation* for different values of Z_c (for these systems F_{max} occurs at Z_{min}, where tip and sample experience the greatest deformation). We also calculated $z(Z_c,t)$, $Z_{min}(Z_c)$, $F_{max}(Z_c)$, and the oscillation amplitude (vs. Z_c) for the Si tip using the same three values of A_o.

3. Results

3.1 SWNT and MWNT probe stiffness

Figure 3 shows the calculated tip-sample interaction force curves for the 40,40 SWNT probe (for ϕ = 0, 20 and 40º) and for the 15-nm-radius Si tip imaging a Si(100)-OH surface. The graph shows that when using the SWNT probe, the tip-sample force decreases with increasing ϕ for tip positions below the point of initial tip-sample contact (zero on the horizontal axis). It also shows that the smooth section of the force curve approaches a straight line as the cantilever descends significantly beyond the contact point, up to the point of lateral probe slippage (illustrated in Figure 4), beyond which it oscillates in an unpredictable fashion. As ϕ increases, the terminal force gradient becomes less steep, indicating a reduction in probe stiffness. The force curve for the Si tip is the steepest of all due to the significantly more repulsive tip-sample interaction forces experienced by this solid and less deformable probe. In the supporting information we provide a comparison between the force curves of a 30,30 SWNT tip and a Si tip of the same radius (~1.7 nm), which shows that the tip-sample repulsive forces are comparable in both cases. Since such fine tips are not the most commonly used in AFM, and since the focus of our study are CNT probes, we restrict our discussion to Si tips with radii greater than 5 nm. Figure 5 shows the smooth linear behavior of the terminal force gradient as a function of ϕ for the SWNT probe, suggesting that it is an ideal measure of CNT probe stiffness. There are two well-defined regions on the graph, in both of which the terminal force gradient varies approximately linearly with ϕ. In the first region, where $\phi < 40°$, it varies with a slope of ~ 1.93 N/m/º, and in the region where $\phi > 40°$, it

is negligible. Thus, if ϕ can be controlled, stiffness modulation is possible for $\phi < 40^{\circ}$ (but not for $\phi > 40^{\circ}$).

Our calculations also indicate that the maximum force a CNT probe can withstand without slipping on a clean and dry Si(100)-OH surface rapidly decreases with increasing tilt angle. For example, Figure 3 shows that this force drops from ~ 68 nN to only ~ 22 nN when ϕ is increased from 0° to 20° for our 40,40 SWNT probe. These values could change for other surfaces or when moisture and impurities are present on the surface, but even in those cases we expect the *general* trend to be similar.

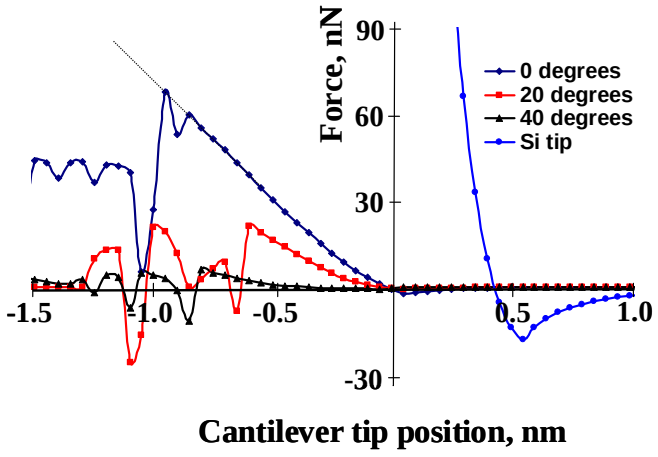

Figure 3. Tip sample interaction force vs. cantilever tip position for the 40,40 SWNT probe shown in Figure 1 (for ϕ = 0, 20 and 40°) and for a 15-nm-radius Si tip imaging a Si(100)-OH surface. The results indicate that for the SWNT probe, the tip-sample force and its steepness decrease with increasing ϕ in the region of tip-sample contact. The dotted line on the 0° curve illustrates the extrapolation of the force curve beyond the point of probe slippage, whose slope we define as the terminal force gradient and use as a

quantitative measure of probe stiffness. The discontinuities in the SWNT force curves are due to lateral probe slippage, as illustrated in Figure 4. Negative values of the tip position indicate tip and sample deformation.

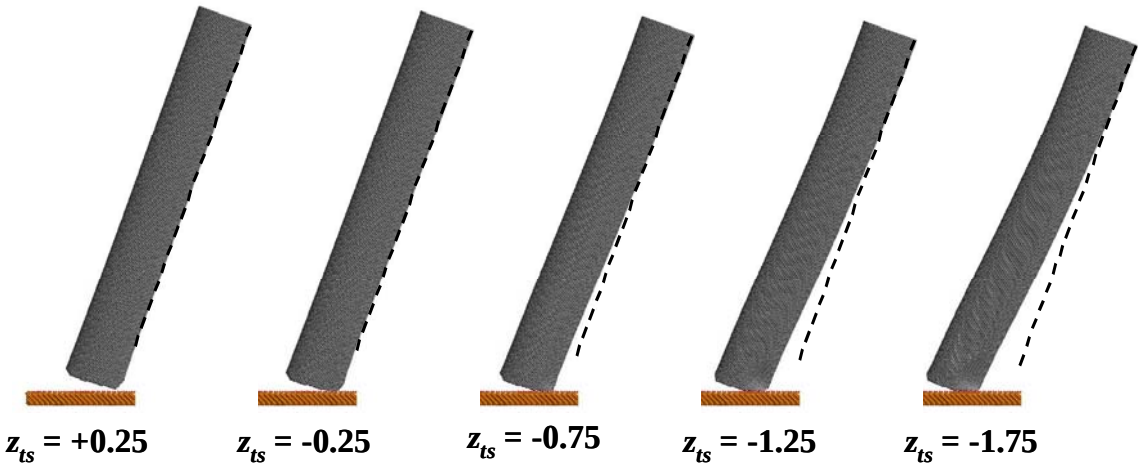

Figure 4. Snapshots of the 40,40 SWNT probe shown in Figure 1 approaching a clean Si(100)-OH surface for different values of z_{ts}. The probe tilt angle is 20°. The pictures show that significant bending and lateral slipping take place when the probe descends below z_{ts} = -0.75 nm. This causes discontinuities in the tip-sample interaction force curves, as shown in Figure 3.

Figure 6 shows the terminal force gradient vs. ϕ for single-, double-, and triple-wall CNT probes with an outer diameter and length of 3.4 and 25 nm, respectively (the corresponding force curves for MWNTs are provided in the supporting information). The results clearly show that MWNT probes with increasing number of walls are stiffer in the vertical direction when compared to SWNT probes, with the probe stiffness being proportional to the number of walls. However, the difference in stiffness between SWNT

and MWNT probes decreases linearly as ϕ increases and becomes negligible at approximately $\phi = 40°$.

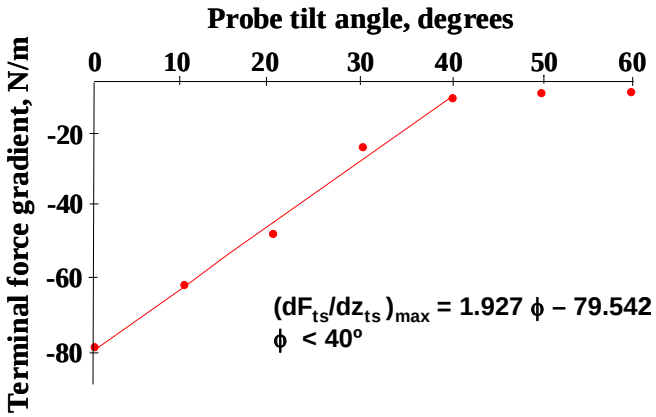

Figure 5. Terminal force gradient vs. ϕ for the 40,40 SWNT probe shown in Figure 1 imaging a Si(100)-OH surface. *Increasingly negative* gradients correspond to *greater* vertical probe stiffness. The graph has two well-defined regions in which the terminal force gradient varies approximately linearly with ϕ. For $\phi < 40°$, it varies with a slope of ~ 1.93 N/m/°, and for $\phi > 40°$, it approaches the horizontal axis.

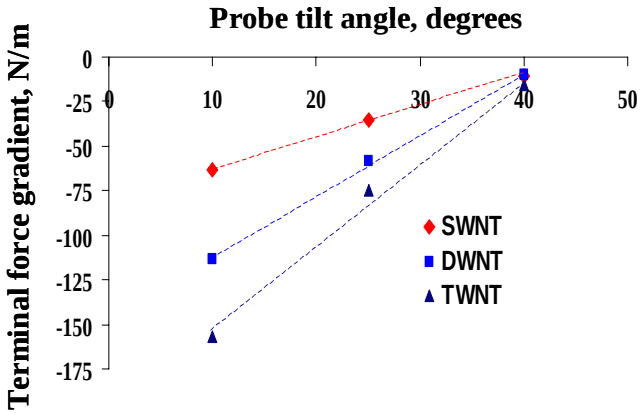

Figure 6. Terminal force gradient vs. ϕ for single-, double-, and triple-wall CNT probes (SWNT, DWNT, and TWNT, respectively) with an outer diameter and length of 3.4 and

25 nm, respectively, and inter-wall spacing of 0.35 nm. MWNT probe stiffness is proportional to the number of walls, but the difference in stiffness between probes containing a different number of walls decreases as ϕ increases and becomes negligible at approximately $\phi = 40°$.

Our simulations show that the primary modes of tip deformation in our systems (see supporting information) are macroscopic bending/shearing and local deformation at the end of the tip (shearing occurs because only one corner of the CNT tip contacts the surface when the probe is tilted). We found that the proportion of strain energy stored in the *local* deformation mode with respect to the macroscopic bending/shearing mode is greater for tilted probes than for vertical probes. For example, we calculated that for a tip position of -0.5 nm (measured on the horizontal axis of Figure 3) and when $\phi = 0º$, approximately 20% of the *total* strain energy of the 40,40 SWNT tip is stored in the 4 nm at the end of the probe (i.e., in 10% of the total probe length). This proportion increases to ~26% when $\phi = 10º$ and to ~64% when $\phi = 20º$ and then decreases slightly for $\phi > 20º$. This may be counter-intuitive, since one would expect that as the probe tilt increases it becomes much easier to bend and that this would cause more strain energy to be stored in the bending mode. However, in the range of tip positions useful for imaging (cantilever tip positions > -0.75 in Figure 3), the *lateral* deformation of the wall at the end of the tip can be significant due to the hollow nature of CNTs. This is more significant for SWNTs than MWNTs.

3.2 Image distortion for highly tilted probes

Figure 7 shows the simulated AFM cross-sectional scans of a 16,16 SWNT lying prone on the surface obtained with the 40,40 SWNT probe at $\phi = 15°$ (previously shown to be in agreement with experiment[19]) and at $\phi = 40°$. The result obtained for $\phi = 40°$ shows a distortion in the geometry of the sample with a significant discrepancy between the calculated and the actual dimensions. MD simulations indicate that the peak in the scan at a horizontal position of 5 nm (showing a measured height of over twice the actual sample height) occurs because the probe is able to contact the sample and the substrate surface simultaneously (Figure 8), which reduces its effective flexibility. The observed distortion in the sample height is counter-intuitive. Normally one would expect a softer probe to be less sensitive to the sample details, which would result in *reduced* measured height. However, as the probe contacts the surface and the sample simultaneously, the repulsive interactions with the sample exert vertical (upward) forces on the side of the probe that reduce its ability to bend downward upon contacting the surface. This results in a greater *effective* probe stiffness (analogous to that of a shorter probe), which opposes the descent of the oscillating cantilever more strongly than if the sample were not present and the probe were only contacting the surface. The net result is a higher reading in a region where the *end* of the SWNT probe is *not* contacting the sample and should not be able to detect it. This type of inappropriate tip-sample contact can also shift the image to the left with respect to the case when a nearly vertical probe is used because the probe can sense the presence of the sample before its imaging end reaches the same horizontal position as the edge of the sample (when traveling from left to right). The right side of

the image is similar for both tilt angles, indicating that for this type of sample the deterioration of the image for high tilt angles is *primarily* due to geometric incompatibility between probe and sample. The results of sections 3.1 and 3.3 show that the decrease in probe stiffness and the occurrence of lateral slippage are also significant for $\phi = 40^{\circ}$. From these results it is evident that modulation of probe stiffness cannot be successfully accomplished unless the probe approaches the sample at a nearly vertical orientation.

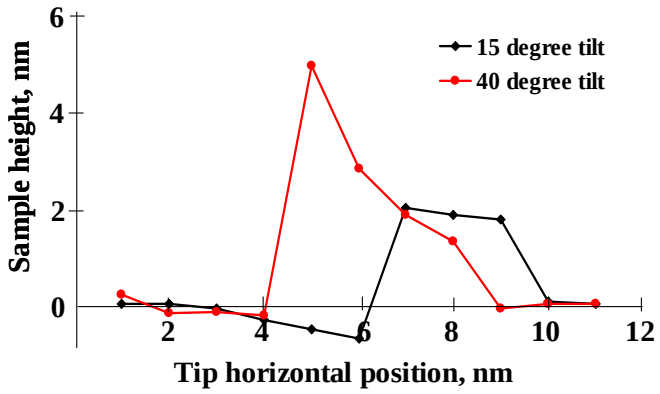

Figure 7. Simulated AFM cross-sectional scan (sample height vs. horizontal position) of a 16,16 SWNT (2.1 nm diameter) lying prone on a Si(100)-OH surface, obtained using the 40,40 SWNT probe model shown in Figure 1 for $\phi = 15$ and 40°. A high-quality image was obtained for $\phi = 15°$, in agreement with the experimental result,[19] but not for $\phi = 40°$.

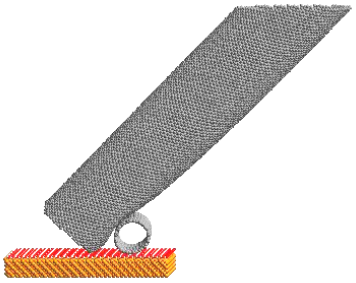

Figure 8. 40,40 SWNT probe imaging a prone 16,16 SWNT at $\phi = 40°$ showing that this tilt angle is inappropriate because it allows the probe to contact the surface *and* the sample at different horizontal positions *simultaneously*. This type of inappropriate contact causes severe lateral shifting and size distortion of the AFM image, as depicted in Figure 7.

3.3 Cantilever oscillation dynamics

Figure 9 illustrates the dependence of Z_{min}, F_{max}, and the cantilever oscillation amplitude on the cantilever rest position for the 40,40 SWNT probe and for the 15-nm-radius Si tip imaging a Si(100)-OH surface with $A_o = 40$ nm. As ϕ increases for the SWNT probe, its lower vertical stiffness allows the cantilever to approach the surface more closely (reaching lower values of Z_{min}) and oscillate with greater amplitude. This also causes greater probe bending, as verified through MD simulations. Note that the separation between curves for $\phi = 0°$ and $\phi = 20°$ is much smaller than the separation between the curves for $\phi = 20°$ and $\phi = 40°$, indicating that the sensitivity of Z_{min}, F_{max}, and the cantilever oscillation amplitude to changes in ϕ increases as ϕ increases.

Various authors have pointed out that the degree of sample damage is lower when using CNT tips vs. conventional Si tips because the maximum tip-sample force is limited by CNT buckling[3-5], but our results show that the tip-sample forces for CNT probes are also lower *in the absence of buckling* and that this is due to the difference in steepness between the tip-sample force curves of CNT and Si tips (Figure 3). The results provided in Section 1 of the supporting information show that lower tip-sample forces can also be obtained through the use of ultra-fine Si tips. The discussion presented here is limited to Si tips of radii greater than 5 nm. As the repulsive portion of the force curve becomes *less* steep, the area under the curve from the point of initial tip-sample contact up to a *fixed* value of F_{max} increases. Since this area represents work used to stop the downward motion of the oscillating cantilever and since the work requirement does not vary significantly with the shape of the force curve, the necessary work (area) can be obtained for a lower value of F_{max} with a *less* steep force curve. Figure 3 shows that the force curve for the Si tip is significantly steeper than any of the force curves for the SWNT tip, and Figure 9b confirms that during imaging this leads to tip-sample forces several times greater for the Si tip. As ϕ increases, the force curves for the SWNT probe become less steep, which results in lower values of F_{max} for greater values of ϕ. Thus we expect a reduction in the degree of sample damage as ϕ increases, *even when there is no change in the imaging parameters.*

Note that we did *not* observe buckling in any of our simulations with 40,40 SWNT vertical probes experiencing repulsive forces up to ~68 nN, which are over three times greater than those observed during imaging with A_o = 40 nm (Figure 9b). For this value of A_o buckling was *not* observed for any probe tilted less than 30°, although moderate

bending did take place for $\phi > 20°$. Consider, for example, the 40,40 SWNT probe tilted 20°. Figure 9b shows that when A_o = 40 nm, the maximum tip-sample forces are ~16.5 nN. Figure 3 shows that for this tilt angle slippage did not occur below ~23 nN (the force curve is smooth up to this value), which, according to Figure 4, corresponds to only *minor* bending.

The behaviors of Z_{min}, F_{max}, and the cantilever oscillation amplitude for A_o = 20 and 30 nm (supporting information) show a similar dependence on ϕ as for A_o = 40 nm (Figure 9), but the observed variations for different values of ϕ are smaller due to the smaller excitation force required to obtain to smaller values of A_o. As expected, the oscillation amplitude and F_{max} increased with increasing A_o (due to greater cantilever excitation force), while Z_{min} decreased (due to increased tip and sample deformation).

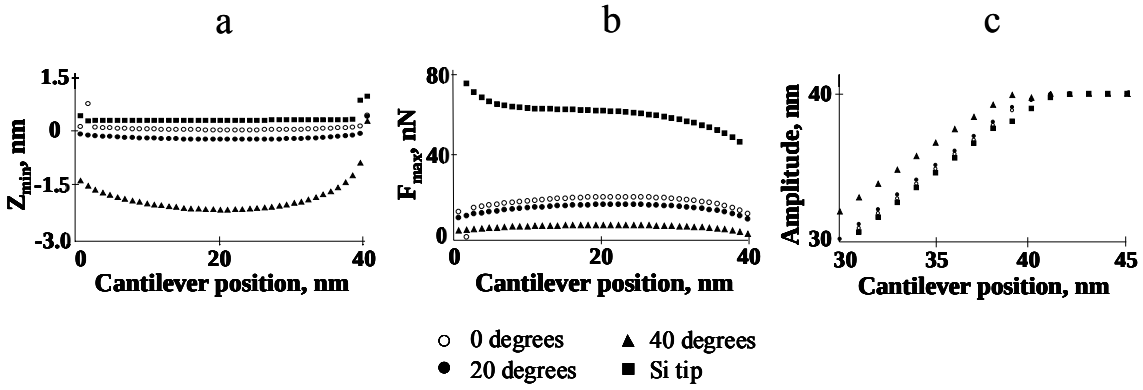

Figure 9. Lowest cantilever position (a) and maximum tip sample force (b) observed *during one full oscillation of the AFM cantilever* and oscillation amplitude (c) vs. cantilever rest position for the 40,40 SWNT probe shown in Figure 1 (for ϕ = 0, 20, and 40º) and for a 15-nm radius Si tip imaging a clean Si(100)-OH surface. A_o = 40 nm in all cases. The discontinuities on the curves (such as the jump in the Z_{min} curve for the Si tip

–black squares– between cantilever positions of 38 and 39 nm) correspond to the well-known transitions between the attractive and repulsive imaging regimes of tapping-mode AFM. [21] Note that $Z_{min} = 0$ corresponds to the AFM cantilever rest position for which the tip (SWNT or Si) is *first* able to contact the surface.

4. Discussion

4.1 Shortcomings of highly tilted probes

One of the standard criteria that are used to select AFM CNT probes is that their tilt angle must be as close as possible to zero with respect to the axis normal to the sample substrate. [1,15,17,18] Experiments conducted using a wide range of probe sizes and theoretical simulations of 1-nm-diameter probes indicate that the image can be significantly distorted when this angle is greater than 30º. [1,17,18] Our simulations confirm this conclusion for a wider range of probe dimensions and provide a quantitative measure of the decrease in vertical probe stiffness as the tilt angle increases. Note that the dimensions of the probes used in our analysis were selected to be in the range of high-quality AFM probes,[1] thus excluding the most obvious causes of imaging artifacts and isolating the effect of the probe tilt angle on image quality. However, we do believe that there are other parameters, such as the probe aspect ratio, which can be tuned/optimized in order to modulate the tip-sample forces, although with a smaller effect than that of adjusting the tilt angle. The results show that the distortion of the image for highly tilted probes is due to the combination of four main factors:

First, as ϕ increases, the probe stiffness (as defined in section 1.0) decreases linearly (Figures 3 and 5), making the probe less sensitive to the fine details of the sample. This is similar to using a sponge probe, whose softness would mask the features of the sample, causing it to appear flat.

Second, as a result of its lower stiffness, the probe is less capable of limiting the range of oscillation of the AFM cantilever, which can lead to probe bending, lateral slipping, and even buckling. Consider, for example, the results of Figure 9a for the 40,40 SWNT probe. The chart shows that when $\phi = 40^{\circ}$ and $A_o = 40$ nm, the cantilever descends below a position of –0.75 nm during every oscillation for most of the range of cantilever rest positions shown, but according to Figure 3 this results in slippage.

Third, as ϕ increases, the likelihood that the geometry of the tip and the sample are incompatible increases. This is the case for SWNT samples, for which a highly tilted probe is able to contact the sample and the substrate surface simultaneously (Figure 8), causing significant distortions and lateral shifting of the image (Figure 7).

Finally, at high tilt angles the supporting Si tip approaches the sample more closely for a given CNT probe length, experiencing greater interactions with the surface and in some cases causing imaging artifacts such as shadowing. [1] This is magnified when severe probe bending and buckling occur. Consider, for example, a 40,40 SWNT probe protruding 10 nm from a 15-nm-radius Si tip tapping at the bottom of a narrow, 4-nm-deep trench. Our calculations show that when $A_o = 10$ nm and $\phi = 40^{\circ}$, the *maximum* repulsive force experienced by the SWNT tip will be ~6.5 nN. Under these conditions, the supporting Si tip can experience attractive forces as large as 2% of this value, which compares to only 0.3% when $\phi = 0°$. These interactions can be quite significant if one

considers that the *repulsive* forces between the CNT probe and the surface act over a very small range (< 0.25 nm) and that the attractive forces between the Si tip and the surface act over very long ranges (> 1 nm) and are significantly greater than the *attractive* forces between the CNT probe and the surface (Figure 3).

Our results show that MWNT probes exhibit greater vertical stiffness than SWNT probes, making them significantly more robust at nearly vertical orientations. However, since this advantage vanishes as ϕ increases and since the outer geometry of MWNTs does not differ from that of SWNTs, MWNTs cannot overcome the deterioration in imaging quality associated with highly tilted probes ($\phi > 40^{o}$).

4.2 Imaging of sensitive samples

We have shown analytically that the tip-sample repulsive forces that take place during tapping-mode AFM imaging can be significantly lowered when CNT tips are used instead of conventional AFM tips. However, it is well known that there is a wide range of organic and biological samples that could be damaged in contact-mode AFM regimes, even when using CNT tips for which further modulation of the tip-sample forces would be advantageous. Various authors have successfully imaged sensitive samples in non-contact mode,[5,7,8] but this type of imaging has two very important limitations: first, it may be subject to tip-induced broadening[3,16] caused by the long-range van der Waals forces between the tip and the sample, and second, since there is no tip-sample contact, one can only obtain information about the bulk geometry of the sample, but not about its elastic properties.

Some biological samples have been successfully imaged in contact mode,[3,4,6,10,11,14,16] but this is generally difficult to accomplish with conventional CNT probes because the range of probe sizes (and stiffness) is limited by the type and size of CNTs that can be controllably manufactured and attached to AFM tips. Additionally, the softer (smaller) CNT probes that would be required to image the softest samples may not be suitable for imaging due to aspect ratio limitations (they would have to be extremely short to reduce bending and prevent buckling, and this could cause interference by the supporting Si tip).

It has also been reported that imaging in a liquid environment facilitates tapping-mode AFM imaging,[16] but this may change the conformation of the sample and affect the tip-sample interactions in a way that precludes imaging in the desired state, especially for non-biological samples. Furthermore, since non-functionalized CNTs are hydrophobic, imaging in an aqueous environment (the most common environment in biological applications) isn't always feasible. [22] (The simulated force curve of a 1.7-nm-radius Si tip, provided in the supporting information, shows that such fine tips could provide an alternative for imaging sensitive samples in aqueous environments).

Thus, in order to further develop the tapping-mode AFM imaging techniques for soft samples, it is necessary to explore new designs and manufacturing methods that can produce softer CNT probes of controlled stiffness.

4.3 Challenges and alternatives

We have shown that CNT probe stiffness can be modulated through adjustments in ϕ, which presents an opportunity for designing probes of the appropriate stiffness for each

type of sample. However, in order not to compromise image quality, any new probe design must meet several important criteria. First, it is necessary that the probe approach the sample at a nearly vertical orientation so that the artifacts described by Figures 7 and 8 do not take place. Second, it is necessary that imaging take place under conditions that do not lead to severe bending or buckling (this may require using lower values of A_o for higher values of ϕ). Third, the AFM probe must be long enough so that the supporting silicon tip does not approach the surface too closely during imaging. Fourth, it is necessary that the probe stiffness be sufficiently high (as stiff as the sample allows) so that the topography of the sample does not get absorbed in the compliance of the probe (a softer probe will cause less damage to the sample, but it will also provide a flatter image and vice-versa). And finally, it is necessary that the CNT probe be well immobilized on the supporting Si tip so that its length and orientation do not change during imaging.

The obvious challenge here is the feasibility of manufacturing softer probes that meet such stringent criteria. Conventional methods to attach straight CNTs to conventional tips offer some versatility, but do not offer a complete solution. Although controlling the probe tilt angle during fabrication is possible with the pore-growth[2] and some of the manual assembly[6,13] methods, straight, tilted probes do not offer the best imaging resolution because they do not approach the sample at the ideal vertical orientation. In order to overcome this challenge, we propose the design and manufacturing of *free-standing* kinked nanotube[23] or nanowire probes (Figure 2) containing a tilted section that modulates stiffness and a vertical section that ensures high imaging resolution. Our results suggest that probes of this type would enable high-quality imaging of delicate samples without the limitations of either highly tilted or too stiff probes.

Manufacturing kinked AFM probes reliably also presents significant challenges, and to our knowledge this has not yet been accomplished. However, we have found in the literature two methodologies that can produce probes of controlled orientation and which could, at least in principle, be modified to grow probes with the desired geometry. Ye et al.[13] have recently reported on an innovative bottom-up approach to manufacturing AFM probes using plasma assisted chemical vapor deposition, whereby probe growth is directed by an electric field at locations that have been pre-determined through nanopatterning of a Si wafer with the catalyst material. After probe growth, the AFM cantilevers are cut to the desired dimensions using micro-machining procedures. The smallest probe diameter that has been reported for this procedure is between 40 and 80 nm, but the authors believe that smaller probes could be obtained by utilizing smaller catalyst particles. [13] Tay and coworkers[24] have also reported on a procedure that allows the manufacturing of probes of controlled orientation using a field emission method to grow tungsten and cobalt (and potentially composite material) nanowires of the desired length and thickness on conventional AFM tips, thus providing an alternative to CNTs. We also believe that the probe design shown in Figure 2b could be manufactured by controllably growing kinked nanotubes on a substrate (using a process similar to that of Ye et al.[13] perhaps with adjustments in the direction of the electrical field or with the introduction of trace amounts of atoms other than carbon during CNT growth to produce the kinks) and then attaching them to the supporting Si tip via the pick-up method,[14] followed by electrical pulse etching[5] to shorten them to the desired dimensions. This method would have the advantage of decoupling nanotube growth from AFM probe manufacturing.

We present our design as a challenge to experimental groups and highly encourage developments in this area, even for samples that are not susceptible to damage by stiff vertical probes. Tapping-mode AFM imaging with probes of varying stiffness could provide, for example, information on the maximum force that the sample is able to withstand without damage and on the difference in stiffness between the sample as a whole and its features. This type of characterization could also be used to selectively image internal (sub-surface) features of multi-layered samples. Finally, there may be other types of probe microscopy, such as chemical force microscopy and scanning tunneling microscopy, where ultra-soft probes could also be useful in minimizing sample damage during imaging.

5. Conclusions

We have investigated the quantitative dependence of the tip-sample interaction forces for single- and multi-wall nanotube AFM probes on their tilt angle with respect to the axis normal to the sample substrate, describing the cantilever dynamics and image distortion mechanisms that can occur when this angle is large. We have also shown that the tip-sample forces that occur during imaging can be significantly lower when using carbon nanotube probes than when using conventional AFM probes (even in the absence of nanotube probe buckling) and explained the difference in terms of the area under the tip-sample interaction force curve. Our results confirm that the ideal probe orientation for non-sensitive samples is along the axis normal to the sample substrate and provide relationships between probe stiffness and tilt angle for single- and multi-wall nanotube

AFM probes of diameters between 3.5 and 5.5 nm. For sensitive samples, we have proposed and discussed the design of specialized kinked AFM probes whereby probe stiffness is modulated through control of the tilt angle of a section of the probe.

Acknowledgement: The authors gratefully acknowledge the contribution of Professor Konstantinos P. Giapis to the probe designs shown in Figure 2 and of Lawrence A. Wade and Professor C. Patrick Collier in revising and discussing the manuscript.

SUPPORTING INFORMATION

1. Comparison of force curves between single-walled carbon nanotube and Si tips of comparable radius

Figure S-1 provides a comparison of the tip-sample interaction force curves obtained with a vertically aligned 30,30 single-walled carbon nanotube (SWNT) tip of radius 1.7 nm and a Si tip of the same radius (with side wall angles of 15º with respect to vertical). The force curve of a larger 15-nm-radius Si tip (see Figure 3 of the paper) is also provided as a reference. The result shows that the forces that emerge during imaging and their rate of change with respect to the tip position are of comparable magnitude for the 1.7-nm-radius tip and for the SWNT tip. The graph also shows that although the magnitudes of the forces are comparable, the curve for the Si tip is shifted to the right with respect to that of the SWNT because of its solid geometry that does not allow it to

penetrate into the surface in the same way the SWNT does (recall that we modeled the substrate as a Si(100)-OH surface whose functional groups can penetrate into the hollow center of the CNT but not into the solid Si tip. Additionally, the SWNT walls are more susceptible to lateral deformation than the Si tip). These force curves constitute an important result concerning the imaging of sensitive samples because they show that if fine Si tips can be manufactured and maintained sharp during the acquisition of the images, they can also lead to reduced sample damage, as do *vertically aligned* SWNTs. This could be advantageous in environments where it is difficult to use SWNT tips, such as when the solvent is water.

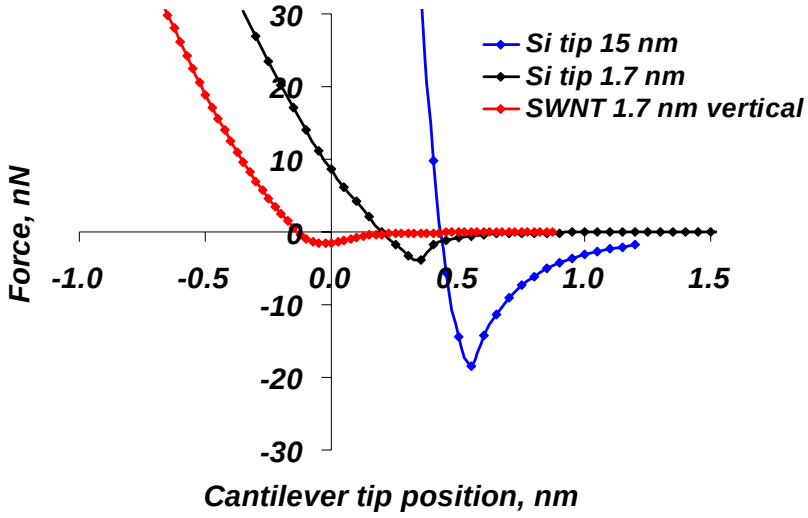

Figure S-1. Comparison of the tip-sample force curves obtained with a 30,30 single-walled carbon nanotube tip and a Si tip (both of radius 1.7 nm) and a 15-nm-radius Si tip. The graph shows that the tip-sample forces are of similar magnitude and slope for the nanotube and the 1.7-nm-radius Si tips.

2. Force curves for single-, double- and triple-walled carbon nanotube probes

Figures S-2, S-3, and S-4 show the tip-sample interaction force curves obtained for single-, double-, and triple-walled carbon nanotube probes of outer diameter 3.5 nm and aspect ratio 7.5. These curves were used to calculate the terminal force gradients shown in Figure 6 of the paper. The graphs show that as the number of internal walls in the probe increases, the force curves become steeper. These curves are similar to those shown in Figure 3 of the paper, although some of them differ slightly in that they exhibit minor slippage before reaching the terminal force gradient. We attribute this to the smaller probe diameter, which makes it more susceptible to lateral bending.

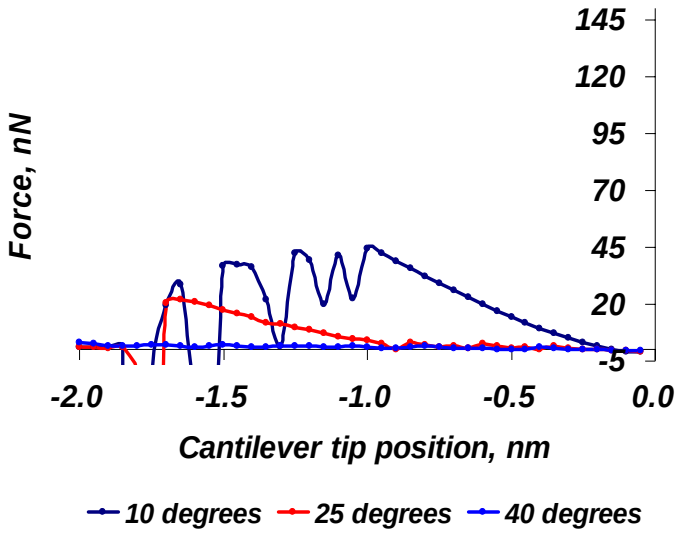

Figure S-2. Tip-sample interaction force vs. cantilever tip position for a 25,25 single-walled carbon nanotube probe (diameter 3.5 nm and aspect ratio 7.5) imaging a Si(100)-OH surface for ϕ = 10, 25, and 40°.

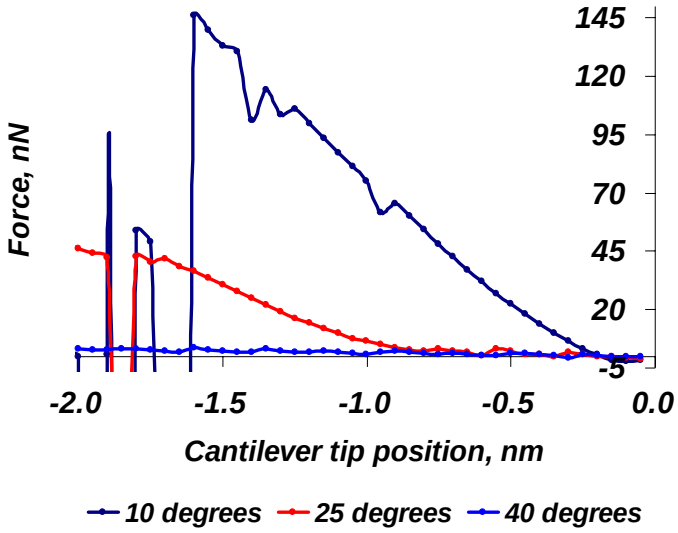

Figure S-3. Tip-sample interaction force vs. cantilever tip position for a 25,25/20,20 double-walled carbon nanotube probe (outer diameter 3.5 nm and aspect ratio 7.5) imaging a Si(100)-OH surface for ϕ = 10, 25 and 40°.

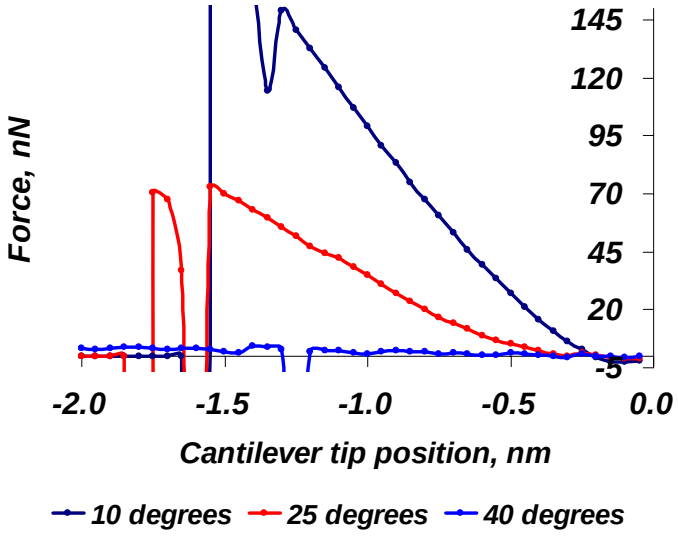

Figure S-4. Tip-sample interaction force vs. cantilever tip position for a 25,25/20,20/15,15 triple-walled carbon nanotube probe (outer diameter 3.5 nm and aspect ratio 7.5) imaging a Si(100)-OH surface for ϕ = 10, 25 and 40°.

3. Cantilever oscillation dynamics for A_o = 20 nm

Figure S-5 illustrates the dependence of Z_{min}, F_{max}, and the cantilever oscillation amplitude on the cantilever rest position for the 40,40 SWNT probe and for the Si tip imaging a Si(100)-OH surface with A_o = 20 nm. These results are qualitatively similar to those of Figure 9 of the paper (for A_o = 40 nm), but the observed variations for different values of ϕ are smaller due to the smaller excitation force amplitude. For A_o = 20 nm the oscillation amplitude and F_{max} are lower, while Z_{min} is greater than for A_o = 40 nm due to the lower excitation force and lower probe and surface deformation.

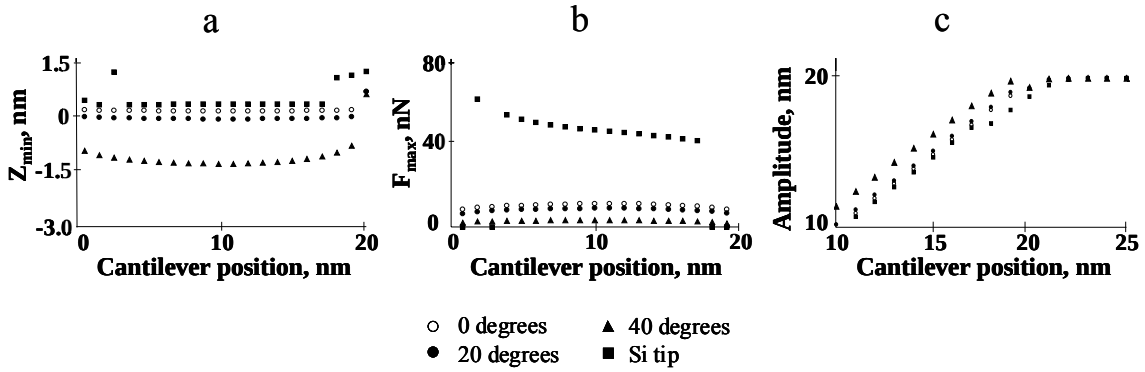

Figure S-5. Lowest cantilever position (a) and maximum tip sample force (b) observed *during one full oscillation of the AFM cantilever* and oscillation amplitude (c) vs. cantilever rest position for the 40,40 SWNT probe shown in Figure 1 of the paper (for ϕ = 0, 20, and 40º) and for a 15-nm radius Si tip imaging a clean Si(100)-OH surface. A_o = 20 nm in all cases. The discontinuities on the curves (such as the jump in the Z_{min} curve for the Si tip –black squares– between cantilever positions of 17 and 18 nm) correspond to the well-known transitions between the attractive and repulsive imaging regimes of

tapping-mode AFM. [21] Note that Z_{min} = 0 corresponds to the AFM cantilever rest position for which the tip (SWNT or Si) is *first* able to contact the surface.

4. Analysis of tip deformation modes

Our molecular simulation results show that the primary modes of CNT tip deformation (for the systems considered) are macroscopic bending/shearing and local deformation at the end of the tip (especially for SWNTs which have softer lateral deformation modes). They also show that local deformation can in some cases represent the main contribution to the strain energy, especially at large tilt angles. This is illustrated in Table S-1, which provides the percentage of the total strain energy in the probe (i.e., not considering the surface) that is stored in the 4 nm (10% of the total probe length) closest to the surface. These results correspond to the 40,40 SWNT probe interacting with a bare Si(100)-OH surface at a cantilever tip position of -0.5 nm (see Figure 3 of the paper). The percentages range from ~20% to 64%, indicating that local deformation is indeed significant. This is also evident in Figure S-6, which depicts the macroscopic and local deformation of the same probe for ϕ = 10º and ϕ = 20º. Figure S-7 shows that the deformation modes can be even more complex when a sample is present. In these cases, in addition to significant local deformation, bending can occur in more than one Cartesian direction simultaneously. Due to these complex deformation modes, a classical uniform-beam analysis of tip deformation [18,21] should only be used to estimate general trends.

Table S-1. Ratio of strain energy stored in the distal 10% portion of the 40,40 SWNT probe (diameter 5.5 nm and aspect ratio 7.5) to the total strain energy as a function of the tilt angle. These results correspond to a cantilever tip position of -0.5 nm with respect to the Si(100)-OH surface (see Figure 3 of the paper).

ϕ	**Local Strain/Total Strain**
0	0.20
10	0.26
20	0.64
30	0.60
40	0.43

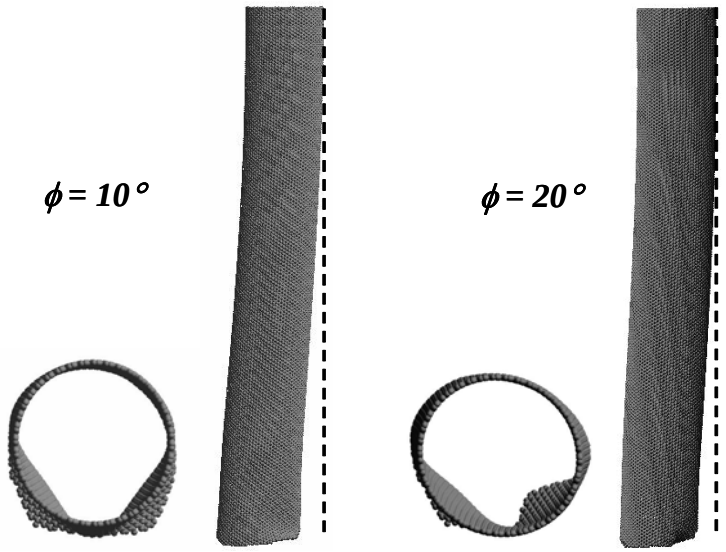

Figure S-6. Illustration of the macroscopic bending/shearing and local end-tip deformation modes for $\phi = 10^{o}$ and $\phi = 20^{o}$ (note that the probe images have been aligned vertically for easier visualization). These results correspond to the 40,40 SWNT probe imaging the bare Si(100)-OH surface for a cantilever tip position of -0.5 nm. The images

show that the local deformation at the end of the tip is significant, in agreement with the results presented in Table S-1, and that macroscopic deformation is a combination of bending and shearing (shearing occurs because only one corner of the probe contacts the surface).

Figure S-7. Illustration of 40,40 single-wall carbon nanotube probe deformation in the presence of a 16,16 SWNT sample (diameter 2.1 nm). The pictures show that significant local deformation can take place in addition to bending in more than one Cartesian direction simultaneously when the probe is compressed against the sample.

REFERENCES:

1. Wade, L.A.; Shapiro, I.R.; Ma, Z.; Quake, S.R.; Collier, C.P. *Nano Lett.* **2004**, 4, 725.

2. Hafner, J.H.; Cheung, C.L.; Woolley, A.T.; Lieber, C.M. *Prog. Biophys. & Mol. Biol.* **2001,** *77,* 73.

3. Umemura, K.; Komatsu, J.; Uchihashi, T.; Choi, N.; Ikwawa, S.; Nishinaka, T.; Shibata, T.; Nakayama, Y.; Katsura, S.; Mizuno, A.; Tokumoto, H.; Ishikawa, M.; Kuroda, R. *Biochem. & Biophys. Res. Comm.* **2001,** *281, 390.*

4. Nishijima, H.; Kamo, S.; Akita, S.; Nakayama, Y. *Appl. Phys. Lett.* **1999,** *74,* 4061.

5. Wong, S.S.; Harper, J.D.; Lansbury, P.T.; Lieber, C.M. *J. Am. Chem. Soc.* **1998,** *120,* 603.

6. Uchihashi, T.; Choi, N.; Tanigawa, M.; Ashino, M.; Sugawara, Y.; Nishijama, H.; Akita, S.; Nakayama, Y.; Tokumoto, H.; Yokoyama, K.; Morita, S.; Ishikawa, M. *Jpn. J. Appl. Phys.* **2000,** 8B, L887.

7. Maeda, Y.; Nishijima, H.; Akita, S.; Matsumoto, T.; Nakayama, Y.; Kawai, T. *Jpn. J. Appl. Phys.* **2001,** *40,* 1425.

8. Bunch, J.S.; Rhodin, T.N.; McEuen, P.L. *Nanotechnology,* **2004,** *15,* S76.

9. Chang, Y.C.; Chang, C.S.; Wang, D.C.; Lee, M-H.; Wang, T-F.; Wu, M-Y.; Fu, T-Y.; Tsong, T.T. *Jpn. J. Appl. Phys.* **2004,** *43,* 4517.

10. Woolley, A.T.; Cheung, C.L.; Hafner, J.H.; Lieber, C.M. *Chem. & Biol.* 2000, *7,* R193.

11. Hohmura, K.I.; Itokazu, Y.; Yoshimura, S.H.; Mizuguchi, G.; Masamura, Y.; Takeyasu, K.; Shiomi, Y.; Tsurimoto, T.; Nishijima, H.; Akita, S.; Nakayama, Y. *J. Elec. Micros.* **2000,** *49,* 415.

12. Hafner, J.H.; Cheung, C.L.; Lieber, C.M. *J. Am. Chem. Soc.* **1999,** *121,* 9750.

13. Ye, Q.; Cassell, A.M.; Liu, H.; Chao, K-J.; Han, J.; Meyyappan, M. *Nano Lett.* **2004,** 4, 1301.

14. Hafner, J.H.; Cheung, C.L.; Oosterkamp, T.H.; Lieber, C.M.; *J. Phys. Chem. B* **2001,** *105,* 743.

15. Song, W.Y.; Jung, K.Y.; O, B-H. *Rev. Sci. Instr.* **2005,** *76,* 025107.

16. Chen, L.; Cheung, C.L.; Ashby, P.D.; Lieber, C.M. *Nano Lett.* **2004,** 4, 1725.

17. Snow E.S.; Campbell, P.M.; Novak, J.P. *J. Vac. Sci. Technol. B* **2002,** 20, 822.

18. Snow E.S.; Cambell, P.M.; Novak, J.P. *Appl. Phys. Lett.* **2002,** 80, 2002.

19. Shapiro, I.R.; Solares, S.D.; Esplandiu, M.J.; Wade, L.A.; Goddard, W.A.; Collier, C.P. *J. Phys. Chem. B* **2004**, 108, 13613.

20. Garcia, R.; San Paulo, A. *Phys. Rev. B* **1999,** *60,* 4961.

21. Garcia, R.; Perez, R. *Surf. Sci. Reports* **2002,** *47,* 197.

22. Stevens, R.M.; Nguyen, C.V.; Meyyappan, M. *IEEE Trans. Nanobiosci.* 2004, *3,* 56.

23. Yao, Z.; Postma, H.W.Ch.; Balents, L.; Dekker, C. *Nature* **1999,** *402,* 273.

24. Tay, A.B.H.; Thong, J.T.L. *Rev. Sci. Instr.* **2004,** 75, 3248.

Chapter 4: Density Functional Theory Study of the Geometry, Energetics, and Reconstruction Process of Si(111) Surfaces*

ABSTRACT. We report the structures and energies from first principles density functional calculations of 12 different reconstructed (111) surfaces of silicon, including the 3x3 to 9x9 dimer-adatom-stacking-fault (DAS) structures. These calculations used the Perdew-Burke-Ernzerhof generalized gradient approximation of density functional theory and Gaussian basis functions. We considered fully periodic slabs of various thicknesses. We find that the most stable surface is the DAS 7x7 structure, with a surface energy of 1.044 eV/1x1 cell (1310 dyn/cm). In order to analyze the origins of the stability of these systems and to predict energetics for more complex less ordered systems, we develop a model in which the surface energy is partitioned into contributions from seven different types of atom environments. This analysis is used to predict the surface energy of larger DAS structures (including their asymptotic behavior for very large unit cells) and to study the energetics of the sequential size change (SSC) model proposed by Shimada and Tochihara for the observed dynamical reconstruction of the Si(111) 1x1 structure. We obtain an energy barrier at the 2x2 cell size and confirm that the 7x7 regular stage of the

---

* Reproduced with permission from Solares, S.D.; Dasgupta, S.; Schultz, P.A.; Kim, Y.H.; Musgrave, C.B.; and Goddard, W.A. III; *Langmuir* **2005,** *21,* 12404.

SSC model (corresponding to the DAS 7x7 reconstruction) provides the highest energy reduction per unit cell with respect to the unreconstructed Si(111) 1x1 surface.

1. Introduction

One of the finest examples of experiment and theory working together to explain a very complex phenomenon is the elucidation of the atomistic structure underlying the 7x7 reconstruction of Si(111). After Schlier and Farnsworth[1] first observed the 7th order spots in the low energy electron diffraction (LEED) pattern in 1959, numerous models of this surface reconstruction were proposed based on various experiments and calculations.[2-4] Most were proven wrong by the first STM experiments (1981).[5] Eventually the surface reconstruction was successfully interpreted in terms of the dimer-adatom-stacking-fault (DAS) model by Takayanagi et al. (1985).[6,7] This model involves dimers, adsorbed atoms, and stacking faults and is now well validated through many theoretical and experimental studies. [8-28] Takayanagi's work was followed by a series of theoretical calculations, including *ab initio* cluster calculations (Northrup[22,23]), empirical and semi-empirical calculations (Qian and Chadi[24,25]; Khor and Das Sarma[12]), and large-scale fully periodic *ab initio* calculations (Brommer et al.[16] and Stich et al.[20]), which demonstrated that the DAS model is fundamentally correct and provided quantitative understanding of its electronic structure.

Despite the successful characterization of the DAS 7x7 surface, many questions remain concerning the dynamical processes involved in forming this complex structure (say from a freshly cleaved surface) and the role these processes may play in the growth and

etching of various structures. Although the reconstruction process has been recently observed in real time[8], little is still known about the thermodynamics of its fundamental steps. First principles computational studies of these dynamical processes may require unit cells many times larger than 7x7 (in order to describe effects such as etch pits and steps) and timescales much larger than nanoseconds. So far, the large number of atoms in the surface unit cell and the complexity of its features have impeded systematic *ab initio* theoretical studies, leading to significant differences in predicted energy and geometric parameters. [12,16-21,24-28] In order to provide a basis for developing an improved understanding of the dynamical processes on Si(111), we plan to develop a ReaxFF[29] reactive force field that will allow dynamical calculations with the thousands to millions of atoms per unit cell required to describe the formation and migration of various species and defects on the surface, while also describing their reaction with adsorbed species from the gas phase. This development will require four major steps: (1) *ab initio* quantum mechanical (QM) characterization of all reasonable surface reconstructions with the best available methods, (2) use of these *ab initio* QM results to develop and train the ReaxFF, (3) use of the ReaxFF in molecular simulations to predict the dynamics of various *experimentally observable* surface reconstruction and reaction processes to validate its accuracy, and (4) application of the validated ReaxFF in molecular dynamics simulations to study new reactive processes with and without adsorbed species.

In this paper we describe the initial stage of this work. Section 2 provides a detailed description of the DAS 7x7 surface and an overview of 12 other relevant Si(111) surface structures. These surfaces will be used to train the reactive force field and lay the foundation for more detailed structure discussions. Section 3 describes the *ab initio*

methods used consistently for all surfaces considered. We utilize the Perdew-Burke-Ernzerhof (PBE)[30] Generalized Gradient Approximation (GGA) of Density Functional Theory (DFT), whereas the Local Density Approximation (LDA) has been employed by previous authors.[16,19-23] Section 4 presents a detailed analysis of the surface energetics and structures of the 12 Si(111) surface reconstructions and the 1x1 surface, all using the same level of DFT. This is the first large scale *ab inito* study on Si(111) using the PBE[30] GGA to examine surface reconstructions for cell sizes up to DAS 9x9. Section 5.1 uses the detailed analysis of the surface reconstructions to develop the Atomic Energy Contribution Model (AECM) for partitioning the surface energy into individual atomic contributions based upon their local structural environments. This is an intermediate step between DFT and a full reactive force field. The AECM effectively reproduces the results of the DFT calculations, enabling the rapid and accurate estimation of surface energies for ordered and disordered structures. Finally, Section 5.2 applies this analysis to calculate the energy of the different structures of the *sequential size change (SSC) model* proposed by Shimada and Tochihara[8] to describe the Si(111) DAS reconstruction path based on real time STM experimental observations. We find that the energy barrier in the reconstruction path is at the 2x2 cell and confirm that the 7x7 regular stage of the SSC model provides the greatest energy stabilization for the surface.

2. Si(111) surfaces

2.1 Overview of the 7x7 DAS structure

Figure 1 shows the top four layers of the DAS 7x7 surface reconstruction using different colors for each layer. The composite view from the top is displayed with stick and ball diagrams. In each case four unit cells are shown so as to clarify the corner hole structure. The faulted and unfaulted halves of the unit cell are distinguished by the stacking pattern. Figure 2 shows the slices for each layer of a single unit cell:

i. The top surface layer has the 12 adatoms (purple) denoted as T_4. Each T_4 atom is bonded to 3 second-layer atoms (red) and has one dangling bond. In each case there is a third layer (dark green) atom directly below the top atom leading to a trigonal bipyramid (TB) structure, as indicated in Figure 3a.

ii. The second layer (red and brown) has 42 atoms, 36 being 4-fold coordinated (red) and 6 being only 3-fold coordinated (brown). The 36 fully coordinated red atoms bond to 1 top layer atom (purple) and 3 third layer atoms [dark green (DG) or light green (LG)]. Of these 36, 6 atoms are bonded to 3 DG, 24 atoms to 2 DG and 1 LG, and 6 atoms to 1 DG and 2 LG. The 6 brown second layer atoms bond only to three third layer atoms (all DG), leaving a dangling bond.

iii. The third layer (green) has 48 atoms:

a. 18 atoms are paired to form nine dimer pairs (light green) along the edges of the one of the triangles, each of which is bonded to two second

layer (red or brown) atoms, another light green atom, and a fourth layer atom (orange).

b. 18 non-dimer atoms (dark green) are bonded to 3 second layer red atoms and 1 fourth layer orange atom.

c. 12 non-dimer atoms (also dark green) have the same coordination as the atoms described in the previous category, but sit below top layer adatoms to form the bottom atom of a trigonal bipyramid as in Fig. 3a.

iv. Finally, the fourth and fifth layers of the unreconstructed bulk silicon structure (orange and blue) each have 49 atoms. One of the fourth-layer atoms (blue) has a dangling bond in the center of the 12-membered ring at the corner of the unit cell. All others are fully tetrahedrally coordinated.

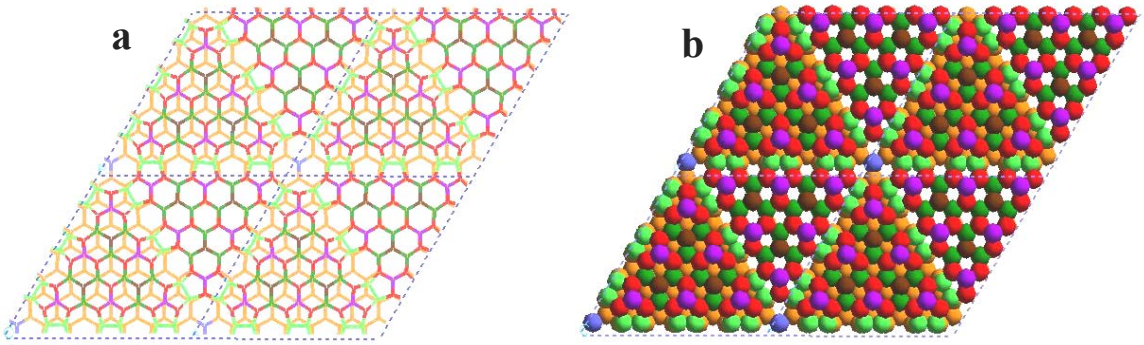

Figure 1. Top view of the DAS 7x7 surface showing four unit cells. The top layer has 12 adatoms (purple) each with a dangling bond. At each corner is a hole centered around a dangling bond 4th layer atom (blue), surrounded by a 12-membered ring formed from 2nd and 3rd layer (red and light green) atoms. The light green atoms are 3rd layer dimers

which connect to form 8-membered rings. The 2nd layer (red and brown) and 3rd layer non-dimer atoms (dark green) form two regions, the upper right with a stacking fault and the lower left without. The brown atoms (2nd layer) also have one dangling bond each. The 4th layer (orange and blue) and all layers below it are unreconstructed.

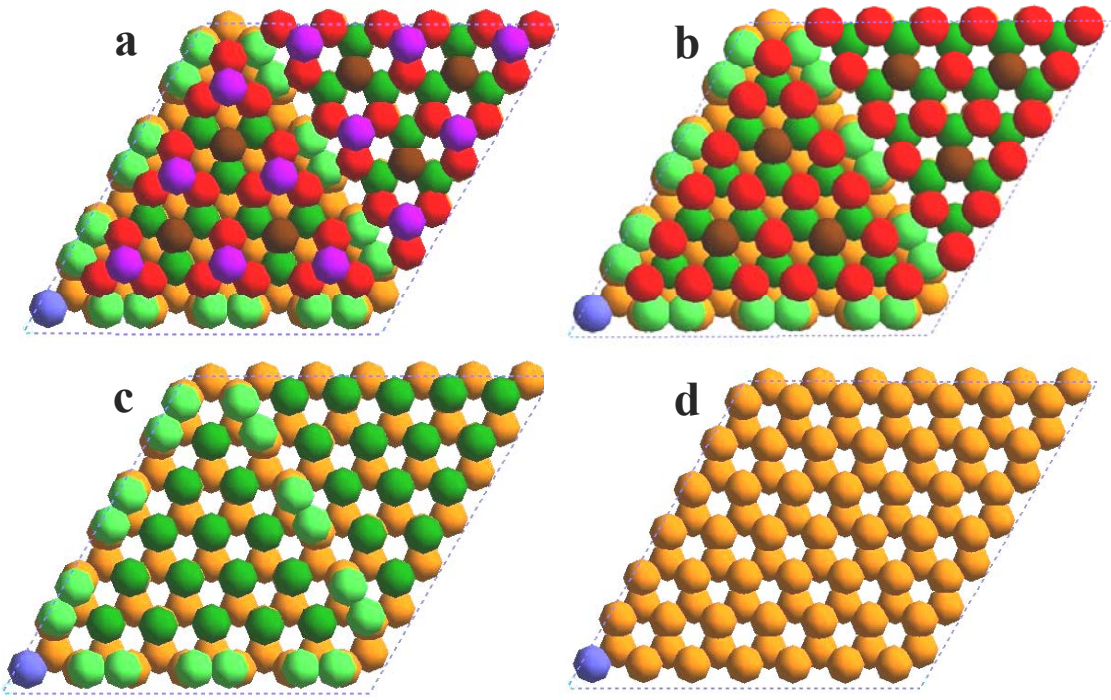

Figure 2. Top view of the DAS 7x7 unit cell (a) showing the top five layers (b) upon removal of the first layer, (c) upon removal of the first two layers, and (d) upon removal of the first three layers. The top layer adatoms (purple) correspond to the bright spots observed in STM experiments. Of the 42 atoms in the second layer (red and brown), 36 (red) are bonded to the adatoms above but 6 (brown) are only connected to atoms in the third layer (green), leaving a dangling bond. The 3rd layer dimers (light green) border the left half of the unit cell. The blue atom, which occupies the center of the corner hole, is in the 4th layer, but there is no 3rd layer atom above it, leading to a dangling bond. The 4th

layer (orange and blue) is the first unreconstructed layer. All layers below the 4th layer are unreconstructed.

The fundamental driving force for this complicated reconstruction is removal of dangling bonds. The DAS unit cell consists of two triangular sub-cells. The lower left half sub-cell in Figure 2b leads to a surface double layer with the normal sphalerite (CAABBC) stacking, while the upper right half sub-cell has a stacking fault between the 2nd (red and brown) and 3rd (green) layers (CAABBA). The broken bonds needed to create the stacking fault are removed by forming dimers at the sub-cell boundary. The cell corner contains a large hole with a twelve-atom ring and a dangling bond atom in the center. Holes with eight-atom rings bridge between each pair of dimers, except at the cell corners (Figure 1). The twelve top-layer adatoms each lead to a trigonal bipyramidal site (denoted T_4 because each adatom sits atop a subsurface atom and has four close neighbors, Figure 3a). The adatoms remove 36 dangling bonds from the second layer (leaving six dangling bonds) and create 12 new dangling bonds. The twelve dangling bonds from the T_4 adatoms (purple), the 6 dangling bonds from the 2nd layer atoms (brown), and the dangling bond from the fourth-layer atom (blue) in the cell corner lead to a total of 19 dangling bonds per unit cell in the Si(111)-7x7 DAS model, as opposed to the 49 dangling bonds that would be present in the unreconstructed Si(111) surface.

Despite the progress in understanding the nature of the DAS 7x7 structure, there remain questions regarding the relative stability of the various Si(111) reconstructed surfaces. The DAS reconstruction leads to a family of [(2n+1)x(2n+1)] DAS surfaces: 3x3, 5x5, 7x7, 9x9, etc. Of these, the 7x7 is the most commonly observed, although others (i.e.,

5x5, 9x9, 11x11, etc.) have been seen on narrow terraces, quenched surfaces, and homo-epitaxially grown islands as metastable states coexisting with 7x7 at certain temperatures.[8] Germanium, which from simple bonding considerations would be expected to yield structures similar to Si, forms a c(2x8) reconstruction[31] rather than a DAS 7x7. To fully understand the Si surface reconstruction, we need a more quantitative description of the structure and relative stabilities of the various reconstructed surfaces and of the fundamental mechanisms and parameters that drive this process.

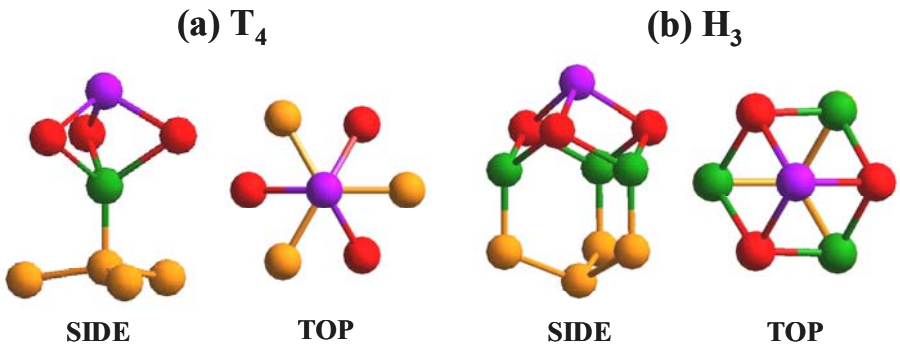

Figure 3. (a) Side and top view of a surface T_4 adatom (purple, 12 per 7x7 unit cell). This adatom sits on top of three 2nd layer atoms (red), directly above a 3rd layer atom (green). All adatoms in the DAS model have this structure. (b) Side and top view of a surface H_3 adatom. The adatom sits on top of three 2nd layer atoms (just like a T_4 adatom), but is located directly above a hollow in the subsurface. H_3 adatoms are *not* present in the DAS reconstructions.

2.2 Si(111) surface reconstruction models

Here we study the following surface reconstructions:

i. *1x1 unreconstructed surface,* unrelaxed and relaxed.

ii. *√3x√3T4:* This surface contains three 1x1 unit cells per supercell with one adatom, leading to one dangling bond in the unit supercell. Here the adatom is bonded to 3 2nd layer atoms and placed directly above a 3rd layer atom to form the same T_4 adatom structure as in the DAS reconstructions (Figure 3a).

iii. *√3x√3H3:* This surface is similar to √3x√3T4 except the adatom is directly above a hollow 3rd layer site, leading to an H_3 site (Figure 3b).

iv. *2x2T4 hexagonal:* This surface contains four 1x1 unit cells with one T_4 adatom (with a dangling bond) and one dangling bond atom in the 2nd layer per supercell.

v. *2x2H3 hexagonal:* This is similar to 2x2T4 hexagonal, except with an H_3 adatom instead of a T_4.

vi. *2x2T4 rectangular:* Similar to *2x2T4 hexagonal* but on a rectangular cell.

vii. *2x2H3 rectangular:* Similar to *2x2H3 hexagonal* but on a rectangular cell.

viii. *2x3H3T4:* This surface contains six 1x1 unit cells per supercell and has one T_4 adatom and one H_3 adatom, leading to two dangling bonds.

ix. *c2x8.* This surface contains 16 1x1 unit cells per supercell with a series of 7- and 8-membered rings, 4 adatoms, and a stacking fault. This is the favored reconstruction for Ge(111) surfaces. [31]

x. *DAS3x3:* This surface has 2 T_4 adatoms, a 12-membered ring hole similar to that of the DAS 7x7 with a 4th layer dangling bond atom, 6 dimer atoms, and a stacking fault.

xi. *DAS5x5:* This surface has 6 T_4 adatoms, a 12-membered ring hole similar to that of the DAS 7x7 with a 4th layer dangling bond atom, 12 dimer atoms, 2 2nd layer dangling bonds, and a stacking fault.

xii. *DAS7x7:* As described above, this surface has 12 T_4 adatoms, a 12-membered ring hole with a 4th layer dangling bond atom, 18 dimer atoms, 6 2nd layer dangling bonds, and a stacking fault.

xiii. *DAS9x9:* This surface has 20 T_4 adatoms, a 12-membered ring hole similar to that of the DAS 7x7 with a 4th layer dangling bond atom, 24 dimer atoms, 12 2nd layer dangling bonds, and a stacking fault.

3. Methods

3.1 Quantum mechanics

Periodic *ab initio* calculations were performed using the SeqQuest software[32] (Sandia National Labs, Albuquerque, NM), a DFT code for periodic and non-periodic systems that uses contracted-Gaussian basis sets with norm-conserving pseudopotentials.[33] In all calculations we used a well-converged double zeta basis set with polarization functions, optimized for bulk Si, and the PBE[30] GGA with restricted (closed shell) and unrestricted (spin-polarized) DFT. In the spin-polarized DFT calculations for systems with net spin, we carried out unrestricted calculations, i.e., in which the N_α spin-up and N_β spin-down

orbitals are optimized independently. The spin polarization is quoted in units of excess electrons of majority spin (N_α - N_β), i.e., twice the total spin projection. For net zero spin systems we perform restricted (closed shell) calculations where the spin-up and spin-down orbitals are taken to be identical. We cannot exclude the possibility that a net zero spin system might prefer an antiferromagnetic state instead; antiferromagnetic spin states were not examined in this study.

Non-periodic (cluster) *ab initio* calculations were performed using Jaguar software (Schrödinger Inc, Portland, OR), a DFT code for non-periodic systems that uses a variety of Gaussian basis sets (including Slater type and Dunning type functions) with exchange-correlation functionals ranging from LDA and GGA to hybrid functionals such as B3LYP and custom functionals. We used 631G**++ basis sets (double-zeta plus polarization) for all cluster calculations.

3.2 Slab models

The surfaces were modeled using a two-dimensional slab consisting of six layers (three double layers) of bulk silicon atoms, on top of which we formed the various reconstructed surfaces. The dangling bonds at the unreconstructed bottom surface were terminated with hydrogen atoms. These hydrogen atoms were held fixed for all geometry optimizations. The number of bulk silicon layers (six) was selected by optimizing the geometry for the 2x3H3T4 surface structure, increasing the total number of bulk layers (and varying number of those layers which were held *fixed*) until the surface energy converged. Figure 4 and Table S-3 of supporting information show the surface energy

obtained for the 2x3H3T4 surface for various numbers of bulk layers and various numbers of fixed bulk layers. Based on this analysis, our surface slab models contain six fully relaxed silicon layers plus one termination layer of fixed hydrogen atoms. The resulting accuracy of 0.028 eV/1x1 cell is acceptable and applies equally to all calculations. This thickness was an effective compromise. Fewer bulk layers give insufficiently accurate surface energies, while more bulk layers make the calculations unnecessarily expensive. Thus, the 9x9 unit cell has 162 atoms per bulk double layer so that our DAS 9x9 model contains 739 atoms (8959 basis functions), while the other DAS models have 79 atoms (3x3), 225 atoms (5x5), and 445 atoms (7x7). In these calculations we used the 0K experimental lattice parameter, a=5.4307 Å, for the Si bulk lattice (for comparison, the computed PBE lattice parameter is 5.479 Å, within 1% of the experimental value). The number of k-points for each calculation was varied according to the unit cell size. For the 1x1 unit cell we used 8 k-points in the direction of each of the cell unit vectors. The number of k-points for the other structures was set to the closest integer, inversely proportional to the cell dimension along each unit vector. Thus, the DAS 9x9, DAS 7x7, DAS 3x3, 2x2H4, etc. used 1, 1, 3, 4, etc. k-points in each direction, respectively.

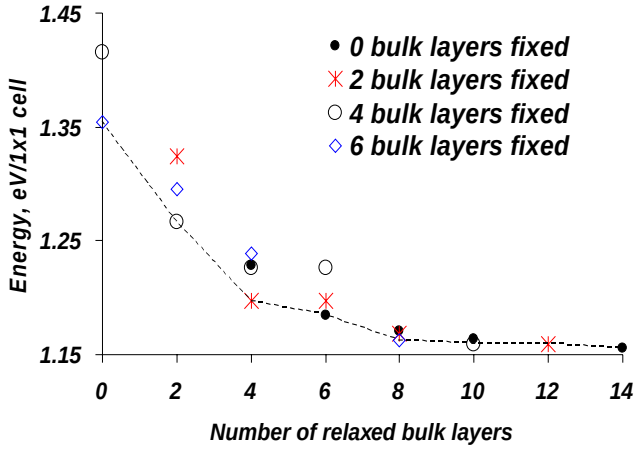

Figure 4. Minimized surface energy for the 2x3H3T4 surface reconstruction for various numbers of *relaxed* bulk silicon layers and 0 to 6 *fixed* bulk silicon layers below the relaxed layers (the terminating hydrogen atoms on the bottom face were kept fixed in all geometry optimizations). The results show that having 6 relaxed bulk Si layers and one fixed H layer leads to a reasonable accuracy of 0.028 eV/1x1 cell with respect to the converged surface energy.

The normalized surface energy per 1x1 unit cell (E_s) is defined as follows:

$$E_s = (E_m - b \times E_b - m \times n \times E_{H1x1}) / (m \times n), \qquad (1)$$

where E_m is the minimized energy of the surface model, b is the number of silicon atoms in the model, E_b is the energy per silicon atom in the bulk crystal, $m \times n$ is the size of the unit cell in terms of 1x1 unit cells, and E_{H1x1} is the energy change per hydrogen obtained when adding a hydrogen atom to the unreconstructed 1x1 unit cell to form a

hydrogen-terminated 1x1 surface. This term was obtained from a 20-bulk-layer 1x1 silicon slab terminated with hydrogen atoms on both faces.

4. Si(111) surface reconstructions – density functional calculations

4.1 Energetics

The results of our DFT calculations of surface formation energies (with respect to the bulk crystal) of different Si(111) surface reconstructions are presented in Table 1, along with previous DFT results. Of all the surfaces we considered, we find that the DAS 7x7 reconstruction gives the lowest surface energy (1.044 eV/1x1 cell), followed by the DAS 5x5 (1.048 eV/1x1 cell), and then the DAS 9x9 (1.055 eV/1x1), in general agreement with the work of previous authors. [19-21,24-27] Relevant to the SSC model,[8] we identify a barrier in the reconstruction path of 0.26 eV/1x1 cell at the 2x2 cell size. The results confirm that the 5x5 and 7x7 regular stages of the model, which correspond to the DAS 5x5 and 7x7 reconstructions, provide the greatest energy reduction with respect to the unreconstructed 1x1 surface. The optimal reconstructed surface (DAS 7x7) is calculated to be ~0.16 eV/1x1 cell below the unreconstructed (relaxed) 1x1 Si(111) surface.

The PBE functional used in the current study does not give qualitatively different results in comparison to the LDA functional used in previous studies. Quantitatively, our predicted surface formation energies for all DAS surface models (including the DAS 7x7 structure) are lower than others in the literature. A comparison of LDA and PBE[30] surface energies for cell sizes up to 3x3 (Table S-4 in the supporting information) gave values that were on average 0.152 eV/1x1 cell *higher* when using LDA than when using

PBE. This trend was observed in all calculations. The largest difference (0.250 eV/1x1 cell) was observed for the 1x1 relaxed surface and the smallest difference for the 2x2H3 surface (0.114 eV/1x1 cell). Thus we attribute the difference between our results and those of other authors primarily to the use of the PBE functional instead of the LDA functional.

The formation energy of the relaxed unreconstructed 1x1 Si(111) surface is computed to be 1.20 eV. Attributing this surface energy solely to the breaking of bonds at the surface (a crude, but not unreasonable, first approximation), this corresponds to each dangling bond adding 1.20 eV to the formation energy. Using this value we can analyze the contribution of the dangling bonds to the surface energy of the DAS 7x7 reconstruction. Consider a 7x7 supercell of the 1x1 surface. For the unreconstructed supercell, the 49 broken bonds incur a total energy cost of 58.8 eV (49 dangling bonds costing 1.20 eV each). As discussed above, the DAS 7x7 structure eliminates 30 of these dangling bonds, leaving only 19 dangling bonds. Ideally, this would stabilize the surface by 36.0 eV (30x1.20 eV). The computed stabilization, however, is only 7.65 eV (0.26 eV per dangling bond removed). While the elimination of the dangling bonds may be the principal driving force for the reconstruction, the strain introduced in the reconstruction plays an important role and significantly reduces the net stabilization given by the elimination of dangling bonds.

Table S-5 of the supporting information compares the calculated surface energies for the different Si(111) reconstructions (with respect to the bulk crystal) to previously published empirical and semi-empirical results, indicating the method used in each case. Our results qualitatively agree with those of Zhao et al.[26], who used a building block

energy contribution model, and those of Takahashi et al.[27], who used a modified embedded atom model.

Since all surface models of Si(111) contain dangling bonds and since these dangling bonds are unable to make good bond pairs, it is plausible that the surface might have unpaired spins. We performed a series of spin-polarized calculations to examine whether the surface might prefer to have net spin rather than be closed shell. The √3x√3 and 1x1 surfaces have one dangling bond per supercell. For these two surfaces, the lowest energy state was indeed found to have net spin, with a net spin polarization of 1 electron per supercell. For all other surfaces we examined (2x2, 2x3, 2x8, 3x3, 5x5, and 7x7, except 2x2H3 rect, which was found to have a net spin of two electrons per supercell), the spin zero closed shell state was the ground state (Table S-6 of the supporting information). We varied the spin from zero to a maximum in which all dangling bond electrons were ferromagnetically aligned. Figure 5 displays the computed surface energy of the DAS 5x5 surface as a function of the net spin polarization. The results are characteristic of the results for the other reconstructed surfaces. The surface energy is lowest for the spin zero case and increases monotonically with increasing number of unpaired electrons. Similar calculations were performed for DAS 3x3 and for the lowest five and the highest spin states of DAS 7x7 (the results are provided in Tables S-7, S-8 and S-9 and Figures S-1 and S-2 of the supporting information). We did not perform the unrestricted spin calculations for the DAS 9x9 structure, but expect that the ground state will also have no net spin.

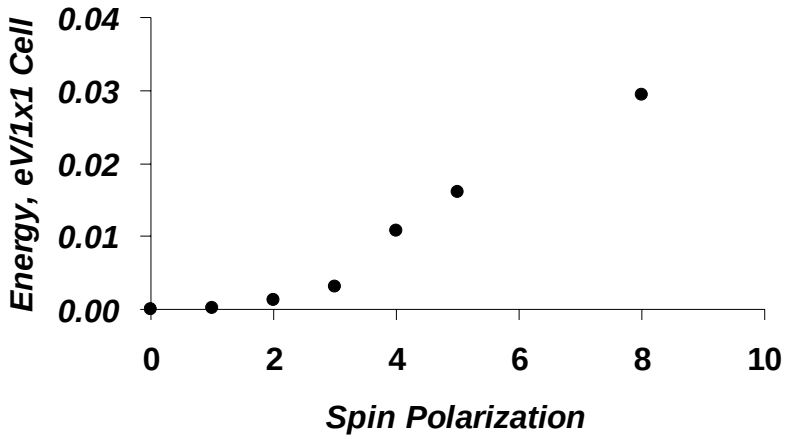

Figure 5. Surface energy for the DAS 5x5 surface model as a function of the spin polarization (number of electrons with unpaired spins). The results show that the surface energy is at a minimum when there are no unpaired spins (spin polarization zero). Similar trends were calculated for the DAS 3x3 and the DAS 7x7 models and for all the 2x2, 2x3, and 2x8 structures analyzed (supporting information). Note: the DAS 5x5 surface contains 9 dangling bonds.

Table 1: First principles surface energies for Si(111) surfaces. Energies are eV per 1x1 unit cell. The reference energy is zero for the bulk crystal unless otherwise indicated, in which case the reference energy is the unrelaxed 1x1 unreconstructed surface.

Surface	**This work**	**Stelnikov et al. (2002)[19]**	**Bechtedt et al. (2001)[21]**	**Stich et al. (1992)[20]**	**Brommer et al. (1992)[16]**	**Northrup (1986)[22,23]**
Method	PBE-DFT	LDA-DFT	LDA-DFT	LDA-DFT	LDA-DFT	LDA-DFT[b]
1x1 unrelaxed	1.224	1.435	0 (ref.)[a]			0 (ref.)[a]
1x1 relaxed	1.200	1.372				-0.17
√3x√3H3 hex.	1.353					-0.067
√3x√3T4 hex.	1.102					-0.28
2x2H3 hex.	1.209					-0.24
2x2T4 hex.	1.083					-0.24
2x2H3 rect.	1.264					-0.17
2x2T4 rect.	1.085					
2x3H3T4	1.184					
c2x8	1.184	1.109	-0.33			
DAS3x3	1.070			1.196		
DAS5x5	1.048			1.168		
DAS7x7	1.044	1.073	-0.36	1.153	1.179	
DAS9x9	1.055					

[a]Absolute energies not provided

[b]Cluster calculations

4.2 Energetics for H_3 and T_4 adatoms

Since there are two possibilities for the local structure of the adatoms, H_3 and T_4 (Figure 3), and since only T_4 adatoms are observed in the DAS structures, we considered it necessary to investigate the fundamental differences between the two adatom types which lead to the observed preference. Table 1 shows that the calculated surface energies of the √3x√3H3 and √3x√3T4 structures are 1.353 eV/1x1 cell and 1.102 eV/1x1 cell, respectively, indicating that the √3x√3H3 surface is *not* as stable as the 1x1 unreconstructed surface, while the √3x√3T4 surface is nearly as stable as the DAS structures. Both surfaces contain one dangling bond per unit cell, and in both cases the adatom sits on top of three unreconstructed silicon atoms, which would otherwise form a 1x1 unreconstructed surface. The only difference between them is that the H_3 adatom sits above a void in the subsurface layer, while the T_4 adatom sits directly above a sub-surface atom.

To better understand these differences, we performed a series of calculations on both surfaces as follows (the results are summarized in Table 2):

i. *Bond energy of hydrogen to the adatom:* For this calculation we bonded a hydrogen atom to the dangling bond of the adatom and computed the bond energy while keeping the Si atoms fixed (optimizing only the H atom). Here we found similar bond energies (3.122 eV for √3x√3H3 and 3.165 eV for √3x√3T4). This suggests that the dangling bond electron has similar character for both and does not participate differentially in any bonds to subsurface atoms.

ii. *Surface strain energy upon removal of the adatom without relaxation:* Here we removed the adatom from the optimized √3x√3H3 and √3x√3T4 surfaces

without relaxation, did a single-point energy calculation, and substracted from it the *relaxed* unreconstructed Si(111) surface energy. This snap strain energy is 0.36 eV for H_3 and 0.61 eV for T4, indicating that the T_4 adatom causes *more* strain in the initial relaxed (111) structure.

iii. *Adatom snap bond energy:* This is the difference in energy between the optimized surface structure and the resulting *unrelaxed* surface structure obtained when the adatom is displaced to infinity with all other atoms kept fixed. The calculated snap bond energies are 4.60 eV for √3x√3H3 and 5.59 eV for √3x√3T4. This is the most substantial difference (1.0 eV), indicating that electronic effects are important.

iv. *Bonding Si to the normal site.* This is the bond energy of a single Si atom on top of a single 1x1 surface atom. This leads to one dangling bond pi orbital and one lone pair on the Si adatom. The calculated bond energy is 2.257 eV, significantly lower than the snap bond energy of the H_3 and T_4 adatoms. This result shows that it is important for the adatom to bend over towards the surface and form three bonds.

These calculations show that the difference in surface energy for √3x√3T4 versus √3x√3H3 cannot be explained by differences in subsurface strain or in the character of the bonds formed by the dangling bond electron alone. Instead the large difference in snap bond energy of 1 eV indicates that the more favorable surface energy of √3x√3T4 is primarily due to electronic effects associated with forming bonds between the adatom and the 1x1 subsurface.

Table 2: √3x√3H3 and √3x√3T4 electronic structure and geometry calculations. All energies are eV per √3x√3 unit cell.

	√3x√3H3	**√3x√3T4**	**$T_4 - H_3$ Difference**
Surface energy	4.059	3.307	-0.751
Surface strain energy (below adatom)	0.351	0.607	0.256
Stabilization due to bonding hydrogen to dangling bond	-3.122	-3.165	-0.043
Stabilization due to adatom snap bond energy	-4.601	-5.594	-0.993
Adatom bond angle, degrees	87.9	87.6	-0.3
Adatom bond length, Å	2.59	2.51	-0.08

There are two differences in the bonds formed by the T_4 and H_3 adatoms, which favor the H_3 configuration. The first of these is the Pauli repulsion between the adatom (purple) and the 2nd layer atom located 2.44 Å directly below it (green) in the T_4 surface, which does not take place in the H_3 structure (see Figure 3). This effect is not directly quantifiable, but our calculations show that it causes the green atom to move downward by ~0.61 Å, which could be significant. The second effect favoring H_3 is the difference in the bond angle strain of the red atom *due to the new bond with the adatom* (this is *not* included in the subsurface strain result of Table 2). We estimated its magnitude by performing DFT cluster calculations (using the 631G**++ basis set) on an SiH_4 molecule having the same bond angles as a 1x1 red atom with an additional bond in the H_3 or T_4 configuration and obtained an energy difference of ~0.13 eV for every three atoms bonded to one adatom.

There are also two differences in bonding which favor the T_4 configuration. The first one can be understood by looking at the new bonds that need to be formed upon placement of the adatom in each case. Figure 6 illustrates the orientation of the bonds between the adatoms and the 2nd layer atoms (labeled A) with respect to the bonds between the 2nd and 3rd layer atoms (labeled B). Adding an H_3 or T_4 adatom to the 1x1 unreconstructed surface requires the formation of three new A bonds. A geometrical analysis of the √3x√3H3 surface reveals that the A and B bonds and the bonds between the 3rd (green) and 4th (orange) layer (denoted C) are all in the same plane, which leads to slightly repulsive interactions resulting from orthogonalizing these three bonds to one another. In contrast, in the √3x√3T4 surface the A bond points in a direction 60º away from the B bond (when observed from above) so that it *cannot* be in the same plane as the B and C bonds, and the coupling is more favorable than in √3x√3H3. The energy difference between these two cases cannot be calculated directly using DFT, but we expect it to be of the same order of magnitude as the energy cost of introducing a stacking fault between the 1st and 2nd layers of the unreconstructed 1x1 surface (calculated to be ~0.048 eV/cell), which changes the Si-Si-Si-Si torsion angle of the atoms in the top four layers from 60° to 0°. However, when compared to the 1 eV difference in bond energy between H_3 and T_4 adatoms, this effect is very small. A much more important factor explaining the strong preference for the T_4 structure is the delocalization of the dangling bond orbitals into the sub-surface layers, which allows the dangling bond orbital (HOMO) to be partially stabilized by using some LUMO character from the C bond that is aligned with the adatom. Figure 7 shows that electronic delocalization is significant in the T_4 structure, with HOMO density in the 3rd and 4th

layers. This cannot occur for H_3 because the adatom sits above a hollow and is not aligned with any of the C bonds. None of the factors discussed above can be considered in isolation, so it is *not* possible to estimate the HOMO delocalization energy in the T_4 surface by simply adding all other contributions. However, if we neglect the small energy difference in the orientation of the adatom bonds illustrated in Figure 6 and consider that the HOMO delocalization effect must compensate for the difference in bond angle strain, sub-surface bond strain, bond energy, and Pauli repulsion, we can expect it to be on the order of ~1 – 1.2 eV.

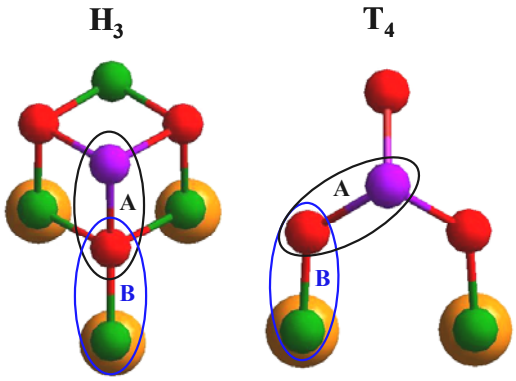

Figure 6. Top view of the orientation of the H_3 and T_4 adatom bonds with respect to those of the unreconstructed surface. The picture shows that the bonds between the adatom and the 2nd layer atoms (A), the bonds between the 2nd and the 3rd layer atoms (B) and the bonds between the 3rd (green) and the 4th (orange) layer atoms are all approximately in the same plane for H_3 adatoms, but not for T_4.

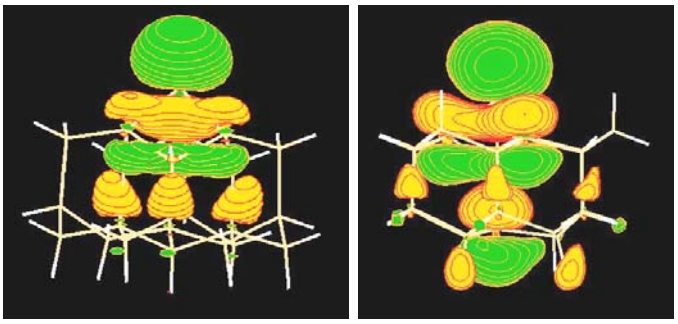

HOMO H3 **HOMO T4**

Figure 7. Highest occupied molecular orbital (HOMO) for clusters containing a single H_3 or T_4 adatom. This is the dangling bond orbital with just one electron. Obvious here is the greater electronic delocalization for the T_4 adatom, with significant density in the third and fourth layers. These calculations used 631G**++ basis sets and the B3LYP functional.

4.3 Geometry Analysis of the DAS 7x7 Reconstruction

The total energy calculations for the DAS 7x7 reconstructed surface indicate that forming this structure leads to ~28.35 eV of strain per 7x7 cell. The strain is evident when one considers the significant deviations in geometry with respect to the bulk structure in terms of atomic layer vertical positions, bond lengths, and bond angles. In this section we examine the details of the optimized 7x7 structure to gain a better understanding of the strain that exists in the structure and lay the foundation for the next section, where we decompose the energy of a reconstructed surface into contributions of different atom types.

4.3.1 Crystal layer positions

Table 3 provides the calculated vertical position of the different layers in the DAS 7x7 surface (a sideview illustrated in Figure 8) and compares them to the bulk structure. Consider first dangling bond atoms 1, 2, and 8. In bulk silicon the vertical distance separating a double layer is 0.784 Å. In the DAS 7x7 reconstruction, atoms 1, 2, and 8 are respectively 1.340, 1.113, and 1.277 Å above the next layer. This is much larger than the bulk value, indicating that significant strain is present, although not as great as that present in the pure T_4 adatoms of the √3x√3T4 structure, which are are 1.507 Å above the next layer. Now consider the vertical position of the atoms in the third (green) layer. Due to the presence of atom 1, atom 6 is displaced 0.607 Å lower than atom 4. Atom 5 (a dimer atom adjacent to the cornerhole) is not located below an adatom, but it is also lower than atom 4 by 0.241 Å. As a result of the downward shifting of atom 6, atom 9, located immediately below, is also displaced downward by approximately 0.333 Å with respect to the bulk structure.

Table 3 also compares our results to other first principles and experimental results available in the literature. Our results compare well with the experimental results of Shigeta and Fukaya,[18] who used reflection high energy electron diffraction (RHEED). The most significant differences are the vertical positions of atom 8 (our result is 0.520 Å higher) and the vertical position of atom 9 (our result is 0.188 Å lower). Our results are in moderate agreement with the *ab initio* results of Stelnikov et al.[19] and Brommer et al.,[16] which were based on LDA rather than PBE calculations. The differences may also be related to the periodicity of the model and the type basis set (their calculations used

plane wave basis set and *3D* periodic supercell models with vacuum space between the slabs, while we used Gaussian basis sets and *2D* periodic models).

4.3.2 Bond lengths

Table 4 provides the bond lengths in the reconstructed surface layers of the DAS 7x7 surface for different types of atom pairs. Most of them exhibit bond lengths that are *longer* than the experimental bulk value of 2.352 Å, except for the bonds between atoms 6 and 9 and between atom 9 and the bulk layers below, which are shorter as a consequence of the vertical displacements in the third layer caused by the adatom. A key parameter in the DAS 7x7 model is the nonbond distance between the adatom and the subsurface atom below it (atoms 1 and 6, respectively, in Figure 8). Proposed values of this distance have ranged from 2.45 to 3.1Å, reflecting the uncertainty remaining in the structure characterization. The value obtained from our periodic *ab initio* calculations ranged from 2.48 to 2.54 Å depending upon the site within the surface reconstruction. The Si-Si dimer bond length is another important distance for which our calculated values range from 2.43 to 2.46 Å depending upon the site. This agrees well with the LDA DFT calculations of Stelnikov et al.[19] (2.442 Å) and Stich et al.[20] (2.446 Å).

4.3.3 Bond angles

Table 5 shows that there are also significant deviations in the bond angles with respect to the tetrahedral bulk structure (109.4º). The most dramatic deviations are the bond

angles of the T_4 adatoms (94.2º), which sit directly above a subsurface atom, and the bond angles between atoms 6, 3, and 5 (95.5º), which are reduced by the downward displacement of atoms 5 and 6, as discussed above. The bond angle centered on atom 2 (100.8º) is also significantly *less* than tetrahedral, indicating that the character of the dangling bond on this atom is different than that of a relaxed 1x1 site, which has a bond angle (110.4º) slightly *greater* than the tetrahedral of the bulk structure. The other dangling bond atom (8) has bond angles (114.1º) significantly larger than those of the 1x1 relaxed structure (this atom belongs to an unreconstructed bulk layer and would be expected to behave similarly to the 1x1 surface atoms). Finally, consider atoms 7 and 9. Atom 7 has average bond angles close to the bulk value (107.9º) but exhibits significant variability depending on location. Due to its significant downward displacement, atom 9 has the largest bond angles (115.6º). This analysis points out that the strain present varies greatly across the different atom types in the reconstruction and motivates the energy decomposition chosen for defining the AECM in the next Section.

Table 3: Vertical layer position (Å) for the DAS 7x7 structure obtained from PBE calculations. The numbers correspond to the atomic vertical positions with respect to the fifth (unreconstructed) layer, as shown in Figure 8. Also shown are comparisons to previously published results. The results of Stelnikov et al.[19] and Hanada et al. [17] use different reference layers as indicated.

Layer	Bulk Crystal	This work	Shigeta and Fukaya (2001)[18]	Hanada et al. (1994)[17]	Stelnikov et al. (2002)[19]	Brommer et al. (1992)[16]
Method	N/A	PBE-GGA	RHEED[a]	RHEED[a,b]	LDA	LDA
L1	6.271	5.275	5.281	L2 + 0.67	L3 + 1.309	5.148
L2	3.919	4.486	4.415			4.173
L3	3.919	3.935	3.853	L2 – 0.54	L2 – 1.108b	3.814
L4	3.125	3.373	3.331			3.221
All dimers	3.135	3.154				
L5	3.135	3.132	3.026	L4 – 0.14		3.081
L6	3.135	2.766	2.699	L4 – 0.48		3.045
L7	0.784	0.887	0.928			0.811
L8	0.784	1.277	0.757			0.788
L9	0.784	0.454	0.642	L7 – 0.34	1.129	0.445

[a]Reflection high energy electron diffraction

[b]Average values for faulted and unfaulted atoms

Table 4: Average bond length for selected pairs of atoms of the DAS 7x7 structure from PBE calculations. All atom numbers correspond to those of Figure 8, except for the 1x1 surface atom.

Atom pair		**Bond length, Å**	**Deviation from experimental bulk, Å**
Bulk	**bulk**	2.352	N/A
Bulk	**1x1 relaxed**	2.352	~0
1	**3**	2.485	0.133
1	**6**[a]	2.504	0.152
2	**4**	2.416	0.064
3	**4**	2.424	0.072
3	**5**	2.475	0.123
3	**6**	2.394	0.042
4	**7**	2.431	0.079
5 (dimer)	**5 (dimer)**	2.449	0.097
5	**7**	2.408	0.056
6	**9**	2.312	-0.040
7	**Bulk**	2.372	0.020
8	**Bulk**	2.389	0.037
9	**Bulk**	2.341	-0.011

[a] Adatom non-bond distance

Table 5: Bond angle averages and ranges for selected atoms of the DAS 7x7 structure from PBE calculations. All atom numbers correspond to those of Figure 8, except for the 1x1 surface atom.

Atoms forming bond angle	Average bond angle, degrees	Bond angle range, degrees
bulk-1x1-bulk relaxed	110.4	N/A
Bulk-bulk-bulk	109.4	N/A
3-1-3	94.2	91.3 – 96.3
4-2-4	100.8	98.7 – 103.0
4-3-6	106.8	105.3 – 107.9
6-3-5	95.5	95.4 – 95.5
ref-7-ref	107.9	101.7[a] – 112.5[b]
ref-8-ref	114.1	N/A[c]
ref-9-ref	115.6	113.7 – 117.2

[a]This angle occurred under atom 4, near the cornerhole.
[b]This angle occurred under atom 5, at the cornerhole.
[c]There is only one bond of this type in the unit cell.

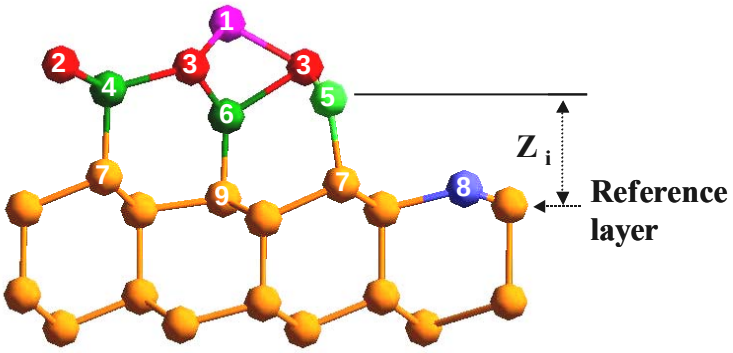

Figure 8. Atom positions corresponding to the dimensions given in Tables 4 and 5. The 4th and 5th (reference) layers are unreconstructed. Atom 8 is the corner hole atom.

5. Atomic energy contribution model (AECM)

5.1 Energy partitioning

In order to better understand the relevant contributions to the surface energy, we classified each surface atom in terms of its local environment using seven types (listed in Table 6). Then we assumed that each type of atom contributes a certain increment to the average surface energy, proportional to a power of its average number density (per 1x1 cell), *independent* of the specific surface structure it is embedded in, as described by the following equation:

$$E_s = \sum_{i=1}^{7} C(i)\rho(i)^{\exp(i)} , \qquad (2)$$

where E_s is the average surface energy per 1x1 cell, *C(i)* and *exp(i)* are the coefficient and exponent corresponding to atom type *i*, respectively, and $\rho(i)$ its average number density per 1x1 cell. This is similar to the model used by Zhao et al.,[26] but is based on feature densities instead of absolute energy contributions and on individual atom features instead of larger structural units. It also introduces exponents for the average feature density, thus allowing for non-linear relaxation effects as described below.

The energy contributions of two of the atom types in Table 6 – the 1x1 surface atom with a dangling bond and the atom at a faulted position – were obtained directly from DFT calculations on a 1x1 unit cell and were assumed to have an exponent of 1 in the expression for E_s. The remaining energy terms were fitted to the *ab initio* surface energies according to the atom type composition for each surface given in Table 7 in order to obtain their coefficients and exponents (listed in Table 6). We found that

exponents different than unity were only necessary for atoms types 8R and 12R (belonging to 8- and 12-membered rings, respectively), whose fitted coefficients are negative, indicating that these configurations help stabilize the surface *in the presence of the other types of atoms* and suggesting that they may play an important role in surface relaxation (such a negative energy contribution does not mean that the configuration is more stable than the bulk diamond structure, only that it contributes to the stability of the reconstructed system containing the strain of various dangling bond configurations).

Table 6: Fitted coefficients and exponents by atom type for the AECM. Note that atoms classified as F or D may also belong to other types simultaneously. For example, all D atoms in the DAS7x7 model are also classified as either 8R or 12R. Both contributions must be added to the total surface energy. Atoms shared by more than one ring were assigned to the largest ring.

Atom Type, *i*	***Coefficient, C(i)***	***Exponent, exp(i)***
Atom corrections		
1x1 dangling bond atom (1x1)	1.2004 (DFT result)	1
H_3 adatom (H3) [a]	3.8933	1
T_4 adatom (T4)	3.2264	1
Dimer atom (D)	0.9936	1
Configuration corrections		
8-membered ring atom (8R)	-0.2617	1.2865
12-membered ring atom (12R)	-0.3133	1.3267
Atom in a faulted position (F)	0.04819 (DFT result)	1

[a]This atom type is not present in the DAS structures.

Table 7: Average atom type composition per 1x1 cell for the Si(111) surface reconstructions used in the construction of the AECM. Each fraction corresponds to the number of features present in the supercell (of size n x n) divided by n^2. For the **infinite** DAS model, the numbers correspond to the average fraction of atoms of each type per 1x1 cell.

Surface	**1x1**	**H3**	**T4**	**8R**	**12R**	**F**	**D**
√3x√3T4 hex.	0	0	1/3	0	0	0	0
√3x√3H3 hex.	0	1/3	0	0	0	0	0
2x2T4 hex.	1/4	0	1/4	0	0	0	0
2x2T4 rect.	1/4	0	1/4	0	0	0	0
2x2H3 hex.	1/4	1/4	0	0	0	0	0
2x2H3 rect.	1/4	1/4	0	0	0	0	0
2x3H3T4	0	1/6	1/6	0	0	0	0
c2x8	0	0	4/16	16/16	0	6/16	10
DAS3x3	1/9	0	2/9	0	12/9	3/9	6/9
DAS5x5	3/25	0	6/25	24/25	12/25	10/25	12/25
DAS7x7	7/49	0	12/49	48/49	12/49	21/49	18/49
DAS9x9	13/81	0	20/81	72/81	12/81	36/81	24/81
DAS11X11	21/121	0	30/121	96/121	12/121	55/121	30/121
DAS13X13	31/169	0	42/169	120/169	12/169	78/169	36/169
DAS Infinite	0.25	0	0.25	0	0	0.5	0

Table 8: Surface energies estimated using the AECM and deviations from the ab initio results.

	Atom Type corrections, eV/1x1 cell	**Configuration corrections, eV/1x1 cell**	**Total surface energy/1x1 cell**	**Error vs. *ab initio* result, eV/1x1 cell**
1x1 relaxed	1.200	0	1.200	0
√3x√3T4 hex.	1.075	0	1.075	-0.027
√3x√3H3 hex.	1.298	0	1.298	-0.055
2x2T4 hex.	1.107	0	1.107	0.024
2x2T4 rect.	1.107	0	1.107	0.022
2x2H3 hex.	1.273	0	1.273	0.064
2x2H3 rect.	1.273	0	1.273	0.007
2x3H3T4	1.187	0	1.187	0.003
c2x8	1.428	-0.244	1.184	$<10^{-3}$
DAS3x3	1.513	-0.443	1.070	$<10^{-3}$
DAS5x5	1.395	-0.347	1.048	$<10^{-3}$
DAS7x7	1.327	-0.283	1.044	$<10^{-3}$
DAS9x9	1.284	-0.228	1.055	$<10^{-3}$
DAS11x11	1.255	-0.187	1.068	N/A
DAS13x13	1.234	-0.156	1.078	N/A
DAS infinite	1.107	0.024	1.131	N/A

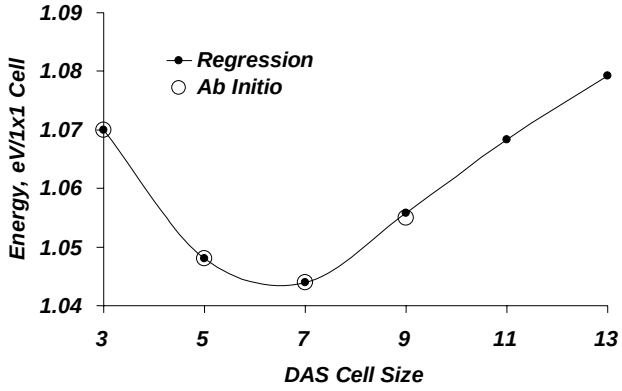

Figure 9. *Ab initio* and AECM surface energies for the DAS surfaces from 3x3 to 13x13. The black open circles are the *ab initio* results, and the dots represent AECM calculations. The graph shows good agreement between the two.

The calculated surface energies using this model and quality of the fit with respect to the *ab initio* results are given in Table 8. The results show that despite its simplicity, the AECM approximation is remarkably good with errors of $< 0.1\%$ for the formation energy of the DAS structures as shown in Figure 9. This figure also shows that the AECM surface energy of the DAS reconstructions increases monotonically for unit cells larger than 7x7, but that the slope becomes gradually smaller as the unit cell size (n) increases. This indicates that the surface energy of DAS models levels off very quickly as a function of n. Extrapolating our AECM surface energy calculations to an infinitely large DAS model (Figure 10), we obtain an energy of 1.131 eV/1x1 cell, lower than the calculated surface energy of the unreconstructed 1x1 surface (1.200 eV/1x1 cell). This infinite case is dominated by the large triangular regions of adatoms and exposed second-

layer atoms (purple and brown respectively in Figures 1 and 2) leading to a surface that resembles the 2x2T4 structure, but with a stacking fault as in all DAS models.

Figure 10 shows the normalized atom energy contributions for DAS [(2n+1)x(2n+1)] structures plotted vs. n^{-1}. As n increases (i.e., as n^{-1} approaches zero), these contributions converge to a constant value, which, as indicated above, adds up to 1.131 eV/1x1 cell. Numbers of all surface features increase linearly as n, except for the area of the faulted and unfaulted triangular regions, which increases as n^2 (and becomes dominant at very large cell sizes).

Finally, we must note that the AECM does *not* capture the energy differences between cells of different geometry containing the same density of surface features, such as the 2x2H3 hexagonal and rectangular surfaces, for which the same energy is predicted (the energy differences between the 2x2H3 and T4 hexagonal and rectangular surfaces are primarily a result of different adatom bond and sub-surface strain energies and are discussed in more detail in the supporting information). Nonetheless, the AECM is sufficiently accurate to analyze general trends in surface reconstruction and allows the rapid estimation of the energy for both periodic and non-periodic systems. The next section applies this analysis to the real-time reconstruction process of the Si(111) 1x1 surface observed by Shimada and Tochihara[8] using STM.

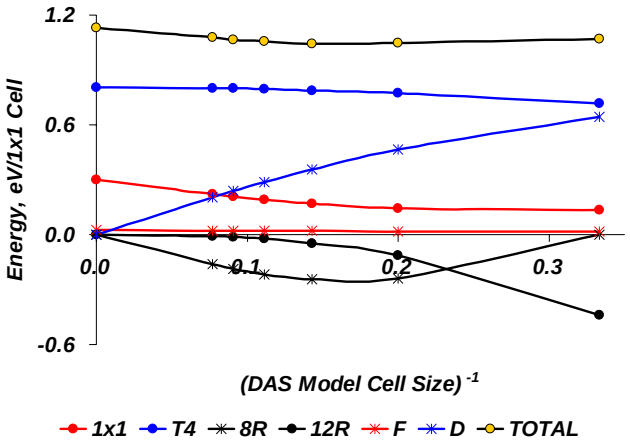

Figure 10. Atom type energy contributions as a function of n^{-1} for DAS [(2n+1)x(2n+1)] models between 3x3 and infinity. The atom type labels and descriptions are the same as in Table 6. The graph shows that the differences between different values of n vanish when n grows to infinity (i.e., when n^{-1} approaches zero). It also shows that the DAS surface energy reaches an asymptotic value in the limit of very large unit cells ($n^{-1} = 0$), calculated to be 1.131 eV/1x1 cell.

5.2. Application of the AECM to real-time reconstruction observations

Shimada and Tochihara[8] recently reported real-time observations of the 1x1 Si(111) reconstruction process using STM. They determined surface structures for the different stages of reconstruction of the faulted half of the DAS unit cell for various cell sizes. They propose the SSC model in which surface reconstruction depends primarily on the reconstruction path of the faulted half of the unit cell. Their experimental observations show that the unit cell grows according to a zipper-like pattern that displaces the row of

dimers around the unit cell, one cell at a time. To determine the reaction energy profile and to compare the results to the calculated surface energy of the different sizes of DAS models we applied the AECM to the different structures of the SSC.

We started with a periodic cell having an array of 16 by 16 1x1 cells of the unreconstructed surface. We then modified the structure according to the different stages of the SSC model. [8] For each stage we determined the average density per 1x1 cell of atoms of each type (listed in Table 6) and calculated the average surface energy *in the reconstructed region* and the total energy of the 16x16 supercell (the energy of the unreconstructed part of the supercell can be easily calculated using the surface energy of the 1x1 relaxed surface). Since the SSC model contains additional structural components that are similar but not identical to those listed in Table 6, and since the size of the reconstructed region is not obvious for each stage, we defined the following rules for the application of the AECM:

i. 7-membered rings are not included in the calculation of the surface energy (these rings are present in the c2x8 reconstruction, but the regression analysis performed in constructing the AECM shows that it is not necessary to assign them an energy contribution).

ii. All atoms containing dangling bonds, which are in the same layer as the surface atoms in the unreconstructed region, are classified as 1x1 atoms (faulted or unfaulted).

iii. Atoms with dangling bonds on the step edges of incomplete cornerholes are treated as 1x1 unfaulted atoms (they are tetrahedral and are not subject to strain, just like regular 1x1 atoms).

iv. Atoms that would be classified as 12R in a perfect cornerhole are treated as 12R atoms (there are 6 in each irregular-odd and 3 x 6 = 18 in each regular-odd SSC structure).

v. Finally, in order to compute the feature densities, it is necessary to define the size of the reconstructed region, which we calculated as $[n^2/2 + (n+2)x(n+2)/2]$, except for the 2x2 cell size whose size was assigned $[n^2/2 + (n+2)x(n+2)/2 + 1]$. This is approximately equal to the size of the faulted half plus half of a unit cell two sizes larger and was estimated based on the area occupied by the reconstructed half, the band of adatoms surrounding it and the atoms below these adatoms.

Figure 11 compares the *ab initio* surface energy of each n-sized periodic DAS structure to the average surface energy *of the reconstructed region* of the corresponding SSC stage. We see that the energy of the SSC regular-odd structures, which lead to DAS structures, shows a minimum at the 7x7 cell size, in agreement with the DFT result. The energy of the irregular-odd and even SSC structures is non-monotonic and has local minima at the 6x6 and 8x8 cell sizes. This curve also exhibits a reaction barrier at the 2x2 cell size and local barriers between *adjacent* even cell sizes. Although the average surface energy for the irregular-odd and even SSC structures is slightly lower than that of the regular-odd structures, the latter are favored in an infinite domain because the former are *not* able to form periodic regular structures, which results in increased energy at the domain boundaries (note that the energy curves in Figure 11 only consider the *average* surface energy in the reconstructed domain but do not take into account what happens outside that domain nor whether periodic structures are feasible for each particular structure).

The higher SSC energy with respect to the *ab initio* results is also a consequence of the non-periodicity of the SSC structures and the fact that the area of an isolated reconstructed region in the SSC model is larger than the corresponding nxn cell, thus leading to a less optimal proportion of surface features.

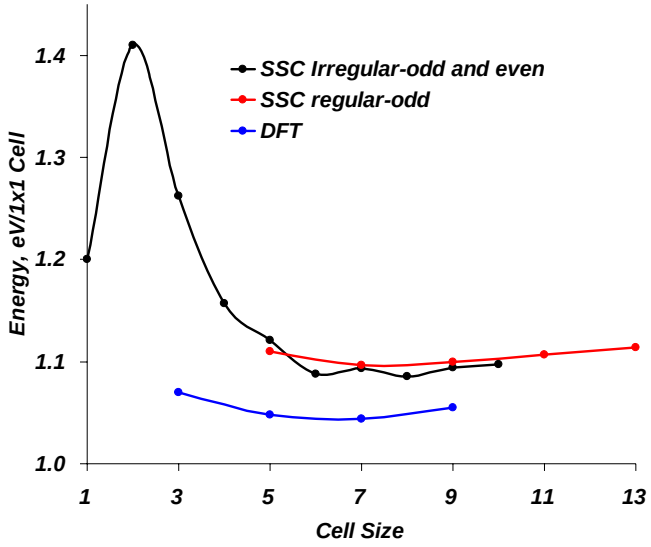

Figure 11. Comparison of DAS and SSC[8] surface energetics. The black dots correspond to the average surface energy of the SSC even-sized and irregular-odd-sized structures *in the reconstructed region*. The red dots provide the corresponding values for the regular-odd-sized structures (which yield DAS structures), and the blue dots indicate the DFT surface energies of the DAS models. These results show that the normalized SSC energy in the reconstructed region follows a trend similar to the DFT-DAS surface energy, explaining the origin of a finite cell size in the optimum reconstruction.

Figure 12 shows the total energy of the 16x16 supercell used in the analysis (relative to the initial unreconstructed structure) for the different SSC stages. [8] Except for n = 2, the total energy decreases monotonically as the size of the reconstructed domain increases. The curves also indicate that the decrease in energy is greater when the reconstructed domain size increases from an odd size to an even size. This monotonic behavior of the total energy suggests that the size of the reconstructed region should increase indefinitely, but the results of Figure 11 show that the greatest *normalized* gain in stability is obtained for the cell size 7x7, thus explaining the origin of a finite cell size.

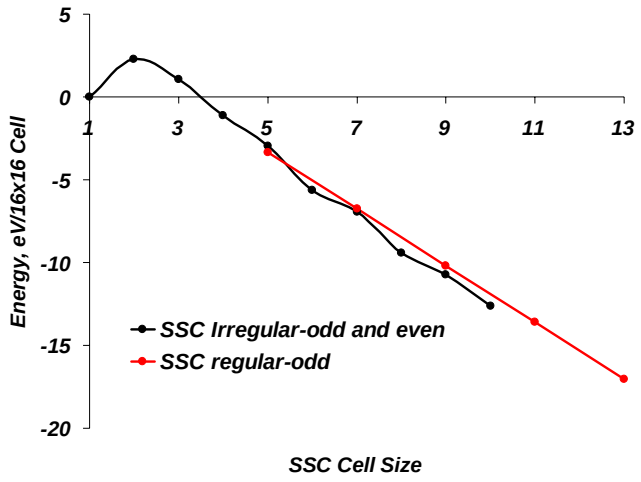

Figure 12. Calculated *total* surface energy for a 16x16 surface cell of Si(111) undergoing the structure changes described by the SSC model of Shimada and Tochihara[8] These calculations do not account for the energy cost of bringing additional atoms into the system, but this is consistent with the Atom type Energy Contributions presented in Table 6 which depend only on the number of features observed in the surface structure. The monotonic behavior of this graph suggests that the cell size of the reconstructed region

should increase indefinitely since the energy seems to decrease indefinitely, but considering the *normalized* surface energy of the reconstructed region leads to a different conclusion (Figure 11).

These results support the experimental conclusions of Shimada and Tochihara[8] that the formation of the faulted half of the unit cell is the key process in the Si(111) surface reconstruction and the experimental observations that the greatest gain in stability is achieved with the DAS 7x7 structure. The AECM analysis provides additional information on the reconstruction energy path and stability of the different stages of the SSC model, plus it identifies the presence of an energy barrier at the 2x2 cell size, which suggests that the reconstruction process does not take place at low temperatures.

6. Conclusions and prospects

We reported here consistent PBE DFT calculations for various surface reconstructions of the Si(111) surface, confirming that the DAS 7x7 structure has the lowest surface energy of 1.044 eV/1x1 cell (1310.12 dyn/cm).

We also develop the Atomic Energy Contribution Model (AECM) for decomposing the surface energy into individual contributions of the type of atomic configuration and apply it to the analyze a real-time reconstruction process, demonstrating a low surface energy pathway leading to the DAS 7x7 structure. This confirms that the rate-determining step in the DAS surface reconstruction is the formation of the faulted half of the unit cell, as has been proposed by Shimada and Tochihara[8] based on STM observations. This approach

should be useful for studying other reconstruction paths, taking into consideration larger domains or following different stages. In addition, generalizations including adsorbates should be useful for examining the inverse reconstruction process that a DAS 7x7 surface undergoes when it is functionalized with hydrogen atoms or methyls. This simple but accurate analysis would also be useful for discrete simulation algorithms such as Monte Carlo and others. We plan next to develop a reactive force field fitted to the *ab initio* results presented here and apply it to real-time dynamic reconstruction and reaction processes on Si(111) surfaces.

Acknowledgement: This research was partially supported by the Microelectronics Advanced Research Corporation (MARCO) and its Focus Center on Function Engineered NanoArchitectonics (FENA). Sandia is a multiprogram laboratory operated by Sandia Corporation, a Lockheed Martin Company, for the United States Department of Energy's National Nuclear Security Administration under contract DE-AC04-94AL85000. We also acknowledge the contribution of Dr. Adri van Duin in discussions regarding the ReaxFF reactive force field and of Dr. Mario Blanco in compiling the structures and force field files from previous research in our group and in useful discussions throughout the project.

SUPPORTING INFORMATION

1. Pseudopotentials and basis sets

The pseudopotentials used in these calculations are standard norm-conserving, non-separable pseudopotentials.[34] The LDA potentials for Si and H were generated using the generalized norm-conserving pseudopotential method. [33] The PBE potentials were generated using Hamann's new method for pseudopotentials. [35] The silicon pseudopotentials included up to l=2 projectors (with standard settings), and the l=2 potential was used as the local potential. The hydrogen atom was also treated as a pseudopotential (rather than with a bare-core potential), with only an l=0 potential. Multiple tests with hydrogen atoms, H_2 molecules, and water molecules verified that the energetics of the bare core hydrogen potential and the hydrogen pseudopotential are almost indistinguishable.

The basis functions are double-zeta plus polarization quality, formed from contracted Gaussians. Hence the Si-*s*, Si-*p*, and the H-*s* have two radial degrees of freedom, and the Si-*d* and H-*p* angular polarization have only one. The PBE basis for Si is a contracted (4s3p1d/2s2p1d) basis, the LDA Si basis is (4s4p1d/2s2p1d), and both the LDA and PBE basis sets for hydrogen are contracted (4s1p/2s1p) basis sets. This nomenclature denotes, for H for example, that four Gaussian *s*-functions are contracted into two independent functions, and one Gaussian *p*-function is used as one independent radial degree of freedom. The *d*-functions are made up of the five pure l=2 functions, i.e., the *s*-

combination is excluded. The Gaussians and contraction coefficients for hydrogen and silicon are listed in Tables S-1 and S-2.

Table S-1: Basis set for hydrogen. The Gaussian decay constants α ($1/bohr^2$) and associated contraction coefficients c_α for the contracted Gaussian basis functions (unnormalized).

H	**s-functions**			**p-function**	
	α_s	c_α (1^{st} zeta)	c_α (2^{nd} zeta)	α_p	c_α
LDA	0.112827	0.104600	0.083940	1.20	1.0
	0.407007	0.399225	0.145755		
	1.260443	0.394750	0		
	4.553255	0.380096	0		
PBE	0.102474	0.087388	0.075281	1.10	1.0
	0.372304	0.405344	0.120939		
	1.230858	0.485455	0		
	4.783324	0.397563	0		

Table S-2: Basis set for silicon. The Gaussian decay constants α (1/bohr^2) and associated contraction coefficients c_α for the contracted Gaussian basis functions (unnormalized).

Si	**s-functions**			**p-functions**			**d-function**	
	α_s	c_α (1st zeta)	c_α (2nd zeta)	α_p	c_α (1st zeta	c_α (2nd zeta)	α_d	c_α
LDA	0.109463	0.335647	1.0	0.077837	0.0395395	1.0	0.4604	1.0
	0.294700	0.501166	0	0.227532	0.212571	0		
	1.301011	-1.026687	0	0.565609	0.242187	0		
	2.602030	0.398914	0	1.131240	-0.174847	0		
PBE	0.104600	0.209953	1.0	0.094241	0.067616	1.0	0.45	1.0
	0.272263	0.559782	0	0.317679	0.318212	0		
	1.300508	-0.991282	0	1.561145	-0.066383	0		
	2.601030	0.334871	0					

2. Slab model calculations

Table S-3 contains the surface energy results for slab models of the 2x3H3T4 surface containing varying numbers of bulk layers, ranging from 2 to 14, and varying number of *fixed* bulk layers. All models were terminated on the bottom surface with a layer of fixed hydrogen atoms.

The results show that the surface energy calculations where all bulk layers are allowed to relax during the geometry optimization are the ones that most closely approach the value of the converged surface energy, and that six bulk layers are sufficient to obtain an

accuracy better than 0.028 eV/1x1 cell. Since this convergence error is common to all models, it should not affect the relative energy differences between them.

Table S-3: Calculated surface energy (eV/1x1 cell) for the 2x3H3T4 surface using slab models with varying numbers of bulk layers and with varying numbers of fixed bulk layers. All models were terminated with a layer of fixed hydrogen atoms on the bottom surface. These results are depicted in Figure 4 *of the paper.*

Total bulk layers	No bulk layers fixed	2 bulk layers fixed	4 bulk layers fixed	6 bulk layers fixed
2	1.483	1.667	N/A	N/A
4	1.228	1.324	1.415	N/A
6	1.184	1.197	1.267	1.354
8	1.170	1.215	1.226	1.296
10	1.164	1.169	1.226	1.238
14	1.156	1.159	1.159	1.162

3. Comparison of PBE and LDA surface energies

Table S-4 compares the surface energies obtained using the PBE and LDA approximations for cell sizes up to 3x3. The results show that the LDA values are consistently higher than the PBE values with an average difference of 0.152.

Table S-4: Comparison of LDA and PBE surface energies for a selected group of surfaces. All energies are in eV/1x1 cell.

Surface	PBE surface energy, eV/1x1	LDA surface energy, eV/1x1 cell	LDA – PBE difference, eV/1x1 cell
1x1 relaxed	1.200	1.451	0.250
√3x√3H3	1.360	1.487	0.127
√3x√3T4	1.110	1.240	0.130
2x2H3	1.209	1.322	0.114
2x2T4	1.084	1.200	0.116
DAS3x3	1.070	1.241	0.172

4. Comparison of PBE DFT Si(111) surface energies to published values from empirical and semi-empirical calculations

Table S-5 compares the ab initio surface energies obtained from our PBE DFT calculations to previously reported empirical and semi-empirical results. Our results are in qualitative agreement with those of Takahashi et al.[27] and Zhao et al.,[26] who used a modified embedded atom model and a building block energy contribution model, respectively.

Table S-5: Comparison of PBE-DFT surface energy for Si(111) surfaces with published results from empirical or semi-empirical methods. The reference energy is zero for the bulk crystal unless otherwise indicated, in which case it is the relaxed 1x1 unreconstructed surface. Energies are in eV/1x1 cell.

Surface	**This work (*ab initio*)**	**Empirical surface energy, Ev/1x1 cell**				
		Takahashi et al. (1999)[27]	**Zhao et al. (1998)[26]**	**Mercer and Chou (1993)[28]**	**Khor and Das Sarma (1989)[12]**	**Qian and Chadi (1987) [24,25]**
Method	PBE-DFT	MEAM[a]	BBEC[b]	TB[c]	MD[d]	TB[c]
1x1 unrelaxed	1.224			1.131	0 (ref.)[e]	0 (ref.)[e]
1x1 relaxed	1.200			1.1	-0.17	-0.17
√3x√3H3 hex.	1.353				-0.075	
√3x√3T4 hex.	1.102			0.860 - 1.338	-0.285	
2x2H3 hex.	1.209				-0.20	
2x2T4 hex.	1.083			0.790 - 1.198	-0.25	
2x2H3 rect.	1.264				-0.166	
2x2T4 rect.	1.085					
2x3H3T4	1.184					
C2x8	1.184			0.780 - 1.189		-0.180
DAS3x3	1.070	1.243	1.196		-0.326	
DAS5x5	1.048	1.211	1.168	0.729 – 1.143	-0.344	-0.395
DAS7x7	1.044	1.206	1.153	0.728 – 1.138	-0.335	-0.403
DAS9x9	1.055	1.226	1.164		-0.325	-0.155

[a]Modified embedded atom model, [b]Building block energy contributions, [c]Tight binding model
[d]Molecular dynamics, [e]Absolute energies not provided.

5. Spin states

Table S-6 contains the calculated high-spin surface energies for non-DAS surface structures. The results show that the for the 1x1, √3x√3H3, and √3x√3T4 surfaces, the lowest energy state has a net spin of one. For all other non-DAS structures the lowest energy state has no net spin. Tables S-7, S-8, and S-9 contain the calculated surface energies for the DAS 3x3, DAS 5x5, and DAS 7x7 surfaces for different numbers of unpaired electrons (spin polarization), including zero. All models contained six bulk Si layers and were terminated with a layer of fixed hydrogen atoms on the bottom surface. The lowest surface energy was obtained for spin zero and increased monotonically with increasing spin polarization. Figures S-1 and S-2 depict the results of Tables S-7 and S-9 (the results of Table S-8 are shown graphically in Figure 5 of the paper).

Table S-6: Calculated high-spin surface energy for non-DAS surface structures with respect to the zero spin state.

Surface	Spin Polarization	Surface energy, eV/1x1 cell
1x1 unrelaxed	1	-0.129
1x1 relaxed	1	-0.106
√3x√3H3 hex.	1	-0.007
√3x√3T4 hex.	1	-0.008
2x2H3 hex.	2	0.012
2x2T4 hex.	2	0.068
2x2H3 rect.	2	-0.002
2x2T4 rect.	2	0.051
2x3H3T4	2	0.008
c2x8	4	0.001

Table S-7: Calculated surface energy for the DAS 3x3 surface as a function of the spin polarization, with respect to the singlet state. These results are shown graphically in Figure S-1.

Spin polarization	Surface energy, eV/1x1 cell
0	0
1	0.011
2	0.019

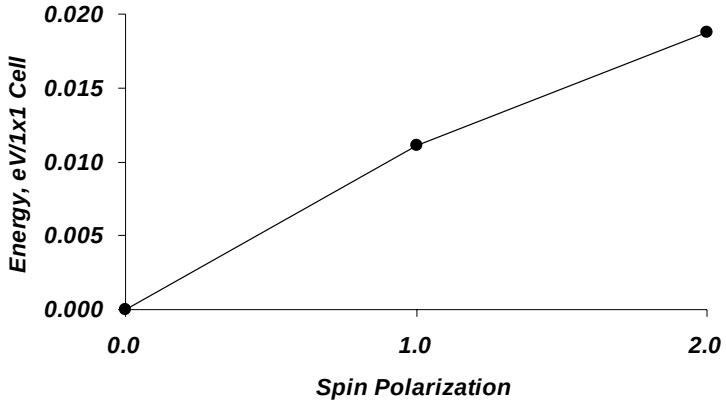

Figure S-1. Calculated surface energy of the DAS 3x3 surface as a function of the spin polarization with respect to the singlet state (Table S-7). Note: the DAS 3x3 surface contains 2 dangling bonds.

Table S-8: Calculated surface energy for the DAS 5x5 surface as a function of the spin polarization with respect to the singlet state. These results are shown graphically in Figure 6 *of the paper.*

Spin polarization	Relative surface energy, eV/1x1 cell
0	0
1	$< 10^{-3}$
2	0.001
3	0.003
4	0.011
5	0.013
8	0.029

Table S-9: Calculated surface energy for the DAS 7x7 surface as a function of the spin polarization with respect to the singlet state. These results are shown graphically in Figure S-2.

Spin polarization	Relative surface energy, eV/1x1 cell
0	0
1	$< 10^{-3}$
2	$< 10^{-3}$
3	$< 10^{-3}$
4	$< 10^{-3}$
5	0.001
19	0.029

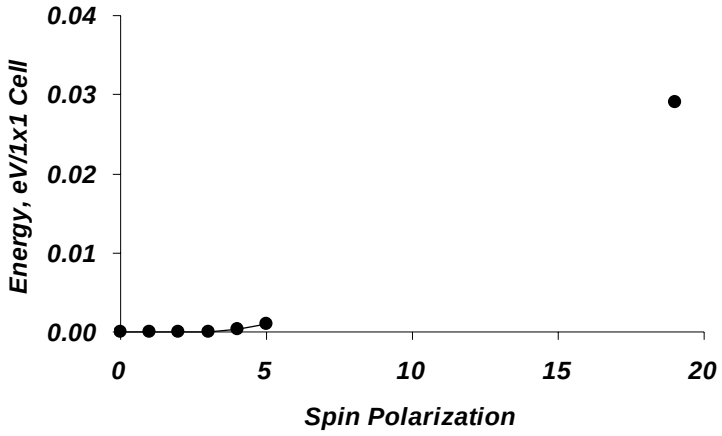

Figure S-2: Calculated surface energy of the DAS 7x7 surface as a function of the spin polarization with respect to the singlet state (Table S-9). Note: the DAS 7x7 surface contains 19 dangling bonds.

6. Comparison of 2x2 hexagonal and rectangular surfaces

Tables S-10 and S-11 provide a comparison of the surface energy, sub-surface strain energy, and adatom snap bond energy (as defined in section 4.2 of the paper) and adatom geometry for hexagonal and rectangular 2x2H3 and 2x2T4 surfaces. The results show that the surface energy is significantly different between the hexagonal and rectangular structures for the 2x2H3 surface, but not for the 2x2T4 surface. The surface energy of the 2x2H3 surface is ~0.22 eV/2x2 cell higher for the rectangular surface, primarily due to lower adatom bond energy (Table S-10). A Mulliken populations analysis of these surfaces (Figures S-3 and S-4) shows that there is significant charge separation in both cases but that the geometry of the hexagonal cell allows this separation to remain local

(thus providing an overall uniform charge distribution when many cells are considered), while the rectangular cell exhibits charge separation between infinite parallel lines in the green (3rd) layer (again considering an infinite number of unit cells) with non-uniform charge distribution around the 2nd layer dangling bond atoms (brown), thus leading to a less favorable energy. Figures S-5 and S-6 show that charge separation also takes place for the 2x2T4 rectangular surface in a similar way, but that the charge distribution remains more uniform in the green layer (except for the green atom directly below the adatom). The adatom in the 2x2T4 rectangular surface can be stabilized by the 3rd layer (green) atom directly below it, which allows the 3rd layer atoms surrounding a 2nd layer dangling bond atom (brown) to all have the same charge and provide a more uniform charge distribution, similar to that of the hexagonal surface, leading to a negligible energy difference between the two surface structures.

Table S-10: 2x2H3 hexagonal and rectangular electronic structure and geometry calculations. All energies are in eV per 2x2 unit cell.

	HEX	**RECT**	**RECT – HEX difference**
Surface energy	4.838	5.058	0.220
Surface strain energy (below adatom)	0.883	0.804	-0.079
Stabilization due to adatom snap bond energy	-6.399	-6.100	0.299
Adatom bond angle, degrees	85.4	85.5	0.1
Adatom bond length	2.61	2.60	-0.01

Table S-11: 2x2T4 hexagonal and rectangular electronic structure and geometry calculations. All energies are in eV per 2x2 unit cell.

	HEX	RECT	RECT – HEX difference
Surface energy	4.333	4.341	0.008
Surface strain energy (below adatom)	0.798	0.923	0.125
Stabilization due to adatom snap bond energy	-6.819	-6.936	-0.117
Adatom bond angle, degrees	94.7	94.1	-0.6
Adatom bond length	2.49	2.47	-0.02

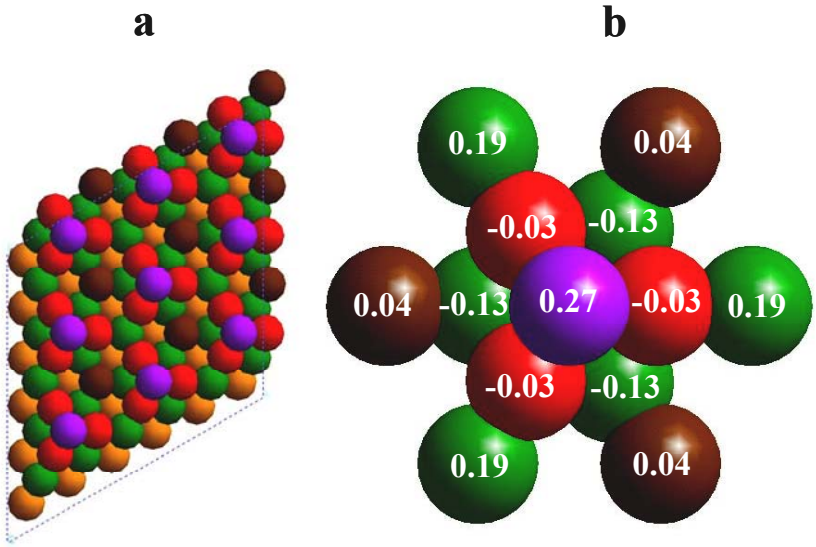

Figure S-3. 2x2H3 hexagonal surface partial atomic charges from Mulliken populations analysis. The results show significant charge separation in the unit cell, but the

hexagonal symmetry allows the overall charge distribution to be uniform when large surface regions are considered.

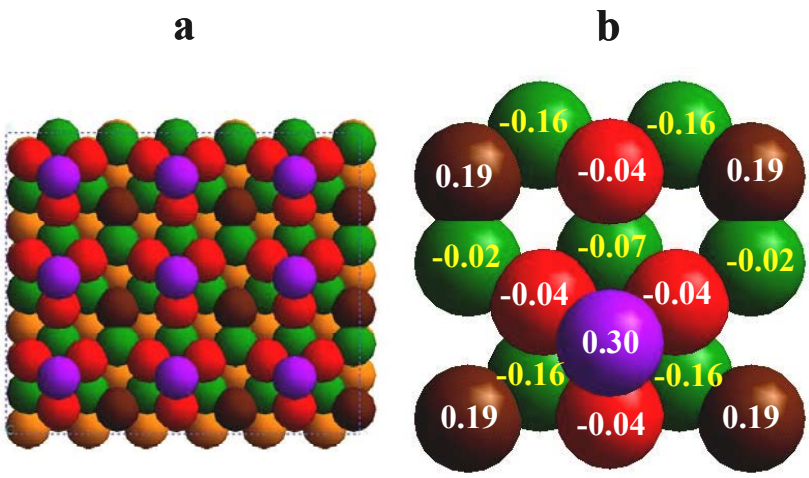

Figure S-4. 2x2H3 rectangular surface partial atomic charges from Mulliken populations. The results indicate that charge separation takes place in the 3rd layer (green with charge values highlighted in yellow) in a non-uniform manner, leading to dipoles between infinite parallel lines oriented with the size of the unit cell. This surface also has uneven charge distribution around the 2nd layer dangling bond atoms (brown).

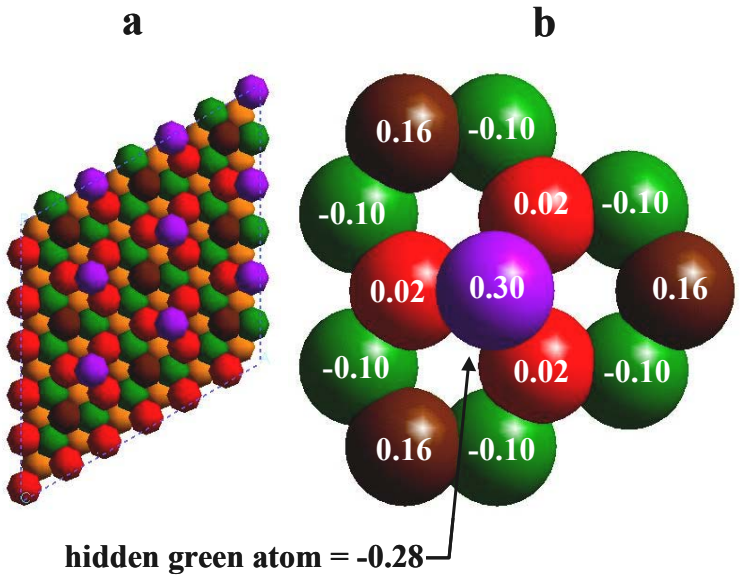

Figure S-5. 2x2T4 hexagonal surface partial atomic charges from Mulliken populations analysis. As with the 2x2H3 hexagonal surface, this structure shows significant charge separation in the unit cell, but the cell symmetry allows the overall charge distribution to be uniform when large surface regions are considered.

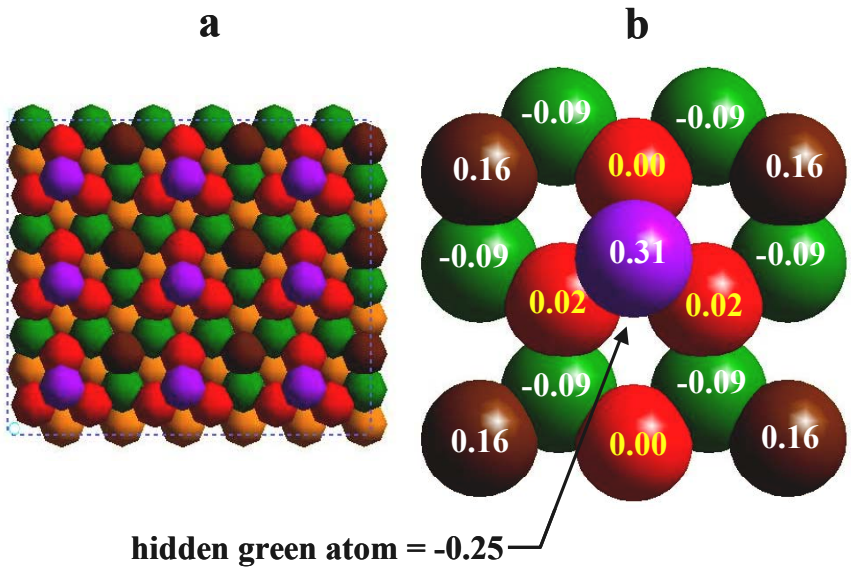

Figure S-6. 2x2T4 rectangular surface partial atomic charges from Mulliken populations analysis. The results show a nearly uniform charge distribution in the 2nd layer (red with charges highlighted in yellow), and also in the green layer (except for the atom directly below the adatom).

REFERENCES:

1. Schlier, R.E.; Farnsworth, H.E.; *J. Chem. Phys.* **1959,** *30,* 917.

2. Harrison, W.A.; *Surf. Sci.* **1976,** *55,* 1.

3. McRae, E.G.; Caldwell, C.W.; *Phys. Rev. Lett.* **1981,** *46,* 1632.

4. McRae, E.G.; *Phys. Rev. B.* **1983,** *28,* 2305.

5. Binnig, G.; Rohrer, H.; Gerber, Ch.; Weibel, E.; *Phys. Rev. Lett.* **1983,** *50,* 120.

6. Takayanagi, K.; Tanishiro, K.; Takahashi, M.; Takahashi, S.; *J. Vac. Sci. Technol.* A **1985,** *3,* 1502.

7. Takayanagi, K.; Tanishiro, Y.; Takahashi, S.; Takahashi, M.; *Surf. Sci.* **1986,** *164,* 367.

8. Shimada, W.; Tochihara, H.; *Surf. Sci.* **2003,** *526,* 219.

9. Shen, T.S.; Chang, C.Y.; Chou, Y.C.; *Surf. Rev. Lett.* **1999,** *6,* 97.

10. Tromp, R.M.; Van Loenen, E.J.; *Surf. Sci.* **1985,** *155,* 441.

11. Qian, G.X.; Chadi, D.J.; *Phys. Rev. B.* **1987,** *35,* 1288.

12. Khor, K.E.; Das Sarma, S.; *Phys. Rev. B* **1989,** *40,* 1319.

13. Huang, H.; Tong, S.Y.; Packard, W.E.; Webb, M.B.; *Phys. Lett. A* **1988,** *130,* 166.

14. Robinson, K.; *J. Vac. Sci. Technol. A* **1988,** *6,* 1966.

15. Ichimiya, A.; *Surf. Sci.* **1987,** *192,* L893.

16. Brommer, K.; Needels, M.; Larson, B.E.; Joannopoulos, J.D.; *Phys. Rev. Lett.* **1992,** *68,* 1355.

17. Hanada, T.; Shozo, I.; Daimon, H.; *Surf. Sci.* **1994,** *313,* 143.

18. Shigeta, Y.; Fukaya, Y.; *Trends in Vac. Sci. Technol.* **2001,** 4, 1.

19. Stelnikov, A.A.; Furthmüller, J.; Bechstedt, F.; *Phys. Rev. B* **2002,** *65,* 115318.

20. Stich, I.; Payne, M.C.; King-Smith, R.D.; Lin, J.S.; *Phys. Rev. Lett.* **1992,** *68,* 1351.

21. Bechstedt, F.; Stelnikov, A.A.; Furthmüller, J.; Käckell, P.; *Phys. Rev. Lett.* **2001,** *87,* 16103.

22. Northrup, J.E.; Phys. *Rev. Lett.* **1986,** *57,* 154.

23. Northrup, J.E.; Proc. of the Eight Intl. Conf. On the Physics of Semiconductors, Editor O. Engstrom, World Scientific, Singapore, **1987.**

24. Qian, G.X.; Chadi, D.J.; *J. Vac. Sci. Technol.* B **1986,** *5,* 1079.

25. Qian, G.X.; Chadi, D.J.; *J. Vac. Sci. Technol. A* **1987,** *5,* 906.

26. Zhao, Y.F.; Yang, H.Q.; Gao, J.N.; Xue, Z.Q.; Pang, S.J.; *Phys. Rev. B* **1997,** 58 13824.

27. Takahashi, K.; Nara, C.; Yamagishi, T.; Onzawa, T.; *Appl. Surf. Sci.* **1999,** *151,* 299.

28. Mercer, J.L. Jr.; Chou, M.Y.; *Physical Review B*. **1993,** *48,* 5374.

29. van Duin, A.C.T.; Dasgupta, S.; Lorant, F.; Goddard W.A. III; *J. Phys. Chem. A*. **2001,** *105,* 9396.

30. Perdew, J.P.; Burke, K.; Ernzerhof, M.; *Phys. Rev. Lett.* **1996,** *77,* 3865.

31. Becker, R.S.; Swartzentruber, B.S.; Vickers, J.S.; *J. Vac. Sci. Technol.* **1988,** 6, 472.

32. Schultz, P.A.; Sandia National Labs., Albuquerque NM, SeqQuest Electronic Structure Code, http://dft.sandia.gov/Quest/

33. Hamann, D.R.; *Phys. Rev. B* **1989,** 40, 2980.

34. Redondo, A.; Goddard W.A. III; McGill, T.C.; *Phys. Rev. B* **1977,** 15, 5038.

35. Hamann, D.R.; unpublished.

Chapter 5: Structure of the Methylated Silicon (111) Surface Prepared through Hydrogenation-Chlorination-Alkylation*

ABSTRACT. Recently we reported STM images of the methylated Si(111) surface, prepared through chlorination-alkylation of the Si(111)-H surface, taken at 4.7 K, indicating that the torsion angle of the methyl group with respect to the subsurface silicon layer is $\phi=23 \pm 3^{o}$. Repulsions between H atoms in adjacent methyl groups are minimum at 30º, while repulsions between H atoms and second layer Si atoms are minimum at 60º. The experimental result of 23º is surprising because it suggests a *tendency* of the methyl group towards the eclipsed configuration (0º) rather than staggered (60º). In contrast, extensive fully periodic quantum mechanical Density Functional Theory studies of this surface give an equilibrium torsion angle of 37.5º, indicating a *tendency* towards the staggered configuration. This discrepancy can be resolved by showing that the CH_3 on the step edges and etch pits interacts repulsively with the CH_3 on the surface unless a stacking fault is introduced between the 1st and 2nd silicon layers of the Si(111)-CH_3 surface terraces. We propose that this could occur during the chlorination-alkylation of the Si(111)-H surface. This stacking fault model predicted $\phi=22.5^{o}$, measured with respect to the *bulk* (corresponding to $\phi=37.5^{o}$ with respect to the second layer Si atoms).

This model can be tested by measuring the orientation of the CH_3 within the etch pits, which will have $\phi=37.5^{o}$, or by making a surface without etch pits, which will have $\phi=37.5^{o}$.

Functionalized Si(111) surfaces have a variety of applications in molecular electronics,[1] sensing,[2-4] photoelectrochemistry,[5] chemical and electrical surface passivation,[6-7] porous Si photoluminescence,[8] and control of photopatterning. [9] Recently we demonstrated experimentally that a two-step chlorination-alkylation procedure can achieve 100% coverage of CH_3 on Si(111), leading to complete surface passivation. [10] Characterization with low-energy electron diffraction (LEED) and scanning tunneling microscopy (STM) at 77 K showed a well-ordered 1x1 structure for Si(111)-CH_3. [10] The STM images at 4 K revealed that the C-H bonds in the methyl groups are rotated 7° *away* from the center of the adjacent methyl groups *toward* an underlying Si atom, giving an H-C-Si-Si torsion angle $\phi = 23 \pm 3°$ (Figure 1). Since the van der Waals repulsions between adjacent methyl groups are lowest for $\phi = 30°$, the experimental result suggests a tendency of the methyl groups towards the *eclipsed* configuration with respect to the surface. Steric interactions between the CH bonds of methyl and the SiSi bonds of the top two layers of the surface are expected to prefer the staggered geometry ($\phi = 60°$). Consequently, we carried out Quantum Mechanics (QM) calculations using the B3LYP and PBE flavors of Density Functional Theory (DFT) and extensive basis sets (supporting information, section 1) on a series of small molecules, including $H_3C\text{-}CH_3$, $H_3Si\text{-}SiH_3$, $H_3C\text{-}SiH_3$, $H_3C\text{-}C\text{-}(CH_3)_3$, $H_3Si\text{-}Si\text{-}(SiH_3)_3$, and $H_3C\text{-}Si\text{-}(SiH_3)_3$, finding that all prefer strongly the staggered configuration ($\phi = 60°$). Similar level periodic boundary condition DFT calculations using PBE and both plane wave and Gaussian basis sets on Si(111)-CH_3 surface slabs give $\phi = 37.5°$, distorting toward the *staggered* configuration and contradicting the experimental result from the 4 K STM data. Interestingly, the deviation with respect to $\phi = 30°$ is of comparable *magnitude* for theory and experiment,

but in the *opposite* direction. The purpose of this work is to demonstrate that the emergence of a stacking fault during the chlorination-alkylation process is energetically favorable and would resolve this discrepancy.

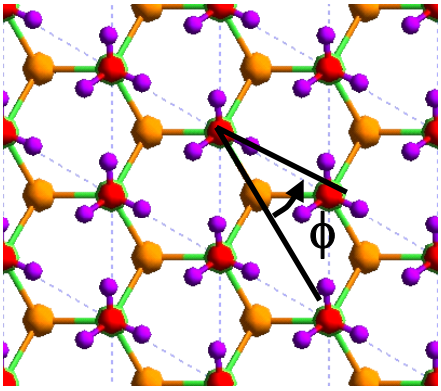

Figure 1. Si(111)-CH_3 surface showing the H-C-Si-Si torsion angle, ϕ, and the hexagonal 1x1 unit cell. ϕ = 60º is staggered, ϕ = 0º is eclipsed, and ϕ = 30º minimizes the H---H van der Waals repulsions. The color code is: purple = hydrogen, red = carbon, green = first-layer silicon (directly below carbon), and orange = second-layer silicon.

Extracting ϕ from the STM data requires: (1) The orientation of the unit cell relative to the overlayer and (2) the registry of observed spots in the STM image with the atop sites on the Si surface. We believe that the registration of the spots relative to the Si atop sites is robust because the Si-C bond length has been determined independently from photoelectron diffraction measurements to be 1.85 Å. [11] The orientation of the lattice planes relative to the imaged STM spots was established by two independent methods. [10] We also verified through DFT calculations that the large electric field present in the STM has a negligible effect on the CH_3 orientation.

Since a single stacking fault between the 1st and 2nd Si layers would have the effect of rotating the apparent torsion of the CH_3 by 60° with respect to the bulk, we carried out DFT calculations with stacking faults on Si(111)-H, Si(111)-Cl, and Si(111)-CH_3. Indeed, with a stacking fault we found that the *apparent* torsion angle with respect to the bulk would change from 37° to 23° (there was no effect on the H-C-Si-Si torsion angle). However, the DFT results showed that a stacking fault is *not* favored for any of these perfect surfaces (Table 1, 1st column). Since no other geometrical explanation can reconcile the experimental and theoretical results we continued to consider how a stacking fault could be stabilized.

Since ~16% of the area on our Si(111)-CH_3 surface was covered by etch pits, we considered whether chemisorbed species on the step edges might stabilize the stacking fault on the terrace. To test this possibility, periodic DFT calculations were performed on Si(111)-H, Si(111)-Cl, and Si(111)-CH_3 models containing an infinite $<11\bar{2}>$ or $<\bar{1}\bar{1}2>$ step edge (Figure 2). [12] The difference in strain between these two step edges was calculated per edge site. The strain energy difference was found to be small for Si(111)-H but not for Si(111)-Cl and Si(111)-CH_3, which exhibit a strong preference for $<\bar{1}\bar{1}2>$ (Table 1, 2nd column).

To understand these differences, consider first Si(111)-H. Here the Si-Si bond lengths and Si-Si-Si bond angles are close to the bulk value for $<11\bar{2}>$ (supporting information, section 4), and all H---H nearest neighbors distances are > 2.97 Å, causing no significant unfavorable interactions (compare to 2.51 Å for polyethylene). In contrast, for Si(111)-Cl some of the nearest neighbor Cl---Cl distances are ~ 3.23 Å for $<11\bar{2}>$, but > 3.84 Å for $<\bar{1}\bar{1}2>$. Since the van der Waals radius of Cl is ~3.95 Å,[13] substantial steric

repulsions are expected for $<1\bar{1}2>$. Indeed, the calculations indicate that Si-Cl bond on $<\bar{1}\bar{1}2>$ is 0.58 eV stronger than on $<1\bar{1}2>$ (Table 1, 2nd column). The contribution of the *reconstructed* $<\bar{1}\bar{1}2>$ step edge (Figure 2b) to the energy of the bare Si(111) surface is lower than that of the *unreconstructed* $<\bar{1}\bar{1}2>$ edge by 0.81 eV/site and lower than that of $<1\bar{1}2>$ (Figure 2a) by 0.56 eV/site (supporting information, section 4). For Si(111)-CH_3, the nearest neighbor H---H distance on $<1\bar{1}2>$ is 2.07 Å (0.44 Å shorter than in polyethylene!), whereas the shortest distance on $<\bar{1}\bar{1}2>$ is 2.29 Å, resulting in a Si-CH_3 bond with significantly lower strain energy on $<\bar{1}\bar{1}2>$ than on $<1\bar{1}2>$ (by 0.67 eV).

The samples in the 4 K STM experiments used the Si(111)-H surface as an intermediate step in preparing the methylated surface. The step edges around the etch pits were verified to be in the $<1\bar{1}2>$ family, and their orientation did not change during the subsequent chlorination and alkylation steps (using PCl_5 and CH_3MgCl in THF).[10] Hence, relief of the strain for Si(111)-Cl and Si(111)-CH_3 through the formation of the more favorable step edge termination shown in Figure 2b requires the introduction of a stacking fault between the 1st and 2nd Si layers *on the terraces*. Note that when the step edge orientation is $<1\bar{1}2>$, the *normal* crystal has the structure in Figure 2a, while the *faulted* crystal has the structure in Figure 2b. Taking the difference in strain energy between the two types of step edges as the driving force for the formation of the stacking fault and dividing this by the stacking fault energy cost yields the number of equivalent faulted sites (Table 1, 3rd column) that this strain energy is able to induce (neglecting the energy of the rows of Si dimers at the borders between faulted and unfaulted regions[12]). Thus, allowing one edge site to transform from the structure of Figure 2a to that of Figure

2b would compensate for ~17 *faulted* sites on Si(111)-Cl and for ~19 *faulted* sites on Si(111)-CH_3. This ratio is greater than the ratio of terrace to edge sites on the experimental Si(111)-CH_3 surface (~13), indicating that a full stacking fault on the terraces is energetically possible.

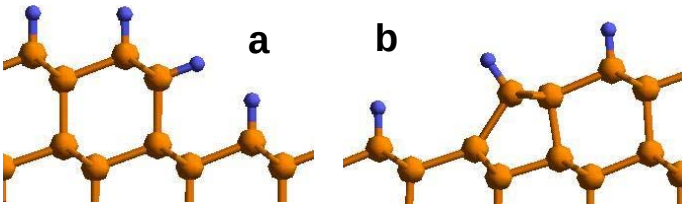

Figure 2. $<1\bar{1}2>$ (a) and $<\bar{1}\bar{1}2>$ (b) step edges for the Si(111)-H surface. The $<\bar{1}\bar{1}2>$ structure (b) has reconstructed to have its substituents perpendicular to the edge surface and to lower its energy. [12]

The theory-derived conclusion that there is a stacking fault in the Si(111)-CH_3 surface is consistent with the STM experiments of Ithckawitz et al,[12] who observed stacking faults on terrace regions adjacent to $<1\bar{1}2>$ steps on Si(111)-Cl. They did *not* observe full stacking faults, but with their method (exposure of a DAS 7x7 Si(111) surface to Cl_2 gas at 673 – 773 K), the (7x7) → (1x1) transformation occurs predominantly along step edges. [12] In some cases they may have also examined the surface structure before it transformed fully into a 1x1 Si(111)-Cl. Since the CH_3MgCl Grignard reagent in our experiments is appreciably larger than Cl_2, it is plausible that steric interactions would play an even more significant role in the formation of a stacking fault in our Si(111)-CH_3 samples.

The Si(111)-CH_3 surfaces were prepared at THF reflux temperature (~65°), at which Si(111) surface reconstructions do *not* occur spontaneously, but we believe they could be induced to accommodate the sterically hindered transition states expected for the Grignard conversion of the surface Cl to CH_3. This process is very exothermic (DFT leads to $\Delta G^{298°}$ = -41.0 kcal/mol after including solvation using the Poisson-Boltzmann continuum model), so that the local temperature may increase the mobility of the atoms on the surface.

The emergence of a stacking fault during the chlorination-alkylation of Si(111)-H to produce Si(111)-CH_3 would resolve the discrepancy between theory and experiment. Thus the experimental torsion angle of 23° with respect to the bulk crystal would correspond to 37° with respect to the second Si layer on the terraces. On the other hand, the calculations find that the CH_3 groups in the etch pits have the normal angle of 37.5° with respect to the bulk. Measuring this would provide an excellent validation of the new model, but current low temperature STM experiments can only observe the top layer. [10]

Despite the consistency of our stacking fault model in explaining the apparent discrepancy between theory and experiment, some questions remain. The theory suggests that there would *not* be a stacking fault if there were no etch pits. Currently the best experimental surfaces exhibit etch pits and step edges, and it is not clear whether unfaulted Si(111)-CH_3 surfaces can be produced through chlorination-alkylation methods or by different synthetic routes. Also, we have not yet predicted the reaction barriers for forming stacking faults on the terraces. Hence, our estimate of the ratio of faulted sites to edge sites is an upper bound. We have also not examined whether the methylation

process starts at the edges at already faulted sites and works in towards the terraces or occurs randomly on the terraces and edges simultaneously. Experimental studies using LEED to examine the orientation of the etch pit CH_3 and STM studies for asymmetric substituents on Si(111) (such as CH_2F) might test our predictions. In addition, theoretical study of the reaction barriers for the chlorination-methylation would provide more insight into the formation mechanism, structure, and energetics of the Si(111)-CH_3 surface.

Table 1. Stacking fault energy cost per surface site of perfect surfaces, differential strain energy per edge site ($<11\bar{2}>$ - $<\bar{1}\bar{1}2>$), and equivalent faulted sites per edge site differential strain.[a]

Surface	**$\Delta E_{stacking\ fault}$[b] eV/1x1 cell**	**δE_{strain} eV/edge site**	**Equivalent faulted/edge sites[a]**
Si(111)	0.048	N/A	N/A
Si(111)-H	0.031	0.05	1
Si(111)-Cl	0.033	0.58	17
Si(111)-CH_3	0.034	0.67	19

[a] Obtained by dividing numbers in the 2nd column by those in the 1st column and meaningful only if δE_{strain} >0 (i.e. favorable stacking fault).
[b]The calculated bulk Si value of $\Delta E_{stacking\ fault}$ is 0.015 eV/1x1 cell.

Summarizing, we use QM to show that in the presence of etch pits the introduction of a CH_3 on each surface Si can induce the formation of a stacking fault between the 1st and 2nd Si layers. This would explain the unexpected experimental CH_3 torsion angle of 23°, reconciling it with the theoretical value of 37.5°. The experimental value of 23° measured with respect to the bulk crystal would correspond to 37° with respect to the 2nd Si layer.

Acknowledgement: Santiago Solares and William Goddard received support from the Microelectronics Advanced Research Corporation (MARCO) and its Focus Center on Function Engineered NanoArchitectonics (FENA), and from NSF grant NSF-CTS-0132002. Support for Lauren Webb and Nathan Lewis was provided by NSF grant NSF-CHE-0213589. Support for Hongbin Yu and James Heath by the Department of Energy and NSF grant NSF-CCF-05204490.

SUPPORTING INFORMATION

1. Computational Methods

Periodic DFT calculations were conducted using two software packages:

(1) SeqQuest (Sandia National Labs, Albuquerque, NM),[14] a general-purpose electronic structure code for periodic and non-periodic systems, with norm-conserving pseudopotentials and optimized contracted *Gaussian* basis sets. SeqQuest calculations were performed using the PBE[15] flavor of DFT with a valence double-zeta basis set plus polarization functions (denoted vDZp) with pseudopotential for silicon and carbon, while for hydrogen both double-zeta and triple-zeta basis sets (6311G basis set) plus polarization functions (denoted vDZp and vTZp, respectively) with and without pseudopotential were used.

(2) Castep21 (Accelrys, San Diego CA), a general-purpose electronic code for 3D periodic structures, which uses ultra-soft pseudopotentials and *plane wave* basis sets. Here we also used the PBE[15] approximation with a plane wave kinetic energy cutoff of 380 eV and with pseudopotentials for all atoms.

For the PBC calculations 8 k-points were used for each horizontal unit cell vector of the 1x1 Si(111) unit cell. The number of k-points for all other structures was adjusted inversely proportional to unit cell dimensions.

All non-periodic DFT calculations were performed using Jaguar 5.5 software (Schrödinger, Portland, OR). For the molecules described in section 1.3 the B3LYP flavor of DFT was used with both Gaussian triple-zeta (6311G**++) and Dunning triple-zeta (cc-PVTZ++) basis sets. The change in free energy for the Grignard reaction [Si(111)-Cl + CH_3-Mg-Cl → Si(111)-CH_3 + $MgCl_2$] in THF solvent (ΔG^{298° = -41.0 kcal/mol) was also estimated using non-periodic DFT at the B3LYP level of theory, but with 631G** basis sets and using the Poisson-Boltzmann continuum solvation model. For this calculation, the Si(111) sites were modeled as Si_4H_9 clusters to which Cl or CH_3 were bonded.

For the MD simulations (see section 1.4.1), Cerius2 software (Accelrys, San Diego, CA) was used with previously reported force field parameters for silicon[16] and hydrocarbons,[13] with the H-C-Si-Si torsional force field parameter adjusted to 2.945 kcal/mol to match the DFT (SeqQuest) calculations on the Si(111)-CH_3 model described in 1.1.1 using vDZp basis sets and pseudopotentials for all atoms. Atomic charges for the MD simulations were computed using the Charge Equilibration method. [17]

All surface unit cell dimensions were based on the calculated PBE equilibrium value of the Si crystal lattice, equal to 5.431 Å.

1.1 Periodic DFT Geometry Optimization of 1x1 Unit Cells

To calculate the optimum torsion angle for various systems resembling our experimental surfaces, the geometry was optimized through minimizing the total energy for the following cases:

1.1.1 Case 1 - Si(111)-CH_3 surface using Gaussian basis functions (SeqQuest)

The Si(111)-CH_3 1x1 unit cell was modeled using a 2D slab with eight bulk silicon layers, terminated by hydrogen on the bottom surface (Si-H bond perpendicular to the surface). The unit cell thus has 13 atoms. Considering the surface to be perpendicular to the z-axis, the lateral unit cell parameters were kept fixed at the crystal value of 3.86 Å. The bottom surface hydrogen atom was kept fixed during the calculations while all the silicon atoms and the methyl group were allowed to relax. All calculations were performed using the vDZp basis set and pseudopotentials for silicon and carbon. For hydrogen, various cases were considered with vDZp and vTZp basis sets (6311G), with and without pseudopotential.

1.1.2 Case 2 - Si(111)-CH_3 surface using plane wave basis functions (Castep21)

The same Si(111)-CH_3 1x1 unit cell was modeled as in case 1, but using a 3D structure, consisting of a 2D surface slab with 20 Å of vacuum above the surface.

1.1.3 Case 3 – Si(111), Si(111)-H, Si(111)-Cl, and Si(111)-CH_3 surfaces with a stacking fault using Gaussian functions (SeqQuest)

A Si(111) unit cell similar to that of case 1 (without functionalization or functionalized with H, Cl and CH_3) was modeled, but a stacking fault was introduced between the 1st and 2nd layers. We also calculated the bulk stacking fault energy using a 12-layer 3D periodic bulk model of the silicon *crystal*.

1.2 Periodic DFT calculation of Strain Energy at the Step Edges

To determine whether binding of chemisorbed species to systems containing etch pits might affect the relative energies for stacking faults, periodic Si(111)-H, Si(111)-Cl and Si(111)-CH_3 unit cells were constructed containing 10 bulk Si layers and a partial double layer of either the $<1\bar{1}2>$ (observed in our experiments) or $<\bar{1}\bar{1}2>$ step edge termination (see Figure S-1). Note that the $<\bar{1}\bar{1}2>$ step reconstructs to have the substituents perpendicular to the edge surface and to lower its energy (see section 4). [12,18] For both step edges, the bond energy of each substituent (H, Cl or CH_3) to the edge site was then computed by removing one of the substituents and substracting this bond energy

from the bond energy on a perfect surface to obtain the strain energy at the edge site. Calculations were also performed on non-functionalized Si structures (see Figure S-2) to obtain the contribution to the surface energy due to the presence of a step edge in a bare 1x1 Si(111) surface. All structures were 1 cell deep, except the *unreconstructed* $<\bar{1}\bar{1}2>$ structure, which was 4 unit cells deep, to allow the formation of dimers between adjacent edge atoms containing two dangling bonds each. The structure of the Si(111)-CH_3 did not change when the cell depth was increased up to 4 unit cells deep.

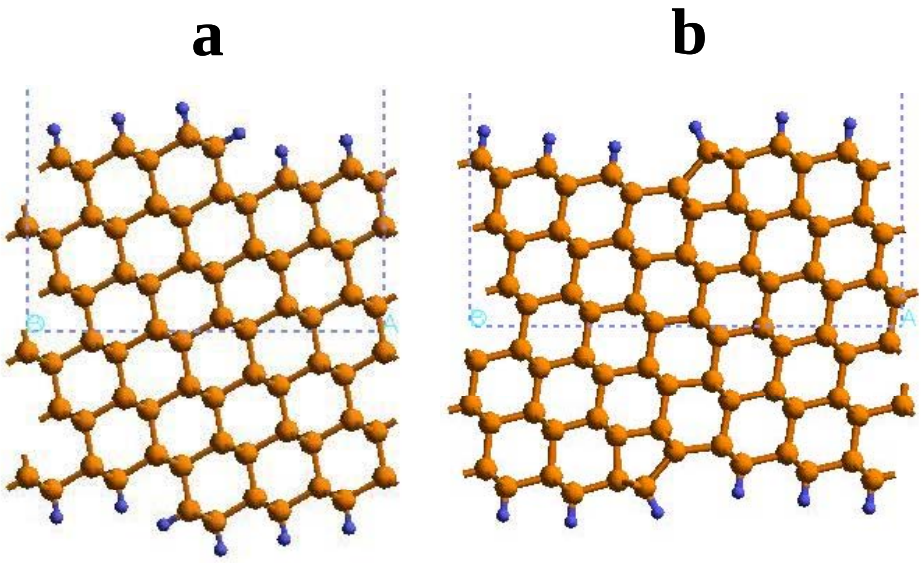

Figure S-1. Side view of the Si(111)-H periodic unit cells used for the calculation of the strain energy difference between the $<11\bar{2}>$ (a) and $<\bar{1}\bar{1}2>$ (b) step edge terminations. The $<11\bar{2}>$ unit cell (a) was obtained by cutting the Si crystal along the $<664>$ plane, and the $<\bar{1}\bar{1}2>$ unit cell (b) was obtained by cutting the crystal along the $<668>$ plane. Similar models were constructed for Si(111), Si(111)-Cl and Si(111)-CH_3.

1.3 Non-periodic DFT Geometry Optimization

To determine the trends in the torsion angles of small systems containing tetrahedral silicon and carbon atoms, the geometry for several molecules was optimized using the triple-zeta 6311G**++ and cc-PVTZ++ basis sets at the B3LYP theory level. This process was performed for fixed torsion angles of 0° (eclipsed) and 60° (staggered) for the CH_3 or SiH_3 groups, as appropriate (see Table S-1), and without any constraints (to calculate the equilibrium torsion angle). The torsional energy barriers were calculated from the difference in total energy between the eclipsed and staggered configurations for the following molecules:

i. *Pure hydrocarbons:* $H_3C\text{-}CH_3$ and $H_3C\text{-}C\text{-}(CH_3)_3$
ii. *Pure silanes:* $H_3Si\text{-}SiH_3$ and $H_3Si\text{-}Si\text{-}(SiH_3)_3$
iii. *Molecules containing silicon, carbon and hydrogen:* $H_3C\text{-}SiH_3$ and $H_3C\text{-}Si\text{-}(SiH_3)_3$ (this molecule resembles the structure of the $Si(111)\text{-}CH_3$ surface most closely)

1.4 Molecular Dynamics Calculations

1.4.1 Role of Methyl-Methyl Interactions

To evaluate the relative importance of the methyl-methyl interactions in determining the H-C-Si-Si torsion angle, the slab geometry was optimized for the periodic $Si(111)\text{-}CH_3$ model described in 1.1.1, but with the C-Si bond length artificially extended to 1 nm (equilibrium bond length is 0.18 nm) and with the H-C-Si-Si torsional barrier set to 0

kcal/mol. This determined the optimum torsion angle preferred by the interactions between the methyl groups, while eschewing any surface effects due to the silicon atoms (calculated to be 30°). Note that this calculation cannot be performed with QM because the artificial lengthening of the Si-C bond causes the remaining CH_3 groups to behave as CH_3 radicals, which are planar and reactive.

2. Torsional Barriers of Small Organic Molecules

Table S-1: Torsional energy barrier for various small molecules at the DFT B3LYP level of QM using the CC-PVTZ++ (and 6311G**++) basis sets. The most stable configuration is staggered for all molecules.

Molecule	**Torsion angle of interest**	**DFT Torsional barrier, kcal/mol**
Pure hydrocarbons		
$H_3C\text{-}CH_3$	H-C-C-H	2.61 (2.70)
$H_3C\text{-}C\text{-}(CH_3)_3$	H-C-C-C	3.62 (3.63)
Pure silanes		
$H_3Si\text{-}SiH_3$	H-Si-Si-H	0.96 (0.93)
$H_3Si\text{-}Si\text{-}(SiH_3)_3$	H-Si-Si-Si	0.76 (0.80)
Molecules containing Si, C and H		
$H_3C\text{-}SiH_3$	H-C-Si-H	1.45 (1.41)
$H_3C\text{-}Si\text{-}(SiH_3)_3$	H-C-Si-Si	1.48 (1.47)

Table S-1 contains the calculated torsional barriers for small organic molecules containing carbon, silicon, and hydrogen at the B3LYP level of theory [calculations at the

HF and Becke 3 (GGA II / PW91) levels were also performed and gave similar results (not shown)]. The lowest energy configuration is *staggered* in all cases, corresponding to a torsion angle of 60°. The torsion angle of interest is indicated in the first column of the table.

3. Periodic DFT Equilibrium Geometry of Si(111)-CH_3

The calculated H-C-Si-Si torsion angle for periodic DFT calculations (using both Gaussian and plane wave basis sets) is shown in Table S-2. We believe that the most accurate results are for case 1 with the vTZp basis and without pseudopotential (in boldface), leading to a torsion angle of 37.5º. This shows that the interactions between H atoms of adjacent methyls dominate (preferring 30º), but are distorted by 7.5º toward the *staggered* configuration (60º). Comparison of case 3 to case 1 shows that introduction of a stacking fault between the 1st and 2nd Si layers does *not* change the torsion angle with respect to the *second* Si layer. The Si-C bond and the H-C-H angle are also listed in Table S-2. All values are close to those calculated for the H_3C-Si-$(SiH_3)_3$ cluster (1.91 Å and 108.0º, respectively).

4. Strain and Geometry of $<1\bar{1}2>$ and $<\bar{1}\bar{1}2>$ Step Edges

Table S-3 contains the calculated strain energy for both types of step edges and the difference between them for each of the substituents (H, Cl, or CH_3). These results show that the strain energy difference is small for Si(111)-H but not for Si(111)-Cl or Si(111)-

CH_3, both of which exhibit a strong preference for the reconstructed $<\bar{1}\bar{1}2>$ structure. Table S-4 provides the surface energy contribution of the step edges in a 1x1 Si(111) surface containing a single infinitely long step. This energy includes one dangling bond on the $<11\bar{2}>$ edge, one dangling bond on the *unreconstructed* $<\bar{1}\bar{1}2>$ edge (the second dangling bond is paired up with a dangling bond on the adjacent edge site), and no dangling bonds on the *reconstructed* $<\bar{1}\bar{1}2>$ edge (the reconstruction eliminates the dangling bonds on the edge as shown in Figure S-2). Although the *reconstructed* $<\bar{1}\bar{1}2>$ structure has greater strain in the bonds and angles, it has the lowest energy of all due to the elimination of the edge dangling bond. The second lowest energy corresponds to the $<11\bar{2}>$ edge, and the highest energy to the *unreconstructed* $<\bar{1}\bar{1}2>$ structure.

Table S-2: Si(111)-CH_3 equilibrium surface geometry from periodic DFT calculations for various basis sets, hydrogen pseudopotentials, and silicon crystal stackings. Standard basis sets (Gaussian or plane waves, as appropriate) and pseudopotentials were used for silicon and carbon in all cases. We consider the triple zeta calculation with no H pseudopotential (in boldface) as the most accurate method.

Basis set used for hydrogen atoms	**H-C-Si-Si torsion angle, degrees**	**Si-C bond length, Angstroms**	**H-C-H bond angle, degrees**
vDZp with H pseudopotential (case 1)	36.2	1.94	107.6
vTZp with H pseudopotential (case 1)	36.2	1.93	106.4
vDZp with no H pseudopotential (case 1)	38.2	1.94	107.8
vTZp with no H pseudopotential (case 1)	**37.5**	**1.93**	**107.7**
Plane waves with pseudopotential (case 2)	38.7	1.89	108.0
VDZp with H pseudopotential and a stacking fault between the 1^{st} and 2^{nd} Si layers (case 3)	36.7	1.93	107.9

Table S-3: Calculated strain energy (eV per site) at the step edges.

	$<11\bar{2}>$	$<\bar{1}\bar{1}2>$	**Difference** $<11\bar{2}> - <\bar{1}\bar{1}2>$
Si(111)-H	-0.01	-0.06	0.05
Si(111)-Cl	0.57	-0.01	0.58
Si(111)-CH_3	0.60	-0.07	0.67

Table S-4: Calculated surface energy contribution due to the presence of a step edge in the bare 1x1 Si(111) surface. The different structures are illustrated in Figure S-2.

Step edge	**Edge dangling bonds**	**Energy, eV/site**
$<11\bar{2}>$	1	1.35
$<\bar{1}\bar{1}2>$ unreconstructed[a]	1	1.60
$<\bar{1}\bar{1}2>$ reconstructed[b]	0	0.79

[a]In this structure, the edge atoms in adjacent positions form dimers to avoid having two dangling bonds each.

[b]The reconstruction eliminates the edge dangling bonds (see Figure S-2).

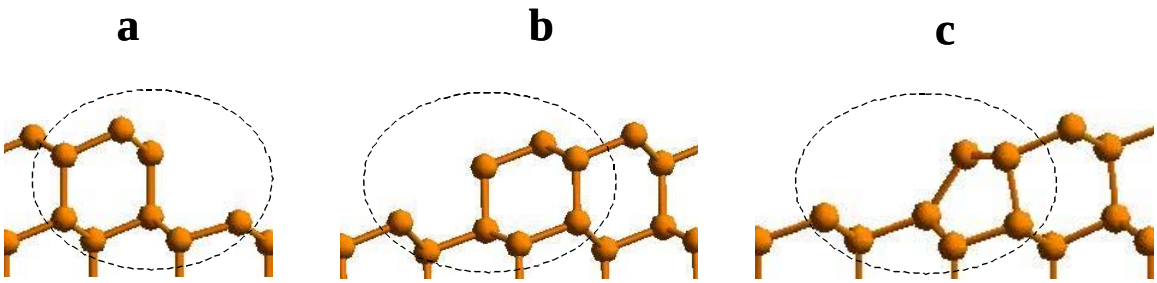

Figure S-2. Structures of the Si(111) surface step edges: (a) $<11\bar{2}>$ edge, (b) *unreconstructed* $<\bar{1}\bar{1}2>$ edge, and (c) *reconstructed* $<\bar{1}\bar{1}2>$ edge.

The most relevant geometry parameters calculated for the $<1\bar{1}2>$ and for the *reconstructed* $<\bar{1}\bar{1}2>$ step edge structures described in section 1. 2 are illustrated in Figure S-3 and are summarized in Tables S-5 and S-6 [we did not calculate these parameters for the *unreconstructed* $<\bar{1}\bar{1}2>$ structure since, according to Table S-4, it has the highest energy and since its substituents are not perpendicular to the edge surface, which leads to additional strain due to nearest neighbor steric interactions]. In general, the $<1\bar{1}2>$ edge has smaller nearest neighbor distances (leading to greater steric repulsions) and has bonds and angles that are closer to those in the bulk crystal (leading to lower bond and angle strain).

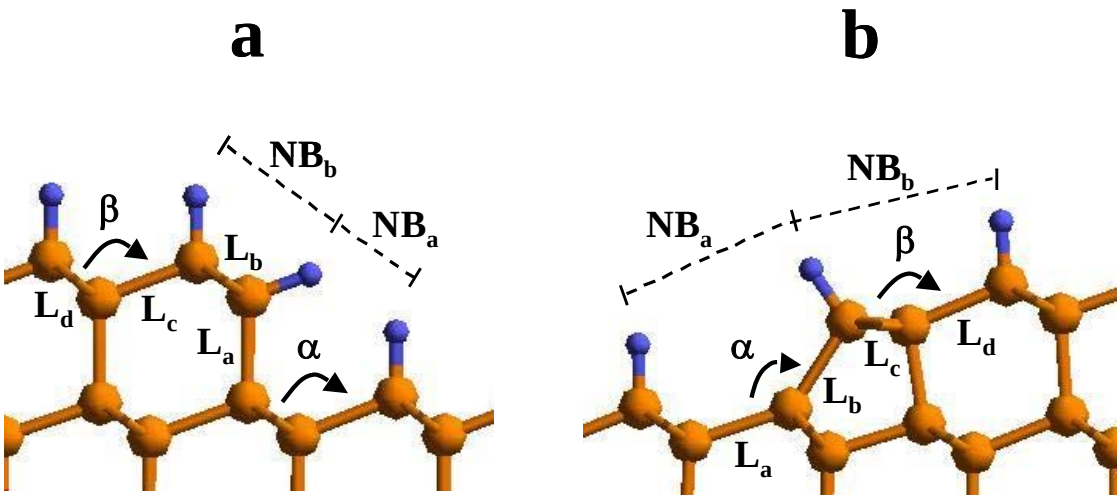

Figure S-3. Relevant geometry parameters of the step edge terminations for Si(111), Si(111)-H, Si(111)-Cl, and Si(111)-CH_3 surfaces. (a) $<1\bar{1}2>$ and (b) reconstructed $<\bar{1}\bar{1}2>$. L_a, L_b, L_c, and L_d represent Si-Si bond lengths, while α and β represent Si-Si-Si bond angles. Their values are summarized in Table S-5. The nonbond distances relevant for understanding the relative strain energies are denoted NB_a and NB_b, and their values are summarized in Table S-6.

Table S-5: Calculated geometry parameters for the $<11\bar{2}>$ and $<\bar{1}\bar{1}2>$ step edge terminations for Si(111), Si(111)-H, Si(111)-Cl, and Si(111)-CH_3 surfaces, as defined in Figure S-3. All distances and angles are given in Å and degrees, respectively (for comparison, the experimental bulk Si-Si bond length and bond angle are 2.36 Å and 109.41°, respectively)

Surface	**L_a**	**L_b**	**L_c**	**L_d**	**α**	**β**
$<11\bar{2}>$						
Si(111)	2.37	2.33	2.37	2.34	109.4	110.8
Si(111)-H	2.37	2.36	2.36	2.35	108.7	110.2
Si(111)-Cl	2.42	2.35	2.37	2.34	110.8	108.8
Si(111)-CH_3	2.41	2.35	2.32	2.35	108.7	106.9
$<\bar{1}\bar{1}2>$						
Si(111)	2.42	2.47	2.38	2.39	134.9	122.3
Si(111)-H	2.42	2.48	2.39	2.39	136.4	121.3
Si(111)-Cl	2.41	2.47	2.39	2.39	137.5	122.3
Si(111)-CH_3	2.43	2.47	2.39	2.41	136.0	121.4

Table S-6: Calculated nearest neighbor distances (Å) for substituents on $<11\bar{2}>$ and $<\bar{1}\bar{1}2>$ step edges for Si(111)-H, Si(111)-Cl, and Si(111)-CH_3 surfaces. In each case, the distance is provided with respect to a neighbor on the step edge, on the pit (NB_a), or on the terrace (NB_b) [see Figure S-3 for notation]. For CH_3, the distances correspond to the smallest H-H distance between adjacent groups.

	$<11\bar{2}>$			$<\bar{1}\bar{1}2>$		
Surface	**Edge-edge**	**NB_a**	**NB_b**	**Edge-edge**	**NB_a**	**NB_b**
Si(111)-H	3.84	2.97	3.61	3.84	4.79	4.91
Si(111)-Cl	3.84	3.23	4.10	3.84	4.29	5.29
Si(111)-CH_3	2.43	2.07	2.52	2.29	2.48	3.89

An important observation in the Si(111)-Cl surface containing the $<11\bar{2}>$ step is the presence of overstretched Si-Si bonds (Figure S-4) caused by the Cl---Cl nearest neighbor repulsions. This is a manifestation of the high surface strain present at the edge and suggests that surface reconstruction processes are likely to occur. We did not observe this for Si(111)-CH_3, although the DFT calculations indicate that this surface has greater edge strain than Si(111)-Cl.

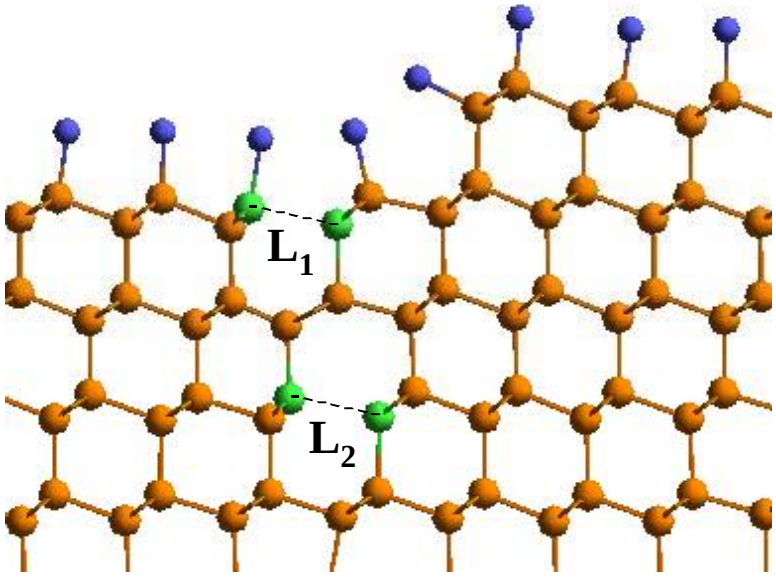

Figure S-4. Illustration of overstretched Si-Si bonds in the chlorinated $<11\bar{2}>$ step edge. The blue atoms are Cl, the orange atoms are bulk Si, and the green atoms are Si with overstretched bonds. In the optimum structure L_1 = 2.82 Å and L_2 = 2.87 Å (compare to L_{bulk} = 2.36 Å)

REFERENCES:

1. Yates, J.T. *Science* **1998,** *279,* 335-336.

2. Pike, A.R.; Lie, L.H.; Eagling, R.A.; Ryder, L.C.; Patole, S.N.; Connolly, B.A.; Horrocks, B.R.; Houlton, A. *Angew. Chem. Int. Ed.* **2002,** *41*, 617-617.

3. Strother, T.; Cai, W.; Zhao, X.S.; Hamers, R.J.; Smith, L.M. *J. Am. Chem. Soc.* **2000,** *122,* 1205-1209.

4. Lin, Z.; Strother, T.; Cai, W.; Cao, X.P.; Smith, L.M.; Hamers, R.J. *Langmuir* **2002,** *18,* 788-796

5. Bansal, A.; Lewis, N.S. *J. Phys. Chem. B* ***1998,*** *102,* 4058-4060.

6. Bansal, A.; Li, X.; Yi, S.I.; Weinberg, W.H.; Lewis, N.S.; *H. Phys. Chem. B* **2001,** *105,* 10266-10277.

7. Webb, L.J.; Lewis, N.S. *J. Phys. Chem. B* **2003,** *107,* 5404-5412.

8. Song, J.H.; Sailor, M.J. *Comments Inorg. Chem.* **1999,** *21,* 69-84.

9. Buriak, J.M. *Chem. Rev.* **2002,** *102,* 1271-1308.

10. Yu, H.; Webb, L.J.; Ries, R.S.; Solares, S.D.; Goddard, W.A. III; Heath, J.R.; Lewis, N.S. *J. Phys. Chem. B* **2005,** *109,* 671-674.

11. Terry, J.; Linford, M.R.; Wigren, C.; Cao, R.Y.; Pianetta, P.; Chidsey, C.E.D. *Appl. Phys. Lett.* **1997,** *71,* 1056-1058.

12. Itchkawitz, B.S.; McEllistrem, M.T.; Boland, J. *Phys. Rev. Lett.* **1997,** *78,* 98.

13. Mayo, S.; Olafson, B.; Goddard, W. A. III. *J. Phys. Chem.* **1990**, 94, 8897.

14. Schultz, P.A. Sandia National Labs., Albuquerque NM, SeqQuest Electronic Structure Code, http://dft.sandia.gov/Quest/

15. Perdew, J.P.; Burke, K.; Ernzerhof, M. *Phys. Rev. Lett.* **1996,** *77,* 3865.

16. Shapiro, I.R.; Solares, S.D.; Esplandiu, M.J.; Wade, L.A.; Goddard, W.A.; Collier, C.P. *J. Phys. Chem. B* **2004,** *108,* 13613.

17. Rappé, A.K. and Goddard, W.A. III. *J. Phys. Chem.* **1991,** *95*, 3358.

18. Redondo, A.; Goddard, W.A. III.; McGill, T.C. *Phys. Rev. B* **1981,** *24,* 6135.

Chapter 6: Quantum Mechanics Calculations of the Thermodynamically Controlled Coverage and Structure of Alkyl Monolayers on Silicon (111) Surfaces*

ABSTRACT. The heat of formation, ΔE, for silicon (111) surfaces terminated with increasing densities of the alkyl groups CH_3- (methyl), C_2H_5- (ethyl), $(CH_3)_2CH$- (*iso*-propyl), $(CH_3)_3C$- (*tert*-butyl), $CH_3(CH_2)_5$- (hexyl), $CH_3(CH_2)_7$- (octyl), and C_6H_5- (phenyl) was calculated using quantum mechanics (QM) methods, with unalkylated sites being H-terminated. The free energy, ΔG, for the formation of both Si-C and Si-H bonds from Si-Cl model componds was also calculated using QM, with four separate Si-H formation mechanisms proposed, to give overall ΔG_S values for the formation of Si(111) alkylated surfaces through a two step chlorination/alkylation method. The data are in good agreement with measurements of the packing densities for alkylated surfaces formed through this technique, for Si-H free energies of formation, ΔG_H, corresponding to a reaction mechanism including the elimination of 2 H atoms, and the formation of a C=C double bond in either unreacted alkyl Grignard groups or tetrahydrofuran solvent.

1. Introduction

Si(111) surfaces have been functionalized by a variety of methods, including reaction with unsaturated alkenes through a radical process catalyzed by a diacyl peroxide initiator,[1,2] use of UV[3-5] or white[6] light, thermal energy,[7,8] transition metal complexes,[9] Lewis acid catalysts,[10-12] electrochemical functionalization,[13,14] radical halogenation,[15] and transmetallation with alkyl Grignard and lithium reagents.[15-17] These surfaces have shown excellent chemical stability under a variety of conditions, and alkylation even at partial coverage of the surface Si sites greatly inhibits the oxidation of the silicon surface. In many cases the surfaces are only partially terminated with alkyls, with proposals that non-alkylated Si atoms are terminated by –OH[2] or –H groups.[18,19] In other cases, significant oxidation of the initially alkylated surface, with the oxide present either in separate phases[20] or as mixed alkyl and Si-O-C bonding,[1] has been proposed.

Other than methyl- and ethyl-terminated surfaces prepared by a two-step chlorination/alkylation process, which have been imaged by scanning tunneling microscopy,[21,22] no direct 2-dimensional structural information is available for such systems. The limiting packing density of long chain, saturated alkyls has been claimed to be 50% of a monolayer of Si atop sites.[2,5,7] In contrast, CH_3-terminated Si(111) surfaces exhibit a 1x1 structure in low energy electron diffraction (LEED)[18,23] and scanning tunneling microscopy (STM) experiments[21,22] and exhibit signals in soft-X ray spectroscopy (SXPS)[18] and infrared (IR) absorption[19,24] measurements which indicate that complete coverage of Si atop sites can be achieved. XPS data[19] and STM data[22] on ethyl-terminated Si(111) surfaces indicate that 80 ± 10% of a monolayer coverage can be

attained for surfaces functionalized with ethyl groups using the chlorination/ alkylation method.

The structures of alkylated Si(111) surfaces have been investigated theoretically, with previous computational studies focusing on long chain alkyl groups such as octyl or octadecyl groups.[25-28] In some cases, 50% coverage was assumed to be the highest packing available for such alkyl groups, and the minimum energy structure was calculated at this coverage level.[25] In other calculations, the energy per chain for octyl or octadecyl groups attached to the surface was calculated to be minimized at 40-60% alkylation of the unreconstructed Si(111) atop sites, and minimum energy structures were calculated at the coverage that produced the minimum energy per chain.[27] For these dynamics simulations with long chain alkyl monolayers, the Van der Waals interactions of the chain tails will dominate the packing interactions. The calculated coverage that minimizes the energy per chain would predict the experimentally-observed coverage only if the strain energy were the only consideration. However, the free energy change of the reaction must control the final surface coverage, and a sufficiently negative (or positive) free energy change per site reacted can cause the free energy minimum to be different from the strain energy minimum. For surfaces prepared by the chlorination/alkylation method, which has a large free energy change that favors the products relative to the reactants, higher coverages and structures with significant bond strain should be accessible thermodynamically, especially for functionalization reactions using very short chain alkyl groups, which should have less strain at higher packing densities.

Herein we report the results of quantum mechanical calculations to obtain the free energy of formation for packed alkyl groups on Si(111) at various surface coverages.

The energy values have been referenced to the energy of the reactants and products of the chlorination/alkylation reaction using alkyl Grignards. This thermodynamic approach allows for the determination of the packing densities and associated structures of alkyl monolayers formed by a reaction with a large driving force, such as reaction of the Cl-terminated Si surface with a Grignard reagent. The surfaces considered represented the bulk of packed surfaces, as repeat unit cells were employed to remove any edge effects for the calculations. Linear alkyl groups investigated were $-CH_3$, $-C_2H_5$, $-C_6H_{13}$, and $-C_8H_{17}$, in addition to the bulkier groups *iso*-propyl, *tert*-butyl, and phenyl (C_6H_5). Functionalization with all of these groups is experimentally accessible using the chlorination/alkylation approach to Si functionalization.[15-20] For all calculations (except for the ethylated surface with 66.7% coverage, which required a 3x3 unit cell), a 2x2 unit cell was used with alkyl surface coverages of 25%, 50%, 75%, and 100%.

2. Methods

The relaxed geometry of all surface structures was first calculated using Molecular Dynamics (MD) and then refined using Quantum Mechanics (QM). Molecular Dynamics simulations (geometry optimization, followed by 5 ps equilibration at 600 K and 15 ps at 300 K, followed by a second geometry optimization) were conducted using Cerius2 software (Accelrys, San Diego, CA), with force-field parameters previously reported for silicon[29,30] and hydrocarbons[31] (any missing parameters required for new combinations of atom types were also taken from the latter force field). Atomic charges for these simulations were obtained using the Charge Equilibration Method (QEQ).[32] The resulting

structures were then used as the initial geometry in QM calculations performed with SeqQuest software[33] within the GGA PBE[34] approximation of Density Functional Theory (DFT). Double-zeta plus polarization basis sets and pseudopotentials were used for all atoms (supporting information).

Surfaces were formed from stacks of bulk crystalline silicon, with the (111) face exposed three double-layers deep and with the bottom surface terminated with hydrogen atoms. This number of bulk silicon layers resting on a fixed hydrogen layer has been shown to be an optimal compromise between accuracy and computation cost through extensive QM geometry optimization calculations on reconstructed Si(111) surfaces.[35] Periodic boundary conditions were used to avoid edge effects. The unit cell consisted of four 1x1 unit cells in all cases (i.e. 2x2), except for the 66%-ethylated surface (3x3) for which all atoms, except for the bottom hydrogen layer, were allowed to relax. Alkylated surfaces were constructed to be H-terminated, and alkyl groups, R-, were bound to the surface, replacing H atoms with a surface coverage of R groups of 25%, 50%, 75%, or 100% (note that only one geometric arrangement of the R groups is possible for each of these coverages on the 2x2 unit cell), as well as 66.7% coverage for $-C_2H_5$ terminated surfaces on a 3x3 surface. For the *iso*-propyl, phenyl, and *tert*-butyl groups, calculations were also performed with two unpaired electrons to determine if dissociation would occur due to the high steric repulsions at 75% or 100% coverage.

In each case, the strain energy of the R groups on the surface was calculated by comparing the average bond energy to that on a hydrogen-passivated Si_{10} cluster, which simulated a 1x1 surface site containing no nearest neighbors and was assigned zero strain

(i.e., the strain energy was calculated as the difference between the average bond energy of the functional group to the surface and the bond energy to the cluster).

To evaluate the free energy of formation of each alkylated surface at room temperature, the free energy of reaction, ΔG^{298°, for the reactions

$$\equiv Si-Cl + CH_3MgCl \rightarrow \equiv Si-CH_3 + MgCl_2 \qquad -41.0\,\text{kcal/mol}\ (1)$$

$$\equiv Si-Cl + C_2H_5MgCl \rightarrow \equiv Si-H + MgCl_2 + C_2H_4 \qquad -24.2\,\text{kcal/mol}\ (2)$$

$$\equiv Si-Cl + C_2H_5MgCl + THF \rightarrow \equiv Si-H + MgCl_2 + C_2H_6 + DHF \qquad -25.8\,\text{kcal/mol}\ (3)$$

$$\equiv Si-Cl + C_2H_5MgCl + THF \rightarrow \equiv Si-H + MgCl_2 + (THF-C_2H_5)' \qquad -43.8\,\text{kcal/mol}\ (4)$$

$$\equiv Si-Cl + C_2H_5MgCl + THF \rightarrow \equiv Si-H + MgCl_2 + (THF-C_2H_5)'' \qquad -45.7\,\text{kcal/mol}\ (5)$$

$$\equiv Si-Cl + C_2H_5MgCl \rightarrow \equiv Si-C_2H_5 + MgCl_2 \qquad -47.1\,\text{kcal/mol}\ (6)$$

was calculated using the Jaguar software (B3LYP flavor of DFT with 631G** basis sets) within the Poisson-Boltzmann continuum solvation model using tetrahydrofuran (THF) as the solvent (assuming a dielectric constant of 7.52 and a solvent radius of 2.526 Å for THF). For this calculation, the silicon site was modeled as a Si-$(SiH_3)_3$ cluster to which either Cl, H, or R were bonded. DHF is dihydrofuran, resulting from the elimination of 2 H atoms from THF to passivate the silicon site as well as the alkyl Grignard. (THF-C_2H_5)' results from bonding the alkyl group to the C atom adjacent to the O atom in THF, and (THF-C_2H_5)" results from bonding to the C atom across the ring from the O atom of THF. The use of these ΔG values allows for the determination of the overall thermodynamics of these reactions over a range of possible reaction schemes.

For the determination of the free energy of formation for a surface (ΔG_S), the reaction energy for the formation of the Si-C bond for ethylation (6) was used across all groups larger than methyl. ΔG_S for the formation of a particular surface of packing density, θ, was calculated by

$$\Delta G_S = \Delta G_a * \theta + \Delta G_H (1-\theta) + \Delta E_s , \qquad (7)$$

where ΔG_a is the driving force for the alkylation reaction, either -41.0 kcal/mol for $–CH_3$ terminated surfaces or -47.1 kcal/mol for all other R groups, θ is the fraction of a unit cell alkylated (i.e., 0.75 for a 75% packed surface), ΔG_H is the ΔG for the formation of the Si-H bond, and ΔE_s is the strain energy *per 1x1 unit cell* calculated through QM for that particular coverage. Using this approach, a value for ΔG_S accompanying the production of a surface having a packing density θ can then be calculated for each possible mechanism for the production of a Si-H bond from Si-Cl. Due to the uncertainty in the mechanism for this reaction, ΔG_S curves for each surface alkylation were prepared using ΔG_H values that spanned the energy values for the mechanisms proposed: -25, -31, -38, and -45 kcal/mol. Given the likelihood that the reaction contains at least one radical based step,[18,19] the overall formation of Si-H bonds can possibly be a combination of most or all of these steps and possibly other mechanisms not considered here, necessitating the use of a spectrum of ΔG values.

3. Results and Discussion

3.1 Calculated Strain Energies

Figure 1 shows the calculated strain energy for CH_3- and C_2H_5-terminated 2 x 2 surfaces at varying packing densities, θ. The CH_3-terminated surface showed a steady increase in the strain energy per molecule as θ was increased. The 2.21 kcal/mol per molecule strain energy at θ = 25% represents the overall unfavorable interaction from binding a single CH_3- group to the Si(111) surface, as the nearest -CH_3 neighboring groups were far enough removed that no strain could result from nearest-neighbor interactions. As θ increased, nearest-neighbor interactions caused an added marginal strain per bonded CH_3-, resulting in slightly higher average strain per bound molecule. The 0.56 kcal/mol energy difference between θ = 25% and θ = 50% was due to such interactions and was seen in the rotation of the -CH_3 groups from their preferred orientation atop the Si atoms of ~60° to an angle of ~50°. Figure 2 shows the twisting of the Si-Si-C-H angle as the number of bonded -CH_3 groups increased. The -CH_3 groups at θ = 25% were staggered relative to the Si-Si bonds underneath, with the torsion angle, ϕ, calculated to be 59.9° at 25%, which represents a minimum in the torsion strain energy. When the CH_3- groups were presented with a neighbor, however, the torsion angle changed from ϕ = 59.9° to ϕ = 50.3° at θ = 50% and to ϕ = 37.8° at θ = 75%, where ϕ remained for higher densities. This twisting results from an attempt to minimize the H---H interactions on adjacent -CH_3 groups, as can be seen in the C-H bonds twisting to point away from the C-H bonds on adjacent Si atoms. As the packing density rose from θ = 50% to θ = 75%, even though ϕ increased from 50.3° to 37.8°, no significant step in

strain energy per molecule was calculated, indicating that the energy minimum represented by the staggered conformation of the CH_3- groups compared to the underlying Si-Si structure on the surface was relatively shallow in comparison to other torsion angles. The minor shift in the torsion angle as θ increased from 75% to100% indicated that a torsion angle of ϕ ~37°presented the fewest unfavorable steric interactions for all neighbor-neighbor interactions.

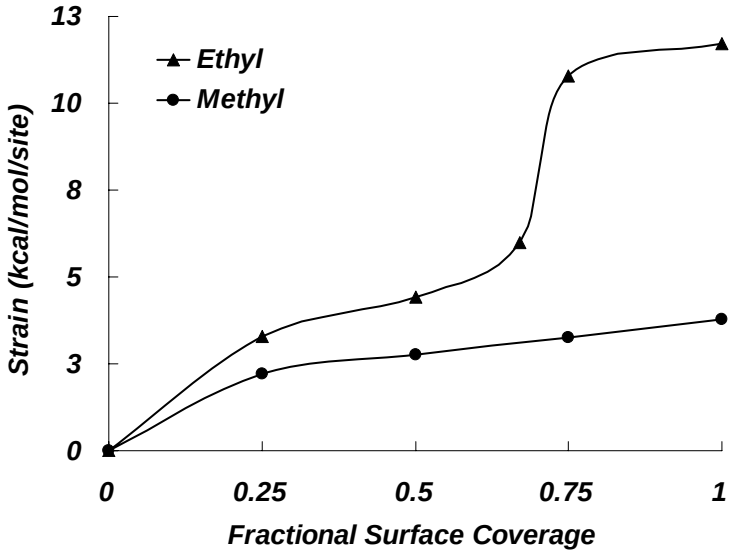

Figure 1. Strain energy per occupied surface site from quantum mechanics calculation for Si(111)-CH_3 and Si(111)-C_2H_5 as a function of surface coverage. The sites not occupied with ethyl or methyl were terminated with hydrogen atoms. The reference is an ethyl or methyl group bonded to a 1×1 site cluster with no nearest neighbors. This picture was taken from reference 22.

The C_2H_5-bound surfaces showed a similar increase in strain energy, ΔE_s, at low packing densities from $0 \leq \theta \leq 50\%$, relative to the strain energy on the CH_3-terminated Si surface. This behavior indicates that the strain is due to -C_2H_5 group rotations into

unfavorable conformations with respect to the underlying Si-Si bonds. However, a large jump in ΔE_s was observed between θ = 66.6% and θ = 75%, indicating that as the packing density increased, the strain forced bonded molecules to distort more than could be accomplished exclusively by rotation of the alkyl groups. Figure 3 shows a side-on view of C_2H_5-terminated surfaces at θ = 66.7% and θ = 75%, demonstrating that to accommodate the larger number of groups on the surface, the ethyl group atoms must distort out of individual tetrahedral geometry to minimize steric interactions between adjacent groups. At θ = 66.7%, the Si-C-C bond angle of 110.6°is very close to the unstrained tetrahedral angle. However, at θ = 75%, this angle increased to between 112.6-116.4°, and the Si-Si-C bond angle roseto between 109.6° and 118.6°, leading to the sharp jump in overall surface strain energy seen in Figure 1. After this jump, the strain energy leveled off at θ = 100%, indicating that each additional molecule added after θ ~75% underwent a similar distortion to bind to the surface. Figure 4 shows the final bond angles for the θ = 100% surface, where the Si-C-C bond angle has risen to 130.8° and the Si-Si-C bond angle has risen to 123.8°, resulting in a significant portion of the 11.72 kcal/mol strain energy for each site.

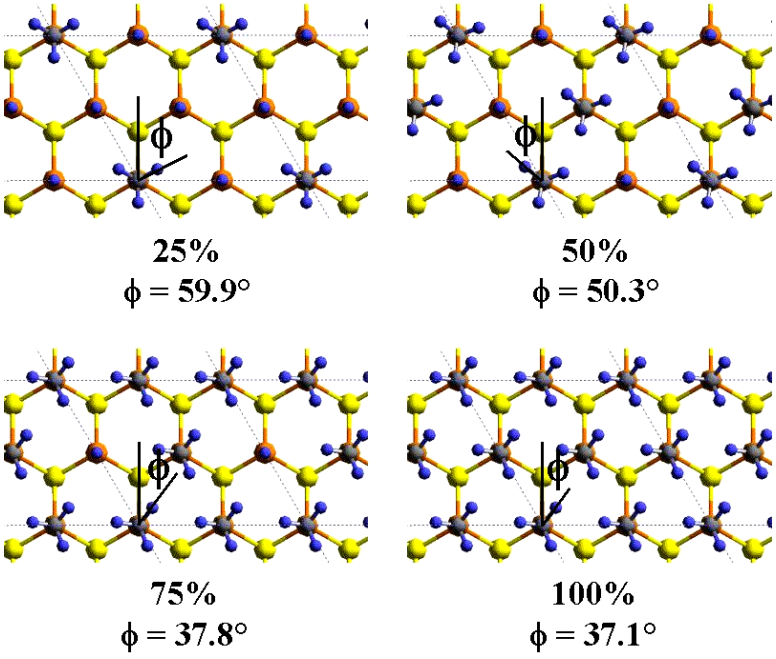

Figure 2. The CH_3-terminated Si(111) surface, at 25%, 50%, 75%, and 100% coverage. The sites not occupied with methyl were terminated with hydrogen atoms. The dotted lines show the 2x2 unit cell used in the calculations. As the packing density, θ, rose the torsion angle shifted from ~59.9° at 25% to ~37.1° at 100%. Note that the torsion angle for the structure with 50% coverage was measured *counterclockwise* from the Si-Si bond while it was measured *clockwise* for 25%, 75% and 100%. This is because in each case there exist two energetically equivalent structures: one in which the angle of interest (between 0° and 60°) occurs in the clockwise direction and one in which it occurs in the counterclockwise direction. In a molecular dynamics simulation, both energy minima are equally likely to occur. Blue = hydrogen, gray = carbon, orange = first layer silicon, and yellow = second layer silicon.

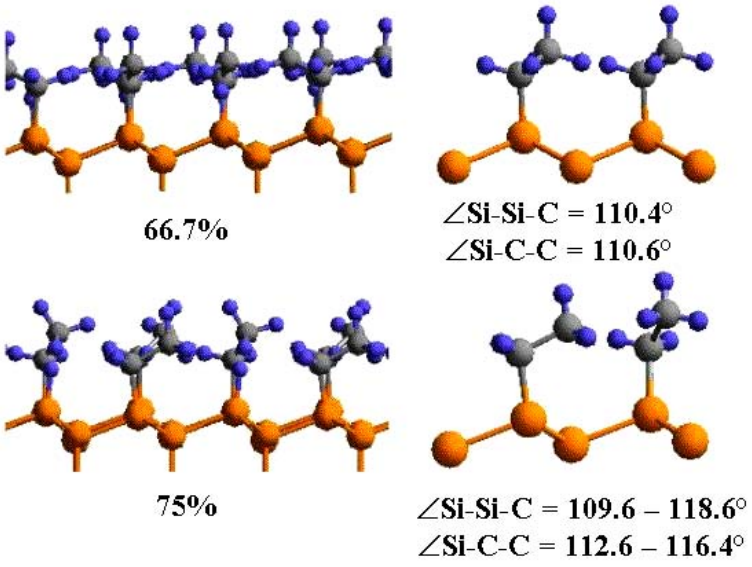

Figure 3. Side view of -C_2H_5 groups bonded to Si(111) at θ = 66.7% and 75% packing density. As the packing density rose, the -C_2H_5 groups became more distorted and bent vertically away from the surface to accommodate their neighbors.

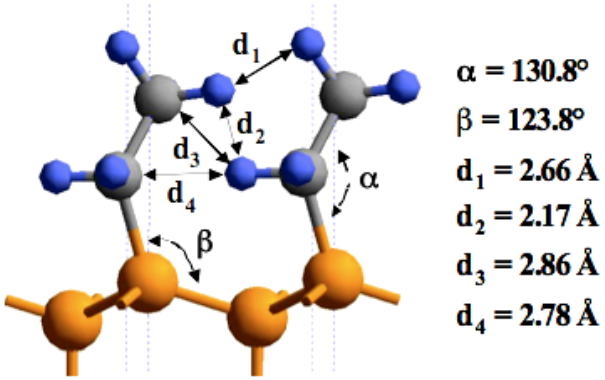

Figure 4. The 100% packed C_2H_5-Si(111) surface, showing significant strain in the bond angles and nearest neighbor nonbond distances. This figure was taken from reference 22.

Figure 5 shows the strain energy for the hexyl, octyl, *iso*-propyl, *tert*-butyl, and phenylated surfaces as a function of the fractional coverage, θ. The surfaces evaluated to compile Figure 5 all had significantly more strain energy per molecule than either the CH_3- or C_2H_5-terminated surfaces at similar values of θ (Figure 1). Due to both the larger surface areas for unfavorable interactions from neighboring alkyl groups, as well as due to branching in the *iso*-propyl, *tert*-butyl, and phenyl groups, at low packing densities these constraints decreased the distance to adjacent bonded groups, resulting in more strain per bonded group relative to termination with methyl or ethyl groups. The strain energy of the two branched groups, *iso*-propyl and *tert*-butyl, rose faster at low packing densities than for any of the other groups. At 50% packing, the phenyl-bonded surfaces, with the same degree of branching at the bonded carbon as the *iso*-propyl group (i.e., two carbon atoms attached to the Si-C carbon), had the lowest strain energy of all groups shown in Figure 5. However, this strain energy quickly rose, and at θ = 75% the strain energy was greater than that of the straight chain groups. When initially presented with neighboring groups, the shorter C-C and C-H bonds of the aromatic phenyl group, as well as the more compact in-plane arrangement of the atoms of the phenyl group, allowed phenyl to pack more efficiently by turning face-to-face. However, this beneficial arrangement was quickly lost as θ increased due to rings in perpendicular directions being forced into unfavorable edge-on interactions (recall that sp^2 carbon atoms are planar and highly stiff to out-of-plane deformation). For the either *iso*-propyl and phenyl groups with θ = 100% as well as for *tert*-butylated surfaces with θ = 75%, the average strain energies corresponded to the triplet state (i.e., a state in which one of the functional groups has dissociated from the surface). This triplet state was lower in energy than the

singlet state under such conditions. This behavior indicates that these specific surfaces are not thermodynamically stable and instead would dissociate if formed.

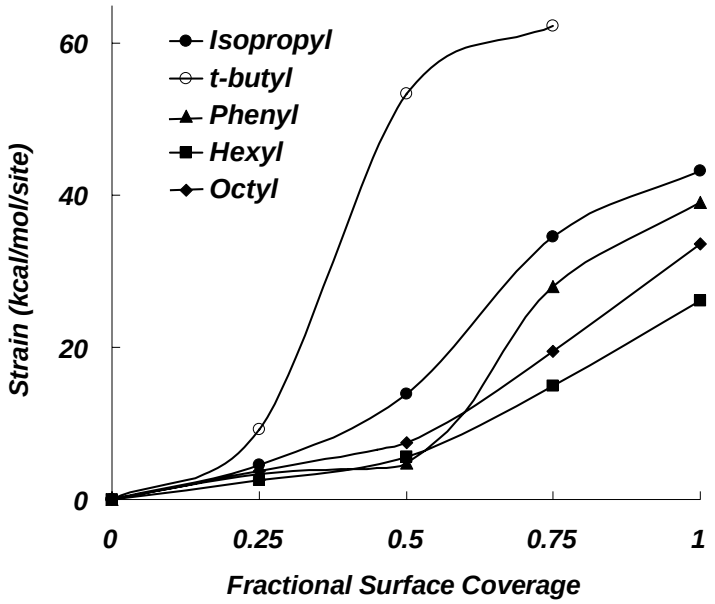

Figure 5. The calculated strain energy for the alkyl groups *iso*-propyl, *tert*-butyl, phenyl, hexyl, and octyl bonded to Si(111) surfaces at increasing packing densities. The energies of the 100% *iso*-propylated and phenylated surfaces, as well as that of the 75% *tert*-butylated surface, correspond to the triplet state (i.e., a state in which one of the functional groups has dissociated from the surface), which was significantly lower in energy than the singlet state. This indicates that these densely packed surfaces are not stable thermodynamically.

Figure 6 shows the conformations of hexyl and octyl groups, respectively, when bonded to the Si(111) surface. As the packing density increased, these chains bonded at increasing *tilt* angles, λ, relative to the surface. At the lowest calculated packing density,

θ = 25%, hexyl and octyl groups packed with tilt angles of λ = 59.9° and λ = 57.1°, respectively. For isolated hexyl and octyl chains on the Si(111) surface, the λ values calculated using MD (64.4° and 63.3°, respectively) were in good agreement with the λ values calculated for θ = 25% using QM, indicating that steric interactions at θ = 25% were negligible. As the packing density was increased in the QM calculations, λ quickly increased for both hexyl and octyl groups, with the groups being near vertical at θ ≥ 75%, especially for the octyl chains. These results stand in contrast to measurement of the surface bonding angles for alkyl surfaces that were presumed to be ~50% packed when formed by hydrosilation.

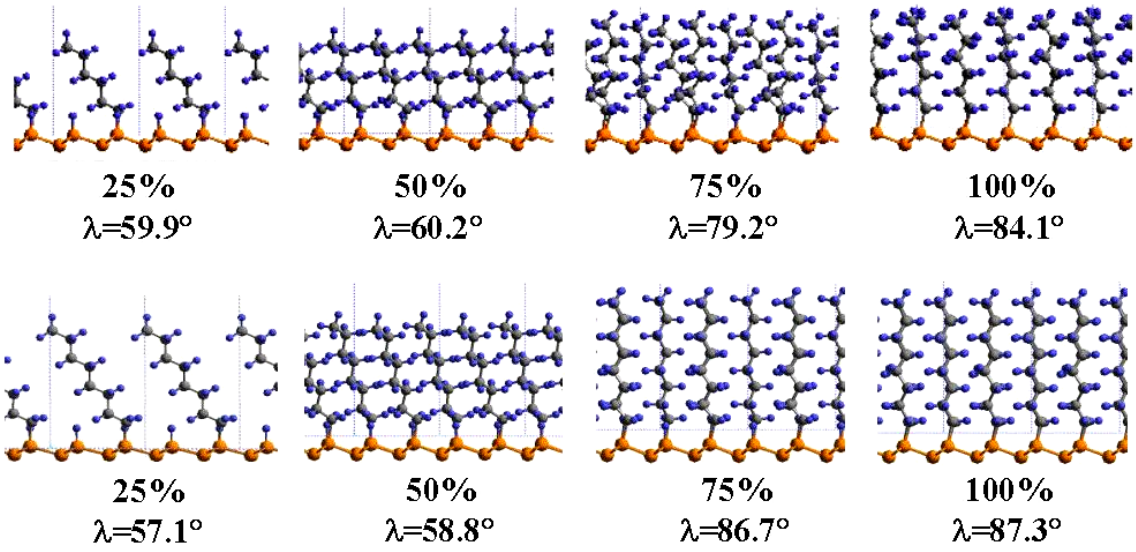

Figure 6. Side view of hexyl- and octyl-Si(111) surfaces at varying packing densities, illustrating how the chain bond angle relative to the Si(111) surface, λ, increased as the packing density rose.

In addition to the energy minimum at $\lambda = 57.1°$, the octyl-terminated surface at $\theta = 25\%$ also exhibited a local energy minimum at $\lambda = 40.5°$. This minimum was ~0.4 kcal/mol/1x1 cell higher in energy than the global minimum surface at this packing density. This second conformation is a consequence of the ability of the octyl chains to overlap their two terminal methylene groups with the base of neighboring chains and thereby induce a favorable Van der Waals interaction that is not possible in the packing of the shorter hexyl chains. As the alkyl chain becomes longer than eight carbon atoms, these favorable van der Waals interactions are expected to increase. This observation is in agreement with the chain tilt angles measured from surface IR dichroism measurements for the longer chain hexadecyl groups,[2] in which $\lambda = 58°$ was deduced for surfaces prepared using heat in neat olefin, but $\lambda = 34\text{-}36°$ was deduced for samples prepared at a higher temperatures. This behavior suggests that the difference in preparation temperature caused a shift from a local minimum to the global minimum.

3.2 Free Energy of Formation of Alkyl Surfaces

For determination of the expected final surface packing density using these QM calculations, ΔG values are required for the surface reactions that result in the alkylation of a Si site as well as for the reactions that produce H-termination of a Si site. However, as mentioned above, several plausible reaction pathways, which have greatly varying ΔG values, could result in H-termination. Without specific data on the reaction products, the free energy for the reaction of Si-Cl to produce Si-H/R can only be bounded into a range of possible ΔG values.

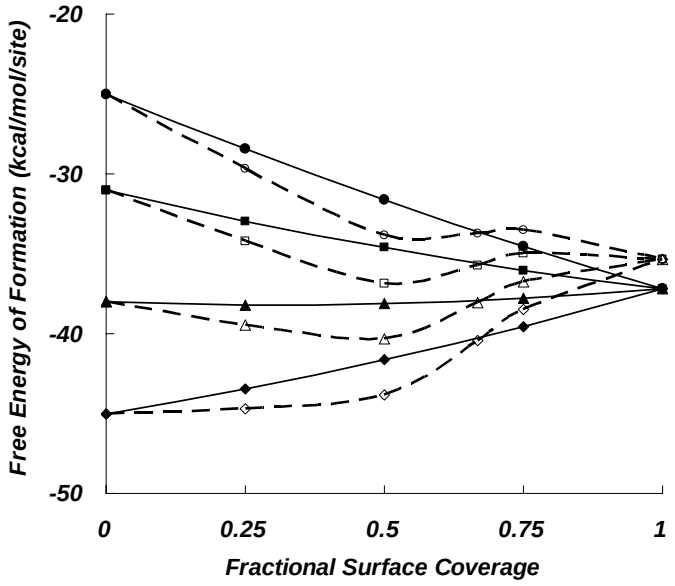

Figure 7. The free energy of formation for CH_3- (solid) and C_2H_5-terminated (dashed) Si(111) surfaces at varying fractional surface coverages for four different ΔG_H values: -25 (circle), -31 (square), -38 (triangle), and -45 kcal/mol (diamond).

Figure 7 shows the free energy of formation, ΔG_S, for CH_3- (solid line) and C_2H_5-terminated (dashed line) surfaces for such a range of processes. The solid lines in Figure 7 show the free energy of formation to form an increasing fraction of CH_3-termination from a Si-Cl surface, with the four different ΔG_H values for the formation of Si-H from Si-Cl (-25, -31, -38, and -45 kcal/mol) spanning the range of ΔG_H values for the proposed reactions. For the two low driving-force energies, at all coverages methylation of a Si-Cl site was thermodynamically preferred over H-termination, as seen by steadily decreasing ΔG values as the packing density increased. As the ΔG_H for the formation of Si-H became more negative, however, at all fractional coverages the H-termination reaction

was calculated to be more thermodynamically favorable than formation of Si-C bonds. Since measurements of the surfaces formed by the two-step chlorination/alkylation reaction indicate that the surface is fully CH_3-terminated,[18,19,21] ΔG_H must either be ≤ -38 kcal/mol (for which the free energy curve is nearly horizontal in Figure 7), or the reaction must have strong kinetic factors that influence the surface formation to favor alkylation over H-termination.

The C_2H_5-termination reaction, as seen in Figure 1, has higher strain energies associated with it, and the step in ΔE_s at θ ~66.7% creates a dip around θ = 50% across all ΔG_H values (Figure 7). The high density of C_2H_5- groups measured on these surfaces,[19,22] θ = 80 ± 20 %, also indicates that the ΔG_H for the Si-H formation is on the more positive side of the energy spectrum being considered and that 100% coverage is not necessarily limited by thermodynamics, but by high reaction barriers caused by the bulky transition states.

Figure 8 illustrates the effects of longer chains on the free energy of formation of these alkylated surfaces, showing the result of the increased strain energy. For both hexyl- and octyl-terminated surfaces for ΔG_H > ~ -43 kcal/mol, the formation of the alkyl bond had a broad, deep minimum at θ ~50%. Only at ΔG_H = -45 kcal/mol was Si-H formation favored over formation of Si-R. The minima for the octyl curves for the more positive ΔG_H values was in good agreement with experimental measurements of the coverage of octyl groups formed through the two-step reaction process.[19,22] Figure 9 shows the free energy of formation for the bulkier groups considered. The sharp divergence in ΔG_S between the *iso*-propyl and *tert*-butyl groups highlights the large difference in the strain energy of the two groups (Figure 9) and leads to a lower predicted surface coverage for

tert-butylated surfaces compared to *iso*-propylated surfaces. The minima for both the *iso*-propyl and *tert*-butyl surfaces lie in the region $25 \leq \theta \leq 50\%$ surface coverage for the -25 and -31 kcal/mol ΔG_H lines, with the *tert*-butyl ΔG_S rising faster as θ increases. X-ray photoelectron spectroscopic measurements of these surfaces show no difference in surface coverage, within experimental error, with $\theta = 40 \pm 20\%$,[19] indicating that steric factors such as the transition state size or energy may have a significant role in determining the final surface packing density of such systems. The deep minima in ΔG_S for the phenyl-terminated surfaces at $\theta = 50\%$ corresponds well with the experimental data for phenyl-functionalized surfaces prepared using the two-step halogenation/alkylation approach.[19]

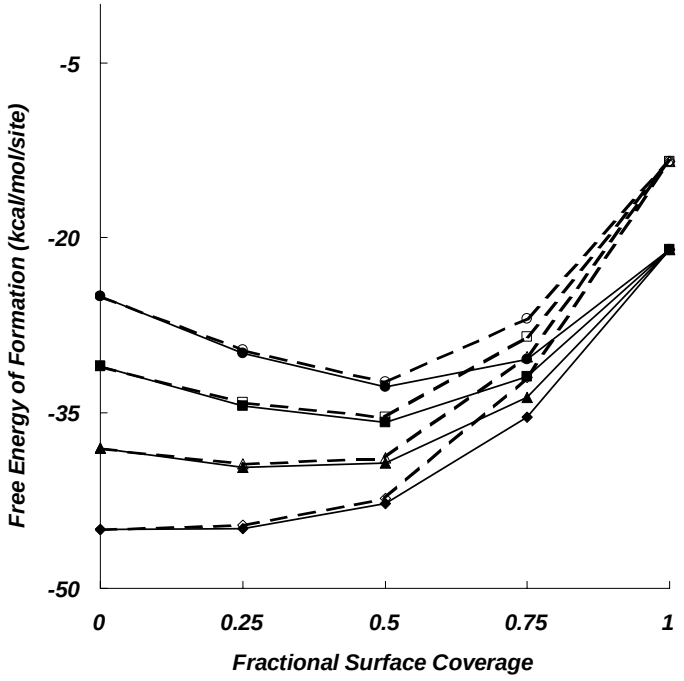

Figure 8. The free energy of formation for hexyl- (solid) and octyl-terminated (dashed) Si(111) surfaces at varying fractional surface coverages for four different ΔG_H values: -25 (circle), -31 (square), -38 (triangle), and -45 kcal/mol (diamond).

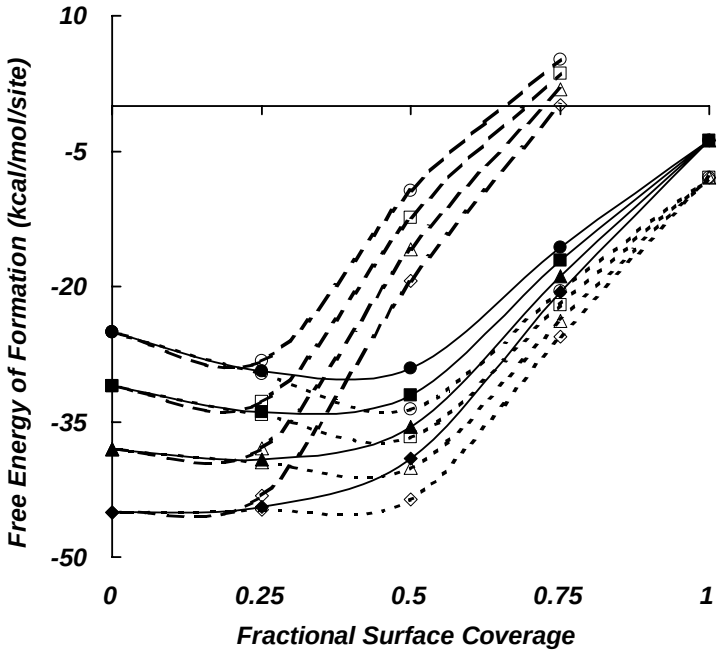

Figure 9. The free energy of formation for *iso*-propyl- (solid), *tert*-butyl- (dashed), and phenyl-terminated (dotted) Si(111) surfaces at varying fractional surface coverages for four different ΔG_H values: -25 (circle), -31 (square), -38 (triangle), and -45 kcal/mol (diamond). The energies of the 100% *iso*-propylated and phenylated surfaces, as well as that of the 75% *tert*-butylated surface, correspond to the triplet state (i.e., a state in which one of the functional groups has dissociated from the surface), which was significantly lower in energy than the singlet state.

4. Conclusions

Quantum mechanical calculations of the strain energies of bonded alkyl groups on the Si(111) surface, as well as of free energies for a collection of possible reaction pathways for the formation of Si-H bonds, have resulted in a framework for evaluation of the composition and structure of alkylated Si(111) surfaces formed by the two-step

chlorination/alkylation reaction. The reaction presumably starts with every atop site reacting to form either a Si-H bond or a Si-C bond. The competing termination reactions for each site are driven by both the thermodynamic energy as well as by various kinetics and steric considerations. The predicted free energy curves for the alkylation of the Si(111) surface most closely correspond with published data on the packing of these alkylated surfaces for ΔG_H values (formation energies for the reaction Si-H → Si-Cl in the presence of Grignard reagents in THF solvent) >~ -31 kcal/mol. This is in accord with expectations for a reaction mechanism for the H-termination of unalkylated surface Si sites that involves the elimination of 2 H atoms and the formation of a C-C double bond in either unreacted Grignard R groups or in the THF solvent.

Acknowledgement: Joseph Nemanick and Nathan Lewis gratefully acknowledge the NSF, grant CHE-021358, for support of this work. Santiago Solares and William Goddard thank the Microelectronics Advanced Research Corporation (MARCO) and its Focus Center on NanoEngineered Architectonics (FENA).

SUPPORTING INFORMATION

1. Pseudopotentials and basis sets

The pseudopotentials used in these calculations are standard norm-conserving, non-separable pseudopotentials[36] generated using Hamann's methods. [37,38] The carbon and silicon pseudopotentials included up to l=1 and l=2 projectors, respectively (with

standard settings), with the *l*=1 and *l*=2 potentials used as the local potential in each case. The hydrogen atom was also treated as a pseudopotential (rather than with a bare-core potential), with only an *l*=0 potential. Multiple tests with hydrogen atoms, H_2 molecules, and water molecules verified that the energetics of the bare core hydrogen potential and the hydrogen pseudopotential were almost indistinguishable.

The basis functions were double-zeta plus polarization quality, formed from contracted Gaussians. Hence, the *occupied* orbitals Si-*s* and Si-*p* and the H-*s*, for example, had two radial degrees of freedom, and the Si-*d* and H-*p* *unoccupied* angular polarization orbitals had only one. The basis sets for hydrogen, carbon, and silicon were contracted (4s1p/2s1p), (5s4p1d/2s2p1d), and (4s3p1d/2s2p1d). This nomenclature denotes, for H for example, that four Gaussian *s*-functions were contracted into two independent functions and one Gaussian *p*-function was used as one independent radial degree of freedom. The *d*-functions (for carbon and silicon) were made up of the five pure *l*=2 functions, i.e., the *s*-combination as excluded. Tables S-1, S-2, and S-3 list the Gaussians and contraction coefficients for hydrogen, carbon, and silicon.

Table S-1: Basis set for hydrogen. The Gaussian decay constants α (1/bohr^2) and associated contraction coefficients c_α for the contracted Gaussian basis functions (unnormalized).

s-functions			**p-function**	
α_s	c_α (1st zeta)	c_α (2nd zeta)	α_p	c_α
0.102474	0.087388	0.075281	1.100000	1.000000
0.372304	0.405344	0.120939		
1.230858	0.485455	0		
4.783324	0.397563	0		

Table S-2: Basis set for carbon. The Gaussian decay constants α (1/bohr^2) and associated contraction coefficients c_α for the contracted Gaussian basis functions (unnormalized).

s-functions			**p-functions**			**d-function**	
α_s	C_α (1st zeta)	c_α (2nd zeta)	α_p	c_α (1st zeta)	c_α (2nd zeta)	α_d	c_α
0.155830	0.219500	1.000000	0.154701	0.107631	1.000000	0.770000	1.000000
0.458320	0.695623	0	0.523908	0.524630	0		
1.40253	0.362537	0	1.442267	1.002503	0		
2.805200	-1.296428	0	4.604695	1.675411	0		
5.610400	0.450261	0					

Table S-3: Basis set for silicon. The Gaussian decay constants α (1/bohr^2) and associated contraction coefficients c_α for the contracted Gaussian basis functions (unnormalized).

s-functions			**p-functions**			**d-function**	
α_s	c_α (1st zeta)	c_α (2nd zeta)	α_p	c_α (1st zeta)	c_α (2nd zeta)	α_d	c_α
0.104600	0.209953	1.0	0.094241	0.067616	1.0	0.450000	1.000000
0.272263	0.559782	0	0.317679	0.318212	0		
1.300508	-0.991282	0	1.561145	-0.066383	0		
2.601030	0.334871	0					

2. K-points

The number of k-points for each calculation was varied according to the unit cell size. 8 k-points were used in the direction of each of the two cell unit vectors for 1x1 unit cells (there are only two unit vectors because the models used are only 2D periodic). The number of k-points for other structures was set to the closest integer, inversely proportional to the cell dimension along each unit vector. Thus, the 2x2 and 3x3 unit cells had 4 and 3 k-points in each direction, respectively.

3. Spin polarization

Calculations of singlet states were performed with restricted (closed shell) DFT. Calculations of doublet (radical) states or dissociated triplet states, necessary for the computation of bond energies and dissociated surface states, were performed with unrestricted (spin-polarized) DFT in which the N_α spin-up and N_β spin-down orbitals are optimized independently.

REFERENCES:

1. Linford, M. R.; Chidsey, C. E. D.; *J. Am. Chem. Soc.* **1993**, *115*, 12631.
2. Linford, M. R.; Fenter, P.; Eisenberger, P. M.; Chidsey, C. E. D.; *J. Am. Chem. Soc.* **1995**, *117*, 3145
3. Terry, J.; Linford, M. R.; Wigren, C.; Cao, R. Y.; Pianetta, P.; Chidsey, C. E. D.; *Appl. Phys. Lett.* **1997**, *71*, 1056.
4. Terry, J.; Mo, R.; Wigren, C.; Cao, R. Y.; Mount, G.; Pianetta, P.; Linford, M. R.; Chidsey, C. E. D.; *Nucl. Instrum. Meth. B* **1997**, *133*, 94.
5. Effenberger, F.; Gotz, G.; Bidlingmaier, B.; Wezstein, M.; *Angew. Chem. Int. Ed.* **1998**, *37*, 2462.
6. Stewart, M. P.; Buriak, J. M.; *Angew. Chem. Int. Ed. Eng* **1998**, *23*, 3257.
7. Sieval, A. B.; Demirel, A. L.; Nissink, J. W. M.; Linford, M. R.; van der Maas, J. H.; de Jeu, W. H.; Zuilhof, H.; Sudholter, E. J. R.; *Langmuir* **1998**, *14*, 1759.

8. Sung, M. M.; Kluth, G. J.; Yauw, O. W.; Maboudian, R.; *Langmuir* **1997**, *13*, 6164.

9. Zazzera, L. A.; Evans, J. F.; Deruelle, M.; Tirrell, M.; Kessel, C. R.; Mckeown, P.; *J. Electrochem. Soc.* **1997**, *144*, 2184.

10. Buriak, J. M.; Allen, M. J.; *J. Am. Chem. Soc.* **1998**, *120*, 1339.

11. Buriak, J. M.; Allen, M. J.; *J. Lumin.* **1998**, *80*, 29.

12. Holland, J. M.; Stewart, M. P.; Allen, M. J.; Buriak, J. M.; *J. Solid State Chem.* **1999**, *147*, 251

13. Henry de Villeneuve, C.; Pinson, J.; Ozanam, F.; Chazalviel, J. N.; Allongue, P. In *Mat. Res. Soc. Symp. Proc.* 1997; Vol. 451, p 185-195.

14. Vieillard, C.; Warntjes, M.; Ozanam, F.; Chazalviel, J.-N.; *Proc. - Electrochem. Soc.* **1996**, *95*, 250.

15. Bansal, A.; Li, X.; Lauermann, I.; Lewis, N. S.; Yi, S. I.; Weinberg, W. H.; *J. Am. Chem. Soc.* **1996**, *118*, 7225.

16. Juang, A.; Scherman, O. A.; Grubbs, R. H.; Lewis, N. S.; *Langmuir* **2001**, *17*, 1321.

17. Royea, W. J.; Juang, A.; Lewis, N. S.; *Appl. Phys. Lett.* **2000**, *77*, 1988.

18. Webb, L. J.; Nemanick, E. J.; Biteen, J. S.; Knapp, D. W.; Michalak, D. J.; Traub, M. C.; Chan, A. S. Y.; Brunschwig, B. S.; Lewis, N. S.; *J. Phys. Chem. B* **2005**, *109*, 3930.

19. Nemanick, E. J.; Hurley, P. T.; Brunschwig, B. S.; Lewis, N. S.; *J. Phys. Chem. B* **2005**, *submitted for publication*.

20. Webb, L. J.; Michalak, D. J.; Biteen, J. S.; Brunschwig, B. S.; Chan, A. S. Y.; Knapp, D. W.; Meyer, H. M.; Nemanick, E. J.; Traub, M. C.; Lewis, N. S.; *J. Phys. Chem. B* **2005**, *submitted for publication*.

21. Yu, H. B.; Webb, L. J.; Ries, R. S.; Solares, S. D.; Goddard, W. A.; Heath, J. R.; Lewis, N. S.; *J. Phys. Chem. B* **2005**, *109*, 671.

22. Yu, H. B.; Webb, L. J.; Solares, S. D.; Cao, P.; Goddard III, W. A.; Heath, J. R.; Lewis, N. S.; *J. Phys. Chem. B* **2005**, *submitted for publication*.

23. Miyadera, T.; Koma, A.; Shimada, T.; *Surf. Sci.* **2003**, *526*, 177.

24. Webb, L. J.; Rivillon, S.; Chabal, Y.; Lewis, N. S.; *J. Phys. Chem., B* **2006**, *in press*.

25. Sieval, A. B.; van der Hout, B.; Zuilhof, H.; Sudholter, E. J. R.; *Langmuir* **2000**, *16*, 2987.

26. Sieval, A. B.; van der Hout, B.; Zuilhof, H.; Sudholter, E. J. R.; *Langmuir* **2001**, *17*, 2172.

27. Yuan, S.-L.; Cai, Z.-T.; Jiang, Y.-S.; *New J. Chem.* **2003**, *27*, 626.

28. Zhang, L.; Wesley, K.; Jiang, S.; *Langmuir* **2001**, *17*, 6275.

29. Shapiro, I. R.; Solares, S. D.; Esplandiu, M. J.; Wade, L. A.; Goddard III, W. A.; Collier, C. P.; *J. Phys. Chem. B* **2004**, *108*, 13613.

30. Solares, S. D.; Esplandiu, M. J.; Goddard III, W. A.; Collier, C. P.; *J. Phys. Chem. B* **2005**, *109*, 11493.

31. Mayo, S. L.; Olafson, B. D.; Goddard, W. A. III; *J. Phys. Chem. B* **1990**, *94*, 8897.

32. Rappé, A. K.; Goddard III, W. A.; *J. Phys. Chem. B* **1991**, *95*, 3358.

33. Schultz, P. A.; Sandia National Labs: Albuquerque, NM, SeqQuest Electronic Structure, p http://dft.sandia.gov/Quest/.

34. Perdew, J. P.; Burke, K.; Ernzerhof, M.; *Phys. Rev. Lett.* **1996**, *77*, 3865.

35. Solares, S.D.; Dasgupta, S.; Schultz, P.A.; Kim, Y.H.; Musgrave, C.B.; Goddard, W.A. III; *Langmuir* **2005**, *21*, 12404.

36. Redondo, A.; Goddard, W.A. III; McGill, T.C.; *Phys. Rev. B* **1977,** *15,* 5038.

37. Hamann, D.R.; *Phys. Rev.;* **1989,** *40,* 2980.

38. Hamann, D.R.; pseudopotential generation program PUNSLDX, unpublished.

Chapter 7: Theoretical Investigation of the Structure and Coverage of the Si(111)-OCH_3 Surface[*]

ABSTRACT. We present a Quantum Mechanical study of the Si(111)-OCH_3 surface structure, strain energy, and charge profile and compare the results to those previously obtained for Si(111)-CH_3 and Si(111)-C_2H_5. We find that 100% coverage is feasible for Si(111)-OCH_3 (similar to the methylated surface), which compares to only ≈ 80% for the ethylated surface. We explain these differences in terms of nearest neighbor steric and electrostatic interactions. We also show through enthalpy and free energy that the formation of the Si(111)-OCH_3 surface from Si(111)-H and methanol is favorable at 300 K. Finally, we investigate the conditions under which stacking faults can emerge on Si(111)-OCH_3, as they do on Si(111)-CH_3 and Si(111)-CH_2CH_3 surfaces when etch pits with sufficiently long edges are present on the surface.

[*] Reproduced with permission from Solares, S.D.; Michalak, D.J.; Goddard, W.A. III; Lewis, N.S.; *J. Phys. Chem. B,* **2006,** *110,* 8171.

Silicon surfaces have been functionalized with a wide variety of organic reagents through a number of methods, including reactions with alkylmagnesium or alkyllithium reagents,[1-14] electrochemical functionalization, ultraviolet light-initiated reactions,[6, 15-18] chemical free-radical activation,[19, 20] thermal activation,[20-26] hydrosilylation reactions,[27-31] or through reactions with alcohols.[32-38] In general, the reported reactions can be divided into those producing surfaces having the functionalized Si in the formal Si(0) oxidation state with Si-C-R bonding or those producing surfaces having the functionalized Si in the Si(I) oxidation state with Si-O-R bonding. The alkylated Si(111) surfaces are the most characterized to date. Simple molecular modeling considerations indicate that $-CH_3$ groups are the only saturated straight chain alkyl that, on steric grounds, can terminate every atop Si site on an unreconstructed Si(111) surface. Consistently, recent low temperature (4 K and 77 K) atomic resolution scanning tunneling microscopy (STM) images of the methyl-terminated Si(111) surface prepared through a two-step chlorination/alkylation process[1, 2] have revealed a well-ordered structure with a nearest neighbor spacing equal to 3.8 Å, corresponding to 100% coverage on the unreconstructed 1x1 Si(111) surface.[11] The equilibrium geometry obtained from Quantum Mechanics (QM) calculations for Si(111)-CH_3 is shown in Figure 1[39] and is in accord with the experimental data on such systems. In contrast, STM images at 77 K of the Si(111)-C_2H_5 surface, prepared through the same method, indicate that the ethyl surface coverage is only ≈80%.[40] At 100% coverage QM calculations indicate that the ethyl-terminated Si(111) surface should contain a significant amount of strain, with large bond angles and short nonbond distances.[40] The equilibrium C-C-Si and C-Si-Si bond angles calculated at

100% coverage are α = 130.8° and β = 123.8°, respectively (Figure 2) which are appreciably larger than the tetrahedral value of 109.4°. The nonbond H---H distances were calculated to be as low as 2.17 Å, much shorter than the calculated values for hydrogen atoms on neighboring methyl groups of Si(111)-CH_3 (2.33 Å) or for hydrogen atoms on neighboring carbon atoms within bulk crystalline polyethylene (2.51 Å).[40] These expectations are therefore also in accord with STM data of C_2H_5-terminated Si(111) surfaces.

In this work we focus on the structure of the Si(111)-OCH_3 surface. Alkoxylated Si surfaces have been prepared either by the slow room temperature reaction of porous or roughened Si(111)-H surfaces with alcohols,[32, 33, 36] by the rapid, oxidatively driven, reaction of Si(111)-H with alcohols,[34, 35] or by reaction of alcohols with Cl-terminated Si(111) surfaces.[35] Methoxylated Si surfaces are also of interest because a common method of electrically passivating Si(111) is to immerse it into I_2 in CH_3OH,[41-45] which forms, at least in part, Si-OCH_3 as well as Si-I bonds.[46, 47] We are interested in modeling the Si(111)-OCH_3 and the Si-I surfaces to calculate the geometry, to estimate the maximum surface coverage that is feasible, and to compare the results to those obtained for Si(111)-CH_3 and Si(111)-C_2H_5.

To calculate the surface structure at 100% coverage, the same type of periodic QM calculations were performed for Si(111)-OCH_3 as were performed on the methylated and ethylated surfaces.[11, 39, 40] SeqQuest software[48] (Sandia National Labs., Albuquerque, NM) and the PBE[49] approximation of Density Functional Theory (DFT) were used on an infinitely repeated 2D periodic 1x1 unit cell that consisted of six layers of bulk silicon atoms, a hydrogen atom terminating the bottom surface, and a -OCH_3 group terminating

the top surface. These calculations yielded the equilibrium surface geometry (Figure 3) as well as the partial charges of the surface atoms as calculated through a Mulliken populations analysis (Figure 4). The surface charge profile is as expected from the electronegativity of the atoms involved. DFT calculations were also performed in the presence of electric fields in the range of –10 to +10 MV/cm, but negligible effects were observed. As shown in Figure 3, the CH_3 groups in the $–OCH_3$ moiety are calculated to be tilted, having a Si-O-C angle, α, of 122.0°, consistent with expectations based on nearest-neighbor interactions between $-OCH_3$ groups and between these groups and the Si(111) surface. Figure 5 shows the behavior of the surface energy as a function of the torsion angle, yielding a minimum in energy for a Si-Si-O-C torsion angle,ϕ, of 32.3°.

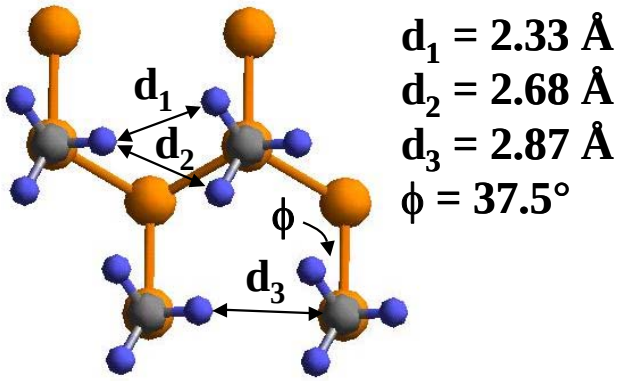

Figure 1. Top view atomistic model showing four adjacent surface sites of the 1x1 Si(111)-CH_3 surface at 100% coverage with the most relevant nonbond distances (d_1, d_2, and d_3) and the torsion angle of the methyl group with respect to the silicon surface, obtained from quantum mechanics calculations.[39] The color code is: blue = hydrogen, gray = carbon, and orange = silicon.

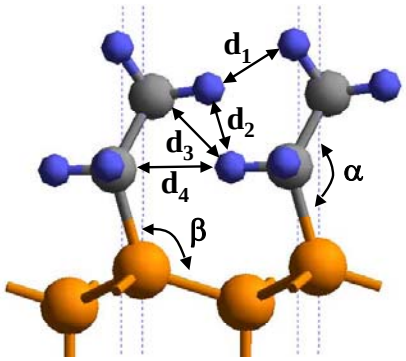

α = 130.8°
β = 123.8°
d_1 = 2.66 Å
d_2 = 2.17 Å
d_3 = 2.86 Å
d_4 = 2.78 Å

Figure 2. Side view atomistic model showing two adjacent surface sites of the 1x1 Si(111)-C_2H_5 surface at 100% coverage with the most relevant bond angles (α and β) and nonbond distances (d_1, d_2, d_3 and d_4), obtained from quantum mechanics calculations.[40] The color code is: blue = hydrogen, gray = carbon, and orange = silicon.

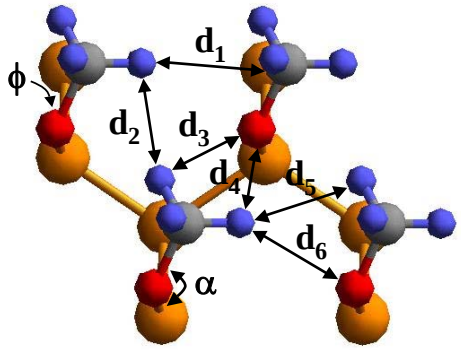

d_1 = 2.78 Å
d_2 = 2.48 Å
d_3 = 2.40 Å
d_4 = 2.42 Å
d_5 = 2.49 Å
d_6 = 2.56 Å
α = 122.0°
ϕ = 32.3°

Figure 3. Top view atomistic model showing four adjacent surface sites of the 1x1 Si(111)-OCH_3 surface with the most relevant nonbond distances (d_1, d_2, d_3, and d_4), and the bond and torsion angles (α and ϕ, respectively), obtained from quantum mechanics calculations. The color code is: blue = hydrogen, gray = carbon, red=oxygen, and orange = silicon.

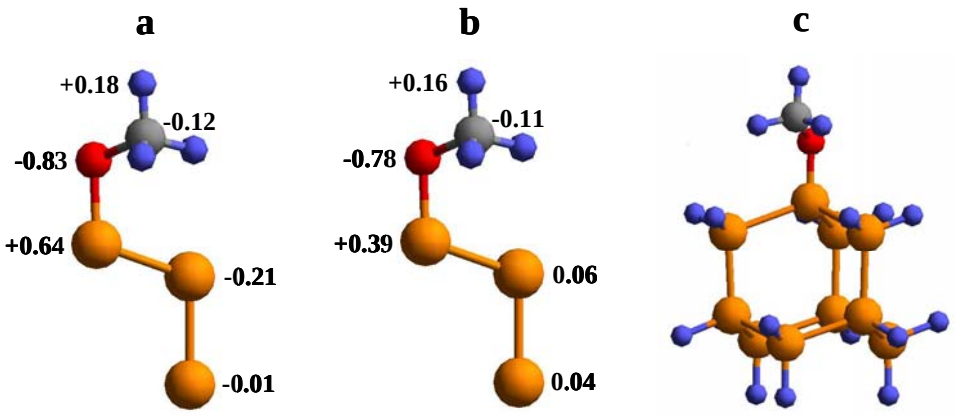

Figure 4. Atomic charges from Mulliken populations analysis (in vacuum) for Si(111)-OCH_3 using an infinitely repeated periodic surface unit cell (a) and a $Si_{10}H_{15}$-OCH_3 cluster (b and c). The atomic charge in the fourth Si layer of the surface unit cell (not shown) is less than 0.01. The charges of the OCH_3 substituent are similar for the cluster and the periodic structure. The silicon charges differ because the cluster was terminated with hydrogen atoms.

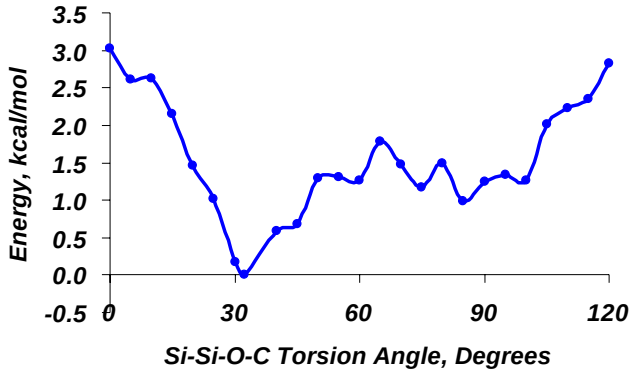

Figure 5. Surface energy as a function of the Si-Si-O-C torsion angle, ϕ, of the Si(111)-OCH_3 surface. The energy values were obtained by changing the torsion angle of the equilibrium surface structure (with all other parameters kept constant) and performing

single-point energy DFT calculations (without relaxation). The equilibrium minimum energy torsion angle is 32.3°.

To quantify the surface strain as a function of the $-CH_3$, $-C_2H_5$, and $-OCH_3$ surface coverage on Si(111), periodic PBE DFT calculations were performed on 1x1, 2x2 and 3x3 unit cells of Si(111)-CH_3, Si(111)-C_2H_5, and Si(111)-OCH_3 surfaces having functional group coverage amounts ranging from 25% to 100% of the Si atop sites. In each case, the remaining Si atop sites were terminated with hydrogen atoms. For each surface, the average bond energy of the appropriate functional group was compared to its bond energy on a Si(111) surface site modeled as a $Si_{10}H_{15}$ cluster having no nearest neighbors (see Figure 4), with the bond to this cluster taken as the reference and assigned zero strain. As expected, the strain energy is greater in the ethylated surface than in the other two cases, especially for surface coverages above 67% (Figure 6). At 100% coverage, the amount of strain in the Si(111)-C_2H_5 surface is three times greater than for Si(111)-CH_3 and seven times greater than for Si(111)-OCH_3. In fact, the strain is lowest in Si(111)-OCH_3 for all values of the surface coverage.

While the strain *vs.* coverage curves for the Si(111)-CH_3 and Si(111)-OCH_3 surfaces are smooth, the curve for Si(111)-C_2H_5 has a distinct jump between 67% and 75% coverage, at which the ethyl groups no longer fit on the surface unless their C-C-Si angle is significantly increased to allow them to have a nearly vertical orientation with respect to the surface (at 100% coverage each functional group is forced to occupy only one unit cell). Based on the structural similarity between the Si(111)-CH_2-CH_3 and Si(111)-O-CH_3 surfaces, it is somewhat surprising that the Si(111)-OCH_3 surface has such low

surface strain. Although the methoxylated surface structure, as shown in Figure 3, would be expected to involve steric repulsions between hydrogen and oxygen atoms whose nearest neighbor nonbond distances can be as low as 2.40 Å, this interaction is not as repulsive as that between hydrogen atoms of a terminal CH_3 group of an ethyl molecule with the $–CH_2–$ groups on a neighboring ethyl group because the hydrogen and oxygen atoms in the Si(111)-OCH_3 overlayer have atomic charges of different signs, which results in a favorable Coulomb interaction of 20.7 kcal/mol (in vaccum), thus compensating for part of the nearest-neighbor repulsion energy.

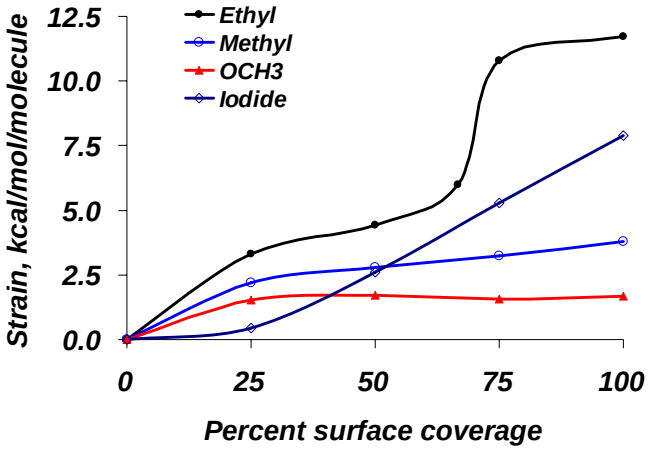

Figure 6. Strain energy per occupied surface site for Si(111)-C_2H_5, Si(111)-CH_3, and Si(111)-OCH_3 as a function of surface coverage from quantum mechanics calculations. The sites not occupied with ethyl or methyl were terminated with hydrogen atoms. The reference is a functional group bonded to a 1x1 site $Si_{10}H_{15}$ cluster with no nearest neighbors (see Figure 4). The results for ethyl and methyl surfaces have been reported previously.[39] The results for the I-terminated surface are included since this is a byproduct in one of the synthetic routes used to prepare the Si(111)-OCH_3 surface.

The strain energy calculations as well as the equilibrium geometry suggest that 100% surface coverage with -OCH_3 is feasible. Experimental observations indicate that -OCH_3 groups can be added to the surface through a relatively slow but spontaneous reaction of methanol with Si(111)-H surfaces in the dark. One possible reaction mechanism could be [Si(111)-H + CH_3-OH → Si(111)-OCH_3 + H_2].[37] Free energy and enthalpy calculations on this reaction were therefore performed using non-periodic QM (Jaguar software, Schrödinger, Portland, OR) at the B3LYP level of theory with 631G** basis sets and the Poisson-Boltzmann continuum solvation model (assuming a dielectric constant of 33.62 and a solvent radius of 2.0 Å for methanol). For this calculation, energies for each reactant and product were calculated as surrounded by the dielectric of methanol and the Si(111) surface sites were modeled as $Si(SiH_3)_3$ clusters to which -H or -OCH_3 groups were bonded. The values obtained were: ΔG^{298° = -4.9 kcal/mol and ΔH^{298° = -5.8 kcal/mol, confirming the feasibility of a spontaneous reaction to alkoxylate the surface from alcohols. Electrochemical experiments indicate that while the hydrogen-terminated silicon surface can be oxidized at BLAH potential vs SCE, the oxidation of a model compound tristrimethylsilylsilane molecule, H-Si[$Si(CH_3)_3$]$_3$, does not occur within the solvent window of methanol. These experiments indicate that the valence band energy is significantly higher in energy than the HOMO for the model compound and that the free energy for spontaneous reaction of the H-Si(111) *surface* with methanol may be significantly more exothermic than what the calculations on the $Si(SiH_3)_3$ *cluster* suggest.

Because most experimental surfaces contain etch pits and step edges, with surface sites located on the edges, strain energy calculations were also performed on unit cells that contained steps. Previous calculations[39] have indicated that a full stacking fault is

energetically favorable on the terraces of the Si(111)-CH_3 surface when etch pits with sufficiently long edges are present on the surface. The stacking fault, which changes the step edge terminations from a $<11\bar{2}>$ step edge to a structure similar to the $<\bar{1}\bar{1}2>$ step edge[50] (see Figure 7), minimizes the total strain energy of the surface by significantly lowering the strain at edge sites.[39] Because ethyl groups are even larger than methyl groups, the Si(111)-C_2H_5 surface is expected to undergo the same transformation, but it is not clear whether such a transformation can also occur for Si(111)-OCH_3. Hence, strain energy calculations were performed for -OCH_3 groups bonding to surface sites on $<11\bar{2}>$ and $<\bar{1}\bar{1}2>$ step edges (Figure 7). The bond energy to $<\bar{1}\bar{1}2>$ was calculated to be *more* favorable than to the isolated binding site by 0.15 eV/site, while the bond energy to $<11\bar{2}>$ was *less* favorable by 0.53 eV/site. Binding to $<\bar{1}\bar{1}2>$ is thus preferred by ~0.68 eV/site with respect to the bond energy to $<11\bar{2}>$. The calculated energy cost of a stacking fault is ~0.074 eV/site, approximately twice the cost of a stacking fault in the Si(111)-CH_3 surface. From the high strain energy of the sites on the $<11\bar{2}>$ step edge and the difference between bonding to $<11\bar{2}>$ and bonding to $<\bar{1}\bar{1}2>$ we conclude (using similar arguments to those presented previously[39]) that the step edges cannot be functionalized with OCH_3 groups unless a stacking fault occurs on the terraces. For a stacking fault to be energetically favorable, however, the ratio of terrace sites to edge sites must be *lower* than the ratio of the difference in energy between bonding to $<11\bar{2}>$ and bonding to $<\bar{1}\bar{1}2>$ to the stacking fault energy cost, equal to ~9 (as compared to ~19 for the methylated surface). For the methylated surface, the energy necessary for the stacking fault to emerge could be provided by the large amount of free energy released during the Grignard reaction used to add methyl groups to the Si(111)-Cl surface ($\Delta G^{298°}$

= -41.0 kcal/mol), which in turn was prepared from the Si(111)-H surface.[39] In the case of the Si(111)-OCH_3 surface prepared through the reaction of Si(111)-H with methanol, no such large change in free energy is present for the reaction, making it unlikely that a stacking fault can occur. In this system, it is more likely that the edge sites simply remain functionalized with hydrogen atoms, which do not experience significant strain at the edges.[39] However, the formation of a stacking fault may still be a possibility for other synthetic routes involving more aggressive surface reactions with a sufficiently low ratio of terrace to edge sites.

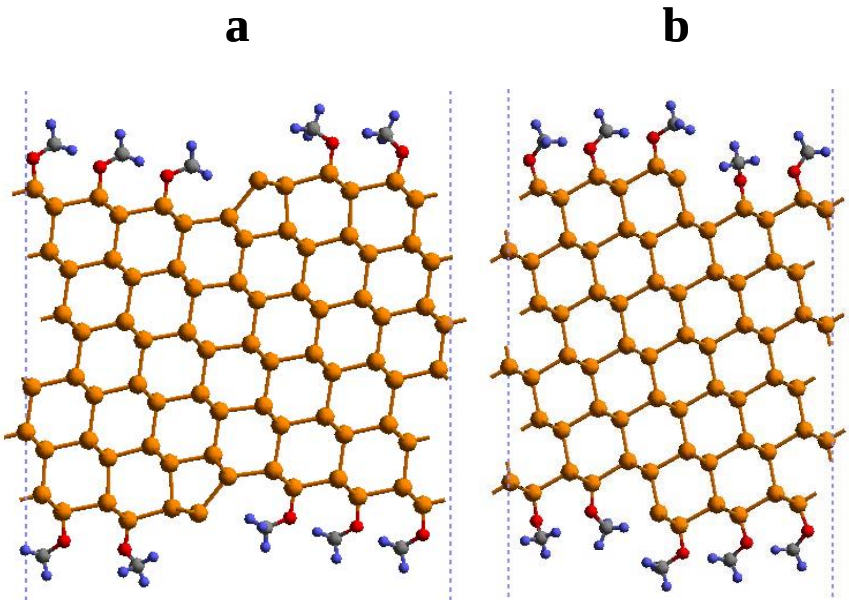

Figure 7. Unit cells used for the strain energy calculations on the Si(111)-OCH_3 surface in the presence of step edges. The unit cell containing a $<\bar{1}\bar{1}2>$ step edge (a) was obtained by cutting the silicon crystal along the $<668>$ plane, and the unit cell containing a $<1\bar{1}\bar{2}>$ step edge (b) was obtained by cutting the silicon crystal along the $<664>$ plane. The step edge surface sites are shown in the pictures without functionalization.

In summary, we have shown that the Si(111)-OCH_3 surface can, in principle, afford a route to achieve full termination of atop Si sites on an unreconstructed Si(111) surface, offering 100% coverage of functional groups with minimal strain in the alkoxyl overlayer. Relative to the Si(111)-CH_3 surface, the chemical and electrical properties of the Si(111)-OCH_3 surface should therefore reflect differences solely arising from changing the Si-C-R bonds into Si-O-C-R bonds, as opposed to coverage, packing, or other major chemical differences arising from residual Si-H bonds, at least on the terraces of such functionalized surfaces.

Acknowledgment: Santiago Solares and William Goddard received support from the Microelectronics Advanced Research Corporation (MARCO) and its Focus Center on Function Engineered NanoArchitectonics (FENA). Nathan Lewis and David Michalak acknowledge the NSF, grant CHE-0213589. David Michalak also thanks the Link Foundation for a fellowship.

SUPPORTING INFORMATION

1. Pseudopotentials and basis sets

The pseudopotentials used in these calculations are standard norm-conserving, non-separable pseudopotentials[51] generated using Hamann's methods[52,53] (the generalized norm-conserving pseudopotential method[2] was used for iodine and the new method[3] for all other atoms). The carbon, oxygen, silicon, and iodine pseudopotentials included up to

l=1, *l*=2, *l*=2, and *l*=3 projectors, respectively (with standard settings), with the *l*=1, *l*=2, *l*=2, and *l*=3 potentials, respectively, used as the local potential in each case. The hydrogen atom was also treated as a pseudopotential (rather than with a bare-core potential), with only an *l*=0 potential. Multiple tests with hydrogen atoms, H_2 molecules, and water molecules verified that the energetics of the bare core hydrogen potential and the hydrogen pseudopotential are almost indistinguishable.

The basis functions were double-zeta plus polarization quality, formed from contracted Gaussians. Hence the *occupied* orbitals Si-*s* and Si-*p* and the H-*s*, for example, had two radial degrees of freedom, and the Si-*d* and H-*p* *unoccupied* angular polarization orbitals had only one. The basis sets for hydrogen, carbon, oxygen, silicon, and iodine were contracted (4s1p/2s1p), (5s4p1d/2s2p1d), (5s5p2d/2s2p1d), (4s3p1d/2s2p1d), and (5s5p1d/2s2p1d) basis sets, respectively. This nomenclature denotes, for H for example, that four Gaussian *s*-functions were contracted into two independent functions, and one Gaussian *p*-function was used as one independent radial degree of freedom. The *d*-functions (for carbon, oxygen, silicon, and iodine) were made up of the five pure *l*=2 functions, i.e., the *s*-combination was excluded. The Gaussians and contraction coefficients for hydrogen, carbon, oxygen, silicon, and iodine are listed in Tables S-1, S-2, S-3, S-4, and S-5.

Table S-1: Basis set for hydrogen. The Gaussian decay constants α (1/bohr^2) and associated contraction coefficients c_α for the contracted Gaussian basis functions (unnormalized).

s-functions			**p-function**	
α_s	c_α (1st zeta)	c_α (2nd zeta)	α_p	c_α
0.102474	0.087388	0.075281	1.100000	1.000000
0.372304	0.405344	0.120939		
1.230858	0.485455	0		
4.783324	0.397563	0		

Table S-2: Basis set for carbon. The Gaussian decay constants α (1/bohr^2) and associated contraction coefficients c_α for the contracted Gaussian basis functions (unnormalized).

s-functions			**p-functions**			**d-function**	
α_s	C_α (1st zeta)	c_α (2nd zeta)	α_p	c_α (1st zeta)	c_α (2nd zeta)	α_d	c_α
0.155830	0.219500	1.000000	0.154701	0.107631	1.000000	0.770000	1.000000
0.458320	0.695623	0	0.523908	0.524630	0		
1.40253	0.362537	0	1.442267	1.002503	0		
2.805200	-1.296428	0	4.604695	1.675411	0		
5.610400	0.450261	0					

Table S-3: Basis set for oxygen. The Gaussian decay constants α (1/bohr^2) and associated contraction coefficients c_α for the contracted Gaussian basis functions (unnormalized).

s-functions			**p-functions**			**d-function**	
α_s	C_α (1st zeta)	C_α (2nd zeta)	α_p	c_α (1st zeta	c_α (2nd zeta)	α_d	c_α
0.193491	0.171240	1.000000	0.132619	0.059909	0.386000	0.220000	0.077290
0.521475	0.875614	0	0.392437	0.313640	1.000000	1.1000000	1.000000
1.426025	1.340022	0	1.057896	1.189398	0		
2.852050	-1.216661	0	3.145166	3.676785	0		
5.70410	0.321921	0	6.769595	-0.683244	0		

Table S-4: Basis set for silicon. The Gaussian decay constants α (1/bohr^2) and associated contraction coefficients c_α for the contracted Gaussian basis functions (unnormalized).

s-functions			**p-functions**			**d-function**	
α_s	c_α (1st zeta)	c_α (2nd zeta)	α_p	c_α (1st zeta)	c_α (2nd zeta)	α_d	c_α
0.104600	0.209953	1.0	0.094241	0.067616	1.0	0.450000	1.000000
0.272263	0.559782	0	0.317679	0.318212	0		
1.300508	-0.991282	0	1.561145	-0.066383	0		
2.601030	0.334871	0					

Table S-5: Basis set for iodine. The Gaussian decay constants α (1/bohr^2), and associated contraction coefficients c_α for the contracted Gaussian basis functions (unnormalized).

s-functions			**p-functions**			**d-function**	
α_s	c_α (1st zeta)	c_α (2nd zeta)	α_p	c_α (1st zeta)	c_α (2nd zeta)	α_d	c_α
0.1266970	0.241525	1.000000	0.082022	0.041662	1.000000	0.270000	1.000000
0.3143620	0.880824	0	0.218520	0.253357	0		
1.407096	-2.139824	0	0.508736	0.375408	0		
2.814300	1.495950	0	1.181286	-0.720357	0		
5.628600	-0.387679	0	2.362700	0.246727	0		

2. K-points

The number of k-points for each calculation was varied according to the unit cell size. 8 k-points were used in the direction of each of the two cell unit vectors for the 1x1 unit cell (there are only two unit vectors because the models used are only 2D periodic). The number of k-points for the other structures was set to the closest integer, inversely proportional to the cell dimension along each unit vector. Thus, the 2x2 and 3x3 unit cells had 4 and 3 k-points in each direction, respectively.

3. Spin polarization

Calculations of singlet states were performed with restricted (closed shell) DFT. Calculations of doublet (radical) states or dissociated triplet states, necessary for the

computation of bond energies, were performed with unrestricted (spin-polarized) DFT, in which the N_α spin-up and N_β spin-down orbitals were optimized independently.

REFERENCES:

1. Bansal, A.; Li, X. L.; Lauermann, I.; Lewis, N. S.; Yi, S. I.; Weinberg, W. H.; *J. Am. Chem. Soc.* **1996,** *118,* 7225.

2. Bansal, A.; Li, X. L.; Yi, S. I.; Weinberg, W. H.; Lewis, N. S.; *Journal of Physical Chemistry B* **2001,** *105,* 10266.

3. He, J.; Patitsas, S. N.; Preston, K. F.; Wolkow, R. A.; Wayner, D. D. M.; *Chem. Phys. Lett.* **1998,** *286,* 508.

4. Mitchell, S. A.; Boukherroub, R.; Anderson, S.; *Journal of Physical Chemistry B* **2000,** *104,* 7668.

5. Okubo, T.; Tsuchiya, H.; Sadakata, M.; Yasuda, T.; Tanaka, K.; *Appl. Surf. Sci.* **2001,** *171,* 252.

6. Terry, J.; Linford, M. R.; Wigren, C.; Cao, R. Y.; Pianetta, P.; Chidsey, C. E. D.; *Appl. Phys. Lett.* **1997,** *71,* 1056.

7. Terry, J.; Linford, M. R.; Wigren, C.; Cao, R. Y.; Pianetta, P.; Chidsey, C. E. D.; *J. Appl. Phys.* **1999,** *85,* 213.

8. Yu, H. Z.; Boukherroub, R.; Morin, S.; Wayner, D. D. M.; *Electrochem. Commun.* **2000,** *2,* 562.

9. Royea, W. J.; Juang, A.; Lewis, N. S.; *Appl. Phys. Lett.* **2000,** *77,* 1988.

10. Webb, L. J.; Nemanick, E. J.; Biteen, J. S.; Knapp, D. W.; Michalak, D. J.; Traub, M. C.; Chan, A. S. Y.; Brunschwig, B. S.; Lewis, N. S.; *Journal of Physical Chemistry B* **2005,** *109,* 3930.

11. Yu, H. B.; Webb, L. J.; Ries, R. S.; Solares, S. D.; Goddard, W. A.; Heath, J. R.; Lewis, N. S.; *Journal of Physical Chemistry B* **2005,** *109,* 671.

12. Hunger, R.; Fritsche, R.; Jaeckel, B.; Jaegermann, W.; Webb, L. J.; Lewis, N. S.; *Phys. Rev. B* **2005,** *72.*

13. Webb, L. J.; Lewis, N. S.; *Journal of Physical Chemistry B* **2003,** *107,* 5404.

14. Juang, A.; Scherman, O. A.; Grubbs, R. H.; Lewis, N. S.; *Langmuir* **2001,** *17,* 1321.

15. Boukherroub, R.; Wayner, D. D. M.; *J. Am. Chem. Soc.* **1999,** *121,* 11513.

16. Cicero, R. L.; Linford, M. R.; Chidsey, C. E. D.; *Langmuir* **2000,** *16,* 5688.

17. Effenberger, F.; Gotz, G.; Bidlingmaier, B.; Wezstein, M.; *Angew. Chem.-Int. Edit.* **1998,** *37,* 2462.

18. Terry, J.; Mo, R.; Wigren, C.; Cao, R. Y.; Mount, G.; Pianetta, P.; Linford, M. R.; Chidsey, C. E. D.; *Nucl. Instrum. Methods Phys. Res. Sect. B-Beam Interact. Mater. Atoms* **1997,** *133,* 94.

19. Linford, M. R.; Chidsey, C. E. D.; *J. Am. Chem. Soc.* **1993,** *115,* 12631.

20. Linford, M. R.; Fenter, P.; Eisenberger, P. M.; Chidsey, C. E. D.; *J. Am. Chem. Soc.* **1995,** *117,* 3145.

21. Boukherroub, R.; Wayner, D. D. M.; Lockwood, D. J.; Canham, L. T.; *J. Electrochem. Soc.* **2001,** *148,* H91.

22. Boukherroub, R.; Wayner, D. D. M.; Sproule, G. I.; Lockwood, D. J.; Canham, L. T.; *Nano Lett.* **2001,** *1,* 713.

23. Boukherroub, R.; Wojtyk, J. T. C.; Wayner, D. D. M.; Lockwood, D. J.; *J. Electrochem. Soc.* **2002,** *149,* H59.

24. Sieval, A. B.; Demirel, A. L.; Nissink, J. W. M.; Linford, M. R.; van der Maas, J. H.; de Jeu, W. H.; Zuilhof, H.; Sudholter, E. J. R.; *Langmuir* **1998,** *14,* 1759.

25. Sieval, A. B.; van den Hout, B.; Zuilhof, H.; Sudholter, E. J. R.; *Langmuir* **2001,** *17,* 2172.

26. Sung, M. M.; Kluth, G. J.; Yauw, O. W.; Maboudian, R.; *Langmuir* **1997,** *13,* 6164.

27. Boukherroub, R.; Morin, S.; Bensebaa, F.; Wayner, D. D. M.; *Langmuir* **1999,** *15,* 3831.

28. Buriak, J. M.; Allen, M. J.; *J. Am. Chem. Soc.* **1998,** *120,* 1339.

29. Buriak, J. M.; Stewart, M. P.; Geders, T. W.; Allen, M. J.; Choi, H. C.; Smith, J.; Raftery, D.; Canham, L. T.; *J. Am. Chem. Soc.* **1999,** *121,* 11491.

30. Schmeltzer, J. M.; Porter, L. A.; Stewart, M. P.; Buriak, J. M.; *Langmuir* **2002,** *18,* 2971.

31. Zazzera, L. A.; Evans, J. F.; Deruelle, M.; Tirrell, M.; Kessel, C. R.; McKeown, P.; *J. Electrochem. Soc.* **1997,** *144,* 2184.

32. Bateman, J. E.; Eagling, R. D.; Horrocks, B. R.; Houlton, A.; *Journal Of Physical Chemistry B* **2000,** *104,* 5557.

33. Bateman, J. E.; Horrocks, B. R.; Houlton, A.; *J. Chem. Soc.-Faraday Trans.* **1997,** *93,* 2427.

34. Haber, J. A.; Lauermann, I.; Michalak, D.; Vaid, T. P.; Lewis, N. S.; *Journal of Physical Chemistry B* **2000,** *104,* 9947.

35. Haber, J. A.; Lewis, N. S.; *Journal Of Physical Chemistry B* **2002,** *106,* 3639.

36. Cleland, G.; Horrocks, B. R.; Houlton, A.; *J. Chem. Soc.-Faraday Trans.* **1995,** *91,* 4001.

37. Boukherroub, R.; Morin, S.; Sharpe, P.; Wayner, D. D. M.; Allongue, P.; *Langmuir* **2000,** *16,* 7429.

38. Warntjes, M.; Vieillard, C.; Ozanam, F.; Chazalviel, J. N.; *J. Electrochem. Soc.* **1995,** *142,* 4138.

39. Solares, S. D.; Yu, H. B.; Webb, L. J.; Lewis, N. S.; Heath, J. R.; Goddard, W. A.; *J. Am. Chem. Soc.*, submitted.

40. Yu, H. B.; Webb, L. J.; Solares, S. D.; Cao, P.; Goddard, W. A.; Heath, J. R.; Lewis, N. S.; *Journal of Physical Chemistry B* submitted.

41. Msaad, H.; Michel, J.; Lappe, J. J.; Kimerling, L. C.; *J. Electron. Mater.* **1994,** *23,* 487.

42. Msaad, H.; Michel, J.; Reddy, A.; Kimerling, L. C.; *J. Electrochem. Soc.* **1995,** *142,* 2833.

43. Gstrein, F.; Michalak, D. J.; Royea, W. J.; Lewis, N. S.; *Journal of Physical Chemistry B* **2002,** *106,* 2950.

44. Michalak, D. J.; Lewis, N. S.; *Appl. Phys. Lett.* **2002,** *80,* 4458.

45. Royea, W. J.; Michalak, D. J.; Lewis, N. S.; *Appl. Phys. Lett.* **2000,** *77,* 2566.

46. Cai, W.; Lin, Z.; Strother, T.; Smith, L. M.; Hamers, R. J.; *Journal of Physical Chemistry B* **2002,** *106,* 2656.

47. Reddy, A. J.; Chan, J. V.; Burr, T. A.; Mo, R.; Wade, C. P.; Chidsey, C. E. D.; Michel, J.; Kimerling, L. C.; *Physica B* **1999,** *274,* 468.

48. Schultz, P. A.; *Sandia National Labs, Albuquerque NM*, http://dft.sandia.gov/Quest/.

49. Perdew, J. P.; Burke, K.; Ernzerhof, M.; *Phys. Rev. Lett.* **1996,** *77,* 3865.

50. Itchkawitz, B. S.; McEllistrem, M. T.; Boland, J. J.; *Phys. Rev. Lett.* **1997,** *78,* 98.

51. Redondo, A.; Goddard, W.A. III; McGill, T.C.; *Phys. Rev. B* **1977,** *15,* 5038.

52. Hamann, D.R.; *Phys. Rev.* **1989,** *40,* 2980.

53. Hamann, D.R.; pseudopotential generation program PUNSLDX, unpublished.

Chapter 8: Density Functional Theory Study of the Crystal Structure and Thermodynamics of η-Cu_3Si

ABSTRACT. Crystalline Cu_3Si is of significant industrial interest, although its crystalline structure and energetics are not yet well understood. In order to increase our understanding of this crystal we performed *ab initio* quantum mechanics calculations on various crystals with the general formula Cu_3Si, including those derived from the trigonal-rombohedral η'-Cu_7Si_2 structure deduced from electron diffraction data by Solberg in 1978, and show that none of them has a favorable heat of formation with respect to pure crystalline copper and silicon. The lowest enthalpy structure is face-centered-cubic with a heat of formation of +0.035 eV/Cu_3Si. Through statistical mechanical calculations on disordered supercell variants of the η'-Cu_7Si_2 crystal with a 3:1 ratio of copper to silicon, we show that the driving force for the formation of Cu_3Si is driven by the *entropic* contribution of the free energy. Thus, although the face-centered-cubic Cu_3Si structure has the lowest enthalpy, it has zero entropy (i.e., only one crystalline arrangement is possible) and is thus not favorable. Our results are consistent with Solberg's experimental results from 1978.

1. Introduction

There have been various studies investigating the growth mechanism and morphology of copper-doped silicon precipitates with chemical composition similar to that of Cu_3Si,[1-10] but until a 1978 study published by Solberg[11] there were no detailed studies of the crystal structure. Before Solberg's study, Nes and Washburn[5] (1971) and Das[12] (1973) had proposed cubic crystal structures based on electron microscopy, but due to the limited experimental data, their structures could not be confirmed without further experimental work. [11]

The Cu/Si phase diagrams[13-14] indicate that the most stable Cu/Si phase at the 3:1 composition and room temperature is the η"-phase. At higher temperatures, the η'- and η-phases become more stable (the latter being the most stable at the highest temperatures). Based on crystallographic data and on the assumption that the η"-phase is a combination of the η'- and η-phases, Solberg[11] proposed structures for the three phases. The deduced structure for the η'-phase has an atomic ratio of copper to silicon of 7:2, which is different than the observed 3:1 ratio, but Solberg argues that the correct ratio can be obtained by substituting copper atoms with silicon at the various available copper positions in the crystal, on average once every four unit cells (i.e., there is disordered silicon occupying the lattice sites of the structure). Solberg's experimental results provide some general guidelines as to which crystal positions in the η'-Cu_7Si_2 structure are likely to undergo the Cu/Si substitutions, but do not provide a conclusive answer as to the relative preferences between them.

To our knowledge, the electronic structure calculations of Magaud et al.[15] are the only ones reported in the literature for Solberg's η'-Cu_7Si_2 structure. However, these calculations do not provide values of the cohesive energy of the crystal and are based on the LMTO (linear muffin tin orbitals) method within the atomic sphere approximation[16], which constrains the potential around each atom in the crystal to be spherical. Hence, more accurate calculations are still required.

From a theoretical standpoint there remain three fundamental questions that must be answered to understand the nature of Cu_3Si:

(1) How does the η'-phase (the representative ordered structure from Solberg's study) compare energetically with other possible crystal structures containing the same Cu:Si ratio?

(2) Within the η'-phase, what are the preferred sites for the Cu/Si substitutions that lead to the 3:1 ratio of copper to silicon?

(3) What is the driving force for the formation of the Cu/Si crystal from the pure components?

These questions are the object of this report. First we present a summary of the experimental findings regarding the crystal structure. Then we report Quantum Mechanics (QM) cohesive energy calculations on various Cu_3Si lattice types, which indicate that the enthalpy of the Cu_3Si structures considered is *not* favorable with respect to the pure components. This finally leads to the analysis of disorder and Cu-Si crystal bonding preferences, which suggests that the driving force for the formation of Cu_3Si is entropic and that Cu/Si surfaces are locally unstable (reactive).

2. Previous Experimental knowledge on the Cu_7Si_2 Crystal Structure

According to the electron phase diagram of reference 12, the Cu/Si η-phase is stable between approximately 23 and 25% at. silicon for temperatures between 560 and 850 °C (according to reference 13, the η-phase occurs in its pure state only between ~23 and 23.5% at. silicon and coexists with the silicon phase above 24%). Reference 12 also indicates that at 25% at. silicon, the stable phase between 457 and 558°C is the η'-phase and that the stable phase below 457°C (including room temperature) is the η"-phase. Thus it is reasonable that the starting point for a structural study of Cu_3Si crystals at room temperature should be that they belong to the η"-phase.

There are several past studies on the growth mechanism and morphology of Cu/Si crystals obtained through precipitation of copper-doped silicon[1-10], most of which provide little or no information on the crystal structure. In 1978, based on previous electron diffraction/microscopy data and on his own electron-diffraction experiments of thin foils of Cu_3Si colonies, Solberg[11] identified the Cu_3Si crystal precipitates at room temperature with the η"-phase (consistent with the phase diagram). By assuming that this phase is a two-dimensional long-period superstructure based on the η'- and η-phases (the former being an ordered structure and the latter disordered), he uses the diffraction data to suggest structures for all three phases. According to this study the η"-phase can be explained in terms of the η'-phase structure (Figure 1) through the introduction of stacking faults which lead to the long-period superstructures. The proposed primitive η'-phase crystal is trigonal-rombohedral and belongs to the $r\bar{3}$ space group, with cell parameters a = 4.72 Å and α = 95.72° (note that this α refers to the cell angle and not to

the blue atomic layers in the crystal structures of Figure 1. The difference should be clear from the context throughout the paper).

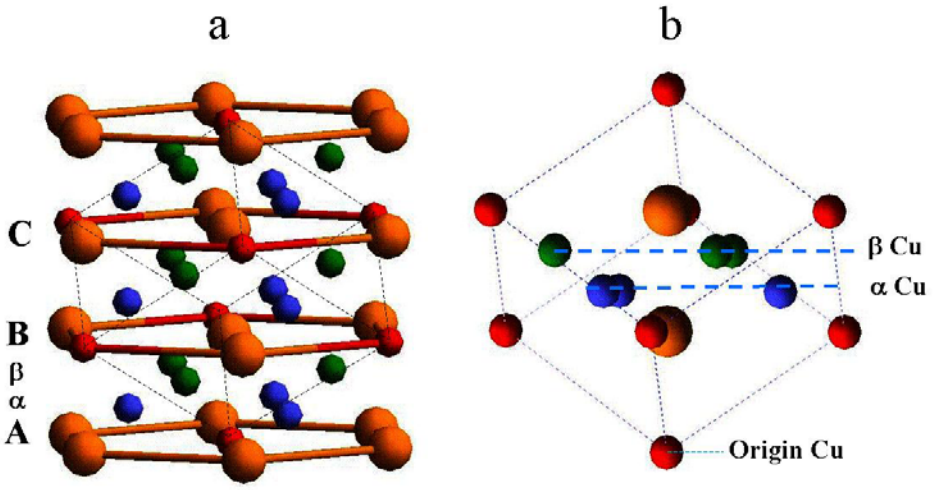

Figure 1. Hexagonal (a) and primitive (b) crystal structures for the Cu_7Si_2 η'-phase. In these structures the red, blue, and green atoms are copper, and the orange atoms are silicon. The silicon-rich layers of the hexagonal structure are labeled in the normal stacking order ABC, but stacking faults are possible (according to Solberg[11] the stacking pattern consistent with his diffraction data is ABCCABBCA… Note that this stacking pattern is not necessarily unique – it is just the one most consistent with Solberg's experimental data). In between the silicon-rich layers there are pure copper layers labeled α and β. The primitive unit cell (b) has experimental cell parameters a = 4.72 Å and α = 95.72° (note that this second α refers to the cell angle and not to the blue atomic layers in the crystal. The difference should be clear from the context throughout the paper).

This ordered η'-phase crystal structure has a copper-to-silicon ratio of 7:2 (as opposed to 3:1), but Solberg contends that the correct ratio of 3:1 is achieved by substitution of a copper atom with a silicon atom on average *every four unit cells.* [11] He proposes that this substitution can take place in one of three different schemes: (i) randomly at all the available Cu sites, (ii) among the six equivalent Cu sites in the α and β layers (blue and green in Figure 1, respectively), and (iii) only at the Cu origin positions (red in Figure 1). Based on a comparison of the calculated and observed diffraction pattern intensities, the third possibility has been discarded. [17] However, the first two alternatives cannot be distinguished on the basis of the experimental results. [11] Since the copper sites in the mixed-type atom planes (α and β) are very different than those at the origin positions, Solberg proposes that option (ii) above represents the true distribution.

The experimental data also shows that the η"-phase is a long period superstructure based on the η'-phase, which Solberg proposes is generated by altering the stacking pattern in the hexagonal structure from the normal ABCABCABC… pattern into, for example, ABCCABBAC…, the pattern consistent with the crystals used in his experiments (See Figure 1a). [11]

3. Quantum Mechanical Cohesive Energy Calculations on Cu_7Si_2 and Cu_3Si Crystal Structures

Our QM calculations were performed with SeqQuest[18] software (Sandia National Labs., Albuquerque, NM), a Density Functional Theory (DFT) electronic structure code, which uses Gaussian basis sets and norm-conserving pseudopotentials (see supporting

information for details on the basis sets, pseudopotentials, wave function grids, and k-points). All calculations used the Perdew-Burke-Ernzerhof approximation of DFT. [20]

We first calculated the cohesive energy of the copper (face-centered-cubic) and silicon (diamond) crystals as the difference between the crystal energy per atom and the energy of one atom in isolation and obtained $E_{cohesive\text{-}Cu}$ = -3.437 eV/atom and $E_{cohesive\text{-}Si}$ = -4.574 eV/atom. We then calculated the cohesive energy of the different Cu_xSi_y crystals using the following formula:

$$E_{cohesive\text{-}rel}\ (Cu_xSi_y) = E(Cu_xSi_y\ \text{cell}) - x^* E_{atom\text{-}Cu} - y^* E_{atom\text{-}Si} - x^* E_{cohesive\text{-}Cu} - y^* E_{cohesive\text{-}Si}\ , \quad (1)$$

where $E_{cohesive\text{-}rel}$ (Cu_xSi_y) is the cohesive energy of the Cu_xSi_y crystal *with respect to the pure Cu and Si crystals* (this provides the *enthalpic* driving force for the formation of the Cu_xSi_y crystal from pure Cu and Si), E(Cu_xSi_y cell) is the calculated QM energy of the unit Cu_xSi_y cell, $E_{atom\text{-}Cu}$ and $E_{atom\text{-}Si}$ are the QM energies of isolated Cu and Si atoms, respectively, and $E_{cohesive\text{-}Cu}$ and $E_{cohesive\text{-}Si}$ are the quantities defined in the previous paragraph.

The calculations for the η'-Cu_7Si_2 structure gave a cohesive energy ($E_{cohesive\text{-}rel}$) value of +0.177 eV/Cu_3Si for the relaxed unit cell (with cell parameters a = 4.92 Å and α = 94.44°) and +1.119 eV/cell for the unit cell dimensions provided in Solberg's experimental study (a = 4.72 Å and α = 95.72°). Both of these values are positive, indicating that there is no *enthalpic* driving force for the formation of the η'-Cu_7Si_2 crystal (i.e., this structure is not energetically favorable unless disorder is introduced). Table 1 contains the calculated cohesive energies (in eV per Cu_3Si) for various crystal

structures with a 3:1 ratio of copper to silicon. The lowest energy was obtained for the face-centered-cubic structure ($E_{cohesive\text{-}rel}$ = 0.035 eV/Cu_3Si), shown in Figure 2, which is still higher in energy than pure copper and silicon. The highest energy ($E_{cohesive\text{-}rel}$ = 1.054 eV/Cu_3Si) was obtained for a 3x1x1 supercell of η'-Cu_7Si_2 containing an added interstitial silicon atom (this result discards the possibility of achieving the 3:1 ratio of copper to silicon by introducing interstitial silicon atoms). All structures considered are less favorable than the pure crystalline components. From these results we conclude that the formation of Cu_3Si crystals must be driven by an *entropic* contribution in the free energy, which requires the presence of disorder in the structure to allow multiple configurations. This is discussed in the next section.

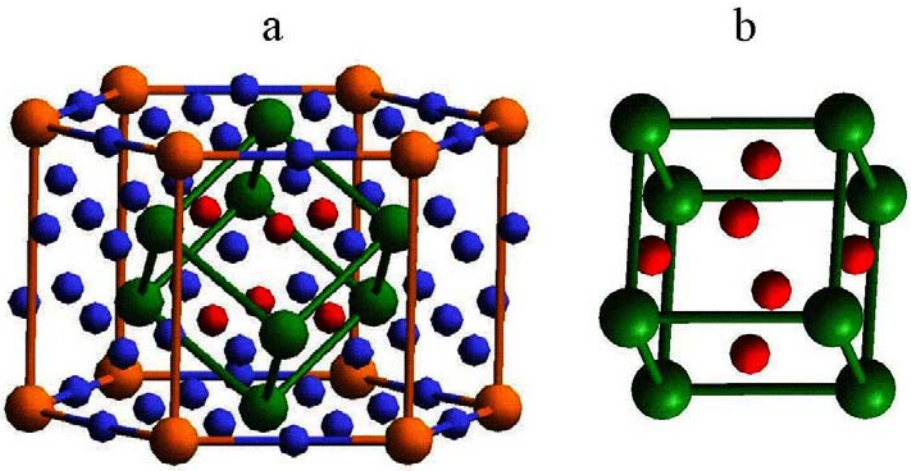

Figure 2. Hexagonal (a) and cubic (b) representation of the face-centered cubic Cu_3Si crystal (lattice constant 3.73 Å). The cubic unit cell contains silicon atoms at the corners and copper atoms at the center of each face. Although this structure has the lowest enthalpy of all the crystals considered, it has a positive energy of formation with respect to pure crystalline copper and silicon and is thus not favorable.

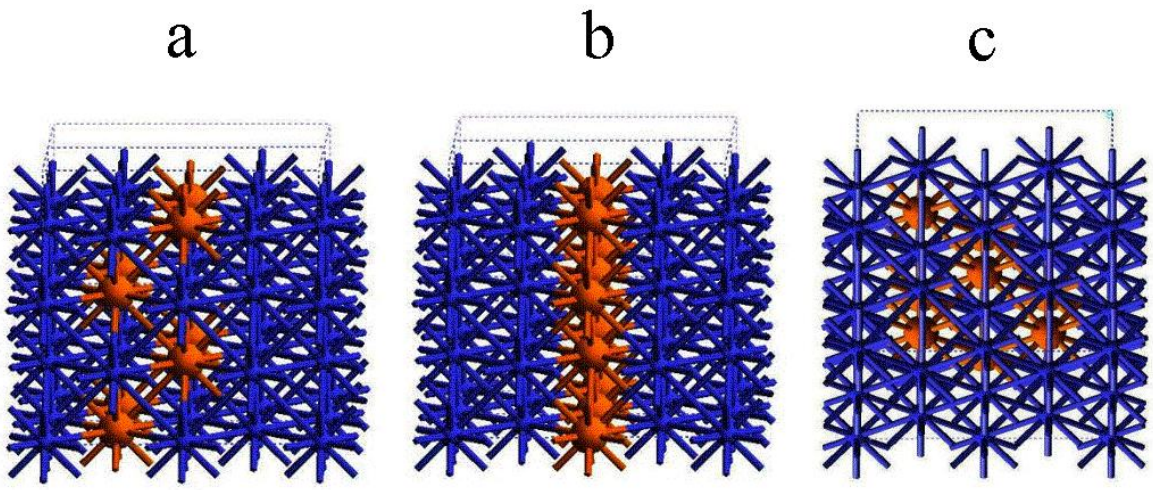

Figure 3. Cu_6Si_2 face-centered-cubic crystals with the copper and silicon atoms rearranged so as to have isolated zig-zag chains (a) and isolated planes (b) of Si atoms (two unit cells are shown in each case) and $Cu_{24}Si_8$ face-centered-cubic crystal (c) containing a silicon pocket surrounded by copper atoms. The lattice constant for all three structures is 3.73 Å (obtained from the optimized Cu_3Si face-centered-cubic structure shown in Figure 2).

Table 1: Cohesive energies of 3:1 Cu-Si crystals with respect to pure copper and silicon, calculated using equation 1. As the data shows, all structures are higher in energy (enthalpy) than the pure components. The most favorable structure is face-centered-cubic (Figure 2), which contains no Si-Si bonds.

Description	**$E_{cohesive\text{-}rel}$ (eV/Cu_3Si)**
Cu_3Si face-centered-cubic cell (lattice constant = 3.73 Å)	0.035
Cu_6Si_2 face-centered-cubic cell with Cu and Si atoms rearranged so as to have isolated parallel zig-zag chains[a] of Si atoms	0.135
Cu_6Si_2 face-centered-cubic cell with Cu and Si atoms rearranged so as to have isolated plains[a] of Si atoms	0.390
Cu24Si8 face-centered-cubic cell with Si atoms arranged in a pocket surrounded by Cu[a]	0.231
4x1x1 η'-$Cu_{27}Si_9$ supercell[b] containing Si-Si-Si bonds of 71 and 110°	0.609
4x1x1 η'-$Cu_{27}Si_9$ supercell[b] containing Si-Si-Si bonds of 180°	0.612
2x2x1 η'-$Cu_{27}Si_9$ supercell[b] containing Si-Si-Si bonds of 105 and 115°	0.114
Cu_6Si_2 base-centered-cubic unit cell with zig-zag Si chains[c]	0.195
$Cu_{12}Si_4$ base-centered-cubic unit cell with zig-zag Si chains[c]	0.115
3x1x1 η'-$Cu_{21}Si_7$ supercell[c] containing an interstitial Si atom	1.054

[a]See Figure 3. The lattice constant for these structures is the same as that of the optimized Cu_3Si face-centered-cubic cell, 3.73 Å.
[b]In these 4x1x1 supercells of η'-Cu_7Si_2 one copper atom has been substituted with silicon to obtain the 3:1 ratio of copper to silicon. The cell parameters were kept fixed during the energy minimization at the relaxed values for η'-Cu_7Si_2 (a = 4.92 Å and α = 94.44°).
[c]See Figure 4.
[d]This structure was produced by adding an interstitial Si atom to a 3x1x1 supercell of η'-Cu_7Si_2 to obtain the 3:1 ratio of copper to silicon. The cell parameters were kept fixed during the energy minimization at the relaxed values for η'-Cu_7Si_2 (a = 4.92 Å and α = 94.44°).

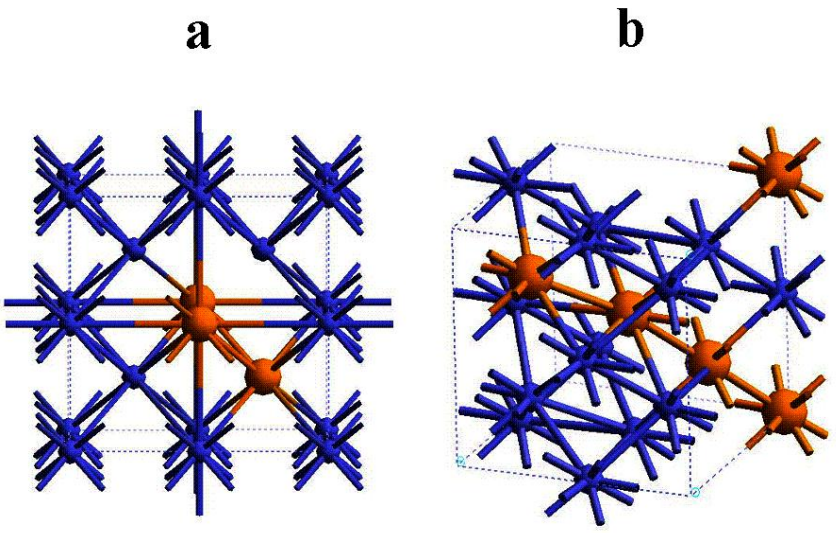

Figure 4. Base-centered-cubic Cu_6Si_2 (a) and $Cu_{12}Si_4$ (b) structures. Structure (a) contains an zig-zag infinite chain of silicon atoms, while structure (b) contains an infinite linear chain.

4. Evaluation of Bonding Preferences for Silicon Atoms distributed in the Face-Centered-Cubic Copper Crystal

The results presented in the previous section indicate that in order for a Cu_3Si crystal to be favorable with respect to pure copper and silicon, it is necessary that multiple configurations be possible. In order to be able to discriminate between various arrangements for a given composition we determined the relative bonding preferences of different configurations with a given composition. To do this we calculated the energy of a face-centered-cubic unit cell containing 32 copper atoms in which an increasing number of them was substituted with silicon. Thus we performed calculations for unit cells containing 2, 3, and 4 silicon atoms. For each number of silicon atoms we calculated the cell energy for various configurations (for example, with the silicon atoms bonded to

each other, isolated, forming various bond angles, etc.) Figure 5 shows three of the configurations analyzed for the unit cell containing three silicon atoms and provides the cell energy relative to the lowest energy obtained for any configuration containing the same number of silicon atoms. The general conclusions of this study are that silicon atoms in the face-centered-cubic Cu lattice prefer to be isolated from each other and with angles as wide as possible with respect to other Si atoms (except for the case when infinite linear chains are formed). This is in agreement with the results from the previous section, which indicate that the lowest energy of any Cu_3Si crystal corresponds to the face-centered-cubic unit cell, the only arrangement in which there are no Si-Si bonds. As it will be shown in the next section, which considers both enthalpic and entropic contributions to the free energy, this structure is not favorable because it only has one possible arrangement and thus has zero entropy. The results of this study are summarized in Table 2.

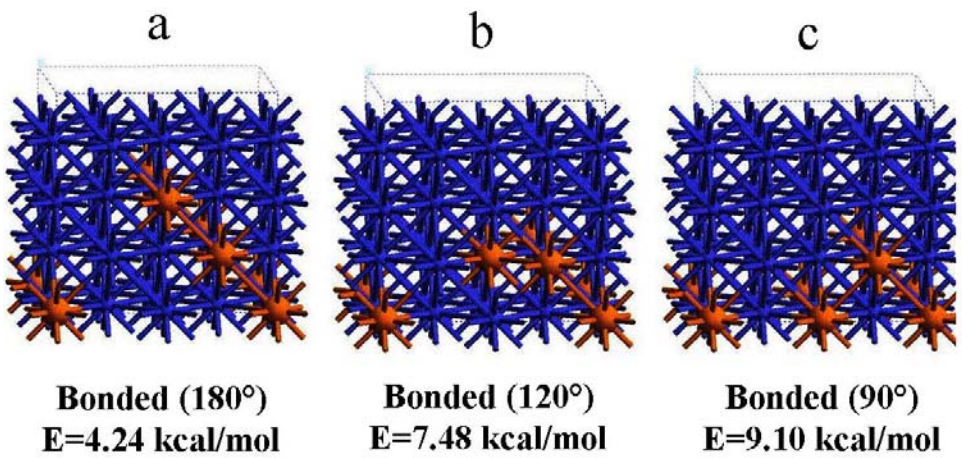

Figure 5. Three of the configurations analyzed for a 32-atom face-centered-cubic copper unit cell containing three silicon atoms in the lattice. The energy of the cell is given relative to the lowest energy configuration of the same compositions, which occurs when the three silicon atoms are as isolated from each other as possible (1-3 neighbors).

Table 2: Relative energies for 32-atom face-centered-cubic copper crystal structures containing 2, 3, and 4 silicon atoms as a function of the atomic arrangement. The energies in each case are given with respect to the most favorable configuration having the same number of silicon atoms.

Number of Si atoms	Configuration Description for the Si atoms	Energy, eV/cell
Structures containing two Si atoms per cell		
2	Bonded	8.74
2	1-3 neighbors forming a Si-Cu-Si angle of 90°	8.00
2	1-3 neighbors forming a Si-Cu-Si angle of 120°	3.70
2	1-3 neighbors forming a Si-Cu-Si angle of 180°	3.17
2	1-4 neighbors (as far as possible from each other in the 32-atom unit cell)	0.00[a]
Structures containing three Si atoms per cell		
3	Bonded forming a Si-Si-Si angle of 180°	4.24
3	Bonded forming a Si-Si-Si angle of 120°	7.48
3	Bonded forming a Si-Si-Si angle of 90°	9.10
3	Bonded forming a Si-Si-Si angle of 60°	11.25
3	2 Si atoms bonded to each other, with the third Si atom being a 1-3 neighbor to one of them	2.51
3	Si atoms are 1-3 neighbors (as far as possible from each other in the 32-atom unit cell)	0.00[b]
Structures containing three Si atoms per cell		
4	Infinite zig-zag Si chain with Si-Si-Si angles of 90°	6.76
4	Infinite straight Si chain with Si-Si-Si angles of 180°	11.20
4	Tight Si chain with Si-Si-Si angles of 60°	8.12
4	Si atoms are 1-3 neighbors (as far as possible from each other in the 32-atom unit cell)	0.00[c]

[a]Reference energy for unit cells containing two Si atoms
[b]Reference energy for unit cells containing three Si atoms
[c]Reference energy for unit cells containing four Si atoms

5. Evaluation of disordered Cu/Si Substitutions in the η'-Cu_7Si_2 Crystal to Produce Cu_3Si

As described above, we did not find any Cu_3Si crystal structure whose enthalpy is lower than that of pure copper and silicon. Even the η'-Cu_7Si_2 structure deduced experimentally by Solberg[11] is higher in enthalpy than the pure components. Hence, it was necessary to evaluate the presence of disorder as the source of stability in these structures. For this, we started with a 2x2x1 supercell of the η'-Cu_7Si_2 structure (Figure 6) and considered seven possible lattice sites where a Cu atom could be substituted with Si to obtain a periodic $Cu_{27}Si_9$ structure (we used the η'-Cu_7Si_2 crystal as the basis of our study because this is the only one supported by experimental data). For each of these structures we calculated the enthalpy and used these values to construct a canonical partition function from which the various thermodynamic functions can be derived. The energies corresponding to the different Cu/Su substitutions are given in Table 3, all of which are higher than that of pure components. It is worth noting that the most favorable substitution in this unit cell corresponds to the origin position. In his conclusions regarding the formation of Cu_3Si from η'-Cu_7Si_2, Solberg[11] proposed that the most likely Cu/Si substitution sites would be the α and β layers, but our results show that the origin site is the most favorable. The relative energy differences between the various substitutions are consistent with the results of the bonding preferences study (section 4). The lowest energy structure (origin substitution) leads to finite 5-atom silicon chains with the widest Si-Si-Si bond angles (180°); the second lowest energy structures (substitution

at sites 3 and 4) lead to finite 5-atom silicon chains in zig-zag configuration; two of the highest energy configurations (substitution at sites 2 and 5) lead to infinite zig-zag silicon chains (along the shortest dimension of the supercell). Although substitutions at sites 1 and 6 do not lead to infinite silicon chains (they also lead to finite 5-atom zig-zag chains), they are high in energy. The 5-atom silicon chains resulting from these substitutions are perpendicular to those obtained from performing substitutions at sites 3 and 4, but there is no other obvious difference between them (see Figure 7)

Since none of the substitutions leads to a favorable heat of formation for the Cu-Si crystal, we conclude that it is the entropic contribution that is most significant in the formation of Cu_3Si.

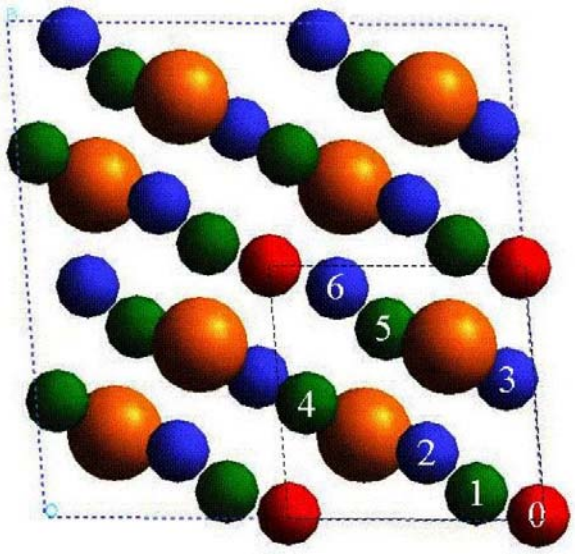

Figure 6. Possible sites for substituting copper atoms with silicon in a 2x2x1 η'-$Cu_{28}Si_8$ supercell. The color code is the same as in Figure 1.

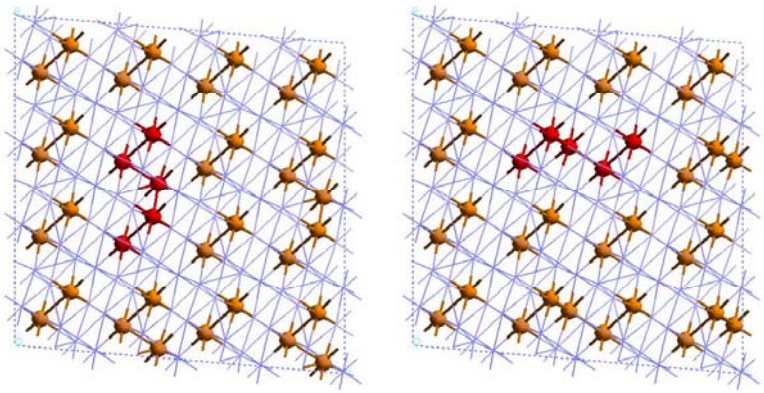

Site 1 substitution **Site 3 substitution**

Figure 7. Illustration of the 5-atom silicon chains formed by Cu/Si substitutions at sites 1 and 3 on a 2x2x1 η'-$Cu_{28}Si_8$ supercell (Figure 6). The energy of the structure on the left (obtained by performing the Cu/Si substitution at site 1) is 0.18 eV/Cu_3Si higher than that of the structure on the right (obtained by performing the Cu/Si substitution at site 3).

Table 3: Cohesive energies for the structures resulting from the different Cu/Si substitutions in the 2x2x1 η'-$Cu_{28}Si_8$ supercell (Figure 6) calculated using Quantum Mechanics. The energies are given with respect to pure crystalline copper and silicon. All the atoms in the unit cell were allowed to relax, but the lattice parameters were kept fixed at the values obtained for the relaxed η'-Cu_7Si_2 unit cell for all calculations.

Substitution Site (in Figure 6)	**$E_{cohesive\text{-}rel}$ (eV/Cu_3Si)**
0 (origin)	0.085
1 (β)	0.123
2 (α)	0.122
3 (α)	0.105
4 (β)	0.105
5 (β)	0.120
6 (α)	0.117

Using the results of Table 3 we calculated the canonical partition function and from it the free energy, which is plotted in Figure 8 as a function of temperature. As the graph shows, the formation of the Cu_3Si crystal containing the various substitutions becomes favorable above ~380 K (~107° C). This scheme, which considers a certain level of disorder, is more consistent with the experimental observations than a purely entropic analysis, but it still introduces constraints into the crystal by requiring that the substitutions take place in 2x2x1 supercells, thus limiting the entropy of the system. One could perform increasingly better approximations by considering larger supercells, which would result in more combinations of Cu/Si substitutions. For comparison purposes we performed these calculations using 8 and 12 unit cells at a time. Since the greatest contribution to the free energy comes from the disorder in the system, we performed these calculations using an average energy for all substitutions (0.111 eV/Cu_3Si), penalizing those combinations where two or three Cu/Si substitutions occur in the same η'-Cu_7Si_2 unit cell, according to the results of section 4. Thus, we introduced energy penalties of 8.0 and 11.0 eV/Cu_3Si for combinations where two or three substitutions occurred in the same unit cell, respectively. These are *approximate* penalties in the same order of magnitude to those previously calculated for different bonding arrangements of silicon atoms in a copper lattice. As in the case where only four unit cells were considered, we calculated the partition functions and derived the free energy expressions, which are also plotted in Figure 8 as a function of temperature. Both of these curves (obtained by considering 8 and 12 unit cells) lead to a slightly lower temperature where the Cu_3Si crystal is in equilibrium with the pure components (~350 K) than when only

four unit cells are considered (~380 K). The curve for 8 unit cells is steeper than that for 4 unit cells, and the curve for 12 unit cells is the least steep of all.

While this study provides insight into the thermodynamics of Cu_3Si crystals, one must also keep in mind that there are many factors it does not include. For example, we did not consider the effect of the long-period superstructures (which according to Solberg are temperature-dependent[11]) on the free energy of the crystal. These curves must also be regarded with caution due to the assumptions made and the approximate energy penalties used, but nonetheless they provide a general explanation for the stability of the Cu_3Si structures.

The fact that the driving force for the formation of Cu_3Si is entropic (and thus temperature dependent) has implications on its reactivity at the crystal surfaces because all structures are locally unstable (i.e., they have higher enthalpy than pure Cu and Si), and the overall crystal stability increases with temperature.

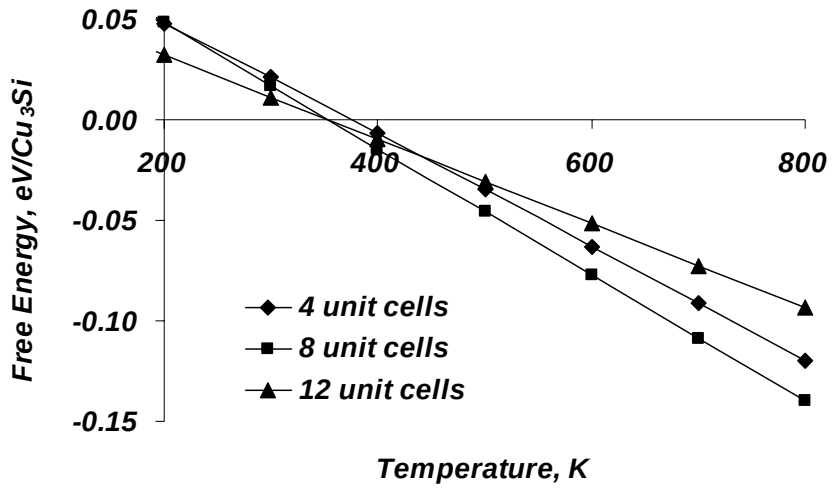

Figure 8. Free energy vs. temperature for Cu_3Si crystals obtained by the substitution of a copper atom with silicon on average every four unit cells in the η'-Cu_7Si_2 structure. The

different curves correspond to the number of unit cells used in the computation of the different numbers of possible arrangements in which the Cu/Si substitutions could be performed to achieve the 3:1 ratio of copper to silicon. The curves for 8 and 12 unit cells consider energy penalties for the arrangements where 2 and 3 substitutions occur in the same η'-Cu_7Si_2 unit cell.

6. Conclusions

We have analyzed the energetics of η'-Cu_3Si crystals using quantum mechanics, and demonstrated that their formation is due to entropic driving forces resulting from the introduction of disordered silicon into the η'-Cu_7Si_2 structure deduced by Solberg in 1978 from electron diffraction and microscopy data.

SUPPORTING INFORMATION

1. Pseudopotentials and Basis Sets

The pseudopotentials used in these calculations are standard norm-conserving, non-separable pseudopotentials[20] generated using Hamann's methods[21,22] (the new method[22] was used for all atoms). The pseudopotentials for both silicon and copper included up to *l*=2 projectors (with standard settings), with the *l*=2 potential used as the local potential in

each case. The basis functions are double-zeta plus polarization quality, formed from contracted Gaussians. Hence the *occupied* orbitals Si-*s* and Si-*p*, for example, have two radial degrees of freedom, and the Si-*d unoccupied* angular polarization orbitals have only one. The basis sets for silicon and copper are contracted (4s3p1d/2s2p1d) and (4s2p5d/2s2p2d) basis sets, respectively. This nomenclature denotes, for Si for example, that four Gaussian *s*-functions are contracted into two independent functions, three Gaussian *p*-functions are contracted into two independent functions, and one *d*-function is used as one independent radial degree of freedom. The *d*-functions are made up of the five pure *l*=2 functions, i.e., the *s*-combination is excluded. The Gaussians and contraction coefficients for silicon and copper are listed in Tables S-1 and S-2.

Table S-1: Basis set for silicon. The Gaussian decay constants α (1/bohr^2), and associated contraction coefficients c_α for the contracted Gaussian basis functions (unnormalized).

s-functions			**p-functions**			**d-function**	
α_s	c_α (1st zeta)	c_α (2nd zeta)	α_p	c_α (1st zeta)	c_α (2nd zeta)	α_d	c_α
0.104600	0.209953	1.0	0.094241	0.067616	1.0	0.450000	1.000000
0.272263	0.559782	0	0.317679	0.318212	0		
1.300508	-0.991282	0	1.561145	-0.066383	0		
2.601030	0.334871	0					

Table S-2: Basis set for copper. The Gaussian decay constants α (1/bohr^2), and associated contraction coefficients c_α for the contracted Gaussian basis functions (unnormalized).

s-functions			**d-functions**			**p-functions**	
α_s	c_α (1st zeta)	c_α (2nd zeta)	α_p	c_α (1st zeta)	c_α (2nd zeta)	α_d	C_α
0.073487	0.175850	1.000000	0.183064	0.025793	1.000000	0.180000	1.000000
0.250364	0.264330		0.536815	0.201790		0.780000	-0.498700
0.905890	-0.773679		1.172893	0.784114			
1.811800	0.349976		2.411359	7.211173			
			6.087753	-0.870556			

2. Wave Function Grids and K-points

The number of k-points for each calculation was varied inversely proportional to the unit cell size according to the formula, K.P. = $65/d_{u.v.}$, where K.P. is the number of k-points in the direction of a given unit vector, and $d_{u.v.}$ is the length of that unit vector.

The wave function grid setting was 0.33 Bohr for all calculations.

REFERENCES:

1. Rieger, H.; *Phys. Status Solidi* **1964,** *7,* 685.
2. Fiermans, L.; Vennik, J.; *Phys. Status Solidi* **1965,** *12,* 277.

3. Fiermans, L.; Vennik, J.; *Phys. Status Solidi* **1967,** *21,* 627.

4. Fiermans, L.; Vennik, J.; *Phys. Status Solidi* **1967,** *22,* 463.

5. Nes, E.; Washburn, J.; *J. Appl. Phys.* **1971,** *42,* 3562.

6. Nes, E.; Washburn, J.; *J. Appl. Phys.* **1972,** *43,* 2005.

7. Nes, E.; Washburn, J.; *J. Appl. Phys.* **1973,** *44,* 3682.

8. Nes. E.; Solberg, J.K.; *J. Appl. Phys.* **1973,** *44,* 486.

9. Solberg, J.K.; Nes, E.; *J. Mat. Sci.* **1978,** *13,* 2233.

10. Solberg, J.K.; Nes, E.; *Philos. Mag.* **1978,** *37,* 465.

11. Solberg, J.K.; *Acta Cryst.* **1978,** *A34,* 684.

12. Das, G.; *J. Appl. Phys.* **1973,** *44,* 4459.

13. Hansen, M.; ***"CONSTITUTION OF BINARY ALLOYS",*** *Research Metallurgist, Metallgesellschaft A.G.,* Frankfurt 1989, pp 630-633.

14. Elliot, R.P.; ***"CONSTITUTION OF BINARY ALLOWS, FIRST SUPPLEMENT",*** *Senior Metallurgist, IIT Research Institute,* Chicago 1986, pp. 384-385.

15. Magaud, L.; Guillet, S.; Lopez-Rios, T.; *Physica B* **1996,** *225,* 225.

16. Andersen, O.K.; *Phys. Rev. B* **1975,** *12,* 3060.

17. Solberg, J.K. ***"Precipitation of Interstitially Dissolved Copper in Dislocation-Free Silicon",*** Thesis, University of Oslo, 1975.

18. Schultz, P. A.; Sandia National Labs: Albuquerque, NM, ***SeqQuest Electronic Structure Code***, http://dft.sandia.gov/Quest/

19. Perdew, J. P.; Burke, K.; Ernzerhof, M., *Phys. Rev. Lett.* **1996,** *77,* 3865.

20. Redondo, A.; Goddard, W.A. III; McGill, T.C.; *Phys. Rev. B* **1997,** *15,* 5038

21. Hamann, D.R.; *Phys. Rev.* **1989,** *40*, 2980.

22. Hamann, D.R.; pseudopotential generation program PUNSLDX, unpublished.